

# **Studies of intensified small-scale processes for liquid-liquid separations in spent nuclear fuel reprocessing**

*By*

**DIMITRIOS TSAOULIDIS**

Department of Chemical Engineering

University College London

Torrington Place, London, WC1E 7JE, UK

**June 2014**

\*A thesis submitted for the degree of

**Doctor of Philosophy**

## Declaration

I, **Dimitrios Tsaoulidis**, declare that the thesis and the work presented in it are my own and have been generated by me as the result of my own original research. Where information has been derived from other sources, I can confirm that this has been clearly indicated in the thesis.

.....

**Dimitrios Tsaoulidis**

*This Thesis is dedicated to my family.*

My parents

**Alexandros Tsaoulidis and Panagiota Papadopoulou**

and my sister

**Alexia Tsaoulidou**

**For their endless & unconditional love, sacrifices, and  
encouragement throughout my life.**

## **Abstract**

The main contribution of the thesis is to study and develop small-scale processes for ionic liquid-based extractions that can intensify the liquid-liquid separations in the spent nuclear fuel reprocessing cycle. The industrial application of small scale processes requires that their hydrodynamics and mass transfer behaviour are well characterised and predicted. In addition, modelling methodologies are proposed to evaluate the applicability of the small scale extractors in reprocessing the large volumes of nuclear waste used in industrial scale.

The first part of the work involves the study of the hydrodynamic behaviour of two-phase (ionic liquid-aqueous) flows. Flow pattern formations within channels have been identified for a wide range of operating conditions and were found to be strongly affected by channel size and material, fluid properties, and flow rates. The main patterns observed were plug flow, annular flow, and drop flow. Subsequently, the work focused on the investigation of the plug flow which has been found to enhance mass transfer because of circulation patterns that develop within the phases. Plug flow was thoroughly investigated in various channel sizes of different material mainly for TBP/ionic liquid (30% v/v) mixtures-nitric acid solutions, relevant to spent nuclear fuel reprocessing. Several hydrodynamic characteristics, such as plug length, plug velocity, film thickness, and pressure drop have been investigated for different ionic liquids, channel sizes, and phase flow rates. Results have been compared with literature, and new (or modified) correlations have been proposed for estimating the plug length, film thickness, and pressure drop. Furthermore, circulation patterns and mixing characteristics within aqueous plugs were investigated by means of  $\mu$ -PIV (micro Particle Image Velocimetry). The mixing within a plug was locally quantified by the non-dimensional circulation time and the results were correlated with the mass transfer performance. Mixing within the plug was found to be affected by several parameters, but the most decisive one was the size of the channel; mixing was enhanced by decreasing the channel diameter. The last stage of the experimental part of this research involves studies of the extraction of dioxouranium(VI) ions from nitric acid solutions into TBP/IL mixtures (30%, v/v), relevant to spent nuclear fuel reprocessing in channels with sizes ranging from 0.5 to 2 mm ID. The effects of ionic liquid type, initial nitric acid concentration, and residence time on the extraction performance of the contactor were studied. Experimental mass transfer coefficients

were compared against predictive models derived from the literature and good agreement was found with those for liquid-liquid contactors. Experimental results were also compared with extraction units already in operation in spent nuclear reprocessing plants. It was found that comparable amount of spent nuclear fuel (1045 tonnes per year) can be reprocessed and extraction of dioxouranium(VI) >99% can be achieved in 4 stages (cycles) with approximately 400 assemblies (one assembly consists of 6 channels of 2 mm internal diameter and 285 cm length). Finally, a numerical finite element model for the hydrodynamics and mass transfer was developed, and the results were compared with the experimental findings. The model used experimental data for the geometric characteristics of the plug flow and predicted reasonably well the experimentally measured extraction efficiencies (with a 11.3 % mean relative error).

## Refereed journal paper

DORE, V., TSAOULIDIS, D. & ANGELI, P. 2012. Mixing patterns in water plugs during water/ionic liquid segmented flow in microchannels. *Chemical Engineering Science*, 80, 334-341.

TSAOULIDIS, D., DORE, V., ANGELI, P., PLECHKOVA, N. V. & SEDDON, K. R. 2013a. Dioxouranium(VI) extraction in microchannels using ionic liquids. *Chemical Engineering Journal*, 227, 151-157.

TSAOULIDIS, D., DORE, V., ANGELI, P., PLECHKOVA, N. V. & SEDDON, K. R. 2013b. Extraction of dioxouranium(VI) in small channels using ionic liquids. *Chemical Engineering Research & Design*, 91, 681-687.

TSAOULIDIS, D., DORE, V., ANGELI, P., PLECHKOVA, N. V. & SEDDON, K. R. 2013c. Flow patterns and pressure drop of ionic liquid–water two-phase flows in microchannels. *International Journal of Multiphase Flow*, 54, 1-10.

DEDIGAMA, I., ANGELI, P., AYERS, K., ROBINSON, J., SHEARING, P., TSAOULIDIS, D. & BRETT, D. 2014a. In situ diagnostic techniques for characterisation of polymer electrolyte membrane water electrolyzers–Flow visualisation and electrochemical impedance spectroscopy. *International Journal of Hydrogen Energy*, 39, 4468-4482.

DEDIGAMA, I., ANGELI, P., VAN DIJK, N., MILLICHAMP, J., TSAOULIDIS, D., SHEARING, P. R. & BRETT, D. J. 2014b. Current density mapping and optical flow visualisation of a polymer electrolyte membrane water electrolyser. *Journal of Power Sources*, 265, 97-103.

TSAOULIDIS, D. & ANGELI, P. 2014. Effect of channel size on mass transfer during liquid-liquid plug flow in small scale extractors. (submitted)

TSAOULIDIS, D. & ANGELI, P. 2014. Hydrodynamics, mixing characteristics and pressure drop in liquid-liquid plug flow in small channels using ionic liquids. (in preparation)

### **Conferences**

Tsaoulidis D., Dore V., Plechkova N., Seddon K.R., Angeli P., 2011. Liquid-liquid flows in Microchannels. In proceedings of the 3rd Micro and Nano Flows Conference, 22-24 August, Thessaloniki, Greece

Tsaoulidis D., Dore V., Angeli, P., 2012. Microchannel extractions using ionic liquids for spent nuclear fuel reprocessing. In proceedings of the 12<sup>th</sup> International Conference on Microreaction Technology 20-22 February, Lyon, France

Tsaoulidis D., Dore V., Plechkova N., Seddon K.R., Angeli P., 2012. Uranium extractions in small channels using ionic liquids. In proceedings of the Nuclear Fuel Cycle Conference, 23-25 April, Manchester, UK

Dore V., Tsaoulidis D., Angeli P., 2012.  $\mu$ -PIV investigation of water/ionic liquid plug flow dynamics in meandering microchannels. In proceedings of 16th International Symposium on Applications of Laser Techniques to Fluid Mechanics, 09-12 July, Lisbon, Portugal

Tsaoulidis D., Dore V., Angeli, P., 2012. Extraction of U(VI) in microfluidic channels using ionic liquids. In proceedings of 3<sup>rd</sup> European Conference on Microfluidics, 03-05 December, Heidelberg, Germany

Tsaoulidis D., Li Q., Angeli, P., 2013. Hydrodynamics and mixing characteristics in small channels using ionic liquids for spent nuclear fuel reprocessing applications. In proceedings of the 8<sup>th</sup> International Conference on Multiphase Flow, Jeju, Korea, May 26-31

Tsaoulidis D., Li Q., Angeli, P., 2013. Flow characteristics of ionic liquid-aqueous two-phase flows in small channels. In proceeding of the 10<sup>th</sup> International Symposium on Particle Image Velocimetry, Delft, The Netherlands, July 1-3

Tsaoulidis D. & Angeli P., 2014. Spent nuclear reprocessing: Intensified extraction of  $\{\text{UO}_2\}^{2+}$  in small channels using ionic liquids. Sustainable Nuclear Energy Conference 2014, Manchester, UK, April 9-11

Tsaoulidis D., Plechkova N., Seddon K. R., & Angeli P., 2014.  $\{UO_2\}^{2+}$  extraction using ionic liquids in intensified extractors. Proceedings of the 22<sup>nd</sup> International Conference on Nuclear Engineering 2014, Prague, Czech Republic, July 7-11.

Tsaoulidis D., Li Q., Chinaud M., & Angeli P., 2014. Two-phase aqueous-ionic liquid flows in small channels of different diameter. 4<sup>th</sup> Micro and Nano Flows Conference, London, UK, September 7-10

### **Symposia**

ICHEME Fluid Separations Special Interest Group (FSSIG) annual research event "What's New in Fluid Separations?" at London Southbank University, London, UK, 8 June 2011.

Dore V., Tsaoulidis D., Angeli P., 2011. "Two-phase liquid flows in microchannels for extraction applications"

ICHEME Fluid Separations Special Interest Group (FSSIG) annual research event "What's New in Fluid Separations?" at Air Products Plc., European Technology Group, Basingstoke, Reading, UK, 16 May 2012. Tsaoulidis D., Dore V., Plechkova N., Seddon K.R., Angeli P., 2012 "Uranium extractions in small channels using ionic liquids." (Prize winner)

The Royal Academy of Engineering, Event: Next Generation Nuclear Energy- The UK's Role. 5 June 2013

### **Competitions**

SET for BRITAIN March 17<sup>th</sup> 2014. "Green Solvents" for Intensified Spent Nuclear Fuel Reprocessing



### Acknowledgements

I would like to express my sincere gratitude to my advisor and supervisor Professor Panagiota Angeli for her continuous support, guidance, motivation, encouragement, and immense knowledge she provided throughout my PhD research. I am truly honoured to have been able to do research under her mentorship.

Besides my supervisor, I would like to thank my second supervisor Professor Asterios Gavriilidis for his encouragement, and his contribution with insightful comments and advices in my work.

I also want to acknowledge the UK Engineering and Physical Science Research Council (EPSRC), and TSI instruments for providing me the appropriate equipment to carry out the experiments.

Special acknowledgements go to Professor Kenneth R. Seddon and Dr. Natalia Plechkova of Queen's University (QUILL) for their collaboration and for supplying the ionic liquids, and Dr Simon Barrass and Mr Mike Gorecki from UCL for their invaluable help with the experimental apparatus. I want to express thanks to Dr Valentina Dore for her collaboration and help in my starting steps on the field of  $\mu$ -PIV. Many thanks to all the PhD students in the department for sharing their lab experience with me. Finally, I would like to thank Dr Maryam Parhizkar for her inestimable support and encouragement all this time, and for sharing her knowledge on the field of micro-fluidics.

I would also like to thank all my friends for their help and support throughout my PhD studies, each one of them with a unique way. I was too lucky having my friends so close to me throughout this new attempt. I want to thank Mr Alexandros Fragkou for his priceless support, understanding, and encouragement these 3 years. I also want to thank Mr Alexandros Koukoudis for his continuous help and support. I also want to thank my friends back in Greece; Mr Ampatzidis Xaris, Mr Chrysostomidis Savvas, Mr Kyrkilis Petros, Mr Mouratidis Pavlos, Mr Saakian Chris, Mr Siamatras Valantis, Mr Tsompanis Stelios, Mr Tsoukalas Ioannis, Mr Velissaropoulos Ioannis, for making the distance too short with their moral support and encouragement during this period.

Last but not least, I would like to express gratitude to my family; my father, Mr Alexandros Tsaoulidis, and my mother, Mrs Panagiota Papadopoulou for their love, belief, support, and sacrifices, as well as for the knowledge that they offered me, and my sister, Ms Alexia Tsaoulidou, for her love, encouragement, and motivation. Without them I would not have been able to face this challenge in my life.

I cannot imagine myself able to achieve this goal without all these people around me.

Thank you all!

## Contents

Abstract .....	1
Refereed journal paper .....	3
Acknowledgements .....	6
Contents .....	8
List of Figures .....	13
List of Tables .....	22
Nomenclature .....	23
<b>•Chapter 1. Introduction &amp; Background .....</b>	<b>26</b>
1.1 Scope of the Thesis .....	26
1.2 Process intensification .....	26
1.3 Micro-technology .....	27
1.4 Spent nuclear fuel reprocessing .....	28
1.5 Ionic liquids .....	29
1.6 Outline of the Thesis .....	29
<b>•Chapter 2. Literature review .....</b>	<b>31</b>
2.1 Multi-phase flows .....	31
2.1.1 Flow patterns in micro and small channels .....	31
2.1.2 Phase separation in micro and small channels .....	38
2.1.3 Flow patterns in pipes .....	40
2.2 Plug flow .....	41
2.2.1 Mechanisms of plug formation in cross-flowing devices .....	41
2.2.2 Plug size .....	43
2.2.3 Film thickness .....	45
2.2.4 Plug velocity .....	47

2.2.5	Internal circulation .....	49
2.2.5.1	Particle image Velocimetry (PIV).....	52
2.2.6	Pressure drop.....	52
2.2.7	Mass transfer .....	57
2.3	Ionic liquid-based extractions: Reprocessing of spent nuclear fuel .....	64
2.3.1	Studies on the extraction mechanisms .....	65
2.3.2	Task specific ionic liquids.....	68
2.3.3	Physicochemical properties of ionic liquids .....	69
2.3.4	UV-Vis spectroscopy .....	71
2.4	Overview .....	72
	<b>•Chapter 3. Experimental details .....</b>	<b>74</b>
3.1	Introduction .....	74
3.2	Materials.....	74
3.2.1	Ionic liquids .....	74
3.2.2	Aqueous solutions.....	75
3.2.3	Particles.....	76
3.2.4	Dioxouranium(VI) nitrate hexahydrate ( $\text{UO}_2(\text{NO}_3)_2 \cdot 6\text{H}_2\text{O}$ ) .....	76
3.3	Characterization of solutions.....	77
3.3.1	Viscosity.....	77
3.3.2	Surface tension and contact angle.....	77
3.4	Experimental setup and procedure .....	78
3.4.1	Pressure drop measurements.....	80
3.4.2	Flow splitting .....	81
3.4.3	UV-Vis spectroscopy .....	82
3.5	Techniques.....	83
3.5.1	PIV measurements .....	83

3.5.1.1	PIV setup used in glass micro-channels .....	83
3.5.1.2	PIV setup used in straight Teflon small-channels.....	86
3.5.2	Image processing .....	88
3.5.3	Estimation of the film thickness .....	90
<b>•Chapter 4. Liquid-liquid flows in micro and small channels: Hydrodynamics and pressure drop.....</b>		<b>92</b>
4.1	Introduction .....	92
4.2	Flow patterns and pressure drop of ionic liquid-water two-phase flows .....	92
4.2.1	Flow patterns.....	94
4.2.1.1	Flow patterns in glass microchannels .....	94
4.2.1.2	Flow patterns in Teflon microchannels.....	98
4.2.1.3	Comparison of flow pattern boundaries in the three test sections .....	100
4.2.2	Effects of flow configuration on pressure drop during liquid-liquid flow.....	102
4.2.2.1	Teflon microchannels .....	102
4.2.2.2	Glass microchannel.....	104
4.2.2.3	Comparison of the pressure drop for the 3 test sections.....	105
4.3	Plug flow characteristics .....	107
4.3.1	Plug formation .....	107
4.3.2	Plug size .....	109
4.3.2.1	Comparison with literature models.....	112
4.3.3	Film thickness .....	114
4.3.4	Plug velocity .....	116
4.3.5	Pressure drop.....	119
4.4	Conclusions.....	122
<b>•Chapter 5. Circulation patterns and mixing characteristics of liquid-liquid flows in small channels.....</b>		<b>124</b>

5.1	Introduction .....	124
5.2	Velocity fields and velocity profiles in plugs .....	124
5.3	Circulation patterns .....	128
5.4	Circulation time, $\tau$ .....	132
5.4.1	Stagnation points and vortex length.....	140
5.5	Conclusions .....	142
	<b>•Chapter 6. Liquid-liquid mass transfer using ionic liquids .....</b>	<b>144</b>
6.1	Introduction .....	144
6.2	Extraction of dioxouranium(VI) at equilibrium .....	144
6.3	Continuous extraction of dioxouranium(VI) in small channels .....	148
6.3.1	Effect of initial nitric acid concentration on dioxouranium(VI) extraction in small channels.....	149
6.3.2	Effects of residence time on dioxouranium(VI) extraction in small channels.	151
6.3.3	Effects of flow rate ratio on dioxouranium(VI) extraction .....	154
6.3.4	Effects of channel size on the mass transfer performance .....	155
6.4	Volumetric mass transfer coefficients .....	158
6.4.1	Effect of initial nitric acid concentration on $k_L\alpha$ .....	158
6.4.2	Effect of residence time on $k_L\alpha$ .....	159
6.4.3	Effect of channel size.....	160
6.5	Scaling aspects of a liquid-liquid small scale extractor .....	162
6.6	Conclusions .....	166
	<b>•Chapter 7. Modelling of a micro-extractor.....</b>	<b>168</b>
7.1	Introduction .....	168
7.2	Model formulation.....	169
7.3	Results and discussion.....	171
7.3.1	Comparison with literature models .....	171

7.3.2	Comparison with numerical model .....	173
7.4	Conclusions .....	178
	<b>•Chapter 8. Conclusions &amp; future developments .....</b>	<b>179</b>
8.1	Overview of thesis.....	179
8.2	Future developments .....	183
	<b>•References.....</b>	<b>186</b>
	Appendix A: Calculation of the circulation time .....	196
	Appendix B: Circulation patterns at the bend of the channel .....	197
	Appendix C: MATLAB code for image processing .....	198
	Appendix D: Sensitivity analysis of diffusion coefficient .....	200
	Appendix E: Numerical model report.....	201

## List of Figures

Figure 2.1: Flow configurations obtained in microchannels (a) Drop flow, (b) Plug (slug) flow, (c) Plug-drop flow, (d) Deformed interface flow, (e) Annular flow, (f) Parallel flow, (g) Plug-dispersed flow, (h) Dispersed flow. (Kashid et al., 2011) .....	33
Figure 2.2: Inertial, viscous and gravitational body forces, relative to interfacial forces, as a function of the channel size and characteristic velocity in microfluidic multiphase systems. (Günther and Jensen, 2006) .....	34
Figure 2.3: Flow patterns map for silicon oil-water flow in a 250 $\mu\text{m}$ microchannel initially saturated with oil. The solid lines indicate the flow pattern transition boundaries, i.e. (I) interfacial forces dominant, (II) interfacial and inertia forces were comparable, (II) viscous forces $>$ inertia $>$ interfacial forces, (IV) inertia and viscous forces were comparable, and (VI) inertia dominant. (Foroughi and Kawaji, 2011).....	36
Figure 2.4: Mixing zone configurations for plug flow formation.....	37
Figure 2.5: $Re_c/Ca_c$ as a function of $Re_d d_h/\epsilon_d$ . ( $\square$ ) surface dominated, ( $\times$ ) transition, ( $\circ$ ) inertia dominated. (Kashid and Kiwi-Minsker, 2011).....	38
Figure 2.6: A schematic of separation devices during liquid-liquid plug or parallel flow. (A) Phase separation using a Y-splitter (Kashid et al., 2007b), (B) Phase separation by capillary forces (Angelescu et al., 2010), (C) Phase separation during parallel flow (Aota et al., 2007) and (D) Phase separation by wettability combined with pressure balance (Scheiff et al., 2011). .....	39
Figure 2.7: Experimental flow pattern transition lines. (Wegmann and Rudolf von Rohr, 2006) .....	40
Figure 2.8: A schematic illustration of the break-up process of a plug at the T-junction of the microchannels. (a) the growing stage, (b) the squeezing stage. (Garstecki et al., 2006).....	42
Figure 2.9: Qualitative schematic of flow streamlines in the liquid slug ahead of elongated bubbles in capillaries. (a) $m > 0.5$ ; (b) & (c) $m < 0.5$ , where $m = (u_b - u_{\text{mix}})/u_b$ . (Taylor, 1961) .....	49
Figure 2.10: Flow fields in a droplet when flowing (velocity of $7.6 \text{ mm s}^{-1}$ ) in straight channels (A) and in bend channels (B). (Malsch et al., 2008).....	51
Figure 2.11: (a) Unit cell without film, (b) Unit cell with thin film, (c) plug flow in the case of a dry wall, and (d) plug flow in the case of a wetted wall. (Jovanović et al., 2011).....	55



Figure 2.12: Schematic representation of the transport mechanisms within a plug. (Ghaini et al., 2011) .....	59
Figure 2.13: Typical cations and anions for the composition of ionic liquids. ....	65
Figure 2.14: Variation of the dioxouranium(VI) extraction coefficient as a function $[\text{HNO}_3]_{\text{aq,init}}$ , at $[\text{TBP}]_{\text{IL,init}}=1.1$ M. (Dietz and Stepinski, 2008): $\Delta$ - $[\text{C}_{10}\text{mim}][\text{NTf}_2]$ , $\blacksquare$ - $[\text{C}_8\text{mim}][\text{NTf}_2]$ , $\diamond$ - $[\text{C}_5\text{mim}][\text{NTf}_2]$ . (Giridhar et al., 2008): $\blacklozenge$ - $[\text{C}_4\text{mim}][\text{NTf}_2]$ . (Billard et al., 2011b): $\circ$ - $[\text{C}_4\text{mim}][\text{NTf}_2]$ . $[\text{U}]=10^{-2}$ M or $10^{-3}$ M. (Billard et al., 2011b) .....	66
Figure 2.15: Dependency of the uranium distribution ratio, $K_U$ , on TBP concentration in $[\text{C}_{10}\text{mim}][\text{NTf}_2]$ at constant (3 M) nitric acid concentration. (Dietz and Stepinski, 2008) .....	67
Figure 2.16: Comparison of distribution ratios for the extraction of U(VI) by $[\text{bmim}][\text{PF}_6]$ , $[\text{bmim}][\text{NTf}_2]$ and 1.1 M TBP/diluent as a function of the initial nitric acid concentration. The diluents are n-dodecane (DD), $[\text{bmim}][\text{NTf}_2]$ and $[\text{bmim}][\text{PF}_6]$ . (Vasudeva Rao et al., 2008) .....	68
Figure 2.17: Generic structure of the ionic liquids synthesized by (Bell and Ikeda, 2011) .....	69
Figure 2.18: Variation of the water in the $[\text{C}_4\text{mim}][\text{NTf}_2]$ phase as a function of $[\text{HNO}_3]_{\text{aq,init}}$ , for various values of TBP loading. $\bullet$ - $[\text{TBP}]_{\text{IL,init}}=0\text{M}$ ; $\square$ - $[\text{TBP}]_{\text{IL,init}}=0.18\text{M}$ ; $\circ$ - $[\text{TBP}]_{\text{IL,init}}=0.55\text{M}$ ; $\blacktriangle$ - $[\text{TBP}]_{\text{IL,init}}=1.1\text{M}$ . (Billard et al., 2011b) .....	70
Figure 2.19: a) Aqueous phase spectra of uranium(VI) before extraction; b) IL-phase spectra after extraction of uranium(VI) from the aqueous phase into $[\text{bmim}][\text{NTf}_2]$ . Extraction of uranium(VI) in 3M $\text{HNO}_3$ reaches 95% with 30%v/v TBP in the IL phase (Wang et al., 2009). .....	72
Figure 3.1: Schematic of contact angle formed by sessile liquid drops on a smooth solid surface. ....	78
Figure 3.2: Schematic of the experimental setup used for the hydrodynamic and mass transfer experiments. ....	79
Figure 3.3: Photographs of the channels used in this work. (A) Glass microchannel (Dolomite microfluidics), and (B) and (C) glass and Teflon tubing (Aquilant Scientific) .....	79
Figure 3.4: T- and Y-junctions for mixing the two liquids. ....	80
Figure 3.5: Schematic representation of the pressure drop configuration. ....	81
Figure 3.6: Flow splitter connected at the end of the test channel. ....	82

Figure 3.7: (A) Schematic and (B) photograph. (C) Side view of the micro-channel. Cross section is circular with internal diameter of 0.2 mm. The observation plane (XY) is positioned downstream about 30 mm away from the T inlet. Drawing not to scale. ....	84
Figure 3.8: Photograph of the experimental setup for simultaneous performance of PIV and mass transfer measurements. ....	86
Figure 3.9: (A) Velocity vector field for single phase run at mixture velocity of $0.015 \text{ m s}^{-1}$ . (B) Velocity profile along Y direction averaged across the channel length, compared with the analytical laminar flow profile (solid line). ....	88
Figure 3.10: (A1-D1) Sample raw images within a plug formation cycle of period $T=1.05 \text{ s}$ and (A2-D2) corresponding mask images. Water is the carrier fluid. ....	90
Figure 3.11: (A) Sample raw image. (B) Binary images for the channel, and (C) water plug, obtained after image processing of (A) and binarization with different thresholds.....	91
Figure 3.12: Image of a “bullet shape” plug with no apparent flat film region. ....	91
Figure 4.1: Ionic liquid-water flow patterns in the glass microchannels with a T-junction inlet, when water was first injected in the channel. ....	95
Figure 4.2: Photographs of ionic liquid-water two-phase flow patterns in microchannels. ....	96
Figure 4.3: Ionic liquid-water flow patterns in the two Teflon microchannels, i.e. FEP and Tefzel, with a T-junction inlet. Symbols correspond to FEP channel, while lines to Tefzel. ..	98
Figure 4.4: Comparison of the flow pattern boundaries in the FEP, Tefzel, and glass microchannels with a T-junction as inlet. ....	101
Figure 4.5: Two-phase pressure drop versus input ionic liquid volume fraction at different ionic liquid flow rates for the FEP microchannel and (a) T-junction, (b) Y-junction inlet. $Q_{IL}$ : (1) = $1.13 \text{ cm}^3 \text{ h}^{-1}$ , (2) = $2.26 \text{ cm}^3 \text{ h}^{-1}$ , (3) = $5.65 \text{ cm}^3 \text{ h}^{-1}$ , (4) = $8.48 \text{ cm}^3 \text{ h}^{-1}$ . Flow pattern symbols: Annular (+), Plug (■), Drop (○), Irregular (Δ) .....	103
Figure 4.6: Two-phase pressure drop versus input ionic liquid volume fraction at different ionic liquid flow rates for the Tefzel microchannel with T-junction as inlet. $Q_{IL}$ : (1) = $1.13 \text{ cm}^3 \text{ h}^{-1}$ , (2) = $2.26 \text{ cm}^3 \text{ h}^{-1}$ , (3) = $5.65 \text{ cm}^3 \text{ h}^{-1}$ , (4) = $8.48 \text{ cm}^3 \text{ h}^{-1}$ , (5) = $11.3 \text{ cm}^3 \text{ h}^{-1}$ . Flow pattern symbols: Annular (+), Plug (■), Drop (○), Irregular (Δ).....	104
Figure 4.7: Two-phase pressure drop versus input ionic liquid volume fraction during plug flow at different ionic liquid flow rates for the glass microchannel with a T-junction as inlet. The pressure drop values for single phase ionic liquid are given on the right. $Q_{IL}$ :	

(1) = 1.13 cm <sup>3</sup> h <sup>-1</sup> , (2) = 2.26 cm <sup>3</sup> h <sup>-1</sup> , (3) = 5.65 cm <sup>3</sup> h <sup>-1</sup> , (4) = 8.48 cm <sup>3</sup> h <sup>-1</sup> , (5) = 11.3 cm <sup>3</sup> h <sup>-1</sup> , (6) = 14.1 cm <sup>3</sup> h <sup>-1</sup> .....	105
Figure 4.8: Comparison of non-dimensional pressure drop in the FEP, Tefzel and glass microchannels with internal diameter of 220 μm, 270 μm, and 200 μm, respectively, with a T-junction as inlet, at a constant ionic liquid flow rate, $Q_{IL} = 2.26 \text{ cm}^3 \text{ h}^{-1}$ .....	106
Figure 4.9: Phase averaged vector fields in the water for different stages of the ionic liquid plug formation cycle, when water is the carrier fluid. Six instantaneous fields per stage were averaged. ....	108
Figure 4.10: Phase averaged vector fields in the water for different stages of the “aqueous plug” formation, when ionic liquid is the carrier fluid. Twenty instantaneous fields per stage were averaged. ....	109
Figure 4.11: Normalised plug length $L_p/ID$ as a function of the $Ca$ at three different channel sizes (Teflon channels) for equal flow rates of the two phases (two-phase system: TBP/[C <sub>4</sub> mim][NTf <sub>2</sub> ] (30%, v/v)-nitric acid solution).....	110
Figure 4.12: Normalised plug length $L_p/ID$ as a function of the $Ca$ for three different volume fractions of the carrier fluid (ionic liquid) in a 0.2 mm ID glass microchannel (two-phase system: [C <sub>4</sub> mim][NTf <sub>2</sub> ]-water). ....	111
Figure 4.13: Plug length $L_p$ as a function of the flow rate ratio of the dispersed phase at (A) constant mixture velocity $u_{mix} = 0.01 \text{ m s}^{-1}$ , and (B) constant velocity of the carrier phase in the 0.2 mm ID glass channel.....	111
Figure 4.14: Plug shape at (A) low and (B) high total volumetric flow rate in a 2mm ID channel. ....	112
Figure 4.15: Relationship between the various parameters affecting the plug length. ....	114
Figure 4.16: Non-dimensional film thickness ( $\delta/ID$ ) as a function of $Ca$ number and comparison with literature correlations. ....	115
Figure 4.17: Plug velocity $u_p$ as a function of the mixture velocity $u_{mix}$ . ....	117
Figure 4.18: Plug velocity $u_p$ as a function of the flow rate ratio $Q_{IL}/Q_{HNO_3}$ at constant mixture velocity of $0.01 \text{ m s}^{-1}$ .....	117
Figure 4.19: Comparison of experimental plug velocity with literature models. ....	118
Figure 4.20: Experimental pressure drop during liquid-liquid plug flow as a function of the mixture velocity in 4 different channels at flow rate ratio equal to 1. ....	119

Figure 4.21: Comparison of the pressure drop calculated by Kashid and Agar (Kashid and Agar, 2007) model to the experimental results of this work for 4 different channel sizes, mixture velocities from 0.01 to 0.16 ms <sup>-1</sup> , and flow rate ratios (q) from 0.5 to 1. ....	120
Figure 4.22: Comparison of the pressure drop calculated via the stagnant film model (Jovanovic et al., 2011) to the experimental results of this work for 4 different channel sizes, mixture velocities from 0.01 to 0.16 ms <sup>-1</sup> , and flow rate ratios (q) from 0.5 to 1. Red highlighted symbols correspond to C=1.7 in Eq (2.2.31). ....	122
Figure 5.1: (A) Ensemble average velocity field within an aqueous plug at $u_{\text{mix}}=0.0028 \text{ m s}^{-1}$ and $\varepsilon_{\text{IL}}=0.6$ in a 0.2 mm ID channel. The magnitude of the velocity is superimposed in grey scale. (B) Vertical profiles of the horizontal component ( $u_x$ ) of the total velocity across half of the aqueous plug. $x_c$ is the axial location of the plug centre, while the spacing between profiles, $\Delta x$ , is approximately equal to 24 $\mu\text{m}$ . [C <sub>4</sub> mim][NTf <sub>2</sub> ] as carrier fluid. ....	125
Figure 5.2: Ensemble average velocity field in grey scale within an aqueous plug at mixture velocity of 0.01 m s <sup>-1</sup> (flow rate ratio equal to 1) in a channel of (A) 0.5 mm ID, and (B) 1 mm ID. Thirty instantaneous fields were averaged. TBP/[C <sub>4</sub> mim][NTf <sub>2</sub> ] (30%, v/v) as carrier fluid. ....	126
Figure 5.3: Vertical profiles of the horizontal component of the total velocity across the aqueous plug at mixture velocity of 0.01 m s <sup>-1</sup> (flow rate ratio equal to 1). $x_c$ is the axial location of the plug centre, while the spacing between profiles, $\Delta x$ , is approximately equal to 0.041 mm and 0.068 mm in the case of the 0.5 mm ID and 1 mm ID, respectively. TBP/[C <sub>4</sub> mim][NTf <sub>2</sub> ] (30%, v/v) as carrier fluid. ....	127
Figure 5.4: Averaged velocity profiles of the horizontal velocity component $u_x$ (normalised with the maximum velocity of the plug) for a plug of length 2.6 mm in a channels of 1 mm ID. TBP/[C <sub>4</sub> mim][NTf <sub>2</sub> ] (30%, v/v) as carrier fluid. ....	128
Figure 5.5: Representative circulation patterns in the top half of water plugs found for the three regimes depending on mixture velocity, as a function of input ionic liquid volume fraction. Sixty instantaneous fields were averaged [C <sub>4</sub> mim][NTf <sub>2</sub> ] as carrier fluid. ....	129
Figure 5.6: Ensemble averaged circulation patterns within aqueous plugs at the same mixture velocity ( $u_{\text{mix}}=0.06 \text{ m s}^{-1}$ ) and flow rate ratio equal to 1 in a channel of A) 0.5 mm ID, and B) 1 mm ID. Thirty instantaneous fields were averaged. TBP/[C <sub>4</sub> mim][NTf <sub>2</sub> ] (30%, v/v) as carrier fluid. ....	130

Figure 5.7: Ensemble averaged circulation patterns in aqueous plugs for different mixture velocities (flow rate ratio equal to 1) in the 1 mm ID channel. Thirty instantaneous fields were averaged. TBP/[C <sub>4</sub> mim][NTf <sub>2</sub> ] (30%, v/v) as carrier fluid. ....	131
Figure 5.8: Ensemble averaged circulation patterns within the water phase at mixture velocity of 0.0037 m s <sup>-1</sup> and flow rate ratio equal to 1, when (A) water is the carrier phase, and (B) ionic liquid is the carrier phase. Sixty instantaneous fields were averaged. [C <sub>4</sub> mim][NTf <sub>2</sub> ] as carrier fluid.....	132
Figure 5.9: Schematic of the flow pattern inside the micro-channel of radius R in 3-D (Eq. (5.4.1)) and 2-D (Eq. (5.4.2)) reference frames. The internal recirculation parameters are sketched inside a single water plug, projected onto the mid-xy plane ( $\pi$ ), where quantities in Eq. (5.4.2) are defined.....	133
Figure 5.10: (A) Circulation pattern, (B) magnitude velocity in gray scale, and (C) non-dimensional circulation time ( $\tau$ ) profile (C) in a 0.2 mm ID channel for $u_{\text{mix}}=0.0028 \text{ m s}^{-1}$ , calculated using Eq. (5.4.2). The minimum of $\tau$ is at the axial location of the vortex cores (i.e. maximum of circulation velocity at the channel centreline). [C <sub>4</sub> mim][NTf <sub>2</sub> ] as carrier fluid. ....	135
Figure 5.11: Non-dimensional circulation time profiles across the water plug for different input ionic liquid volume fraction at low mixture velocities. Exp#1: $u_{\text{mix}}=0.0028 \text{ m s}^{-1}$ , $\epsilon_{\text{IL}}=0.6$ , $L_p=0.34 \text{ mm}$ ; Exp#2: $u_{\text{mix}}=0.0037 \text{ m s}^{-1}$ , $\epsilon_{\text{IL}}=0.5$ , $L_p=0.43 \text{ mm}$ ; Exp#3: $u_{\text{mix}}=0.0042 \text{ m s}^{-1}$ , $\epsilon_{\text{IL}}=0.4$ , $L_p=0.55 \text{ mm}$ . [C <sub>4</sub> mim][NTf <sub>2</sub> ] as carrier fluid. ....	136
Figure 5.12: Non-dimensional circulation time profile across the upper half of aqueous plug of different lengths at constant mixture velocity ( $u_{\text{mix}}=0.01 \text{ m s}^{-1}$ ) in the 1 mm ID channel. TBP/[C <sub>4</sub> mim][NTf <sub>2</sub> ] (30%, v/v) as carrier fluid. ....	136
Figure 5.13: Non-dimensional circulation time profile across the upper half of the aqueous plug for constant plug length ( $L_p=2.6 \text{ mm}$ ) at different mixture velocities ( $u_{\text{mix}}$ ) in the 1 mm ID channel. TBP/[C <sub>4</sub> mim][NTf <sub>2</sub> ] (30%, v/v) as carrier fluid. ....	137
Figure 5.14: Non-dimensional circulation time profile along the upper half of the aqueous plug for 4 channel sizes at the same mixture velocity $u_{\text{mix}}=0.01 \text{ m s}^{-1}$ .and equal flow rates of the two phases. TBP/[C <sub>4</sub> mim][NTf <sub>2</sub> ] (30%, v/v) as carrier fluid. ....	138
Figure 5.15: Non-dimensional circulation time as a function of the non-dimensional plug length for the three TBP/ionic liquid mixtures (30%, v/v) at mixture velocity of 0.02 m s <sup>-1</sup> . ....	138

Figure 5.16: Maximum circulation velocity at the centre of the plug as a function of the Ca number.....	139
Figure 5.17: Minimum of non-dimensional circulation time as a function of Ca number and for varying input ionic liquid volume fraction.....	140
Figure 5.18: Horizontal velocity component, $u_x$ , relative to the plug velocity, $u_p$ , as a function of the dimensionless radius of the plug for different plug lengths at mixture velocity of $0.01 \text{ m s}^{-1}$ ( $Q_{\text{mix}}=28.3 \text{ cm}^3 \text{ h}^{-1}$ ) for the estimation of the location of the stagnation point. ....	141
Figure 5.19: Horizontal velocity component $u_x$ relative to the plug velocity as a function of the dimensionless radius of the plug ( $L_p=2.6 \text{ mm}$ ). ....	142
Figure 6.1: Dioxouranium(VI) distribution coefficient $K_U$ between a nitric acid aqueous solution and TBP/[C <sub>4</sub> mim][NTf <sub>2</sub> ] (30% v/v) as a function of initial nitric acid concentration .....	146
Figure 6.2: UV-Vis aqueous phase spectra of dioxouranium(VI) (a) before and (b) after the extraction with different nitric acid concentrations. ....	146
Figure 6.3: Dioxouranium(VI) distribution coefficients ( $K_U$ ) between a nitric acid solution and different TBP/IL (30% v/v) systems as a function of initial nitric acid concentration, $[\text{HNO}_3]_{\text{aq,init}}$ . ....	147
Figure 6.4: Dioxouranium(VI) extraction (%E) and extraction efficiency (%E <sub>eff</sub> ) as a function of initial nitric acid concentration into TBP/[C <sub>4</sub> mim][NTf <sub>2</sub> ] (30% v/v) in a 10 cm capillary. ....	149
Figure 6.5: Dioxouranium(VI) extraction (%E) and extraction efficiency (%E <sub>eff</sub> ) as a function of initial nitric acid concentration into different TBP/IL (30% v/v) systems in a 10 cm capillary. The lines are used just to aid interpretation.....	151
Figure 6.6: Dioxouranium(VI) extraction (%E) as a function of residence time from different nitric acid solutions into TBP/[C <sub>4</sub> mim][NTf <sub>2</sub> ] (30%, v/v). Lines correspond to dioxouranium(VI) %extraction at equilibrium at 3 different initial nitric acid concentrations. ....	152
Figure 6.7: Absorption spectra of dioxouranium(VI) in TBP/[C <sub>4</sub> mim][NTf <sub>2</sub> ] (30% v/v) extracted from a 3 M nitric acid solution at different residence times in a 0.5 mm ID channel and at equilibrium after 3 h of mechanical shaking. ....	153

Figure 6.8: Dioxouranium(VI) extraction (%E) as a function of residence time from nitric acid solutions of 3 M into different TBP/IL (30%, v/v) systems. Lines correspond to dioxouranium(VI) %extraction at equilibrium into the three different ionic liquids.....	154
Figure 6.9: Dioxouranium(VI) extraction (%E) as a function of phase flow rate ratio from nitric acid solutions into TBP/[C <sub>4</sub> mim][NTf <sub>2</sub> ] (30%, v/v). Horizontal lines corresponds to dioxouranium(VI) extraction at equilibrium.....	155
Figure 6.10: Extraction efficiency (%E <sub>eff</sub> ) of dioxouranium(VI) into TBP/[C <sub>4</sub> mim][NTf <sub>2</sub> ] (30%, v/v) as a function of the residence time at constant mixture velocity ( $u_{\text{mix}} = 0.03 \text{ m s}^{-1}$ ) in the 3 different channels.....	156
Figure 6.11: Extraction efficiency (%E <sub>eff</sub> ) of dioxouranium(VI) into TBP/[C <sub>4</sub> mim][NTf <sub>2</sub> ] (30%, v/v) as a function of the mixture velocity ( $L_{\text{ch}} = 10.5 \text{ cm}$ ). (mean relative error 4.3%)	157
Figure 6.12: Total volumetric mass transfer coefficient ( $k_L \alpha$ ) as a function of $[\text{HNO}_3]_{\text{aq,init}}$ in the 0.5 mm ID channel ( $L_{\text{ch}} = 10 \text{ cm}$ ). Symbols correspond to the three different ionic liquids. ....	158
Figure 6.13: Total volumetric mass transfer coefficient ( $k_L \alpha$ ) as a function of residence time at $[\text{HNO}_3]_{\text{aq,init}} = 3 \text{ M}$ . Symbols correspond to the three different ionic liquids. ....	159
Figure 6.14: Mass transfer coefficient as a function of the mixture velocity for the 3 different channels and channel length $L_{\text{ch}} = 10.5 \text{ cm}$ . TBP/[C <sub>4</sub> mim][NTf <sub>2</sub> ] (30%, v/v) used for the extractions. ....	160
Figure 6.15: Mass transfer coefficient as a function of the mixture velocity for the 3 different channels at the same residence time ( $\sim 10 \text{ s}$ ). TBP/[C <sub>4</sub> mim][NTf <sub>2</sub> ] (30%, v/v) used for the extractions. ....	161
Figure 6.16: Mass transfer coefficient as a function of the channel length for the 3 different channels at constant mixture velocity $u_{\text{mix}} = 0.03 \text{ m s}^{-1}$ . TBP/[C <sub>4</sub> mim][NTf <sub>2</sub> ] (30%, v/v) used for the extraction. ....	162
Figure 6.17: Schematic of a 4 stage extraction. ....	163
Figure 7.1: Geometry and boundaries of the unit cell computational domain.....	170
Figure 7.2: Comparison of experimental $k_L \alpha$ with those predicted by correlations for the 3 different channels. ....	172
Figure 7.3: Circulation patterns (A) obtained by model in both plug and slug, and (B) obtained experimentally in the plug for Case 3. ....	174

Figure 7.4: Total velocity field in the computational domain for Case 3 predicted by (A) the numerical model, and (B) the experimental PIV results (Insight 4G, Tecplot). .....	175
Figure 7.5: Evolution of the concentration profile within the aqueous plug for Case 3 at different residence times as taken from numerical solution. ....	176
Figure 7.6: Extraction efficiency ( $\%E_{\text{eff}}$ ) of dioxouranium(VI), predicted by the numerical model, as a function of the residence time in 3 different channel sizes at constant mixture velocity of $0.03 \text{ m s}^{-1}$ . ....	177
Figure 7.7: Comparison of predicted extraction efficiencies of dioxouranium(VI) against the experimental ones as a function of the residence time at three different flow rate ratios ( $q=Q_{\text{IL}}/Q_{\text{HNO}_3}$ ) for constant $Q_{\text{mix}}=84.82 \text{ cm}^3 \text{ h}^{-1}$ in the 1 mm ID channel. ....	178
Figure A 1: Comparison between non dimensional circulation time profiles found using Eq. (5.4.1) and Eq. (5.4.2) for the same experimental conditions.....	196
Figure B 1: Ensemble averaged circulation pattern within a single water plug at a bend for different orientations of the plug centre (i.e. 0, $t_1$ , and 45 degree, $t_2$ ), when water (A) and ionic liquid (B) was the carrier. Sixty instantaneous fields were averaged .....	197
Figure D 1: Concentration of dioxouranium(VI) in the ionic liquid phase as a function of time for different diffusion coefficients. ....	200



## List of Tables

Table 1.1: Definition of process intensification .....	27
Table 2.1: Dimensionless numbers for the characterisation of the two-phase flow .....	35
Table 2.2 Correlations for the wall film thickness ( $\delta$ ) for gas-liquid Taylor flow .....	45
Table 2.3: Correlations for the bubble velocity $u_B$ for gas-liquid Taylor flow .....	49
Table 2.4: $k_L\alpha$ of different types of contactors.....	58
Table 2.5: Mass transfer coefficients during liquid-liquid plug and parallel flow. ....	62
Table 3.1: Properties of pure ionic liquids. ....	75
Table 3.2: Properties of TBP/ ionic liquid mixtures (30%, v/v) .....	75
Table 3.3: Spectral properties of fluorescent micro-spheres.....	76
Table 3.4: Properties of dioxouranium(VI) nitrate hexahydrate, $\text{UO}_2(\text{NO}_3)_2 \cdot 6\text{H}_2\text{O}$ .....	77
Table 4.1: Properties of test fluids. ....	93
Table 4.2: Contact angles ( $\theta^\circ$ ) on a borosilicate glass and Teflon plate. ....	94
Table 6.1: Volumetric mass transfer coefficient ( $k_L\alpha$ ) as a function of IL (TBP/[C <sub>4</sub> mim][NTf <sub>2</sub> ] (30%, v/v)) to aqueous phase ratio at initial nitric acid concentration of 1 M and 3 M in a 0.5 mm ID channel ( $L_{\text{ch}}=10$ cm). ....	159
Table 6.2: Conditions of solvent extraction capillaries for >90% extraction efficiency per stage. ....	164
Table 6.3: Chemical engineering attributes of solvent extraction contactors typical for a nuclear recycling plant throughput of 5 tonnes/year (Nash and Lumetta, 2011).....	165
Table 7.1: Parametric values used in the numerical simulations. ....	173
Table 7.2: Properties of the fluids used for the simulations.....	173

## Nomenclature

A	Cross sectional area [m <sup>2</sup> ]
Bo	Bond number = $\frac{ID^2 \Delta \rho g}{\gamma}$ [dimensionless]
[C] <sub>aq,init</sub>	Initial concentration of dioxouranium(VI) in aqueous phase [mol L <sup>-1</sup> ]
[C] <sub>aq,fin</sub>	Final concentration of dioxouranium(VI) in aqueous phase [mol L <sup>-1</sup> ]
[C] <sub>aq,eq</sub>	Concentration of dioxouranium(VI) in aqueous phase at equilibrium [mol L <sup>-1</sup> ]
Ca	Capillary number = $\frac{\mu u}{\gamma}$ [dimensionless]
Dh	Hydraulic diameter [m]
D	Diffusion coefficient [m <sup>2</sup> s <sup>-1</sup> ]
E	extraction [%]
E <sub>eff</sub>	Extraction efficiency [%]
Fr	Froude number = $\frac{u}{(gL^*)^{0.5}}$
g	Gravity [9.81 m s <sup>-2</sup> ]
[HNO <sub>3</sub> ] <sub>aq,init</sub>	initial concentration of nitric acid [mol L <sup>-1</sup> ]
ID	Internal diameter [m]
K <sub>U</sub>	Distribution coefficient of dioxouranium(VI) [dimensionless]
k <sub>L</sub>	Overall mass-transfer coefficient [m s <sup>-1</sup> ]
k <sub>L</sub> α	Overall volumetric mass transfer coefficient [s <sup>-1</sup> ]
l*	Vortex length [dimensionless]
L	Length [m]
L*	Characteristic length [m]
P	Pressure [Pa]
ΔP	Pressure drop [kPa]
q	Flow rate ratio [dimensionless]
Q	Volumetric flow rate of fluid [m <sup>3</sup> s <sup>-1</sup> ]
r	Radius [m]
R	Radius of the channel [m]
Re	Reynolds number = $\frac{\rho u ID}{\mu}$ [dimensionless]
u	Velocity [m s <sup>-1</sup> ]

V	Volume [m <sup>3</sup> ]
We	Weber number = $\frac{\rho u^2 1D}{\gamma}$ [dimensionless]
w	Width [m]
CMPO	(octyl(phenyl)-NN-diisobutylcarbamoylmethylphosphine oxide)
HDEHP	(bis(2-ethylhexyl)phosphoric acid)
TBP	tributylphosphate
TTA	(2-thenolyltrifluoroacetone)

### *Greek letters*

$\alpha$	Specific interfacial area [m <sup>2</sup> m <sup>-3</sup> ]
$\gamma$	Interfacial tension [N m <sup>-1</sup> ]
$\delta$	Film thickness [ $\mu$ m]
$\varepsilon$	Volume fraction [dimensionless]
$\theta$	angle [°]
$\lambda$	Viscosity ratio ( $\mu_d/\mu_c$ )
$\mu$	Dynamic viscosity [kg m <sup>-1</sup> s <sup>-1</sup> ]
$\rho$	Density [kg m <sup>-3</sup> ]
$\sigma$	Surface tension [N m <sup>-1</sup> ]
$\tau_{re}$	Residence time [s]
$\tau$	Non-dimensional circulation time in 2-D [dimensionless]
$\tau_{3-D}$	Non-dimensional circulation time in 3-D [dimensionless]
$\tau_f$	Non-dimensional formation time [dimensionless]

### *Subscripts*

c	continuous phase
cap	cap
ch	channel
circ	recirculation
d	dispersed phase

Eff	efficiency
film	film
g	gas phase
max	maximum
min	minimum
mix	mixture
l	liquid phase
IL	ionic liquid
p	plug
o	oil
UC	unit cell
w	water

# Chapter 1.

## Introduction & Background

### 1.1 Scope of the Thesis

The scope of the thesis is to study and develop small-scale processes for ionic liquid-based extractions that can intensify the liquid-liquid separations of the spent nuclear fuel reprocessing cycle. In addition, modelling methodologies are proposed to evaluate the applicability of the small-scale extractors in reprocessing large volumes of nuclear waste in industrial scale.

### 1.2 Process intensification

Process intensification aims at reducing the physical size of a plant, while increasing its production efficiency and ultimately resulting in cheaper and sustainable technologies. Process intensification is considered as one of the most promising development paths for the chemical process industry and one of the most important progress areas for chemical engineering research ([Van Gerven and Stankiewicz, 2009](#)). It can be achieved by using multifunctional equipment and by increasing the rates of reactions with sophisticated equipment/operating reactor configurations or using completely new energy sources. Numerous definitions of process intensification have been proposed (**Table 1.1**), which, despite their common focus on innovation, are often quite diverse in nature.

**Table 1.1: Definition of process intensification**

Process intensification...	References
...devising exceedingly compact plant which reduces both the main plant item and the installations costs.	(Ramshaw, 1983)
...strategy of reducing the size of chemical plant needed to achieve a given production objective.	(Cross and Ramshaw, 1986)
...development of innovative apparatuses and techniques that offer drastic improvements in chemical manufacturing and processing, substantially decreasing equipment volume, energy consumption, or waste formation, and ultimately leading to cheaper, safer, sustainable technologies.	(Stankiewicz and Moulijn, 2000)
...technologies that replace large, expensive, energy-intensive equipment or process with ones that are smaller, less costly, and more efficient or that combine multiple operations into fewer devices (or a single apparatus).	(Porcelli, 2003)
...integrated approach for a process and product innovation in chemical research and development, and chemical engineering in order to sustain profitability even in the presence of increasing uncertainties.	(Becht et al., 2009)

### 1.3 Micro-technology

Micro-technology is an important area in process intensification, which offers numerous potential benefits for the process industries. The pressing demands for sustainable, efficient, and safer flow processes make micro-fluidic devices an attractive option. Their novelty dictates a new approach in design, which requires familiarization with the various manufacturing techniques and materials, and with differences in fluid behaviour and dominant phenomena in micro-scale (Gavriilidis et al., 2002). The absence of inertial and turbulent effects in these devices, due to the low ratio between the inertial forces and the viscous forces offers new possibilities for physical, chemical and biological applications. In many areas, micro-technology is already established, and mass production with high precision is possible. The thin fluidic films intensify mass transfer, while the increased surface to volume ratio favours interfacial transfer rates and allows the manipulation of

interfaces to obtain favourable flow patterns (Hessel et al., 2005). Also, the short-length scales result in small diffusion distances and easy temperature profiling where needed, giving the opportunity to manipulate substances in a better and more reliable way, which gives rise to claims that every molecule has the same processing experience (Kashid et al., 2005). However, there are still challenges and uncertainties in terms of the application of micro-devices. The most controversial issue is to scale-out the existing technology. The proposed theories of bundling together multiple duplicates of the micro-channel or unit bring out problems like reactor monitoring and control, as well as equal flow and pressure drop distribution. With more advanced and more complex microfluidic devices, the need for a detailed investigation of the fluid mechanics (interfacial phenomena, wall roughness, wettability, and capillary effects) in such systems is growing.

### 1.4 Spent nuclear fuel reprocessing

The worldwide energy demands are growing rapidly due to expansion of the population and the force for economic development, while the fossil fuel resources are decreased. Furthermore, their extensive use should be restricted because of the emitted CO<sub>2</sub> and its impact on climate change. Nuclear energy from fission can be considered an alternative energy source since it can provide huge amounts of carbon free electricity, and significant expansion is anticipated. For nuclear power production, there are two fuel cycle options that are of relevance, i.e. the once through cycle with permanent disposal of spent fuel, and the closed cycle with reprocessing and recycle of uranium(VI) and plutonium(IV). Both cycles require efficient and safe waste management strategies, while issues such as non-proliferation, sustainability and even public perception need also to be taken into account since they are very important for informing policy. In order to exploit the potential of nuclear power and maximize the resource utilization, closing of the nuclear fuel cycle by reprocessing the spent fuel and recycle the uranium(VI) and plutonium(IV) back into reactor systems, is of vital importance.

### 1.5 Ionic liquids

Ionic liquids (ILs) in general are salts with low melting points (below 100° C) and very interesting properties, such as negligible vapour pressure, ability to dissolve organic, inorganic and polymeric materials, high thermal stability, and miscibility with water and other solvents, etc. (Seddon et al., 2000). Ionic liquids are extraordinarily tuneable salts and they can be easily tuned by the appropriate choice of anion and cation. Recently, considerable attention has been given to the application of ionic liquids in chemical separations, often as replacements for the conventional organic solvents employed in traditional liquid-liquid or membrane-based systems for the separation of metal ions or organic solutes, as a consequence of their unique properties. Because many ionic liquids are non-flammable and non-explosive, they are much safer than conventional organic solvents. They also have a very wide “electrochemical window” so they are very resistant to oxidation and reduction processes. Although they are polar solvents, ionic liquids are weakly coordinating and solvating. Lately, ionic liquids have been proposed for possible use in spent nuclear fuel reprocessing as promising alternatives to volatile organic compounds (VOCs) in the solvent extraction of metal ions, since the undesirable properties of VOCs pose several threats and problems both to plant operation and to environment. In addition to their unique properties, ionic liquids exhibit high resistance to radiation, which makes them particularly suitable for extractions involving radioactive materials.

### 1.6 Outline of the Thesis

This thesis consists of 8 chapters. **Chapter 1** (current chapter) provides information about the scope and the structure of the thesis, whilst background evidence about the motivation of this research is also presented. In **chapter 2**, a critical review on literature topics relevant to the thesis is given. Among others, studies on two-phase flows in microchannels, formation of plug flow, and use of ionic liquids in spent nuclear reprocessing are included. **Chapter 3** gives a detailed description of the experimental setup, materials, procedures and characterisation methods used throughout the investigation. In **chapter 4**, hydrodynamic results of liquid-liquid flows in small-channels are presented. Observations on flow patterns, plug length, film thickness, pressure drop, etc. in the various channels are discussed and



compared with existing models in the literature, and correlations based on the current experimental data are proposed. **Chapter 5** investigates the circulation patterns and the mixing characteristics of liquid-liquid flow in small channels by means of Particle Image Velocimetry (PIV). From the details of the velocity profiles within both phases, useful information about the recirculation time, location of the stagnation points and size of the circulation vortices is extracted. In **chapter 6**, the extraction of dioxouranium(VI) from nitric acid solutions by using ionic liquids in different channels is studied. The effects of parameters, such as channel size, type of ionic liquid, residence time on the mass transfer performance of the extractors are discussed. In addition, a comparison based on experimental results with extraction units already in operation in spent nuclear reprocessing plants is discussed. A numerical model was developed in **chapter 7** to solve the velocity field and predict the mass transfer in the aqueous/ionic liquid system during plug flows. The model used experimental data for the geometric characteristics of the plug flow pattern. Comparisons of the mass transfer coefficient with literature models are also included. Finally, in **chapter 8**, the conclusions of the thesis and future recommendations for optimization of the ionic liquid-based processes are given.

# Chapter 2.

## Literature review

### 2.1 Multi-phase flows

Operations in intensified channels have emerged as an important area of research and have found numerous applications in (bio)chemical analysis and synthesis, reactors, micro-power generation, fuel cells and thermal management systems. Because of their large surface to volume ratio, micro-reactors offer enhanced mass transfer rates and, therefore, they are used to carry out fast, mass transfer limited reactions. Unlike the scale-up uncertainties associated with large-scale conventional reactors, micro-reactors are scaled out by simple duplication of individual units. A number of applications in small channels involve two fluid phases, i.e. gas-liquid and liquid-liquid. Understanding of the flow characteristics and flow patterns, pressure drop and mass/heat transfer is essential in the design and the precise control of the multiphase devices. Compared to macro-contactors the flow configurations appearing in liquid-liquid micro-contactors are influenced by a variety of factors, which can be categorized into 3 groups: a) channel properties (dimensions, orientation, channel material, inlet size, mixing zone, wall roughness and wettability), b) fluid properties (density, surface tension, viscosity), and c) operation conditions (fluid flow rates, flow rate ratios temperature, pressure drop). Although there are many studies concerning gas-liquid flows, the number of studies that have been reported on the flow behaviour of two immiscible liquids in micro-channels does not mirror the numerous applications.

#### 2.1.1 *Flow patterns in micro and small channels*

In liquid-liquid systems, the flow pattern describes the spatial distributions of the two phases in the microchannels and is strongly related with the performance of the micro-reactors, since it influences the pressure drop, and heat and mass transfer within the reactor. A number of

different flow patterns can occur, which mainly depend on flow rates, flow rate ratio, channel size, inlet geometry, etc. Depending on the fluid properties and the channel material, either phase can wet the channel wall and for phases with similar wettabilities both phases can intermittently adhere to the wall, rendering ordered, stable and well-defined patterns more difficult to form than in gas-liquid flows (Wegmann and Rudolf von Rohr, 2006). The generation of a unified theory for the prediction of flow patterns for liquid-liquid flows is quite difficult due to the wide variation of physical properties of the two phases, the chemistry, and the hydrodynamics. Controlling the hydrodynamics could decrease pressure drop, improve mass transfer and facilitate product separation from the reaction mixture (Dessimoz et al., 2008).

One of the problems in studying and reporting liquid-liquid flow patterns is the lack of coherence in the terminology used by various investigators for the different flow regimes. The basic flow patterns that someone can identify in microchannels with internal diameter from 0.1 to 10 mm are the following:

- Drop flow, in which plugs of size smaller than the diameter of the channel are formed. (**Figure 2.1a**)
- Plug flow (or slug or segmented flow), where one fluid forms individual plugs cylindrical in shape. (**Figure 2.1b**)
- Plug-drop flow, where the dispersed phase flows in the form of irregular plugs and drops. (**Figure 2.1c**)
- Intermittent flow (or deformed interface flow), where the dispersed phase flows to a certain distance either in the form of parallel or annular flow and then produces irregular droplets. (**Figure 2.1d**)
- Annular flow (wavy, smooth), where one fluid occupies the space adjacent to the tube wall and surrounds the other fluid (with the lower density) that flows in the center of the tube. (**Figure 2.1e**)
- Parallel flow (wavy, smooth), where the two liquids are separated with the lighter fluid flowing on the top of the heavier liquid. (**Figure 2.1f**)
- Plug-dispersed flow, where part of the continuous phase flows in the form of small droplets in the dispersed phase. (**Figure 2.1g**)

- Dispersed flow, where very fine droplets of one phase are formed into the other phase. This flow regime is observed when the total flow rate is increased. (**Figure 2.1h**)

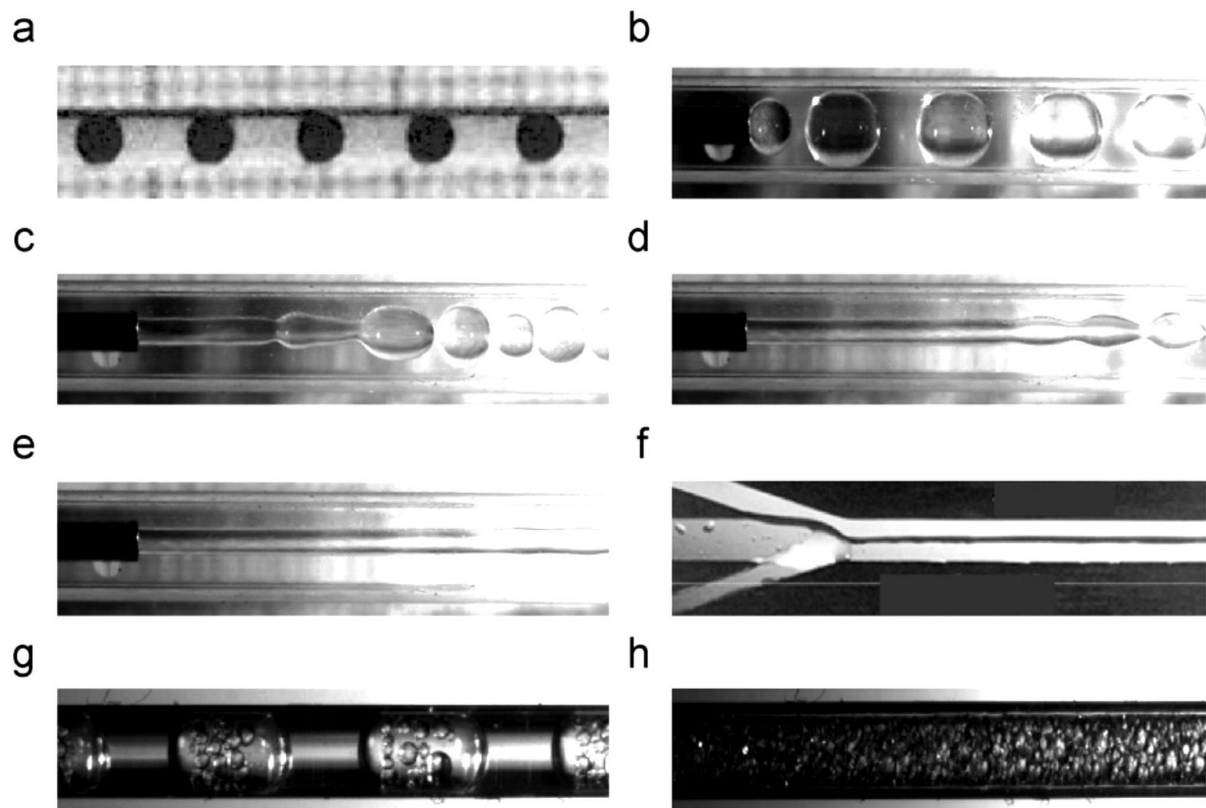


**Figure 2.1: Flow configurations obtained in microchannels (a) Drop flow, (b) Plug (slug) flow, (c) Plug-drop flow, (d) Deformed interface flow, (e) Annular flow, (f) Parallel flow, (g) Plug-dispersed flow, (h) Dispersed flow. (Kashid et al., 2011)**

These patterns can be further sub-divided to other flow regimes. By an order-of-magnitude reduction in the diameter of the flow channel from 10 mm to 1 mm, significant differences have been reported on the configuration of the flow patterns that are formed for the same flow conditions. Two-phase flows in large channels are mainly dominated by gravitational and inertia forces, whilst in the case of the two-phase flows in microchannels, the interfacial tension and viscous forces are significant because of the small characteristic distances and the low Re numbers ( $Re < 2000$ ), while gravity and inertia effects become negligible (Kreutzer et al., 2005b). The relative importance of these forces is shown in **Figure 2.2**.

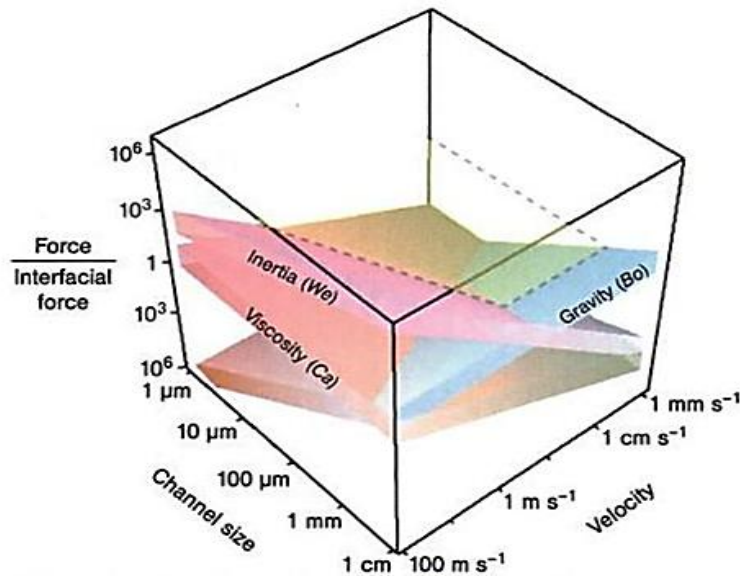


**Figure 2.2: Inertial, viscous and gravitational body forces, relative to interfacial forces, as a function of the channel size and characteristic velocity in microfluidic multiphase systems. (Günther and Jensen, 2006)**

The occurrence of different flow patterns in small channels is attributed to the competition between these forces, i.e. interfacial, inertia and viscous forces. The interfacial force tends to minimize the interfacial energy by decreasing the interfacial area, i.e. formation of droplets and plugs (**Figure 2.1b**). Inertia force tends to extend the interface in the flow direction and keep the fluids continuous (**Figure 2.1f**) (Joanicot and Ajdari, 2005). Moreover, if there is a sufficient velocity difference across the interface, the interface could become wavy due to shear instability. The viscous force dissipates the energy of perturbations at the interface and tends to keep the interface smooth (Foroughi and Kawaji, 2011, N. Kashid et al., 2011).

Over the past few years there was an attempt to determine as many as possible impacts that affect the flow configuration in liquid-liquid microchannel flows, as well as the stability of these flow patterns (Burns and Ramshaw, 2001, Dessimoz et al., 2008, Kashid and Agar, 2007, Ahmed et al., 2006). The different flow patterns that can be obtained in microchannels have been investigated not only for operational conditions, such as flow rates and volumetric flow ratio, and properties of the fluids (Lin and Tavlarides, 2009), but also for different geometry of the mixing zone and channel (N. Kashid et al., 2011), as well as for the channel wall roughness and wettability (Jovanović et al., 2011, Kuhn et al., 2011). Salim et al. (Salim

et al., 2008) investigated the flow of two immiscible liquids in two types of microchannel, i.e. glass and quartz, and they found that the flow formation was highly affected by the first injected fluid. Furthermore, they demonstrated that drop and plug velocities are proportional to the superficial velocity of the mixture, with a proportionality coefficient depending on the flow pattern.

To define the different parameters responsible for the flow formation, flow pattern maps are used, where the axes represent the superficial velocities or the volumetric flow rates of phases, mixture velocity or total volumetric flow rate against the fraction of one of the phases while dimensionless numbers have also been used (**Table 2.1**). Depending on the dimensionless numbers, different zones where the specific forces are dominant can be defined.

**Table 2.1: Dimensionless numbers for the characterisation of the two-phase flow**

Dimensionless numbers	Definition
Reynolds number	$Re_i = \frac{\rho_i u_i ID}{\mu_i} = \frac{\text{inertia forces}}{\text{viscous forces}}$
Capillary number	$Ca_i = \frac{\mu_i u_i}{\gamma} = \frac{\text{viscous forces}}{\text{interfacial forces}}$
Weber number	$We_i = \frac{\rho_i u_i^2 ID}{\gamma} = \frac{\text{inertia forces}}{\text{interfacial forces}}$
Bond number	$Bo = \frac{ID^2 \Delta \rho g}{\gamma} = \frac{\text{buoyancy forces}}{\text{interfacial forces}}$

It is worth mentioning, that flow pattern mapping is a multi-parametric procedure and it is hard to extrapolate the results found for a specific set of conditions. An example of a flow pattern map based on dimensionless numbers of the two immiscible phases is shown in **Figure 2.3**.

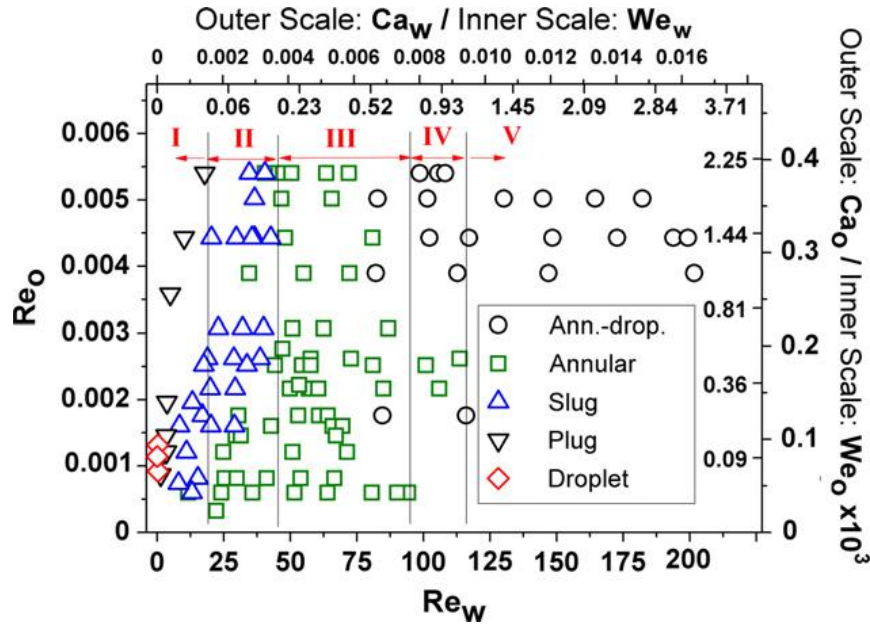


**Figure 2.3:** Flow patterns map for silicon oil-water flow in a 250 μm microchannel initially saturated with oil. The solid lines indicate the flow pattern transition boundaries, i.e. (I) interfacial forces dominant, (II) interfacial and inertia forces were comparable, (III) viscous forces > inertia > interfacial forces, (IV) inertia and viscous forces were comparable, and (V) inertia dominant. (Foroughi and Kawaji, 2011)

In general, the main flow patterns which have been observed and studied extensively are plug (or segmented), drop, annular and parallel flow. Annular and parallel flows are observed when the inertia forces dominate over the interfacial forces at  $We > 1$  which, however, were easily destabilised by changing flow rates and volumetric flow ratios (Zhao et al., 2006). Further increase of the  $We$  number ( $We > 10$ ) will cause turbulence, and chaotic or deformed annular flows are observed. Plug flow has received particular attention from many investigators, due to the promising benefits that offer in numerous applications. In most of the works, Y- and T-junctions or co-flowing configurations (Figure 2.4) are utilised as mixing zones (Garstecki et al., 2006, Kashid and Agar, 2007, Salim et al., 2008, Dessimoz et al., 2008, Foroughi and Kawaji, 2011). However, flow patterns do not change significantly among the different channel geometries and mixing zones (Kashid and Kiwi-Minsker, 2011).

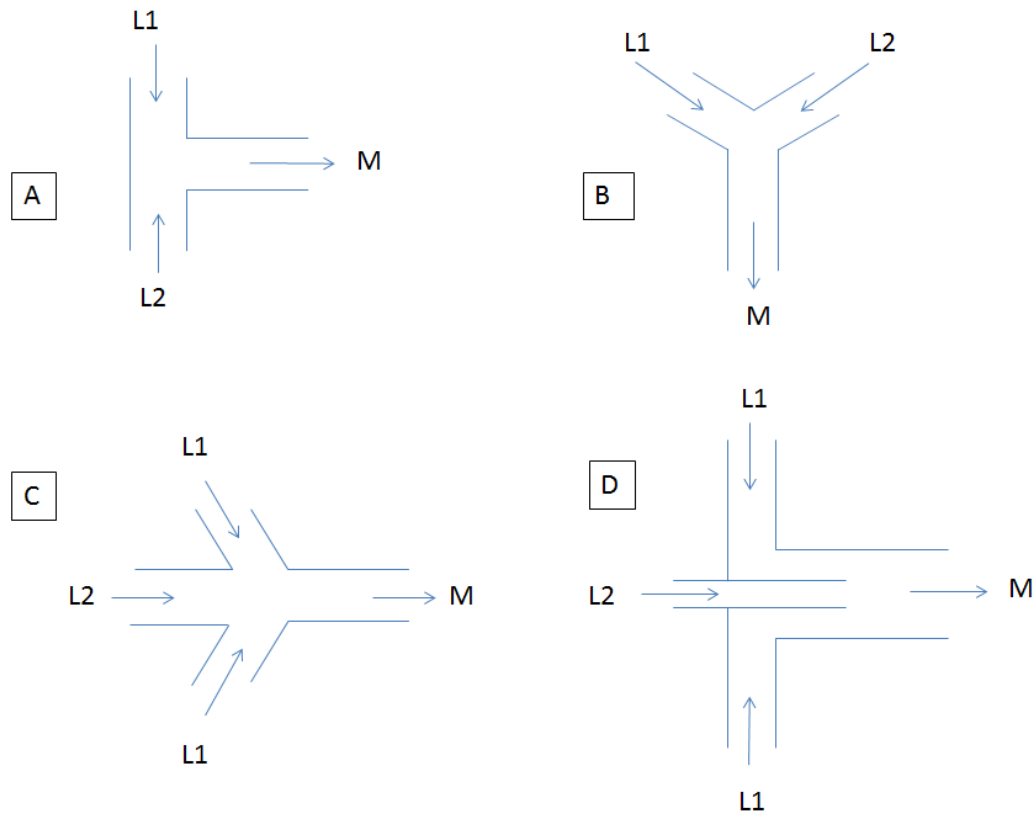


**Figure 2.4: Mixing zone configurations for plug flow formation.**

Although the exact position of the transition boundaries between the flow patterns are inherently related to the liquid-liquid system studied, the arrangement of the regions of the different flow patterns are similar to a number of systems. Models based on the Capillary, Reynolds and Weber numbers have been developed in order to allow an a priori prediction of the flow patterns using fluid properties and flow velocities. A general criterion for flow pattern identification in a given microchannel was given in terms of dimensionless ratio of Reynolds to Capillary ( $Re_c/Ca_c$ ) numbers as a function of the product of Reynolds number and hydraulic diameter ( $Re_d d_h/\epsilon_d$ ) by Kashid and Kiwi-Minsker ([Kashid and Kiwi-Minsker, 2011](#)) and was applied to different literature data which are summarised in **Figure 2.5**.



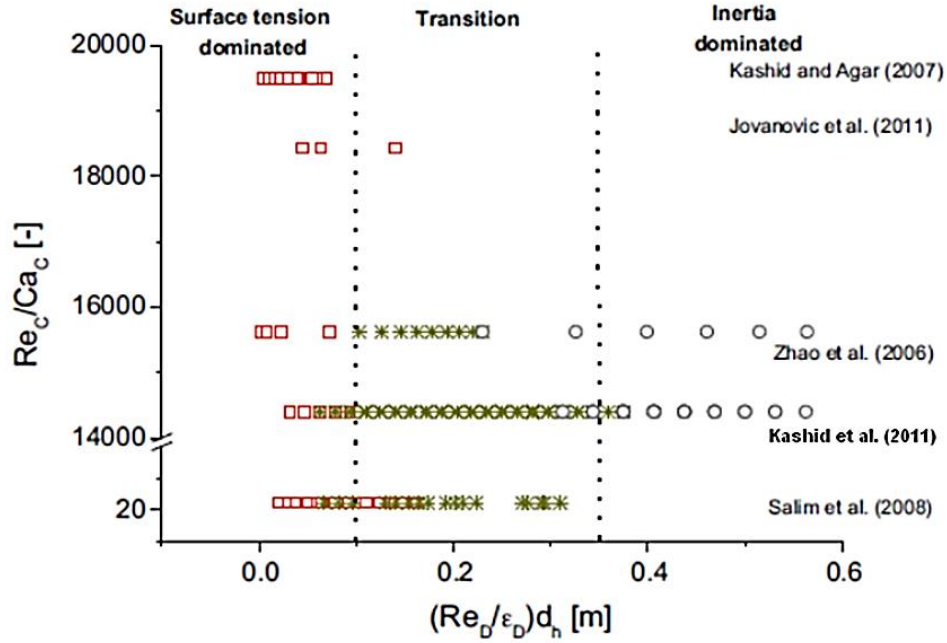


**Figure 2.5:  $Re_c/Ca_c$  as a function of  $Re_d d_h / \epsilon_d$ . ( $\square$ ) surface dominated, ( $\times$ ) transition, ( $\circ$ ) inertia dominated. (Kashid and Kiwi-Minsker, 2011)**

It can be concluded that the most significant impact on the formation of the flow patterns originated from the fluid properties, channel size, channel wettability, flow rate ratio and interfacial tension. A comprehensive flow pattern map should be dependent on the fluid and microchannels characteristics, and thus correlate the flow regimes using the relative forces responsible as well as the surface roughness.

### 2.1.2 Phase separation in micro and small channels

Extraction involves three basic steps: (I) mixing of the two liquid phases, (II) contacting of the two phases, (III) separating the two phases from each other. As mentioned previously, micro-fluidic devices have been developed for a wide range of applications because of the many advantages, such as short analysis time, reduction of the sample, reagents, and waste volumes, more effective reaction due to large specific area, and smaller space requirement. Phase separation of the multiphase micro-flows is a very important issue for controlling micro-flow networks. The phase separation requires a single phase flow in each output of the micro-device. Separation of the two phases based on density difference is inappropriate for

small scale microfluidic devices, where gravitational forces are negligible. Another important issue is to control the pressure difference between the two phases due to pressure loss in each phase and the Laplace pressure generated by the interfacial tension between the separated phases. The microfluidic extraction devices can be categorized based on the way that the immiscible fluids flow within them. Co-current and counter-current parallel flow, and segmented flow are two common flow patterns in extraction processes. The phase separation in these systems is usually achieved by methods that incorporate micro-fabrication of materials with very different surface properties to exploit the different fluid properties of the two phases (i.e. hydrophobicity). In addition, separation by capillary forces and balanced pressure conditions has been widely used (Kralj et al., 2007, Kashid et al., 2007b, Castell et al., 2009, Scheiff et al., 2011, Gaakeer et al., 2012). These methods are effective because they utilize interfacial tension and wetting, which are dominant effects in the microchannels. A general schematic of the phase separation during parallel or segmented flow is shown in **Figure 2.6**.

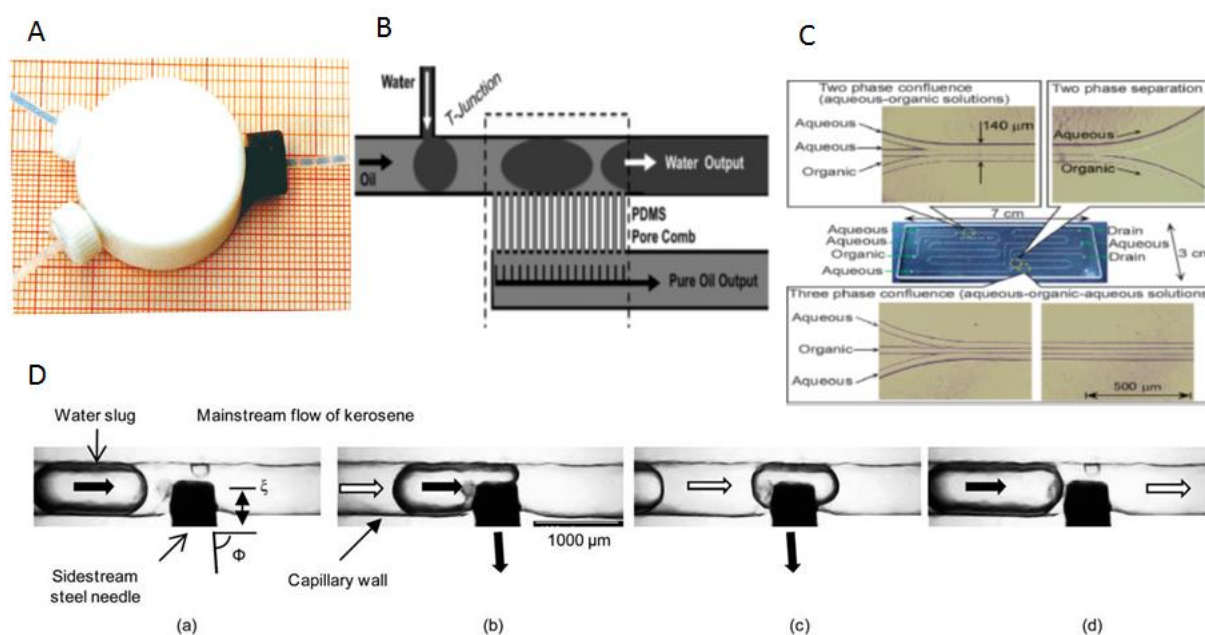


**Figure 2.6:** A schematic of separation devices during liquid-liquid plug or parallel flow. (A) Phase separation using a Y-splitter (Kashid et al., 2007b), (B) Phase separation by capillary forces (Angelescu et al., 2010), (C) Phase separation during parallel flow (Aota et al., 2007) and (D) Phase separation by wettability combined with pressure balance (Scheiff et al., 2011).

### 2.1.3 Flow patterns in pipes

Macro-scale reactors differ substantially from micro-scale ones in terms of flow patterns where gravity and inertia forces are the dominating forces. Studies in pipes have been performed by many investigators in order to enhance the knowledge of the flow patterns and estimate the area of contact. As in the case of microchannels wettability was found to affect the flow configuration. Different parameters, such as pipe orientation, i.e. horizontal, vertical or inclined (Lum et al., 2006), pipe size and the flow orientation of the two immiscible fluids (Rodriguez and Oliemans, 2006), fluid properties, i.e. viscosity (Beretta et al., 1997), pipe material (Angeli and Hewitt, 2000) and flow rates (Wegmann and Rudolf von Rohr, 2006) influence the flow patterns. An indicative flow pattern map can be seen in **Figure 2.7**. Angeli and Hewitt (Angeli and Hewitt, 2000) investigated this effect by using two horizontal pipes made of stainless steel and acrylic, whilst Wegmann and Rudolf von Rohr (Wegmann and Rudolf von Rohr, 2006) used pipes made of glass. They observed a substantial difference in the flow patterns (stratified, stratified/mixed and dispersed flow) between the pipes.

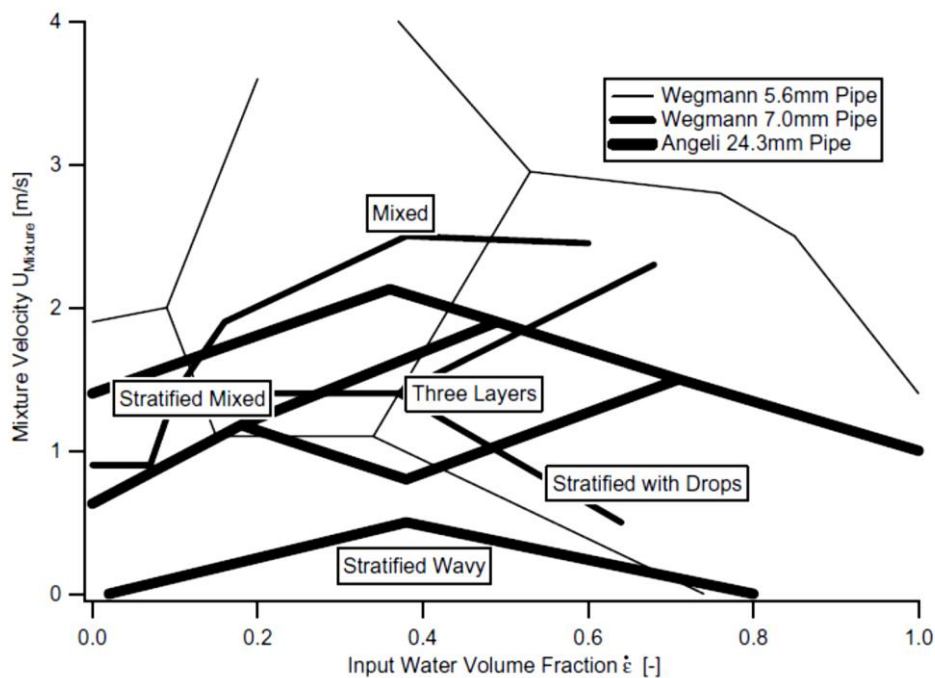


**Figure 2.7: Experimental flow pattern transition lines. (Wegmann and Rudolf von Rohr, 2006)**

## 2.2 Plug flow

Liquid-liquid plug flow in small channels plays an important role in many applications such as (bio)chemical and material synthesis, food science, and encapsulation. The development of microfluidic devices and methods to produce monodisperse plugs (or bubbles) by means of controlling and manipulating fluid flows within length scales from micro- to milli-meter, has gained considerable attention in the last decade. Several droplet-based applications have been investigated so far, including mixing enhancement (Song et al., 2003), crystallization of proteins (Zheng et al., 2004), and clinical diagnostics (Srinivasan et al., 2004). Microfluidic devices can facilitate the formation of monodisperse plugs, since the internal dimensions can be fabricated within the micrometer scale. There are several microfluidic designs reported in the literature that can produce plug (segmented) flow. These include cross flowing micro-devices (T-shaped channels) (Kashid et al., 2007b), flow focusing micro-devices (Garstecki et al., 2005), and co-flowing microdevices (Foroughi and Kawaji, 2011). Each of these methods utilizes a specific flow configuration to promote the uniform generation of monodisperse droplets. The size and uniformity of the droplets depend on the physical properties of the two fluids, as well as on the dimensions and geometric profile of the microdevice.

### 2.2.1 Mechanisms of plug formation in cross-flowing devices

The T-shaped configuration is one of the most commonly used for the development of plug flow, because of the high level of control and uniformity of the flow patterns, as well as the simplicity of the design. So far, many studies, both experimental (Thorsen et al., 2001, Tice et al., 2004, Garstecki et al., 2006, Christopher et al., 2008) and numerical (Van der Graaf et al., 2006, De Menech et al., 2008, Gupta et al., 2009, Gupta and Kumar, 2010) have been performed on the formation of droplets at a T-shaped configuration to provide an understanding on the flow hydrodynamics. Depending on the forces that dominate, the break-up mechanisms can be distinguished into two types, i.e. shear-driven mechanism (Thorsen et al., 2001) and squeezing mechanism (Garstecki et al., 2006). Thorsen et al. (Thorsen et al., 2001) investigated the droplet formation in T-junction and they observed that by increasing the flow rate and the viscosity of the continuous phase, the droplet size decreases and

proposed a model to predict the size of the droplet by analysing the balance between the interfacial and the viscous forces of the continuous phase. Garstecki et al. (Garstecki et al., 2006) focused on the scaling law of droplet formation. They found that at low  $Ca$  ( $Ca < 0.01$ ) and  $We$  numbers, where interfacial forces dominate over shear stress, the break-up is triggered by the squeezing mechanism. The break-up of the droplet occurs due to the build-up of pressure caused, as a result of the high resistance to the flow of the continuous phase in the thin film that separates the droplet from the channel walls when the droplet occupies almost the entire cross section of the main channel (squeezing mechanism), while the effect of the shear stress can be considered negligible (Figure 2.8) (Garstecki et al., 2006, van Steijn et al., 2007, Xu et al., 2013).

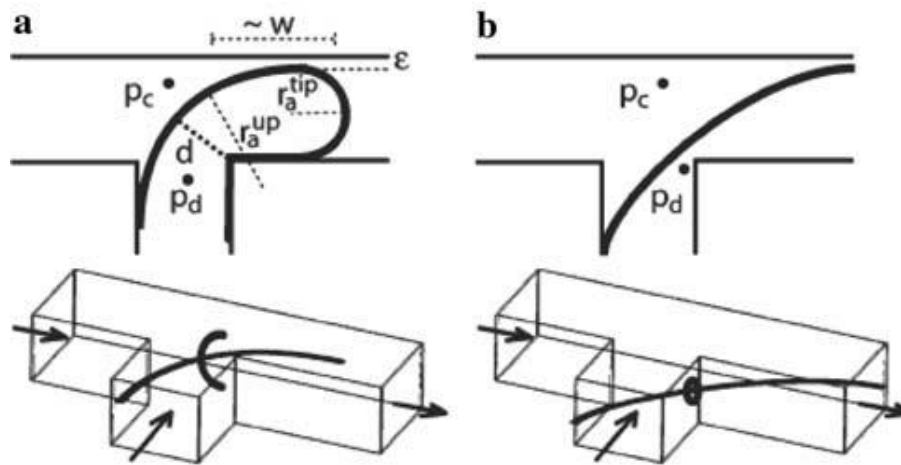


**Figure 2.8: A schematic illustration of the break-up process of a plug at the T-junction of the microchannels. (a) the growing stage, (b) the squeezing stage. (Garstecki et al., 2006)**

At values above a critical  $Ca$  number ( $Ca \sim 0.015$ ) the shear-driven mechanism also contributes to the droplet formation (De Menech et al., 2008). The shear stress acts to tear off the tip of the dispersed phase, whilst the interfacial tension acts to minimize its surface area. Although a T-shaped configuration favours the formation of plug flow, further increase on the flow rate ratio leads to a change on the flow regime and thus parallel flow will be observed.

### 2.2.2 Plug size

The size of the plug is a very important parameter, since it has a direct relation to the performance of the liquid-liquid system. Plug size affects the intensity of the recirculation and subsequently affects heat and mass transfer. For the prediction of the plug size different influencing factors, i.e. total volumetric flow rates, flow rate ratios, channel widths of the main and side channels, and fluid superficial velocities have been investigated and scaling laws and semi-empirical correlations have been suggested (Kreutzer et al., 2005b, Hoang et al., 2013, Christopher et al., 2008, van Steijn et al., 2010, Garstecki et al., 2006). In these models the plug size is independent on the Ca number and is affected by the flow rate ratio and the channel geometry (Garstecki et al., 2006, van Steijn et al., 2007).

The model proposed by Garstecki et al. is based on the squeezing mechanism (Garstecki et al., 2006) and is given by Eq. (2.2.1):

$$\frac{L_p}{w} = 1 + \alpha \frac{Q_d}{Q_c} \quad (2.2.1)$$

where  $L_p$  is the length of the plug,  $\alpha$  is a fitting parameter of order one, and  $Q_d$  and  $Q_c$  are the flow rate of the dispersed and the continuous phase, respectively. Similarly to the above law van Steijn et al. (van Steijn et al., 2010) proposed a predictive model for liquid droplets and gas bubbles without any fitting parameters. Their model has been experimentally validated in T-junctions with  $0.33 \leq w_{in}/w \leq 3$  and  $0.1 \leq h/w \leq 0.5$  for  $Ca < 0.01$ , where  $w_{in}$ ,  $w$  and  $h$  are the width of the side channel, width of the main channel and height of the main channel, respectively.

Based on the above models, Leclerc et al. (Leclerc et al., 2010) proposed a semi-empirical correlation (Eq. (2.2.2)), based on experiments with gas-liquid Taylor flow in T-shaped square microchannels.

$$\frac{L_b}{w_g} = 1.03 \left( \frac{w_g w_l}{w^2} \right) + 2.17 \frac{w_g u_g}{w_l u_l} \quad (2.2.2)$$

where  $L_b$ ,  $w_g$ ,  $w_l$ ,  $w$ ,  $u_g$ ,  $u_l$  are the length of the bubble, channel width of the gas phase, channel width of the liquid phase, channel width of the main channel, gas velocity, and liquid velocity, respectively.

In the same way, Xu et al. (Xu et al., 2013) proposed a correlation (Eq. (2.2.3)) that includes the effects of slug velocity  $u_{UC}$ , capillary diameter  $d$ , and aqueous to organic phase flow rate ratio  $q$ . The capillary diameters for the correlation were 0.6 and 0.8 mm.

$$L_p = 0.0116u_{UC}^{-0.32}ID^{1.25}q^{0.89} \quad (2.2.3)$$

The aforementioned models showed good agreement with one another for low Ca numbers (i.e. squeezing regime) and demonstrated that the size of the plug depends on the microchannel geometry and the flow rates of the two phases, whilst is independent of the fluid properties. However, as mentioned earlier, the shear stresses start to play an important role as the Ca number increases (shear driven regime). This illustrates the fact that the effects of fluid properties should be also considered, when predicting plug size for a large range of operating conditions for process engineering applications. Factors, such as surface wettability, channel depth, and fluid properties also affect the flow and single scaling laws may not always be valid (Abadie et al., 2012, Gupta et al., 2013, Xu et al., 2006). Moreover, it was found that the viscosity ratio ( $\mu_d/\mu_c$ ) affected the droplet size when the viscosity values were in the same order of magnitude, whilst when the ratio was considerably low the droplet size was independent (Christopher et al., 2008).

Qian and Lawal (Qian and Lawal, 2006) conducted numerical simulations on the formation and the size of Taylor bubbles in a 1 mm ID capillary for  $0.000278 < Ca < 0.01$ , and  $15 < Re_{ub} = \rho ID u_b / \mu < 1500$ . They proposed the following correlation for the estimation of the bubble length based on 148 sets of data

$$\frac{L_b}{ID} = 1.637\varepsilon_g^{-0.107}(1 - \varepsilon_g)^{-1.05}Re^{-0.0075}Ca^{-0.0687} \quad (2.2.4)$$

Laborie et al (Laborie et al., 1999) studied experimentally gas-liquid Taylor flow in capillaries of internal diameter varying between 1 and 4 mm, for  $55 < Re_{ub} = \rho ID u_b / \mu < 2000$ ,  $0.13 < Bo < 5$ , and  $0.0015 < Ca < 0.1$ , and proposed Eq. (2.2.5) for the estimation of the plug length

$$\frac{L_b}{ID} = 0.0878 \frac{Re_{ub}^{0.63}}{Bo^{1.26}} \quad (2.2.5)$$



### 2.2.3 Film thickness

The presence of the film between the dispersed plug and the channel wall offers multiple advantages such as prevention from cross contamination between the segments in biological devices, and enhancement of the heat and mass transfer in chemical engineering processes. Film thickness can be affected by different parameters such as fluid properties, average velocity, flow rate ratio, and channel size.

Many investigations on the deposition of the liquid film on the capillary have been performed, both experimentally (Irandoost and Andersson, 1989, Jovanović et al., 2011) and numerically (Heil, 2001, Taha and Cui, 2004) to estimate the magnitude of the film. While there are many applications that employ liquid-liquid plug flow, limited knowledge about the film thickness is available. In contrast, the film present in gas-liquid flows has been investigated in numerous studies. In most of the works, it was found that the film thickness (normalized by the channel radius) depends on a single parameter, i.e. the capillary number (Ca). As the velocity, and yet the Ca number, was increased the film thickness was also increased. The rate of the film increase follows an asymptotic trend till a threshold Ca number is reached, due to the tube confinement. In **Table 2.2** the most referenced models on film thickness regarding gas-liquid systems and the Ca number range that the models are valid, are presented (Angeli and Gavrilidis, 2008).

**Table 2.2 Correlations for the wall film thickness ( $\delta$ ) for gas-liquid Taylor flow**

Dimensionless film thickness	Range of Ca number	Reference
$\frac{\delta}{R} = 0.5\sqrt{Ca}$ (2.2.6)	$7.5 \cdot 10^{-5} < Ca < 0.01$	(Fairbrother and Stubbs, 1935)
$\frac{\delta}{R} = 1.34Ca^{2/3}$ (2.2.7)	$Ca < 0.003$	(Bretherton, 1961)
$\frac{\delta}{R} = 0.36(1 - \exp(-3.1Ca^{0.54}))$ (2.2.8)	$9.5 \cdot 10^{-4} < Ca < 1.9$	(Irandoost and Andersson, 1989)
$\frac{\delta}{R} = \frac{1.34Ca^{2/3}}{1+2.5(1.34Ca^{2/3})}$ (2.2.9)	$10^{-3} < Ca < 1.4$	(Aussillous and Quéré, 2000)



Different methods have been applied to define with accuracy the magnitude of the film thickness for the whole range of Ca numbers. These techniques involved video recording (Aussillous and Quéré, 2000), volumetry (Bretherton, 1961), conductimetry (Fairbrother and Stubbs, 1935), light absorption (Irandoost and Andersson, 1989), interferometry (Han and Shikazono, 2009), and optical microscopy (Dore et al., 2012, Mac Giolla Eain et al., 2013).

Most investigations on film thickness in segmented flow, originate from the initial attempts by Taylor (Taylor, 1961) to measure it experimentally and the theoretical analysis by Bretherton (Bretherton, 1961) of the film thickness across a bubble moving in a horizontal flow at low Ca numbers ( $<0.003$ ). The bubble was assumed to be inviscid with spherical caps. From their analysis it was found that the dimensionless film thickness was a function of  $Ca^{2/3}$ . In the same sense Aussillous and Quere (Aussillous and Quéré, 2000) developed an empirical correlation based on Bretherton's (Bretherton, 1961) solution by measuring the film thickness in vertical gas-liquid flows. In their work they classified two different regimes for the interpretation of the film thickness, i.e. the visco-capillary and the visco-inertia regime. In the visco-capillary regime, the film thickness depends only on Ca number, and the correlation proposed agreed well with Taylor's (Taylor, 1961) data; for low Ca numbers their model also agreed with Bretherton's (Bretherton, 1961) model. In the visco-inertia regime, where Ca number is higher ( $Ca > 10^{-3}$ ) they found a deviation from Taylor's (Taylor, 1961) findings, since inertia becomes important, and the film thickness increases.

The effect of inertia has been investigated by Edvinsson and Irandoost (Edvinsson and Irandoost, 1996) by using finite element analysis of Taylor flow in a cylindrical capillary. The effects of Ca, Re, and Fr numbers over a wide range were studied, and the simulations revealed that the film thickness was also dependent on Re and Fr numbers. By increasing the Re number the film thickness and the velocity difference between the two phases also increased, while the effect of Fr number (Froude number) was more obvious at higher Ca numbers, with results depending on the flow orientation (downward or upward flow).

The shape of the plug/bubble plays a crucial role on the correct estimation of the film thickness. Depending on the forces that dominate the flow, the profile of the plug will vary. At low Ca numbers, plugs are sufficiently long to maintain hemispherical caps and a uniform flat film along them. By increasing the Ca number the profile of the plug changes, and thus

both the rear and the front cap of the plug lose their hemispherical shape. The front cap becomes sharper and the rear cap becomes more flat, hence the area of uniform film thickness diminishes. This makes the choice of the location for the estimation of the film thickness quite difficult. To overcome the problem of the plug profile the film thickness can be defined by using indirect techniques that give film thickness as an average over the whole length of plug (Taylor, 1961, Irandoust and Andersson, 1989). Han and Shikazono (Han and Shikazono, 2009) measured the film thickness in gas-liquid horizontal flows and found that the film thickness changes according to the measuring positions due to gravity. They proposed an empirical correlation based on Ca number, Re number and We number. They found that by increasing the Ca number, an increase in the Re number results to an initial reduction of the film thickness till a threshold before it increases again. Mac Giolla Eain et al. (Mac Giolla Eain et al., 2013) have also measured the film thickness in horizontal liquid-liquid flows and have reported the effects of the plug length and the fluid properties of the carrier fluid on film thickness.

#### 2.2.4 Plug velocity

Knowledge of the plug velocity is key parameter in the design of contactors, since it defines the residence time, i.e. the time that the droplet remains in the contactor, while it affects the intensity of the internal circulations within the plug and thus the mixing efficiency. The velocity of the plug within a channel is highly affected by the forces acting on it, i.e. viscous, inertia and interfacial forces.

For a plug that is sufficiently long to maintain a uniform film thickness region (as discussed in section 2.2.3), the velocity profile far away from the rear and front cap is that of an ideal laminar flow, given by Eq. (2.2.10) and Eq. (2.2.11) for the dispersed and the continuous phase, respectively (Lac and Sherwood, 2009, Jovanović et al., 2011, Gupta et al., 2013).

$$u_d = 2u_{\text{mix}} \frac{[1 - \frac{R_i^2}{R^2}] + \frac{1}{\lambda} [\frac{R_i^2}{R^2} - (\frac{r^2}{R^2})]}{(1 + \frac{R_i^4}{R^4})(\frac{1}{\lambda} - 1)} \quad \text{for } 0 < r < R_i \quad (2.2.10)$$

$$u_c = 2u_{\text{mix}} \frac{\left[1 - \frac{R_i^2}{R^2}\right]}{\left(1 + \frac{R_i^4}{R^4}\right)\left(\frac{1}{\lambda} - 1\right)} \quad \text{for } R_i < r < R \quad (2.2.11)$$

Where  $R_i$  is the radius of the plug, and  $R$  the radius of the channel. The droplet velocity can be calculated by averaging the droplet fluid velocity and is given as

$$u_{\text{droplet}} = u_{\text{mix}} \frac{\left[2 + \frac{R_i^2}{R^2}\right]\left[\frac{1}{\lambda} - 2\right]}{\left(1 + \frac{R_i^4}{R^4}\right)\left(\frac{1}{\lambda} - 1\right)} \quad (2.2.12)$$

If there is a large difference between the viscosities of the two phases, then the viscosity ratio ( $\lambda = \mu_d / \mu_c$ ) tends to zero and Eq. (2.2.12) becomes

$$u_{\text{droplet}} = u_{\text{mix}} \frac{R^2}{R_i^2} \quad (2.2.13)$$

which however, does not take into account the flow of the continuous phase and is accurate for gas-liquid flows.

Similarly, the film velocity can be obtained by Eq. (2.2.14) as follows

$$u_{\text{film}} = u_{\text{mix}} \frac{\left[1 - \frac{R_i^2}{R^2}\right]^2}{\left(1 + \frac{R_i^4}{R^4}\right)\left(\frac{1}{\lambda} - 1\right)} \quad (2.2.14)$$

Gupta et al. (Gupta et al., 2013) found good agreement between the analytical solutions given by Eqs. (2.2.10) and (2.2.11), and the CFD simulations.

To evaluate the bubble velocity in gas-liquid flows, the dimensionless number,  $m$ , which gives the relative velocity between the bubble and the continuous phase, is used,

$$m = \frac{u_b - u_{\text{mix}}}{u_b} \quad (2.2.15)$$

In **Table 2.3**, empirical correlations for the prediction of the bubble velocity during gas-liquid Taylor flow, as well as the analytical solution of Bretherton (Bretherton, 1961) are summarised.

**Table 2.3: Correlations for the bubble velocity  $u_b$  for gas-liquid Taylor flow**

Correlation	Range of Ca number	Reference
$m = \sqrt{Ca}$ (2.2.16)	$7.5 \cdot 10^{-5} < Ca < 0.01$	(Fairbrother and Stubbs, 1935)
$m = 1.29(3Ca)^{\frac{2}{3}}$ (2.2.17)	$10^{-3} < Ca < 10^{-2}$	(Bretherton, 1961)
$m = (\frac{\mu}{\sigma})^{\frac{1}{2}}[-0.1 + 1.78\sqrt{u_b}]$ (2.2.18)	$7 \cdot 10^{-6} < Ca < 2 \cdot 10^{-4}$	(Marchessault and Mason, 1960)
$\frac{u_b}{u_m} = \frac{1}{1 - 0.61Ca^{0.33}}$ (2.2.19)	$2 \cdot 10^{-4} < Ca < 0.39$	(Liu et al., 2005)

### 2.2.5 Internal circulation

Taylor (Taylor, 1961) suggested three patterns for slug flow (Figure 2.9) that depend on Ca number. At high Ca numbers ( $m > 0.5$ ), a single stagnation point at the front part of the bubble was suggested, which indicates a complete bypass flow (Figure 2.9a). By decreasing the Ca number ( $m < 0.5$ ) two possible flow patterns were proposed; in the first case a stagnation ring around the bubble front part was formed (Figure 2.9b), whilst in the other case two stagnation points were formed, one inside the liquid slug and another one at bubble front part (Figure 2.9c).

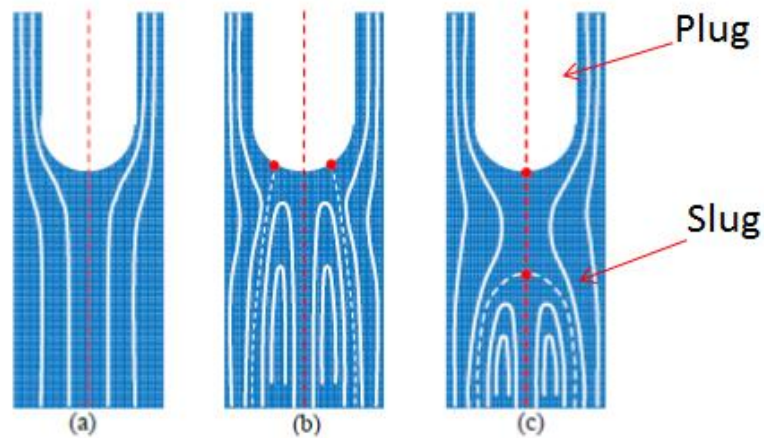


**Figure 2.9: Qualitative schematic of flow streamlines in the liquid slug ahead of elongated bubbles in capillaries. (a)  $m > 0.5$ ; (b) & (c)  $m < 0.5$ , where  $m = (u_b - u_{mix}) / u_b$ . (Taylor, 1961)**

The shear between the wall surface and the plug axis produces internal circulations within the plug, which reduce the thickness of the boundary layer at the interface, thereby enhancing the diffusive penetration, heat and radial mass transfer (Kashid et al., 2005, Talimi et al., 2012). The length of the plug and the slug, the velocity of the mixture, and the thickness of the film affect the intensity of the circulations.

Tice et al. (Tice et al., 2003) investigated the formation of plugs of multiple reagents and subsequently the mixing within the plug. They concluded that the optimal mixing within the plugs depends on the initial distribution of the reagents, which was established by the eddy flow at the tip of the forming plug. King et al. (King et al., 2007) investigated the effect of plug length on the formation of internal circulation and they reported the cases where circulation was absent. They found that at short plugs and low flow velocities internal circulation is minimal, since zero velocity gradients exist. Circulation times increased in value as a function of the velocity till a threshold value beyond which the internal circulation no longer increases. For small segments the contribution of the liquid-liquid friction to the phase internal flow is the decisive factor and liquid/wall friction is minimal due to its small contact area (Malsch et al., 2008).

The geometry of the channel has also a decisive impact on the formation of the flow patterns inside a plug (**Figure 2.10**). When a plug is flowing in straight channels usually the internal flow patterns observed at the upper and bottom half of the segments are symmetric over the centre of the channel. In bend channels flow circulation is asymmetric as a result of the channel curvature. This leads to more complex flow fields, but also results to higher mass transfer over the whole segment and an improved mixing efficiency.

The mixing inside the segments is quantified by using two dimensionless parameters. The first is the relative vortex length which gives the ratio of the main vortex length over the length of the segment.

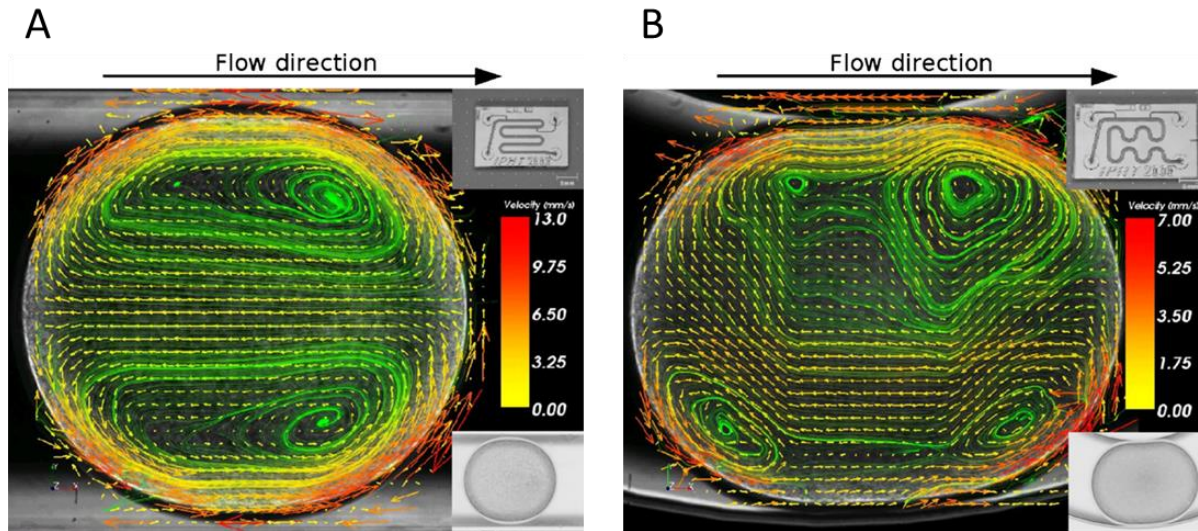


**Figure 2.10: Flow fields in a droplet when flowing (velocity of  $7.6 \text{ mm s}^{-1}$ ) in straight channels (A) and in bend channels (B). (Malsch et al., 2008)**

Ufer et al. (Ufer et al., 2011) investigated a two-phase system of water/ethylacetate and found that this ratio varies between 0.3 and 0.75 and increased by increasing the velocity of the plug. Scheiff et al. (Scheiff et al., 2013) investigated the internal circulation in viscous ionic liquid plugs and they found that the vortices in the ionic liquid plugs occupy the entire plug. The other parameter of quantifying the mixing is the dimensional circulation time. This is defined as the ratio of the average time to displace material from the one to the other end of the plug to the time that the plug needs to travel a distance of its own length (Thulasidas et al., 1997, Dore et al., 2012). The structure of the internal circulation, i.e. the location of the stagnation points are essential for quantifying the mixing inside the two phases. Thulasidas et al. (Thulasidas et al., 1997) showed that for Poiseuille flow the radial position of the centre of the toroidal vortex,  $r^0$  and the radial position of the stagnation streamline,  $r^1$  are given by Eq (2.2.20) and Eq. (2.2.21), respectively.

$$r^0 = \frac{R}{\sqrt{2}} \sqrt{2 - \psi} \quad (2.2.20)$$

$$r^1 = R \sqrt{2 - \psi} \quad (2.2.21)$$

Where  $\psi = u_b/u_{\text{mix}}$ . At  $\psi=2$  the  $r^0$  and  $r^1$  become 0 which corresponds to the point of complete bypass.

### 2.2.5.1 Particle image Velocimetry (PIV)

For understanding the mixing characteristics in two-phase microfluidic systems, details of the velocity profiles within the phases are required. Micro Particle Image Velocimetry ( $\mu$ -PIV) can be used to extract multipoint information of the velocity inside a single liquid plug or slug with high accuracy and spatial resolution and in a non-intrusive manner (Santiago et al., 1998, Lindken et al., 2009). Important mixing characteristics, such as the recirculation time, can then be derived from the velocity fields and other measured parameters, such as the location of stagnation points, and vortex cores. There have been a number of studies involving the application of  $\mu$ -PIV on gas-liquid flows (Thulasidas et al., 1997, Günther et al., 2004, Waelchli and Rudolf von Rohr, 2006, van Steijn et al., 2007, Malsch et al., 2008), but only limited ones for liquid-liquid systems (Kashid et al., 2005, Sarrazin et al., 2006, Wang et al., 2007, King et al., 2007, Kinoshita et al., 2007). In these studies  $\mu$ -PIV has been used to visualize the internal recirculation in aqueous slugs or plugs during aqueous/oil two-phase flows. Kinoshita et al. (Kinoshita et al., 2007) obtained three-dimensional velocity information and circulation patterns inside a moving aqueous droplet by confocal microscopy, while other investigators (Kashid et al., 2005, Sarrazin et al., 2006) qualitatively compared velocity fields acquired from PIV with CFD simulations, proving the suitability of the experimental technique for these flows. More recently, Fang et al. (Fang et al., 2012) proposed a technique to locally enhance DNA concentration by using a plug flow micro-device. PIV velocity data within water plugs were used to locally quantify the shear strain rate, while mixing was investigated by using a continuous dye. Although previous investigations qualitatively related the velocity profiles from PIV to the mixing features, the latter was mainly quantified numerically or experimentally from dye dispersion. Local characterisation of mixing rate via parameters such as circulation time, important for mass transfer operations, is still missing in the literature for liquid-liquid plug flow configurations.

### 2.2.6 Pressure drop

Knowledge of pressure drop during two-phase flow in microchannels is essential for the design of energy efficient systems. However, despite its importance only relatively few studies are available in literature concerning pressure drop in liquid-liquid microchannel



flows (Chakrabarti et al., 2005, Kashid and Agar, 2007, Salim et al., 2008, Jovanović et al., 2011), compared to those available for gas-liquid flows (Triplett et al., 1999, Chen et al., 2002, Kawahara et al., 2002, Kreutzer et al., 2005b).

Two-phase pressure drop can typically be correlated with two models, i.e. homogeneous or separated. Homogeneous fluid models are well suited to emulsions and flow with negligible surface forces, where the two-phase mixture can be treated as a single fluid with appropriately averaged physical properties of the individual phases. Separated flow models consider that the two phases flow continuously and separated by an interface across which momentum can be transferred (Angeli and Hewitt, 1999). The simplest patterns that can be easily modelled are separated and annular flow (Brauner, 1991, Rovinsky et al., 1997, Bannwart, 2001). In this case, momentum balances are written for both phases with appropriate interfacial and wall friction factors.

Salim et al (Salim et al., 2008) investigated oil-water two-phase flows in quartz and glass microchannels. Their pressure drop measurements were interpreted by using the homogeneous and Lockhart-Martinelli models, where the two-phase pressure drop is correlated to the pressure drop of each single phase:

$$\left(\frac{\Delta P}{L}\right)_{TP} = \left(\frac{\Delta P}{L}\right)_c + \eta \varepsilon_d \left(\frac{\Delta P}{L}\right)_d \quad (2.2.22)$$

where  $(\Delta P/L)_{TP}$  is the two-phase pressure drop per unit capillary length,  $(\Delta P/L)_c$  and  $(\Delta P/L)_d$  are the continuous and dispersed single-phase pressure drops per unit capillary length, respectively.  $\varepsilon_d$  is the dispersed phase volume fraction and  $\eta$  is a fitting factor which depends on the wettability of the wall. In the case of quartz microchannel, according to their experimental results  $\eta$  was equal to 0.67, while in the case of glass microchannel it was equal to 0.8.

The homogeneous model is not suitable for plug flow because of the use of dynamic viscosity of the two-phase mixture, the fact that it does not take into account the influence of plug length on the pressure drop, and the absence of surface tension. Salim et al. (Salim et al., 2008) also found out that the pressure drop depends on the first injected fluid, and the type of the microchannel material. Although the separated model considers the contributions of each phase separately, it is not suited to plug flow. In the plug flow, pressure drop is usually



modelled as a series of unit cells, composed of a dispersed plug and a continuous slug as it can be seen in **Figure 2.11**. Frictional pressure drop ( $\Delta P_{Fr}$ ) of the individual phases and the pressure drop due to the interfacial effects ( $\Delta P_I$ ) need to be taken into account in the calculation of the two-phase pressure drop.

The overall pressure drop can be written as:

$$\Delta P_{\text{plug flow}} = \Delta P_{Fr} + \Delta P_I = (\Delta P_{Fr,c} + \Delta P_{Fr,d}) + \Delta P_I \quad (2.2.23)$$

The frictional pressure drop,  $\Delta P_{Fr}$  is calculated from the Hagen-Poiseuille equation for a cylindrical tube and is expressed as a function of the unit length ( $L_{UC}=L_d+L_c$ , where  $L_d$  and  $L_c$  are the lengths of the dispersed plug and the slug, respectively) and the dispersed phase length fraction ( $k=L_d/L_{UC}$ ):

$$\Delta P_{Fr,d} = \frac{8\mu_d u_{mix} k L_{UC}}{R^2} \quad (2.2.24)$$

$$\Delta P_{Fr,c} = \frac{8\mu_c u_{mix} (1-k) L_{UC}}{R^2} \quad (2.2.25)$$

$$u_{mix} = \frac{Q_c + Q_d}{A} \quad (2.2.26)$$

where  $\mu_d$  and  $\mu_c$  are the viscosity of the dispersed and continuous phase, respectively, and  $u_{mix}$  is the superficial velocity which is determined from the total flow rate.

The interface pressure drop,  $\Delta P_I$  is obtained from the Young-Laplace equation:

$$\Delta P_I = \frac{2\gamma}{R} \cos\theta \quad (2.2.27)$$

Kashid and Agar ([Kashid and Agar, 2007](#)) investigated the effects of various operating conditions on pressure drop in a PTFE microchannel reactor with a Y-junction as mixing zone. They developed a theoretical prediction for pressure drop based on the capillary pressure and the hydrodynamic pressure drop without the presence of a continuous film and for a constant contact angle between the dispersed plug and the channel wall (**Figure 2.11a**).

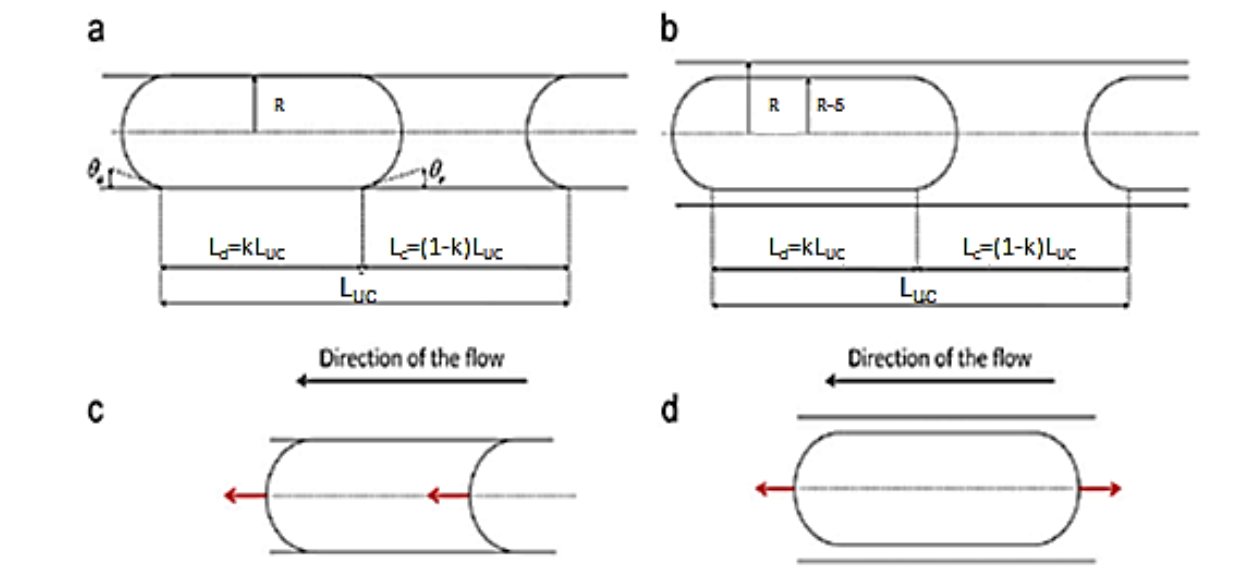


**Figure 2.11: (a) Unit cell without film, (b) Unit cell with thin film, (c) plug flow in the case of a dry wall, and (d) plug flow in the case of a wetted wall. (Jovanović et al., 2011)**

Their proposed model overestimated the experimental pressure drop, because when a liquid film is present (**Figure 2.11b**) there is no direct contact between the dispersed phase plugs and the channel wall, so the contact angle values become different from the dry channel wall case. Moreover as it can be seen in **Figure 2.11c** and **Figure 2.11d** the interfacial pressure drop should be different depending on the presence of film or not. More specific, in the case of dry wall, the interfaces of the plug are deformed in the direction of the flow, thus the interfacial pressure drop over the plug is acquired by adding the interfacial pressure drops at the front and back of the plug. In contrast, in the case of wetted wall the interfaces of the plug are deformed in opposite directions, and the interface pressure drop over the plug is acquired by subtracting the interfacial pressure drops at front and back. The front meniscus has a positive contribution to the pressure drop and the rear meniscus has a negative contribution. The frictional pressure drop was calculated by taking into account the superficial velocity of the mixture. However, if a thin film is present then the plug travels at a higher velocity than the continuous phase (Warnier et al., 2008).

Jovanovic et al. (Jovanović et al., 2011) tried to overcome these drawbacks by developing a pressure drop model which incorporates the effect of film thickness, surface shape, slug size, and capillary diameter. Furthermore, they determined the parameters with the highest impact

on the pressure drop. They investigated two liquid-liquid systems (i.e. water-toluene and ethylene glycol/water-toluene) in fused silica capillaries. They presented two models, i.e. the stagnant film and the moving film. It was found that the film velocity has negligible effect on the pressure drop; therefore the stagnant model was chosen to predict the experimental pressure drops. In their model they also assumed a fully developed Hagen-Poiseuille flow, which is disturbed by the caps of the dispersed phase plug, causing an excess pressure drop. The frictional pressure drop is described by Eq. (2.2.24) and Eq. (2.2.25) for the dispersed and continuous phase, respectively and the interface pressure was described by Bretherton's solution for the pressure drop over a single bubble in a capillary (Bretherton, 1961). The plug flow was modelled as a series of unit cells (**Figure 2.11b**). The film at the wall is reducing the radius of the channel through which the dispersed plug is travelling.

$$R_{ch}=R-\delta \quad (2.2.28)$$

where  $\delta$  is the liquid film thickness and is calculated as a function of the Ca number,

$$\delta = 1.34RCa^{2/3} \quad (2.2.29)$$

which is valid for  $\delta$  below  $0.01R$ . In the systems where the continuous phase has a considerably higher viscosity than the dispersed phase the Bretherton's equation should be corrected by a factor of  $2^{2/3}$  as explained by Schwartz et al. (Schwartz et al., 1986, Bico and Quere, 2000). The interface pressure is then calculated by taking into account the Laplace pressure and the change in curvature due to the presence of the liquid film surrounding the plug

$$\Delta P_I = C \left( 3Ca^{\frac{2}{3}} \right) \frac{\gamma}{ID} \quad (2.2.30)$$

Assuming ideally semispherical caps, the constant  $C$ , which accounts for the influence of the interface curvature, was found to be 7.16 (Bretherton, 1961) for  $Ca < 5 \times 10^{-3}$  and  $We \ll 1$  and for conditions where inertia is absent. Inserting Eqs. (2.2.24), (2.2.25), (2.2.29) and (2.2.30) in equation (2.2.23) results in the plug flow pressure drop equation for the stagnant film ( $\Delta P_{SF}$ ) case:

$$\Delta P_{SF} = \frac{8u_p\mu_d kL}{(R - \delta)^2} + \frac{8u_{mix}\mu_c(1 - k)L}{R^2} + \frac{L}{L_{UC}} C(3Ca)^{\frac{2}{3}} \frac{\gamma}{d} \quad (2.2.31)$$

The pressure drop was found to be highly affected by the unit cell size. By changing the flow ratios, the sizes of the continuous and dispersed phases changed, thus varying the total number of interfaces in the system, and consequently the frictional and interface pressure drop terms.

### 2.2.7 Mass transfer

The characterisation of mass transfer is essential for the design of the micro-reactor. In liquid-liquid flows most studies have focused on the estimation of overall mass transfer coefficients, while no model based on theory has been developed so far. The overall volumetric mass transfer coefficient ( $k_L\alpha$ ) is a characteristic parameter of a system used to evaluate the performance of the contactors, and is a combination of the mass transfer coefficient ( $k_L$ ), which depends mainly on the diffusivity of solute, characteristic diffusion length and interfacial hydrodynamics, and of the specific interfacial area ( $\alpha$ ), which depends on the flow pattern. The prediction of the overall volumetric mass transfer coefficient remains difficult due to secondary phenomena, like interfacial instabilities.

Mass transfer coefficients in micro-reactors are much higher than those obtained in conventional macro-contactors as it can be seen in **Table 2.4**. One common drawback of conventional contactors is the inability to predict precisely flow characteristics and interfacial area, because of the complexities of the governing hydrodynamics. This often leads to uncertainties in the design and causes limitations on the performance than can be achieved. Mass transfer rates in micro-reactors can be up to 2 orders of magnitude higher. In addition, consecutive reactions can be efficiently suppressed by strict control of residence time and its distribution ([Kashid et al., 2011](#)).

**Table 2.4:  $k_L\alpha$  of different types of contactors**

References	Contactors	$\alpha$ ( $\text{m}^2/\text{m}^3$ )	$k_L\alpha$ ( $\text{s}^{-1}$ )
(Fernandes and Sharma, 1967)	Agitated contactor	32-311	$(48-83) \cdot 10^{-3}$
(Verma and Sharma, 1975)	Packed bed column	80-450	$(3.4-5) \cdot 10^{-3}$
(Charpentier, 1981)	Bubble column	50-600	$(5-240) \cdot 10^{-3}$
(Kies et al., 2004)	-Spray column	75-170	$(15-2.2) \cdot 10^{-3}$
	-Stirred tank	100-2000	$(30-400) \cdot 10^{-3}$
(Dehkordi, 2001, Dehkordi, 2002)	-Two impinging jets reactor	1000-3400	0.28
	-Air operated two impinging reactors	350-900	0.075
(Kashid et al., 2007b)	Capillary microchannel, ID=0.5-1mm	830-3200	0.88-1.67

There are two transport mechanisms that promote mass transfer in liquid-liquid plug flow, i.e. convection and diffusion (**Figure 2.12**). The convection is achieved through the internal circulations within each phase, while the diffusion is due to concentration gradients between a plug and a slug. The diffusive penetration is enhanced more by the internal circulations that renew the interface (Burns and Ramshaw, 2001, Dumann et al., 2003, Kashid et al., 2005, Ghaini et al., 2010).

In liquid-liquid systems several parameters that affect the performance of the extractor, such as channel size, flow patterns, fluid properties, mixing zone, and flow orientation, have been investigated (Burns and Ramshaw, 2001, Zhao et al., 2007, Kashid et al., 2007b, Dessimoz et al., 2008, Su et al., 2010, Ghaini et al., 2010, Tsaoulidis et al., 2013a, Tsaoulidis et al., 2013b, Sarrazin et al., 2008). A number of investigations have focused on the development of numerical and empirical models to describe the mass transfer for fixed interface location (Kashid et al., 2007a, Raimondi and Prat, 2011, Skelland and Wellek, 1964). Harries et al.

(Harries et al., 2003) developed a numerical model during liquid-liquid plug flow to investigate the hydrodynamics within both segments and the mass transfer of dissolved chemical species within and across the segments interface.

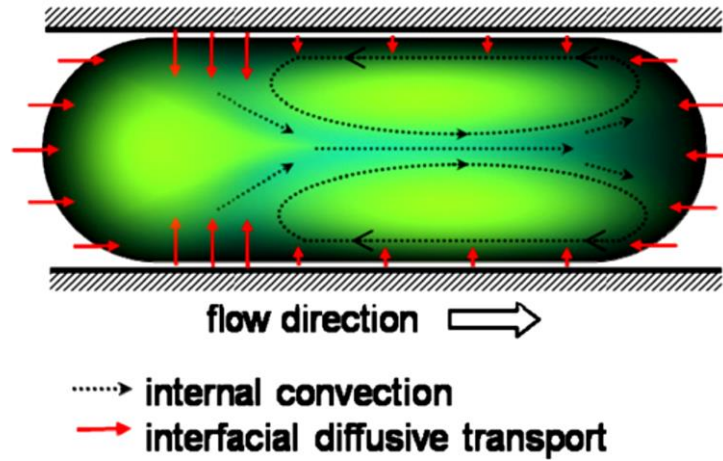


**Figure 2.12:** Schematic representation of the transport mechanisms within a plug. (Ghaini et al., 2011)

Their model showed good agreement with experimental results. Raimondi et al. (Di Miceli Raimondi et al., 2008) carried out numerical simulations of the mass transfer during liquid-liquid plug flow in square microchannels, where it was assumed that mass transfer did not deform the interface, since the hydrodynamics were decoupled from the mass transfer. Kashid et al. (Kashid et al., 2010) performed dimensional analysis to obtain a relationship (Eq. (2.2.32)) between the mass transfer coefficient and various independent variables. In their studies however, they did not take into account the effect of contacting geometry and microchannel shape.

$$k_L \alpha \frac{L}{u_{mix}} = a Ca^b Re^c \left( \frac{ID}{L} \right)^d \quad (2.2.32)$$

As far as the gas-liquid systems are concerned, a number of models for the prediction of the  $k_L \alpha$  have been developed based on both empirical correlations, and on film and penetration theory. These models provide estimates of the mass transfer coefficient in the continuous liquid phase, while the mass transfer resistance in the gas phase is considered negligible. In these models the individual contributions of the caps of the plugs, and of the fully developed film separating the plugs from the channel wall are estimated. Bercic and Pintar (Berčič and

Pintar, 1997) proposed a model for the calculation of the mass transfer coefficient in small channels (Eq. (2.2.33)), that includes only the contribution of the caps because of the rapid saturation of the film, which is given by

$$k_L \alpha = \frac{0.111 u_p^{1.19}}{((1-\varepsilon_d) L_{UC})^{0.57}} \quad (2.2.33)$$

However, the absence of any parameter related to the channel size limits the application of the model to different two-phase systems. Van Baten and Krishna (Van Baten and Krishna, 2004) and Irandoust and Andersson (Irandoust and Andersson, 1989) included in their models the contributions of both bubble caps and film (Eq. (2.2.34)). Van Baten and Krishna (Van Baten and Krishna, 2004) evaluated the contribution of the caps according to the Higbie penetration theory (Eq. (2.2.35)), whilst the transfer through the film was obtained based on mass transfer in a falling film in laminar flow (Eqs. (2.2.36) & (2.2.37)).

$$k_L \alpha = k_{L,cap} \alpha_{cap} + k_{L,film} \alpha_{film} \quad (2.2.34)$$

$$k_{L,cap} \alpha_{cap} = 2 \frac{\sqrt{2}}{\pi} \sqrt{\left( \frac{D_c u_p}{ID} \right)} \frac{4}{L_{UC}} \quad (2.2.35)$$

$$k_{L,film} \alpha_{film} = \frac{2}{\sqrt{\pi}} \sqrt{\frac{D_c u_p}{L_{film}}} \frac{4 L_{film}}{ID L_{UC}}, \quad Fo < 0.1 \quad (2.2.36)$$

$$k_{L,film} \alpha_{film} = 3.41 \frac{D_c}{\delta} \frac{4 L_{film}}{ID L_{UC}}, \quad Fo > 1 \quad (2.2.37)$$

$$Fo_{film} = \frac{D_c L_{film}}{u_p \delta^2} \quad (2.2.38)$$

Similarly, Vandu et al. (Vandu et al., 2005) suggested a model based only on the contribution of the film in circular and square capillaries.

$$k_L \alpha = C \sqrt{\frac{D_c u_g}{L_{UC}}} \frac{1}{ID} \quad (2.2.39)$$

Apart from the overall volumetric mass transfer coefficient ( $k_L \alpha$ ) the mass transfer performance of a system can also be characterised by the extraction efficiency ( $\%E_{eff}$ ). The extraction efficiency is the ratio of the amount transferred to the maximum amount transferable.

$$\%E_{\text{eff}} = \frac{[C]_{\text{aq,fin}} - [C]_{\text{aq,init}}}{[C]_{\text{aq,eq}} - [C]_{\text{aq,init}}} \quad (2.2.40)$$

Moreover, the mixing in the liquid-liquid system can be characterised by dimensionless numbers, such as, Sherwood number (Sh), which is the ratio of convective mass transfer to the molecular diffusion, and Schmidt number (Sc), which is the ratio of the viscous diffusion rate to the molecular diffusion. In addition to these, the Fourier number (Fo) can also give an idea about the dynamics of diffusive transport process.

$$\text{Sh} = \frac{k_L L^*}{D} = \frac{\text{convective mass transfer}}{\text{molecular diffusion}} \quad (2.2.41)$$

$$\text{Sc} = \frac{\mu}{\rho D} = \frac{\text{viscous diffusion}}{\text{molecular diffusion}} \quad (2.2.42)$$

$$\text{Fo} = \frac{\tau D}{R^2} = \frac{\text{species diffusion rate}}{\text{species storage rate}} \quad (2.2.43)$$

In **Table 2.5** the mass transfer coefficients during liquid-liquid plug and parallel flow are presented. The mass transfer performance of different types of micro-reactors was investigated for reacting and non-reacting systems.



Table 2.5: Mass transfer coefficients during liquid-liquid plug and parallel flow.

References	Multi-phase system	Conditions	Equation	$k_L \alpha$ ( $s^{-1}$ )
(Burns and Ramshaw, 2001)	-Kerosene/acetic acid/water + NaOH	-Glass chip reactor, $d_H=380\mu m$ - $U<35mm/s$ -Plug flow	$k_L \alpha = \frac{1}{\tau_{re}} \ln \left( \frac{[C]_{aq,eq} - [C]_{aq,init}}{[C]_{aq,eq} - [C]_{aq,fin}} \right)$	order of magnitude of 0.5
(Kashid et al., 2007b)	-Kerosene / acetic acid / water -Water / iodine / kerosene -Water / succinic acid / n-butanol	-Y-junction and capillary tubing (Teflon), $d_c=0.5-1mm$ , $L=100-300mm$ - $U=10-70mm/s$ -Plug flow	$k_L \alpha = \frac{1}{\tau_{re}} \ln \left( \frac{[C]_{aq,eq} - [C]_{aq,init}}{[C]_{aq,eq} - [C]_{aq,fin}} \right)$	0.02-1.4
(Zhao et al., 2007)	-Water / succinic acid / n-butanol	-Stainless steel microchannel, T-junction, $d_c=0.4-0.6mm$ - $U=0.005-2.5m/s$ -Parallel flow	$k_L \alpha = \frac{1}{\tau_{re} \left[ 1 + \frac{Q_{aq}}{mQ_{or}} \right]} \ln \left( \frac{[C]_{aq,eq,inlet} - [C]_{aq,inlet}}{[C]_{aq,eq,outlet} - [C]_{aq,outlet}} \right)$	0.067-17.35
(Dessimoz et al., 2008)	-Hexane / trichloroacetic acid / water + NaOH	-Glass chip reactor, T-, Y-junction, $d_c=269-400\mu m$ - $U<50mm/s$ -Plug flow	$k_L \alpha = \frac{1}{\tau_{re}} \ln \left( \frac{[C]_{or}}{[C]_{or,0}} \right)$	0.2-0.5

(Ghaini et al., 2010)	-Saturated n-butyl formate-water	-Y-junction and capillary tubing, $d_c=1\text{mm}$ - $U=10\text{-}70\text{mm/s}$ -Plug flow	$k_L\alpha = \frac{1}{\tau_{re}} \ln\left(\frac{[C]_{aq,eq} - [C]_{aq,init}}{[C]_{aq,eq} - [C]_{aq,fin}}\right)$	0.7-1.57
(N. Kashid et al., 2011)	-Water-acetone-toluene	-T-square (TS): $d_H=400\mu\text{m}$ , $L=56\text{mm}$ , $U=0.1\text{-}0.42\text{m/s}$ -T-trapezoidal (TT): $d_H=400$ , $L=75\text{mm}$ , $U=0.1\text{-}0.42\text{m/s}$ -Y-rectangular (YR): $d_H=269\mu\text{m}$ , $L=40\text{mm}$ , $U=0.228\text{-}0.9\text{m/s}$ -Concentric (CC): $d_c=1600\mu\text{m}$ , $L=200\text{mm}$ , $U=0.008\text{-}0.083\text{m/s}$ -Caterpillar (CT): $d_H=150\mu\text{m}$ , $L=5\text{mm}$ , $U=0.74\text{-}4.44\text{m/s}$ -Plug flow	$k_L\alpha = \frac{1}{\tau_{re}\left[\frac{1}{K_{\varepsilon_1}} + \frac{1}{1 - \varepsilon_1}\right]} \ln\left(\frac{[C]_{aq,eq} - [C]_{aq,init}}{[C]_{aq,eq} - [C]_{aq,fin}}\right)$	0.01-0.74
(Assmann and von Rohr, 2011)	-Water-vanillin-toluene	-PDMS capillary reactor: $d_c=300\mu\text{m}$ , $L=13.5\text{mm}$ - $U>0.08\text{m/s}$	$k_L\alpha = \frac{1}{\tau_{re}} \ln\left(\frac{[C]_{aq,eq} - [C]_{aq,init}}{[C]_{aq,eq} - [C]_{aq,fin}}\right)$	5.5-11

## 2.3 Ionic liquid-based extractions: Reprocessing of spent nuclear fuel

Nuclear energy from fission can provide substantial amounts of carbon free electricity and process heat. However, one of the main concerns in the use of the nuclear power generation is the management of the irradiated nuclear fuel from the reactor (spent fuel) which can remain toxic for thousands of years. Efficient spent fuel reprocessing through a series of operations can separate uranium to be reused as reactor fuel and reduce the volume and toxicity of the rest of the spent fuel that needs to be stored or disposed. One of the common operations in reprocessing is extraction that involves the flow of two immiscible liquids. Commercially the PUREX process is commonly used where uranium(VI) is extracted from nitric acid solutions of the spent fuel using extractants such as tributylphosphate (TBP) in diluents of large aliphatic chain hydrocarbons (i.e. kerosene, dodecane) (Giridhar et al., 2008). The need to use volatile organic compounds (VOCs) as solvents or the subsequent generation of VOCs, introduce safety risks (Visser and Rogers, 2003). Recently ionic liquids (ILs) have been suggested as alternatives to organic solvents because of their negligible volatility and flammability at common industrial conditions (Rogers and Seddon, 2002, Plechkova and Seddon, 2008), which reduce solvent loss and make them inherently safe and environmentally friendly.

Ionic liquids (ILs) are salts with low melting points (below 100°C) composed exclusively of ions (Wasserscheid and Welton, 2008, Chiappe and Pieraccini, 2005). The ability to tune the properties of ionic liquids by the choice of the anion and the cation (Figure 2.13) and optimise them for a particular application (Seddon et al., 2000) has expanded significantly their use in synthesis, catalysis and separations in recent years (Binnemans, 2007, Murali et al., 2010). Their high resistance to radiation (much higher than the commonly used TBP/kerosene mixtures) makes ionic liquids particularly suitable for extractions in spent fuel reprocessing.

For use in extraction applications with aqueous solutions, hydrophobic ionic liquids are required. The hydrophobicity of the ionic liquids depends on the alkyl chain length of the associated cation and on the anion. Recently, the bis(trifluoromethylsulfonyl)imide anion,  $[(CF_3SO_2)_2N]^-$  (abbreviated to  $[Tf_2N]^-$ ), has become a popular anion choice for synthesizing hydrophobic ionic liquids that are chemically and thermally more robust and of lower viscosity compared to the majority of ILs (Binnemans, 2007).

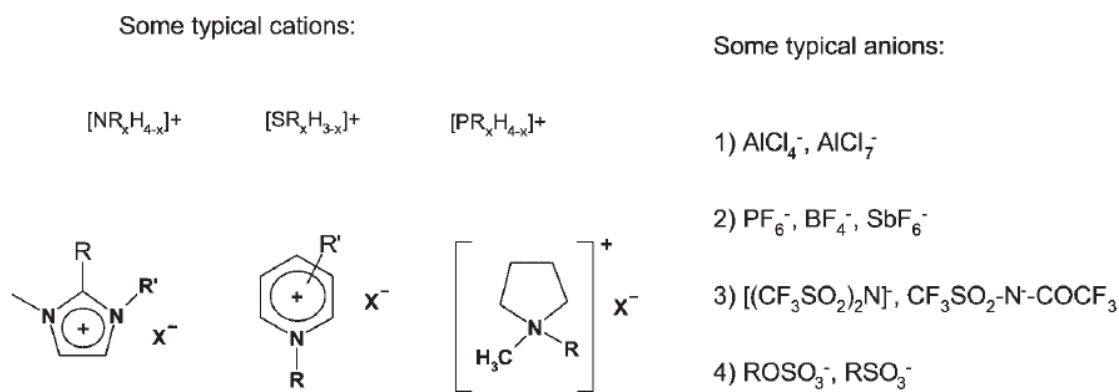
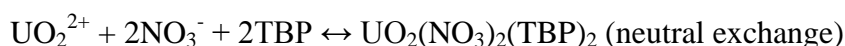
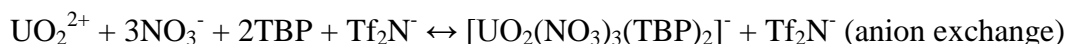


Figure 2.13: Typical cations and anions for the composition of ionic liquids.

### 2.3.1 Studies on the extraction mechanisms

Studies of uranium(VI) extraction from nitric acid solutions to ionic liquids suggest different mechanisms of the extraction, i.e. cation exchange, anion exchange and solvation, depending on the nature of extractant, concentration of counteranion, structure of the ionic liquid and the aqueous phase composition (Dietz and Dzielawa, 2001, Wei et al., 2003) which are different to those occurring in traditional solvents. Given the substantial differences between ILs and conventional molecular solvents, it is conceivable that the complexes found in ILs are different from the complexes known in molecular solvents. The dioxouranium(VI) extraction proceeds via a double cationic exchange at low acidity and via an anionic exchange at high acidity. Many equilibrium studies have been performed so far to identify the extraction mechanisms (Dietz and Stepinski, 2008, Giridhar et al., 2008, Billard et al., 2011b, Wang et al., 2009, Murali et al., 2010). According to the mechanisms, ionic liquid is released to the aqueous phase and metal ions are extracted. The ion exchange processes results in the loss of the ionic liquid phase and contaminate the aqueous phase.



The equilibrium distribution coefficients  $D_U$  for IL with the same anionic part ( $\text{NTf}_2^-$ ) but different cationic parts can be seen in **Figure 2.14**. As it can be seen at low initial nitric acid concentration,  $[\text{HNO}_3]_{\text{aq,init}}$ , values of the distribution coefficients strongly depend on the cationic part of the IL. By contrast at high  $[\text{HNO}_3]_{\text{aq,init}}$  the values of  $K_U$  follow a similar curve for the different ILs, suggesting that the extraction mechanism is independent of the cationic part of the IL. The  $[\text{HNO}_3]_{\text{aq,init}}$  value at which the mechanism is changing from cation-dependent to cation independent is varying from 0.02 M for  $[\text{C}_{10}\text{mim}][\text{NTf}_2]$  to ca. 1.5 M for  $[\text{C}_4\text{mim}][\text{NTf}_2]$ .

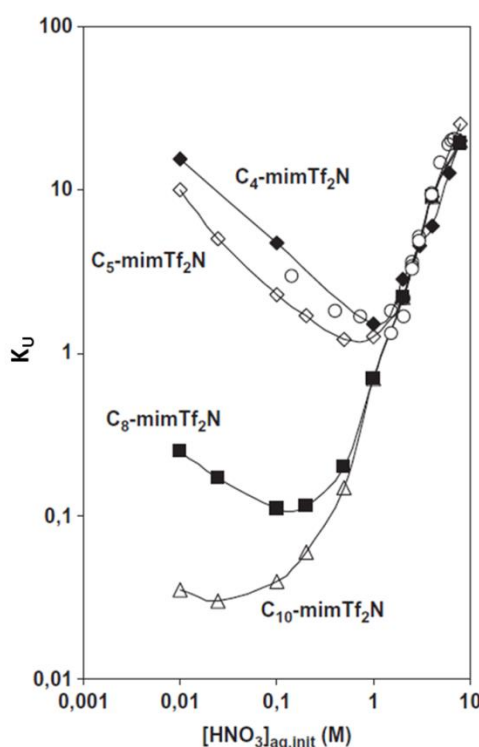


**Figure 2.14:** Variation of the dioxouranium(VI) extraction coefficient as a function  $[\text{HNO}_3]_{\text{aq,init}}$ , at  $[\text{TBP}]_{\text{IL,init}}=1.1$  M. (Dietz and Stepinski, 2008):  $\Delta$  -  $[\text{C}_{10}\text{mim}][\text{NTf}_2]$ ,  $\blacksquare$  -  $[\text{C}_8\text{mim}][\text{NTf}_2]$ ,  $\diamond$  -  $[\text{C}_5\text{mim}][\text{NTf}_2]$ . (Giridhar et al., 2008):  $\blacklozenge$  -  $[\text{C}_4\text{mim}][\text{NTf}_2]$ . (Billard et al., 2011b):  $\circ$  -  $[\text{C}_4\text{mim}][\text{NTf}_2]$ .  $[\text{U}]=10^{-2}$  M or  $10^{-3}$  M. (Billard et al., 2011b)

Regarding the ionic liquid  $[\text{C}_{10}\text{mim}][\text{NTf}_2]$ , the shape of the distribution curve indicates that the uranium(VI) extraction involves partitioning of the neutral dioxouranium(VI)-TBP-nitrato complex as observed in alkanes. This is illustrated in **Figure 2.15**, where one can notice the dependence of  $K_U$  on TBP concentration which resembles that obtained for dodecane. This observation suggests that the hydrophobicity of the IL cation affects the extraction of neutral compounds (Cocalia et al., 2005).

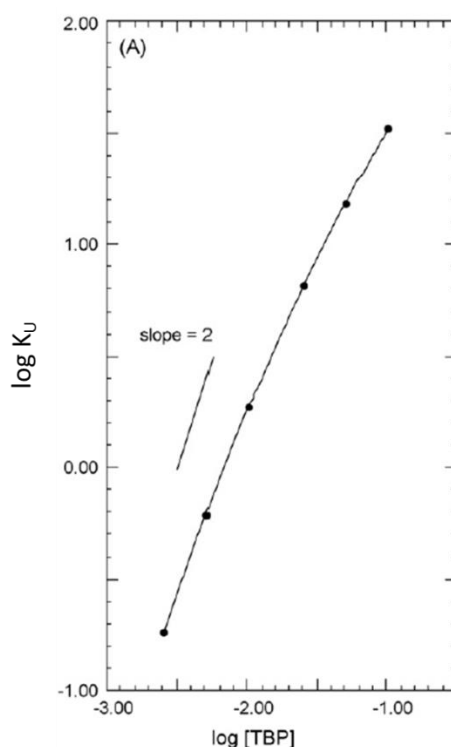


**Figure 2.15: Dependency of the uranium distribution ratio,  $K_U$ , on TBP concentration in  $[C_{10}mim][NTf_2]$  at constant (3 M) nitric acid concentration.**(Dietz and Stepinski, 2008)

Ionic liquids are in general non-coordinating and in the absence of an extractant, do not extract metal ions from the aqueous phase (**Figure 2.16**). To enable extractions in spent fuel reprocessing many investigators have dissolved in the ionic liquids known extracting moieties (other than TBP) such as CMPO (octyl(phenyl)-N,N-diisobutylcarbamoylmethylphosphine oxide) (Visser and Rogers, 2003, Nakasima et al., 2003), TTA (2-thenolyltrifluoroacetone) (Jensen et al., 2003), HDEHP (bis(2-ethylhexyl)phosphoric acid) or Cyanex-272 (Cocalia et al., 2005).

In traditional solvents such as dodecane, the apparent stoichiometry of dioxouranium(VI) extraction by TBP is  $UO_2^{2+} + 2NO_3^- + 2TBP \leftrightarrow UO_2(NO_3)_2(TBP)_2$ , which suggest that the extracted dioxouranium(VI) forms a complex with two nitrates and TBP (Cocalia et al., 2005, Vasudeva Rao et al., 2008). Comparisons of TBP/ionic liquid mixtures with the TBP/dodecane system showed different trends as a function of the nitric acid concentration (**Figure 2.16**). At low nitric acid concentrations,  $[C_4mim][NTf_2]$  exhibits a high extraction of dioxouranium(VI) from low nitric acid concentrations in contrast to TBP/dodecane. TPB/dodecane system increases till  $[HNO_3]_{aq,init} = 3$  M and then decreases, which is attributed to the non-availability of free TBP, due to significant extraction of nitric acid and also to the

conversion of dioxouranium(VI) ion to the less extractable anionic dioxouranium(VI) nitrate species at high  $[\text{HNO}_3]_{\text{aq,init}}$ . The significant extraction of dioxouranium(VI) by the ILs at high nitric acid concentrations can be attributed to an ion exchange mechanism in which the  $\text{UO}_2(\text{NO}_3)_3^-$  anions are exchanged with the anion of the ionic liquids.

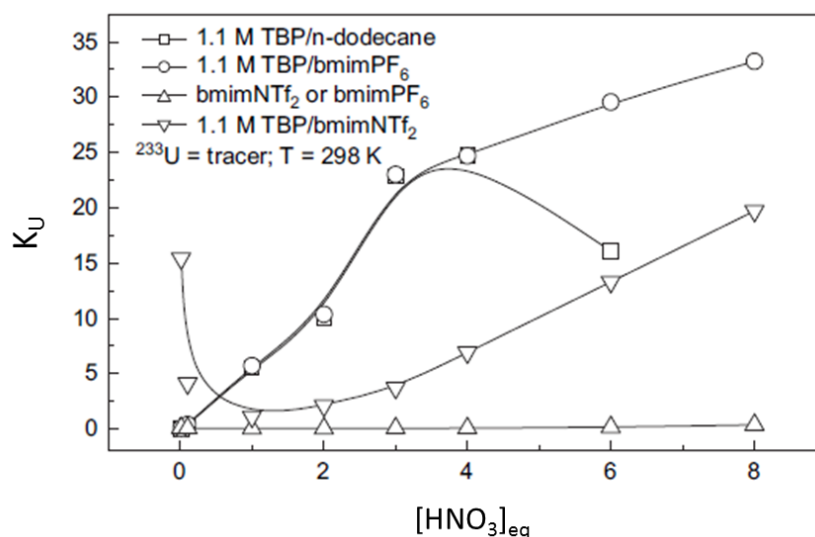


**Figure 2.16:** Comparison of distribution ratios for the extraction of U(VI) by [bmim][PF<sub>6</sub>], [bmim][NTf<sub>2</sub>] and 1.1 M TBP/diluent as a function of the initial nitric acid concentration. The diluents are n-dodecane (DD), [bmim][NTf<sub>2</sub>] and [bmim][PF<sub>6</sub>]. (Vasudeva Rao et al., 2008)

### 2.3.2 Task specific ionic liquids

Another promising approach for metal extraction lies in the concept of task-specific ionic liquids (TSILs). These compounds, consisting of extracting entities grafted onto the cation of the ionic liquid combine the properties of ionic liquids with those of extracting compounds, and thus behave both as the organic phase and the extracting agent, suppressing the problems encountered through extractant/solvent miscibility and facilitating species extraction and solvent recovery. One case of TSILs is the inclusion of quaternary ammonium cations in [Tf<sub>2</sub>N]<sup>-</sup> based ionic liquids which gave in some cases very high partition coefficients for uranium(VI). Studies on the extraction of uranium(VI) using ionic liquids based on quaternary ammonium cation and bearing phosphoryl groups resulted in distribution coefficients  $D_U$  of 170 (Ouadi et al., 2007).

Bell and Ikeda (Bell and Ikeda, 2011) investigated the key factors for optimising the separation of uranium(VI) from nitric acid solutions using novel hydrophobic ammonium based ionic liquids (**Figure 2.17**). It was found that the extraction of uranium(VI) from the aqueous phase to ionic liquid phase could proceed through either a cationic exchange at low nitric acid concentrations, and neutral partitioning or anionic exchange mechanism at higher nitric acid concentration. The findings seem to be in agreement with those of the previous investigators.

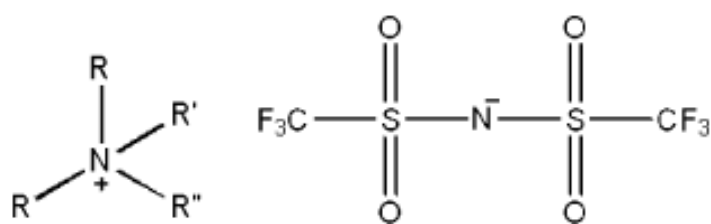


**Figure 2.17: Generic structure of the ionic liquids synthesized by (Bell and Ikeda, 2011)**

### 2.3.3 Physicochemical properties of ionic liquids

The physical properties of ionic liquids play an important role on the efficiency of phase separations. In ionic liquid-based extractions, the viscosity of an ionic liquid affects the mass transfer efficiency. For imidazolium-based ionic liquids ( $C_n\text{mim}$ ), the viscosity increases by increasing the alkyl chain length due to the increased van der Waals interactions, while the choice of the anion also affects the viscosity as it participates in hydrogen bonding (Kagimoto et al., 2010). For  $[C_n\text{mim}][\text{NTf}_2]$  ionic liquids an almost linear increase of the viscosity to the length of the alkyl group has been observed (Dzyuba and Bartsch, 2002). It is known that water has a strong impact on the viscosity of ILs. Even when ionic liquids are immiscible with water they absorb some water. The amount of water present in the ionic liquid at equilibrium depends also on the initial  $\text{HNO}_3$  concentration of the aqueous phase. TBP was also found to affect the amount of water absorbed at low nitric acid concentrations (see **Figure 2.18**) (Billard et al., 2011b, Giridhar et al., 2008).

Decreasing the solubility of ionic liquids in water plays an important role in ionic liquid-based extraction. The anion has the primary effect on water miscibility, whilst the cation seems not to affect miscibility much (Seddon et al., 2000). The order of increasing



hydrophobicity for the anions is  $\text{Br}^-$ ,  $\text{Cl}^- < [\text{BF}_4]^- < [\text{PF}_6]^- < [\text{NTf}_2]^-$  (Toh et al., 2006). Metal ions are poorly soluble in ILs except when coordinated with, or solvated by, hydrophobic molecules added to the IL phase, or with hydrophilic complexing anions that can facilitate metal ion transport into the IL phase.

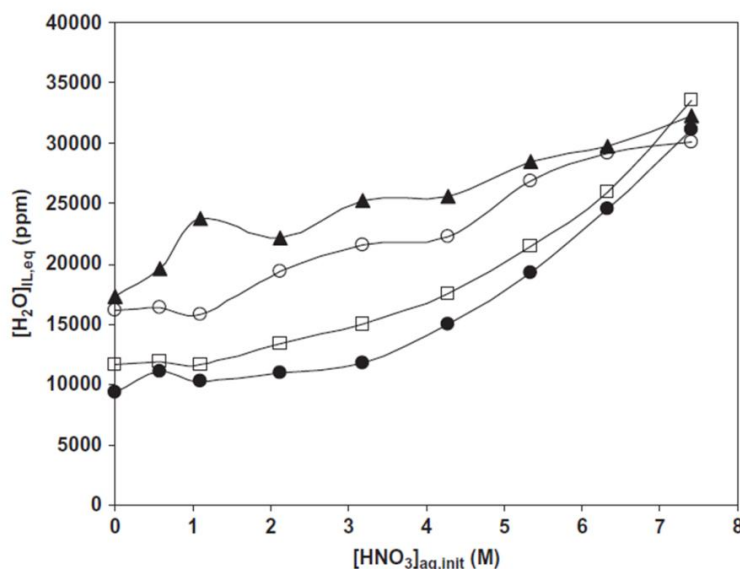


**Figure 2.18:** Variation of the water in the  $[\text{C}_4\text{mim}][\text{NTf}_2]$  phase as a function of  $[\text{HNO}_3]_{\text{aq,init}}$ , for various values of TBP loading. • -  $[\text{TBP}]_{\text{IL,init}}=0\text{M}$ ; □ -  $[\text{TBP}]_{\text{IL,init}}=0.18\text{M}$ ; ○ -  $[\text{TBP}]_{\text{IL,init}}=0.55\text{M}$ ; ▲ -  $[\text{TBP}]_{\text{IL,init}}=1.1\text{M}$ . (Billard et al., 2011b)

The densities of ionic liquids are also affected by the choice of the cation and anion. For imidazolium ionic liquids the density decreases slightly as the alkyl chain of the cation increases in length. In addition, the absorption of water by ionic liquids by increasing nitric acid concentration can also cause a decrease in the density (Giridhar et al., 2004). Regarding imidazolium-based ionic liquids, by increasing the alkyl chain it was found that the surface tension decreased due to the orientation of hydrocarbon tails on the surface (Kilaru et al., 2007). The vapour pressure of an ionic liquid is usually unmeasurable at room temperature. Studies on the thermal stability of ionic liquids showed that the type of the associated anion has the primary effect on the thermal stability of the ionic liquids (Holbrey and Seddon, 1999). Although ionic liquids are not flammable, studies showed that they are not safe to use near fire, since the products that formed during thermal decomposition for some ionic liquids are sensitive to combustion (Smiglak et al., 2006). Another outstanding property of the ionic liquids is the wide electrochemical window that they exhibit, which enables them to be unaffected from oxidation or reduction for a wide range of voltage. However, an increase in

the water content of ionic liquids would narrow their electrochemical window. Determination of the toxicity of the ionic liquid is also important, since extractions may result in the release of ionic liquid, which if hazardous will cause further contamination. It should be noted that there are cases, where ionic liquids exhibit even more toxicity to microorganisms than VOCs. The toxicity of imidazolium based ionic liquids depends mainly on the length of the alkyl chain; the shorter the chain length the lower the toxicity (Romero et al., 2008). Moreover, studies on the radiolysis of ionic liquids, when subjected to doses of gamma radiation, showed better stability compared to TBP/kerosene mixtures (Allen et al., 2002).

#### 2.3.4 UV-Vis spectroscopy

Differences between ionic liquids and traditional solvents would give rise to differences in the stoichiometry of the extracted species. Although slope analysis may be sufficient to determine such stoichiometries, the exact amount of nitrate ions in the aqueous phase and of the free ligand in the ionic liquid phase are largely unknown and this hampers the use of this graphical method. Different inner-coordination environments are observed for the dioxouranium(VI)-nitrate complexes formed in the different ionic liquids and other organic solvents (dodecane). Qualitative differences in the coordination environment of the extracted dioxouranium(VI) species are implied by changes in peak intensity patterns and locations for UV-Vis spectral bands when the solvent is changed (Bell and Ikeda, 2011). Optical absorption spectra have proven useful in distinguishing differences in the coordination environment in organic solvents. Given the complexity of the ionic liquid medium, speciation of dioxouranium(VI) complexes is not an easy task. UV-Vis spectroscopy is useful technique for the specification of uranium(VI) complexes, because each oxidation state of uranium(VI) gives a typical spectrum. Although the dioxouranium(VI) ion has no f-electrons, electronic transitions are possible between the molecular orbitals formed by interaction between ligand and dioxouranium(VI) atomic orbitals. The absorption spectra are in the 350-525 nm range. The differences in the coordination environment between ILs and conventional solvents have been under investigation in the last few years. Studies of the spectra of uranium(VI) containing solutions in ionic liquids ( $[C_{10}mim][NTf_2]$ ) and in dodecane after contacting with the appropriate uranium(VI)/HNO<sub>3</sub> solutions showed that there are equivalent dioxouranium(VI) inner sphere coordination environments in both solvents (Cocalia et al., 2005). The typical spectra of the ligands have a minor influence on the spectral fine structure,

while water has a pronounced effect on the spectroscopic behaviour of dioxouranium(VI) in ionic liquids with weakly coordinating anions (Nockemann et al., 2007). The UV-Vis spectra of the ionic liquid phase ( $[\text{C}_4\text{mimNTf}_2]$ ) after the extraction of uranium(VI) from nitric acid solutions are shown in **Figure 2.19**. Because of the low molar absorption coefficient of uranium(VI) in ILs the concentration of dioxouranium(VI) should be sufficiently high (ca.  $10^{-2}$  M). It can be seen that the excitation peaks of dioxouranium(VI) in the ionic liquid have been slightly shifted compared to that of dioxouranium(VI) in the aqueous phase, because the chemical environment in the IL is probably more favourable for the formation of a dioxouranium(VI)-nitrate acid complex (Wang et al., 2009). The absorption shape is changing as the nitric acid concentration is increasing, which implies a change in the stoichiometry of the extracted species from low to high acidities of the aqueous phase.

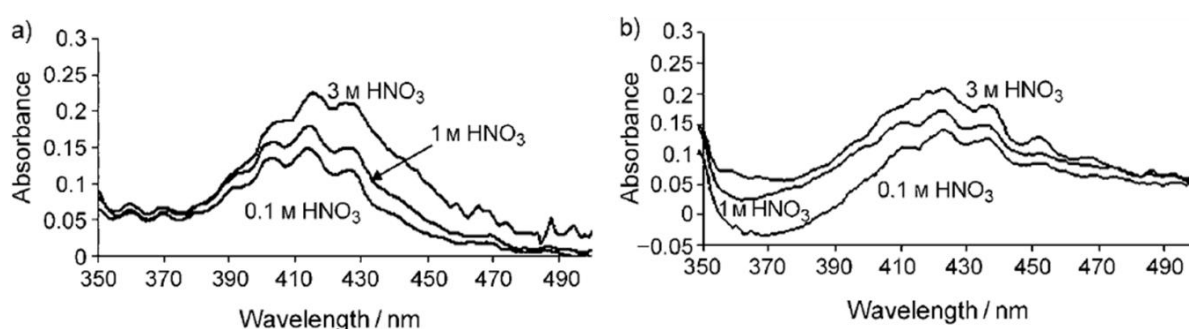


**Figure 2.19:** a) Aqueous phase spectra of uranium(VI) before extraction; b) IL-phase spectra after extraction of uranium(VI) from the aqueous phase into  $[\text{bmim}][\text{NTf}_2]$ . Extraction of uranium(VI) in 3M HNO<sub>3</sub> reaches 95% with 30%v/v TBP in the IL phase (Wang et al., 2009).

## 2.4 Overview

The hydrodynamic behaviour of two-phase flows and particularly of plug flow has been extensively studied by many investigators. However, most of the studies involved conventional fluids and little is known concerning the hydrodynamics when ionic liquids are involved. In addition, studies of liquid-liquid flows are usually limited to either sub-millimetre channels or to much larger ones, but not for channels with few millimetres in diameter. Moreover, the reprocessing of spent nuclear fuel by using ionic liquids seems a promising and interesting method. A number of investigations have been conducted on the extraction of uranium(VI) from nitric acid solutions by TBP/ionic liquid mixtures. However,

all the extractions with ionic liquids have been carried out in equilibrium, while no reported cases of continuous extraction during plug flow are available.

In the following studies, the hydrodynamics and mass transfer during liquid-liquid flow with ionic liquids in channels with a range of diameters are presented. Flow patterns, as well as several hydrodynamic characteristics, such as plug length, plug velocity, film thickness, and pressure drop have been investigated, whilst predictive correlations have been proposed. In addition, continuous extractions of uranium(VI) with ionic liquids were studied during plug flow. Finally a numerical finite element model for the hydrodynamics and mass transfer was developed.

# Chapter 3.

## Experimental details

### 3.1 Introduction

This chapter gives a detailed description of the experimental part of the thesis. The properties of the fluids and the materials used, as well as the corresponding suppliers and product details are stated. Characterisation methods used throughout the investigation are also discussed. Finally, the experimental procedures and the equipment used for each set of experiments are discussed in detail.

### 3.2 Materials

#### 3.2.1 *Ionic liquids*

The ionic liquids used in this work are 1-butyl-3-methylimidazolium bis{(trifluoromethyl)sulfonyl}amide  $[\text{C}_4\text{mim}][\text{NTf}_2]$ , 1-decyl-3-methylimidazolium bis{(trifluoromethyl)sulfonyl}amide  $[\text{C}_{10}\text{mim}][\text{NTf}_2]$ , and trihexyltetradecylphosphonium bis{(trifluoromethyl)sulfonyl}amide  $[\text{P}_{66614}][\text{NTf}_2]$ . They were prepared at the QUILL research centre following a standard routine ([Bonhote et al., 1996](#)) and their properties are summarised in **Table 3.1**.

**Table 3.1: Properties of pure ionic liquids.**

Properties (at room temperature)	[C <sub>4</sub> mim][NTf <sub>2</sub> ]	[C <sub>10</sub> mim][NTf <sub>2</sub> ]	[P <sub>66614</sub> ][NTf <sub>2</sub> ]
<sup>1</sup> Viscosity, $\mu / \text{kg m}^{-1} \text{s}^{-1}$	0.052	0.124	0.296
<sup>1</sup> Density, $\rho / \text{kg m}^{-3}$	1420	1260	1065
<sup>2</sup> Surface tension, $\sigma / \text{N m}^{-1} (\cdot 10^{-3})$	31.26	28.54	29.83
<sup>1</sup> Properties of ionic liquids measured at the QUILL research centre.			
<sup>2</sup> Properties of ionic liquids measured at UCL laboratory.			

For the extraction experiments, tributylphosphate (TBP) 97% with density and viscosity of  $972.7 \text{ kg m}^{-3}$  and  $3.88 \cdot 10^{-3} \text{ kg m}^{-1} \text{s}^{-1}$ , respectively, was also dissolved in the ionic liquids. TBP was obtained from Sigma-Aldrich. The properties of the saturated TBP/ionic liquid mixtures used for the experiments are shown in **Table 3.2**.

**Table 3.2: Properties of TBP/ ionic liquid mixtures (30%, v/v)**

Properties (room temperature)	TBP/[C <sub>4</sub> mim][NTf <sub>2</sub> ]	TBP/[C <sub>10</sub> mim][NTf <sub>2</sub> ]	TBP/[P <sub>66614</sub> ][NTf <sub>2</sub> ]
Viscosity, $\mu / \text{kg m}^{-1} \text{s}^{-1}$	0.029	0.072	0.183
Density, $\rho / \text{kg m}^{-3}$	1286	1174	1037
Interfacial tension, $\gamma / \text{N m}^{-1} (\cdot 10^{-3})$	10.01	11.51	11.92
Surface tension, $\sigma / \text{N m}^{-1} (\cdot 10^{-3})$	29.31	28.32	28.53

### 3.2.2 Aqueous solutions

Deionised water or nitric acid solutions of different molarities were used for the hydrodynamic and mass transfer experiments. The HNO<sub>3</sub> solutions were prepared in the UCL

laboratory from aqueous nitric acid (65%) solutions of general purpose grade (~14.4 M) by Fisher Scientific ( $\rho = 1370\text{--}1400 \text{ kg m}^{-3}$ ,  $\mu = 0.0023 \text{ kg m}^{-1} \text{ s}^{-1}$ ).

### 3.2.3 Particles

To study the flow within the capillaries, the aqueous phase was seeded with fluorescent microsphere suspensions at 1% concentration by weight (Thermo Scientific). The fluorescent micro-spheres are made of polystyrene and were dyed with red or blue fluorescent dyes. The refractive index and the density are 1.59 and  $1.06 \text{ g cm}^{-3}$ , respectively. The spectral properties of the fluorescent microspheres are shown in **Table 3.3**. The size of the particles varied between 1 and  $3.2 \text{ }\mu\text{m}$  depending on the channel size.


**Table 3.3: Spectral properties of fluorescent micro-spheres**

Specified colour	Excitation max (nm)	Emission max (nm)
Red	542 (green)	612 (red)
Blue	365 (UV)	447 (blue)

### 3.2.4 Dioxouranium(VI) nitrate hexahydrate ( $\text{UO}_2(\text{NO}_3)_2 \cdot 6\text{H}_2\text{O}$ )

To simulate the nuclear waste,  $\text{UO}_2(\text{NO}_3)_2 \cdot 6\text{H}_2\text{O}$  dissolved in nitric acid solution was used.  $\text{UO}_2(\text{NO}_3)_2 \cdot 6\text{H}_2\text{O}$  is a yellow crystalline solid. It contains nitric acid and is mildly chemically toxic. It is non-fissile (depleted) uranium, containing less than 1.0% U-235, which means that it cannot sustain a nuclear chain reaction. It is radioactive, but chemically stable. Some of the properties are presented in **Table 3.4**. At all experiments the initial concentration of dioxouranium(VI) in the nitric acid solutions was 0.05 M. The concentration of  $\text{UO}_2^{2+}$  in the two phases was detected by a UV-Vis spectrometer (USB2000+, from Ocean Optics).

**Table 3.4: Properties of dioxouranium(VI) nitrate hexahydrate,  $\text{UO}_2(\text{NO}_3)_2 \cdot 6\text{H}_2\text{O}$** 

	Molar mass	$502.13 \text{ g mol}^{-1}$
	Density	$2810 \text{ kg m}^{-3}$
	Melting point	$60 \text{ }^\circ\text{C}$
	Solubility in water	$\sim 660 \text{ g L}^{-1}$
	Solubility in TBP	soluble

### 3.3 Characterization of solutions

#### 3.3.1 Viscosity

Viscosity measurements were performed before each set of two-phase experiments to estimate the actual viscosity values of the ionic liquids. Although the ionic liquids used in this research are hydrophobic, they still absorb small amounts of water (hygroscopic) depending on the initial nitric acid concentration in the aqueous phase. The absorbed water is expected to affect their viscosity (Billard et al., 2011b). To estimate the viscosity of the saturated ionic liquid, prior to the experiments the ionic liquids were stirred with water or nitric acid solutions. Saturation was confirmed, when the viscosity did not change over time. The viscosities of the ionic liquids were measured using a digital Rheometer DV-III Ultra (Brookfield) at room temperature and were found to decrease by 15-20% when saturated with aqueous phase compared to the values of pure ionic liquids.

#### 3.3.2 Surface tension and contact angle

Surface and interfacial tensions of the two liquids were measured with a Kruss DSA 100 drop analyser system by the pendant drop method. The liquid was injected from a needle, and a droplet was formed in air on the tip of the needle. The droplet was then optically observed, and the surface tension was calculated from the shape of the drop using the DSA1 software for DSA 100 system. In order to measure the interfacial tension between the two liquids the needle was immersed into the aqueous solution and a droplet of ionic liquid was formed. The



properties of the fluids used for the experiments are given in each relevant section of the thesis.

The contact angles of the liquids with substrates made from the same materials as the channel walls were also measured using the Kruss DSA 100 system. Both liquid-air-solid and liquid-liquid-solid contact angles were obtained. In the former case a drop of the liquid was placed on top of a flat plate made by borosilicate glass or Teflon in air and the contact angles were found from the still images taken. In the latter case, the plate was immersed in water and a drop of ionic liquid was put on top of it. Depending on the value of  $\theta^\circ$  (**Figure 3.1**) the wettability of the surface could be characterised as, spreading ( $\theta=0^\circ$ ); good wetting ( $\theta<90^\circ$ ); incomplete wetting ( $\theta=90^\circ$ ); poor wetting ( $\theta>90^\circ$ ), and no wetting ( $\theta=180^\circ$ ) for the ionic liquid phase. The contact angle of a liquid drop is described by the mechanical equilibrium of the drop under the action of three interfacial tension forces (Young equation).

$$\gamma_{F1/F2} \cos \theta = \gamma_{S/F2} - \gamma_{S/F1} \quad (3.3.1)$$

where  $\gamma_{F1/F2}$ ,  $\gamma_{S/F2}$ ,  $\gamma_{S/F1}$  represent the fluid 1-fluid 2, solid-fluid 2 and solid-fluid 1 interfacial tensions, respectively.

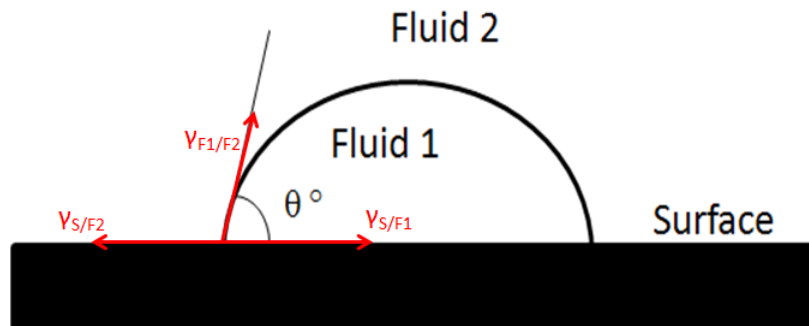


**Figure 3.1:** Schematic of contact angle formed by sessile liquid drops on a smooth solid surface.

### 3.4 Experimental setup and procedure

The experimental setups, operating conditions, and procedures followed for the study of the hydrodynamics and mass transfer in the two-phase small scale contactors are discussed below. In general, the experimental setup comprises five main sections: fluids delivery in the mixing zone, flow visualization, pressure drop measurement, online separation, and

dioxouranium(VI) ion detection (**Figure 3.2**). Depending on the nature of the measurements and the application, the setup was slightly modified for each set of experiments.

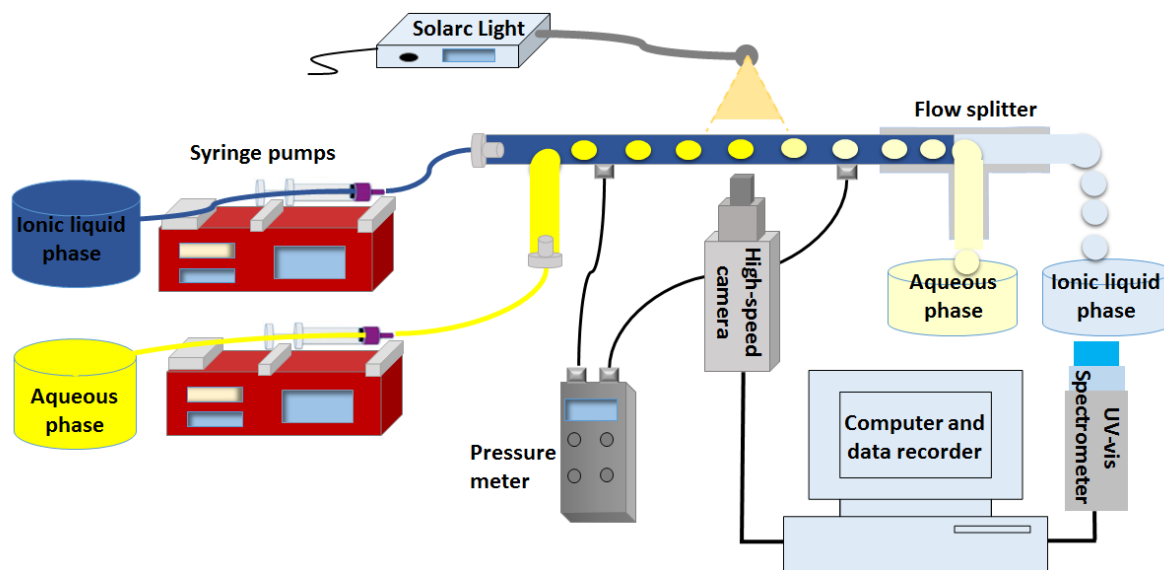


**Figure 3.2:** Schematic of the experimental setup used for the hydrodynamic and mass transfer experiments.

Hydrodynamics, pressure drop, and mass transfer during liquid-liquid flows were investigated in two different systems, viz. in glass microchannels with circular cross section of 0.2 mm ID (**Figure 3.3A & B**) using an ionic liquid and deionised water, and in Teflon channels of different sizes, i.e. 0.2-2 mm ID (**Figure 3.3C**) using either different TBP/ionic liquid mixtures (30%, v/v) (**Table 3.2**) and aqueous nitric acid solutions, relevant to spent nuclear fuel reprocessing, or ionic liquid and deionised water. The internal diameter of the microchannels was measured using a microscope (Nikon Eclipse ME 600).



**Figure 3.3:** Photographs of the channels used in this work. (A) Glass microchannel (Dolomite microfluidics), and (B) and (C) glass and Teflon tubing (Aquilant Scientific)

For all the experiments, two high precision double syringe-pumps (KdScientific) fed the two liquids separately to the mixing zone. The pumps were calibrated and the maximum uncertainty of the flow rates was  $\pm 2\%$ . Two inlet configurations (T- and Y-junction) (**Figure 3.4**) were used for bringing the fluids into contact, both made of Teflon. In the T-junction, the two fluids entered the mixing zone perpendicularly, whilst the angles of the inlets in the Y-junction were  $120^\circ$ .



**Figure 3.4: T- and Y-junctions for mixing the two liquids.**

For all the experiments the aqueous phase was seeded with 1 or  $3.2\ \mu\text{m}$  fluorescent polymer micro-beads suspension at 1% concentration by weight, depending on the channel size. The length of the test section varied from 10 to 31.5 cm. The flow visualisation section comprised a CMOS high-speed camera (Photron Fastcam-ultima APX) connected to a computer for data storage, and a light source. Images (2MP 10-bit) were acquired continuously at 2000-8000 Hz (depending on the total flow rate) at a distance of 8 cm downstream the inlet.

### 3.4.1 Pressure drop measurements

For the pressure drop measurements, a differential pressure meter Comark C9555 (range: 0- $\pm 200$  kPa, accuracy  $\pm 0.2\%$ ) was used, connected to two pressure ports before and after the microchannel, as illustrated in **Figure 3.5**. To measure the pressure drop in the glass microchannel, two side channels (referred as t2 in **Figure 3.5**), with a length of 5 cm each, were added to connect the main channel to the pressure ports. For pressure drop measurements in the Teflon microchannels the pressure ports could be connected directly to the pressure meter, and in this case the side channels t2 were removed. To connect the pressure ports to the differential pressure meter PTFE tubing was used, which was filled with

the heavier phase (i.e. ionic liquid) to ensure that aqueous phase will not enter into the side tubings. Initially, single phase experiments with ionic liquid were performed and results were compared with the Hagen-Poiseuille equation, to confirm the reliability of the method (<2% error). Subsequently, the aqueous phase was introduced in the channel and pressure drop during two-phase flow was recorded.

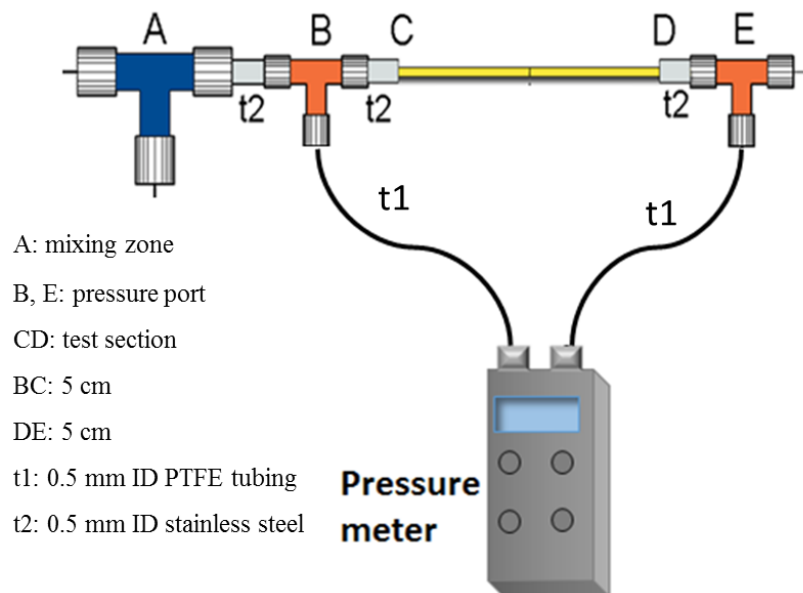


**Figure 3.5: Schematic representation of the pressure drop configuration.**

### 3.4.2 Flow splitting

In order to separate the two phases online an in-house flow splitter was connected at the end of each test section (see

**Figure 3.6).** The splitter had two side channels made of stainless steel and PTFE that have different wettabilities for the two liquids used. The internal diameter and the length of the side channels were chosen based on the pressure drop that was created on the flow splitter [similar to (Scheiff et al., 2011)]. With this configuration pure ionic liquid phase was obtained from the PTFE outlet and aqueous solution from the stainless steel outlet. However, at high mixture velocities the separation was not always 100% efficient and a mixture of ionic liquid and aqueous solution was collected from the steel outlet.

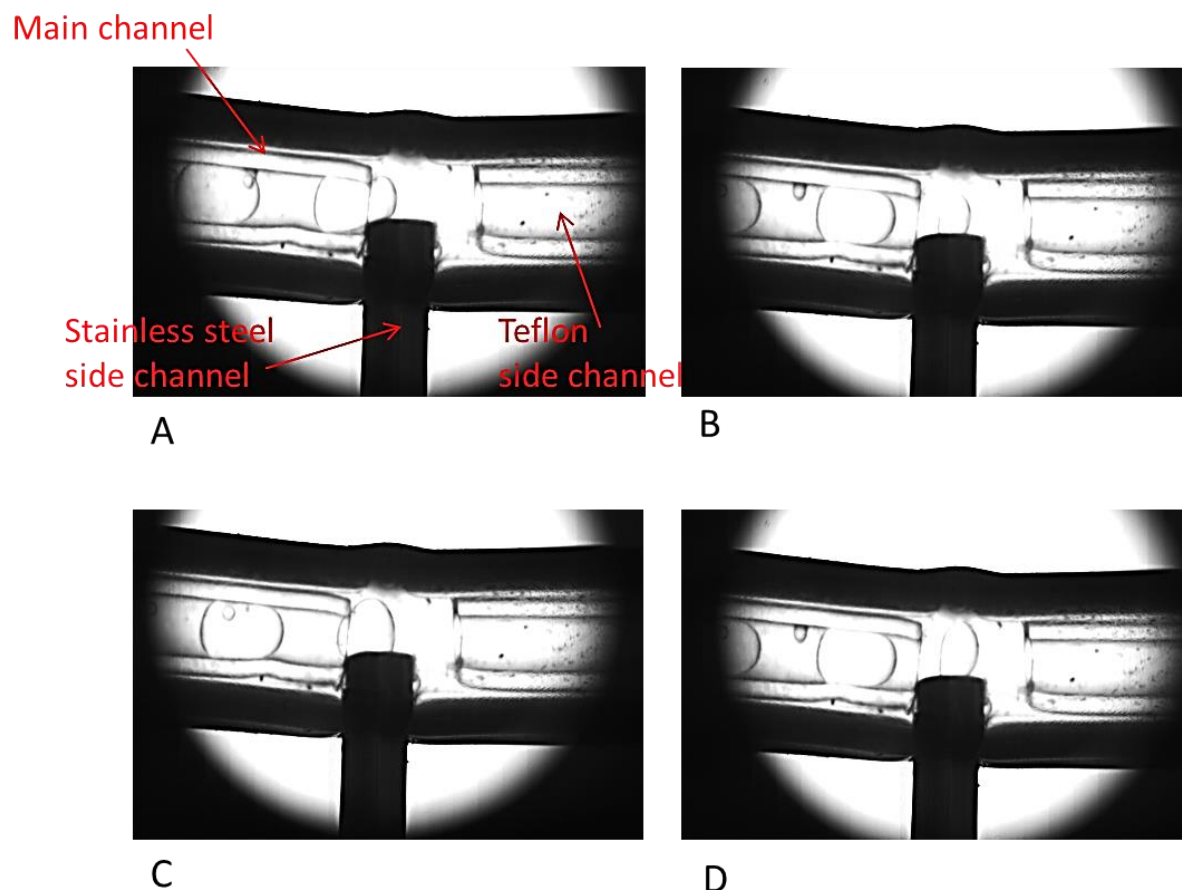


**Figure 3.6: Flow splitter connected at the end of the test channel.**

### 3.4.3 UV-Vis spectroscopy

For the dioxouranium(VI) detection in the ionic liquid and aqueous nitric acid phases a UV-Vis spectrometer (USB2000+, from Ocean Optics) was used. After the online separation of the two phases the samples were collected in rectangular plastic cuvettes with spectral range from 350-900 nm. To minimise the error from discrepancies between the cuvettes the same cuvette was used for one set of experiments. A calibration curve was plotted by making a number of solutions of accurately known concentrations of dioxouranium(VI) in the TBP/ionic liquid and in the nitric acid solutions. For each solution the absorbance at the wavelength of strongest absorption was measured. Then a graph was plotted of the absorbance against the concentration. The concentration of the samples after the extraction was calculated based on that calibration curve.

## 3.5 Techniques

### 3.5.1 PIV measurements

PIV was carried out in two different ways depending on the size of the channel, fluid properties and materials, and the application. In order to study hydrodynamic characteristics within the glass microchannel of 0.2 mm ID, Particle Image Velocimetry was performed by using conventional pulsed laser illumination and a straddle mode CCD camera (section 3.5.1.1). However, to study the circulation patterns within aqueous nitric acid plugs and be able to perform velocimetry experiments online with extraction experiments in larger channels (where acidic solutions are used) the PIV was carried out in a non-conventional way, by using continuous bright field illumination and high-speed imaging (section 3.5.1.2). The use of acid aqueous solutions in the investigated process would alter the pH and consequently fluorescence features of the seeding particle suspensions in water commonly employed in standard epi-fluorescent microscopy. This effect can bring difficulties in imaging pH sensitive fluorophores, when processes require the variation of the acidity of the solvent.

#### 3.5.1.1 PIV setup used in glass micro-channels

The experimental set up used for PIV measurements in the glass microchannel with internal diameter of 0.2 mm is depicted in **Figure 3.7**. Velocimetry measurements were carried out in the T-junction, in the straight channel, as well as in the bend, as shown in **Figure 3.7C**. The channel was etched in a quartz chip, which was sealed through thermal bonding (Dolomite microfluidics).

A UV double pulsed Nd:YAG laser (Litron Lasers) illuminated the micro-fluidic device from a 45° angle with a 355 nm beam (volume illumination). The observation region was 30 mm away from the inlet. The laser beams excited the particles which emitted blue light within a band centred on 445 nm. Particle blue fluorescence was detected by a 12bit 4 MPixels 16 fps CCD camera (TSI instruments), focused on the test section, after passing through a narrow pass band filter centred at 445 nm. The optical train (TSI instruments) mounted on the camera allowed 20× magnification, flat-field, and aberration correction to be achieved. The used optical system provided a field of view of the order of 1 mm and a pixel size projected back onto the flow of 0.53 μm.

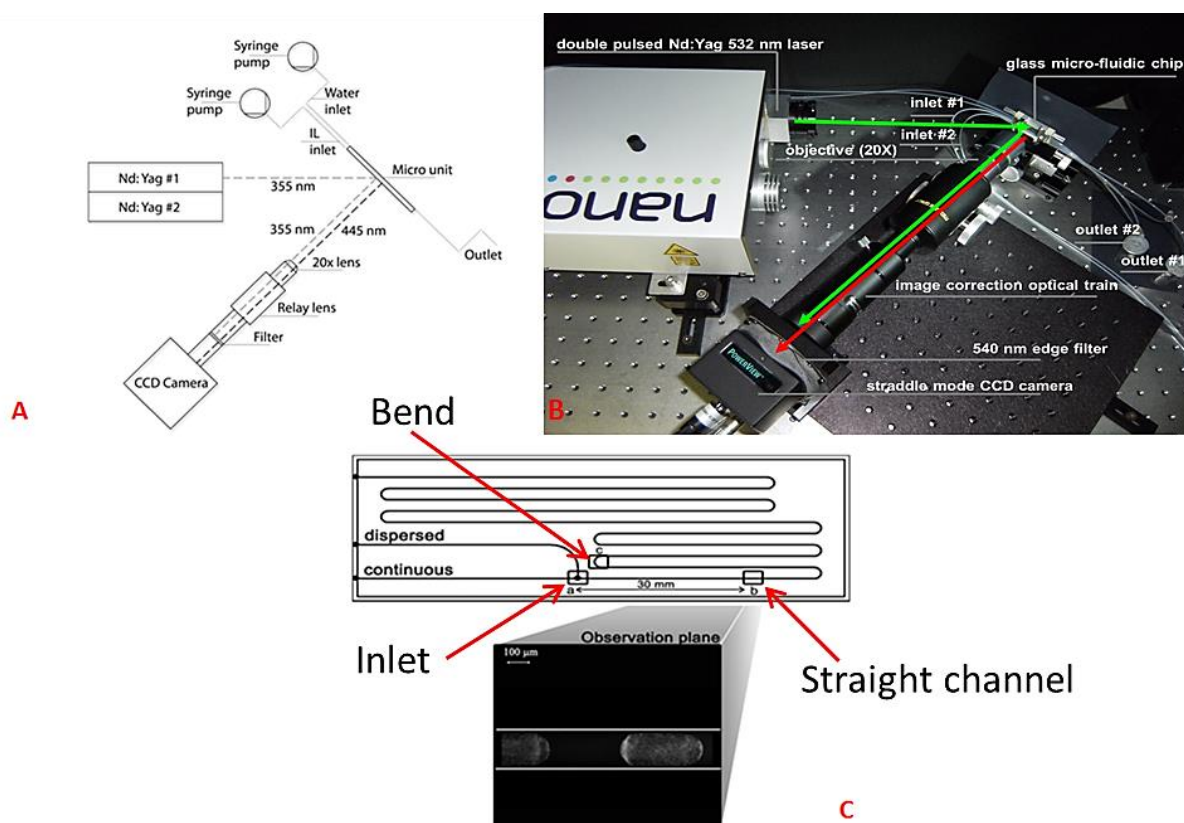


**Figure 3.7: (A) Schematic and (B) photograph. (C) Side view of the micro-channel. Cross section is circular with internal diameter of 0.2 mm. The observation plane (XY) is positioned downstream about 30 mm away from the T inlet. Drawing not to scale.**

The focal plane was located approximately at the centre of the channel along the  $z$  direction (the focal plane was located with a precision traverse, which had been pre-calibrated using the front wall as a reference and maximizing the channel width, giving an uncertainty of  $\pm 1 \mu\text{m}$ ). According to the numerical aperture of the magnification lens ( $\text{NA}=0.42$  and  $n=1.00$ ) and features of seeding particles the depth of field was of the order of  $10 \mu\text{m}$  (Olsen and Adrian, 2000). The refractive index of the ionic liquid  $[\text{C}_4\text{mim}][\text{NTf}_2]$  (i.e. 1.51, (Deetlefs et al., 2006)) matched well that of the channel material (i.e. 1.54) and refraction at the inner channel wall/liquid interface can be neglected, as the ionic liquid in all cases studied with PIV was in contact with the channel wall. However, since the refractive index of the dispersed phase (water) is 1.33, distortion due to mismatch is expected in the regions where the two caps of the plug are formed. In addition, the external channel wall was flat and it was not necessary to add a third medium for refractive index matching (Han and Shikazono, 2009). Furthermore, typical distortion/reflection effects due to refraction at solid/liquid and



liquid-liquid interfaces as described by Budwig (Budwig, 1994) were not observable on the acquired images.

Images were acquired in straddle mode by a frame grabber and stored in the hard disk of a PC. Image acquisition was synchronized with laser pulses in such a way that image pairs were captured at a maximum frequency of 7 Hz, while the time lag between the two images of a pair (i.e.  $\Delta t$ , the time lag between two laser pulses) was adjusted according to the expected velocity inside the channel. For the present experiments,  $\Delta t$  was varied between 20 and 1000  $\mu\text{s}$ , depending on the combination of flow rates inside the channel.

In order to measure velocity components inside a regular grid drawn on the measurement plane, the domain in each image was to be sampled into rectangular-shaped interrogation windows properly overlapped to satisfy the Nyquist sampling criterion (Meinhart et al., 1999). A standard PIV algorithm (TSI instruments) was used to reconstruct the displacement of each window across the two images of a pair via a cross-correlation routine with sub-pixel accuracy. The two-component velocity field could thus be reconstructed within the Eulerian grid in which the domain had been discretized, by employing the spatial calibration ratio and the time lag between the correlation images. In the present experiments a square domain discretization of  $32 \times 32$  pixels with 50% overlap was implemented that provided robust statistics and a velocity spatial resolution of 8.48  $\mu\text{m}$ . By properly adjusting the time lag, the maximum displacement between the two images of a pair never exceeded 25% of the window size. This criterion minimizes the effect of the error increase on velocity measurements as the maximum displacement increases. The uncertainty of the velocity measurements can be estimated from the diffraction limited theory (Meinhart et al., 1999). The effective particle diameter projected back onto the flow,  $d_{\text{eff}}$ , given by the diffraction limited point spread function  $d_s$  was calculated to be 1.6  $\mu\text{m}$  (3-4 pixels). This allows a location of the particle image correlation peak to be determined within one tenth of the particle image diameter,  $d_{\text{eff}}$ , which results in a displacement uncertainty of 0.16  $\mu\text{m}$  in this case. For the minimum time lag employed in the present investigation (i.e. 20  $\mu\text{s}$ ) and corresponding average velocity of 0.067 m/s the uncertainty is found to be of the order of 0.01%.



### 3.5.1.2 PIV setup used in straight Teflon small-channels

A non-conventional bright field micro-Particle Image Velocimetry ( $\mu$ -PIV) system was used to measure the velocity field inside the aqueous plugs and to study hydrodynamic properties of the two-phase system such as plug size, and film thickness in the larger Teflon channels. The advantages of using white bright field illumination combined with high-speed recording among others are the simplicity of the system, since no lasers and complicated optics are required and the increased time resolution that is challenging in fluorescence microscopy. In addition it enables the performance of simultaneous measurements within mass transfer (Figure 3.8).

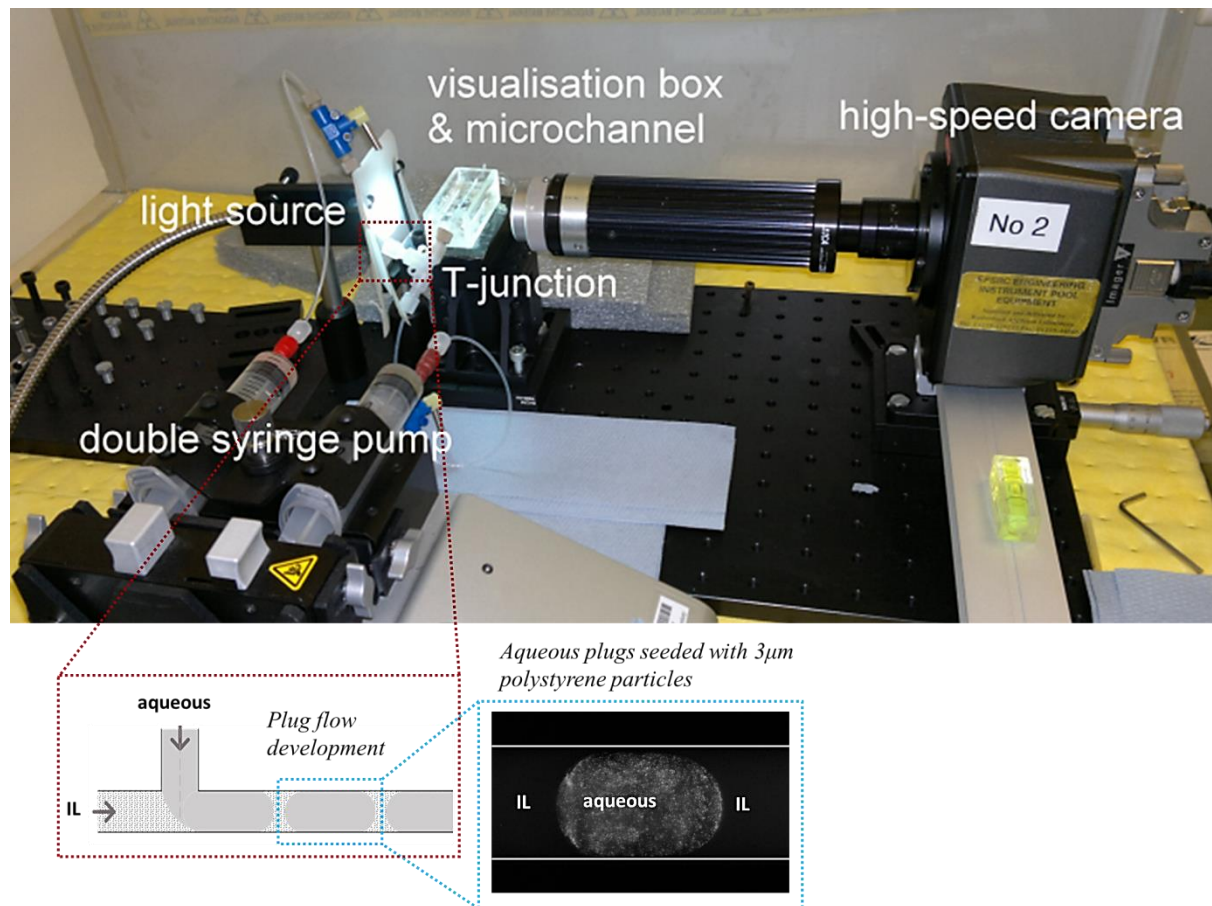


**Figure 3.8: Photograph of the experimental setup for simultaneous performance of PIV and mass transfer measurements.**

The aqueous phase which contained the polymer microspheres ( $3.2\ \mu\text{m}$ ) and the channel were backlit using a 60 Watt continuous white arc lamp, and images were obtained with particles appearing dark on a bright background, since they have lower light transmission. A CMOS high-speed camera (Photron Fastcam-ultima APX) with a maximum resolution of  $1024 \times 1024$

pixels, and equipped with a 5x magnification lens, acquired 2MP 10-bit images continuously at 2000-8000 Hz (depending on the total flow rate). The field of view was determined by the objective lenses of the camera (extending lenses: 0.75 $\times$ , 0.5 $\times$ , 0.25 $\times$ , and shortening lenses: 1.5 $\times$ , 2 $\times$ ) depending on the length of the aqueous plug, whilst the pixel size varied from 2.58 to 5.75  $\mu\text{m}$ . Both the camera and the microchannel were placed at micro-meter stages and traverses, which allowed a 3-D relative motion between them so as to focus precisely on the desired observation plane, approximately located at the channel mid-plane. The precision traverse was pre-calibrated by using the front wall of the channel as a reference. The capillary was enclosed in a flat visualization box filled with water to minimise reflections at the interface.

To calculate the velocity fields in  $\mu$ -PIV image pairs are required. The commercial TSI PIV platform Insight 4G was used to calculate the displacement of each window across the two frames of an image pair via a cross-correlation routine. The time interval between an image pair was chosen depending on the expected velocity inside the channel and the required spatial resolution. In the current study a square discretization domain of 32 $\times$ 32 pixels with 50% overlap to satisfy the Nyquist sampling criterion was used (Meinhart, 1999). In addition, a peak height validation of 1.2 was performed on all data to eliminate spurious vectors. A velocity spatial resolution of up to 46  $\mu\text{m}$  was achieved along the x and y-axes, while the effective depth of field was varied between 30 and 100  $\mu\text{m}$  (as calculated from the characteristics of the LEICA Monozoom 7 optical system). The 2-D velocity field ( $u_x$  and  $u_y$ ) was reconstructed within the Eulerian grid in which the domain was discretised, by employing the spatial calibration ratio and the time interval between the correlation frames.

The system was validated by performing single aqueous phase experiments and comparing velocity profiles with the analytical solutions for laminar circular channel flow. In **Figure 3.9** results for single phase experiments are presented (average velocity equal to 0.015  $\text{m s}^{-1}$ ). The average velocity profile in **Figure 3.9A** matches well the analytical solution. The uncertainty of velocity measurements was estimated based on the standard deviation of velocity data (order of 10%) and plotted in the form of error bars on **Figure 3.9B**.

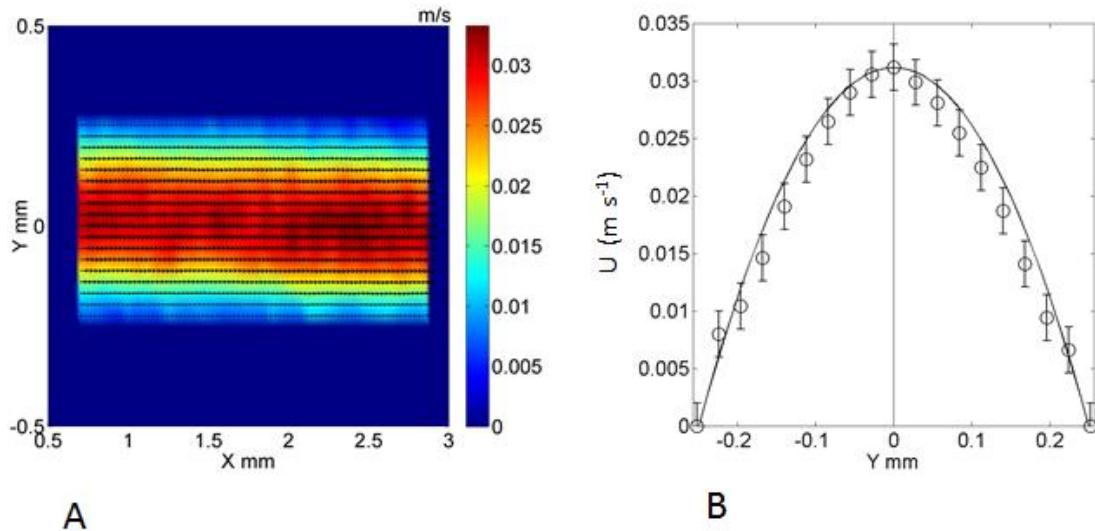


**Figure 3.9: (A) Velocity vector field for single phase run at mixture velocity of  $0.015 \text{ m s}^{-1}$ . (B) Velocity profile along Y direction averaged across the channel length, compared with the analytical laminar flow profile (solid line).**

### 3.5.2 Image processing

Under the investigated experimental conditions, the flow is segmented (or plug) with either the ionic liquid or water as the carrier medium. Dispersed plugs are formed periodically at the inlet; however, the flow can be considered steady state in the main channel with respect to a reference frame attached to each moving plug/slug interface, in which case ensemble averaging is possible. An in house pre-processing routine was then developed to properly mask the raw images in a way that presence of spurious vectors in the unseeded liquid (i.e. ionic liquid) is prevented and ensemble average could be performed in the other.

Sample images acquired at the inlet during a plug formation cycle are shown in **Figure 3.10A1-D1**. The shape of the interface changed with time in a periodic manner, so a stationary mask for the PIV vector fields could not be employed. For each stage of the plug formation cycle, images were then pre-processed as follows:

1. Image smoothing is obtained by applying a median filter. Pixel intensity in the seeded liquid is thus more uniform, making image binarization by thresholding easier and more accurate.
2. Image binarization is obtained by setting a threshold pixel value to discriminate the water medium.

3. Edges are further smoothened by filling possible holes in the domain and applying morphological transformations to the binary images, like recursive erosion and dilatation.

The channel location is identified by pre-processing the same images, but binarizing them using a lower threshold value. By combining the two binary masks for the channel and aqueous phase via image multiplication, the location of both media was known and edges can be further refined for the generation of the aqueous phase mask. Resulting masks for the same sample images in **Figure 3.10A1-D1** are presented in **Figure 3.10A2-D2**. Given the periodic nature of the flow, the same masks can be used for corresponding stages of different cycles and phase ensemble average can then be performed among the related instantaneous vector fields. Background subtraction was also performed prior to cross-correlating the images in order to maximize signal/noise ratio.

Once the plug has been formed at the inlet, the shape of the interface is stationary in the main channel. The same mask can thus be employed to extract averaged velocity fields within single plugs (or slugs) in the straight channel, provided each image has been shifted to match the absolute reference frame, defined in the very first frame of the sequence (i.e. the reference frame is attached to the moving plug/slug interface). Therefore images were pre-processed as follows:

1. The plug was detected in the first frame of the first image pair, and inscribed in a rectangular window (Region of Interest, ROI). The mask for the whole image sequence is then generated as described above (steps 1, 2, and 3).
2. For each image pair that follows, the rectangular region most similar to the ROI (i.e. the plug or slug) was detected in the first frame of the pair via a cross-correlation routine and shifted to match the reference frame attached to the original ROI in both frames.

Steady state could then be assumed and ensemble average over the image sequence was performed after the background subtraction. All the final vector fields in the aqueous medium were validated by their signal/noise ratio in the corresponding cross-correlation maps (i.e. ratio between the highest and the second highest peak) and only a small percentage of spurious vectors was found close to interfaces (order of 1%). The spurious vectors were

replaced by using a median test in local  $3 \times 3$  neighbourhoods (Westerweel and Scarano, 2005), provided there was no valid secondary peak in the correlation maps.

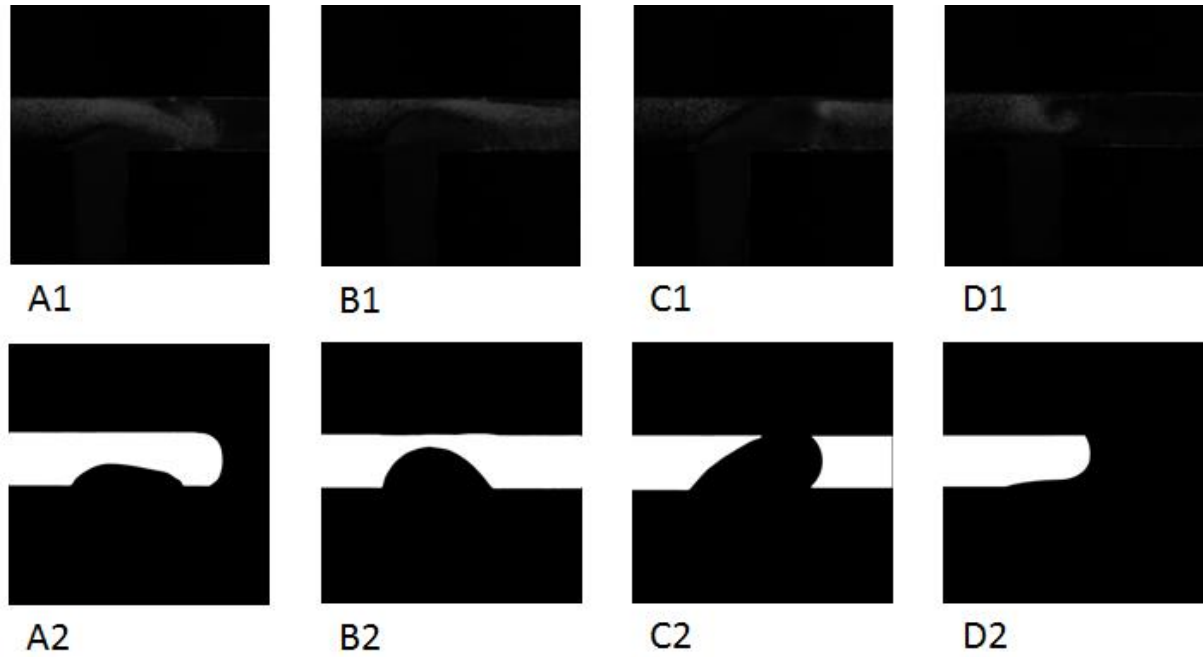
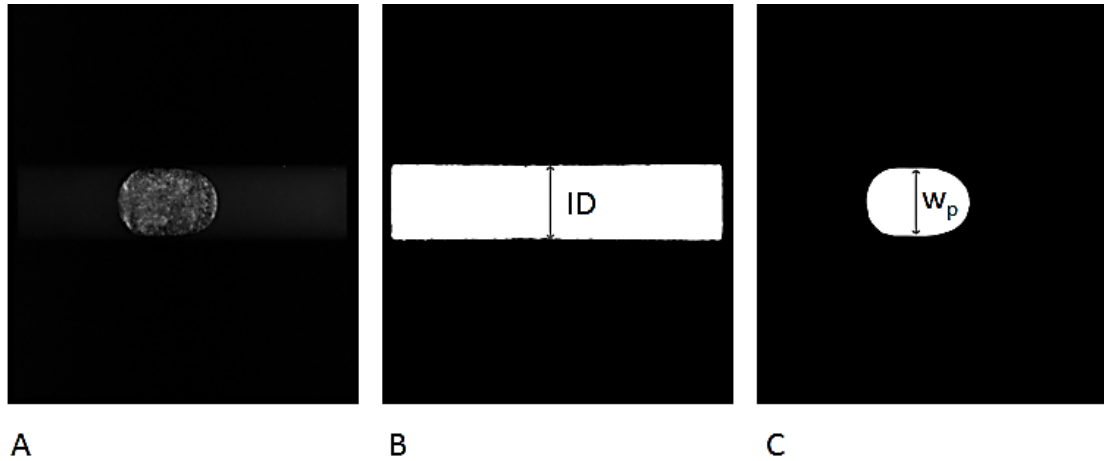


Figure 3.10: (A1-D1) Sample raw images within a plug formation cycle of period  $T=1.05$  s and (A2-D2) corresponding mask images. Water is the carrier fluid.

### 3.5.3 Estimation of the film thickness

To measure the film thickness of the plug the same image processing routine (as explained in section 3.5.2) has been developed. The film thickness was then obtained from Eq. (3.5.1) with a pixel accuracy (error: 2-5%) by subtracting the width of the plug ( $w_p$ ) from the channel diameter (ID) and dividing by two (see Figure 3.11 ).

$$\delta = \frac{ID - w_p}{2} \quad (3.5.1)$$



**Figure 3.11: (A) Sample raw image. (B) Binary images for the channel, and (C) water plug, obtained after image processing of (A) and binarization with different thresholds.**

The film thickness evaluation varied depending on the shape of the plug. As the total volumetric flow rate and channel size increased the plug acquired a “bullet shape”. In these cases, there is no constant film thickness region (red highlighted) as shown in **Figure 3.12** and the film thickness was estimated by averaging the width of the plug at the points where the front and rear caps of the plug end and substituting in Eq (3.5.1).

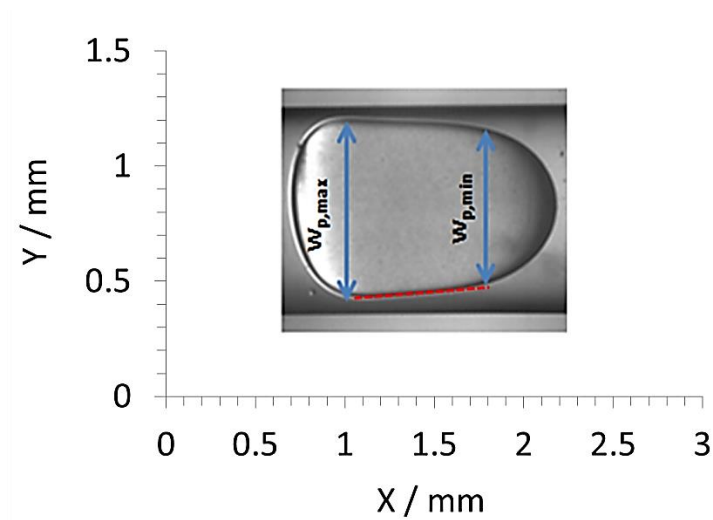


**Figure 3.12: Image of a “bullet shape” plug with no apparent flat film region.**

Most of the experimental details and the properties of the materials used throughout this research have been explained in this chapter. Further details regarding the conditions and the techniques for each specific experiment will be given at each particular chapter.

## Chapter 4.

# Liquid-liquid flows in micro and small channels: Hydrodynamics and pressure drop.

### 4.1 Introduction

In this chapter the hydrodynamic characteristics and the pressure drop of liquid-liquid flows in small circular channels are presented. Two liquid-liquid flow systems are considered for the experiments, i.e. ionic liquid-deionised water, and TBP/ionic liquid (30% v/v)-nitric acid solutions. The channels tested were made either of glass or Teflon. Channel sizes varied in internal diameter from 0.2 to 2 mm.

The first part of this chapter focuses on the flow patterns formed in 3 channels of different size and material, as well as on the associated pressure drop during the various flow patterns observed. Subsequently, in the second part the work focuses on the hydrodynamic characteristics (i.e. plug formation, plug length, plug velocity, and film thickness) and pressure drop during plug flow for various operating conditions, whilst investigating the scale up effects.

### 4.2 Flow patterns and pressure drop of ionic liquid-water two-phase flows

An ionic liquid,  $[C_4mim][NTf_2]$ , and de-ionised water were used as test fluids, with their properties summarised in **Table 4.1**. The experimental setup (**Figure 3.2**) and details about the system were discussed in [section 3.4](#). Both inlets (T- and Y- junction) were used and the test sections were made of two types of Teflon, FEP and Tefzel, with internal diameter (ID) of 220  $\mu m$  and 270  $\mu m$  respectively, and of borosilicate glass with an internal diameter of 200  $\mu m$ . Flow patterns and pressure drop measurements were carried out for different flow rates



that varied from 0.07 to 11.5 cm<sup>3</sup> h<sup>-1</sup> for the ionic liquid and of from 0.017 to 215 cm<sup>3</sup> h<sup>-1</sup> for water. The ionic liquid volume fraction ( $\varepsilon_{IL}$ ) varied from 0.05 to 0.8. In all cases, the flow rate of ionic liquid was kept constant and that of water was either increased or decreased. Pressure drop of single phase water and single phase ionic liquid were measured along the microchannels at various flow rates and very good agreement was found with the Hagen-Poiseuille equation.

**Table 4.1: Properties of test fluids.**

Properties (20 °C)	[C <sub>4</sub> mim][NTf <sub>2</sub> ]		Deionised Water
	<u>pure</u>	<u>saturated</u>	
Viscosity, $\mu$ / kg m <sup>-1</sup> s <sup>-1</sup>	0.052	0.041	0.001
Surface tension, $\sigma$ / N m <sup>-1</sup>	31.26·10 <sup>-3</sup>	31.55·10 <sup>-3</sup>	73.14·10 <sup>-3</sup>
Density, $\rho$ / kg m <sup>-3</sup>	1420		1000
Interfacial tension, $\gamma$ / N m <sup>-1</sup>	12.29·10 <sup>-3</sup>		

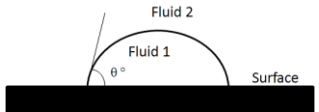
Initial experiments with the glass capillary showed that the patterns were highly affected by the phase that initially filled the microchannel. The air-liquid-solid and the liquid-liquid - solid contact angles (**Table 4.2**) revealed that none of the two liquids preferentially wets the glass channel wall; in fact the liquid-liquid-solid angle is  $\sim 90^\circ$ . To ensure that water will be the continuous phase, in a typical experiment the channel was filled with the minimum flow rate of water before the required flow rate of the ionic liquid was introduced. When steady state was reached, the pressure drop was measured and the flow configuration was recorded. Subsequently, the flow rate of water was increased stepwise. After a set of experiments was completed, the same procedure was repeated with the next chosen flow rate of ionic liquid. The same experiments were also performed by injecting the water at its maximum flow rate for a particular ionic liquid flow rate and decreasing it stepwise. The flow patterns and pressure drop recorded were the same for both procedures. A few experiments were carried out with the ionic liquid initially filling the channel and indicative results will be discussed.

In the case of the Teflon microchannels, the flow patterns were independent of the first injected fluid. Nevertheless, for consistency, the same procedure as with the glass microchannel was followed. Water, however, could not remain as the continuous phase, because (as it can be seen from **Table 4.2**) the ionic liquid seems to wet more the Teflon



microchannels (contact angles less than  $90^\circ$ ), and becomes the continuous phase. Flow pattern and pressure drop measurements were recorded for both Teflon microchannels when steady state was reached.

**Table 4.2: Contact angles ( $\theta^\circ$ ) on a borosilicate glass and Teflon plate.**

	[C <sub>4</sub> mim][NTf <sub>2</sub> ]- Deionised water	[C <sub>4</sub> mim][NTf <sub>2</sub> ]- Air	Deionised water-Air
<b>Borosilicate glass</b>	94°	43°	55°
<b>Teflon</b>	70°	64°	102°

When a set of experiments was completed, the microchannel was cleaned by injecting dichloromethane (CH<sub>2</sub>Cl<sub>2</sub>) to remove any residual ionic liquid. Air was then injected to dry the channel. This procedure was performed to ensure reproducibility of the experimental conditions.

#### 4.2.1 Flow patterns

It was found that the configuration of the inlet, T- or Y- junction, did not affect significantly the flow patterns that were formed or the range they occupied in the flow pattern map. For this reason, only the flow patterns observed with the T-junction will be discussed. In contrast, flow rates, phase volume fraction, and channel wettability had a significant effect on the flow configurations. The main patterns seen in the glass microchannel were plug, plug & drop train, and dispersed flow. In the Teflon microchannels, the main flow patterns observed were annular, plug and drop flow. These patterns could be further subdivided into regimes that have mixed characteristics and appeared usually at the boundaries between the different patterns.

##### 4.2.1.1 Flow patterns in glass microchannels

As discussed previously, the flow patterns in the glass microchannel are highly affected by the fluid that first fills the channel. In all flow configurations shown here, water was first injected in the channel; thus, water is in contact with the channel wall and is always the continuous phase. The different flow configurations obtained are presented in the flow pattern

map in **Figure 4.1** in terms of overall mixture velocity,  $u_{\text{mix}}=(Q_{\text{IL}}+Q_{\text{w}})/A$ , against input ionic liquid volume fraction,  $\varepsilon_{\text{IL}}=Q_{\text{IL}}/Q_{\text{mix}}$ .

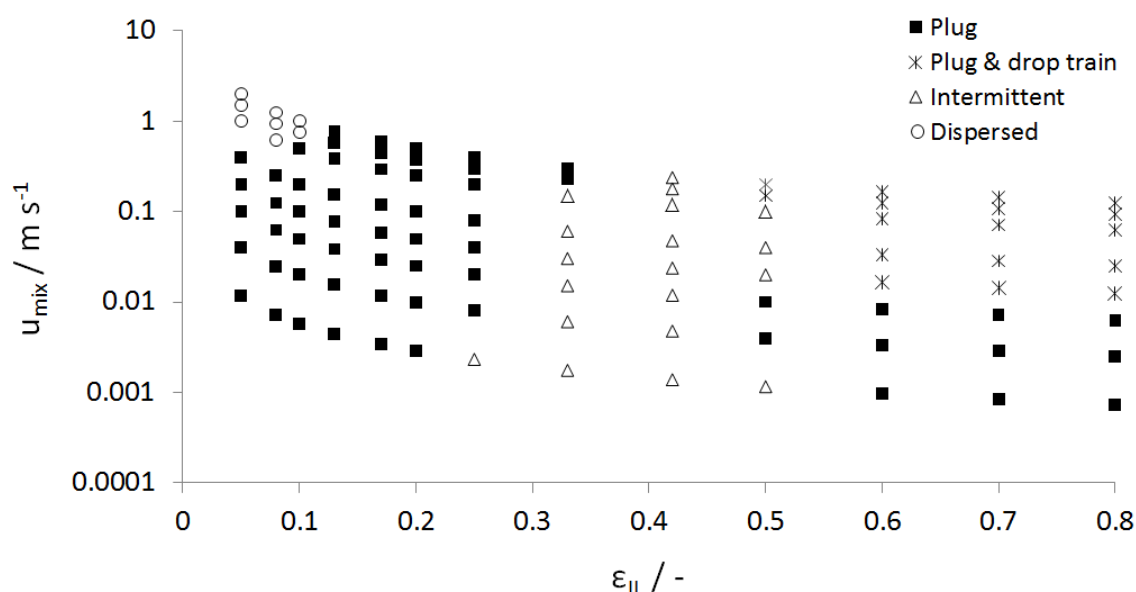


**Figure 4.1:** Ionic liquid-water flow patterns in the glass microchannels with a T-junction inlet, when water was first injected in the channel.

#### Plug flow

In this pattern, one liquid forms convex shaped plugs (dispersed phase), with length longer than the channel diameter that are separated by slugs of the other liquid (continuous phase), while a thin film of the continuous phase surrounds the dispersed plugs (**Figure 4.2 (a)**). In the glass microchannels ionic liquid is flowing as the dispersed phase, while water is the continuous phase. Plug length varied depending on the flow rates. Two types of plugs were seen; short size plugs of 0.2-2 mm at low ionic liquid volume fractions (0.05-0.25) and elongated plugs (>2 mm) at high ionic liquid volume fractions (0.5-0.8). In some cases, in agreement with liquid-liquid flow in larger channels, some isolated drops were observed in the slugs between the plugs. As it can be seen in **Figure 4.1**, plug flow occupies a large area of the flow pattern map at low and high ionic liquid fractions. At mixture velocities between 0.5-1.0 m s<sup>-1</sup> and ionic liquid volume fractions lower than 0.13, the interfacial forces which are responsible for stabilising the shape of the plugs, are overcome by inertia forces and disturbances appeared at the head and tail of the plugs, with undulations forming along the length of the plug (**Figure 4.2 (b)**). It was also found that the length of the ionic liquid plugs decreased slightly and that of the water slugs increased with increasing water flow rate, at a

constant ionic liquid flow rate. These size variations were more evident at low total flow rates,  $u_{\text{mix}} < 0.01 \text{ m s}^{-1}$ , and ionic liquid volume fractions  $\epsilon_{\text{IL}} > 0.6$  where the plug length varied by 5-10%.

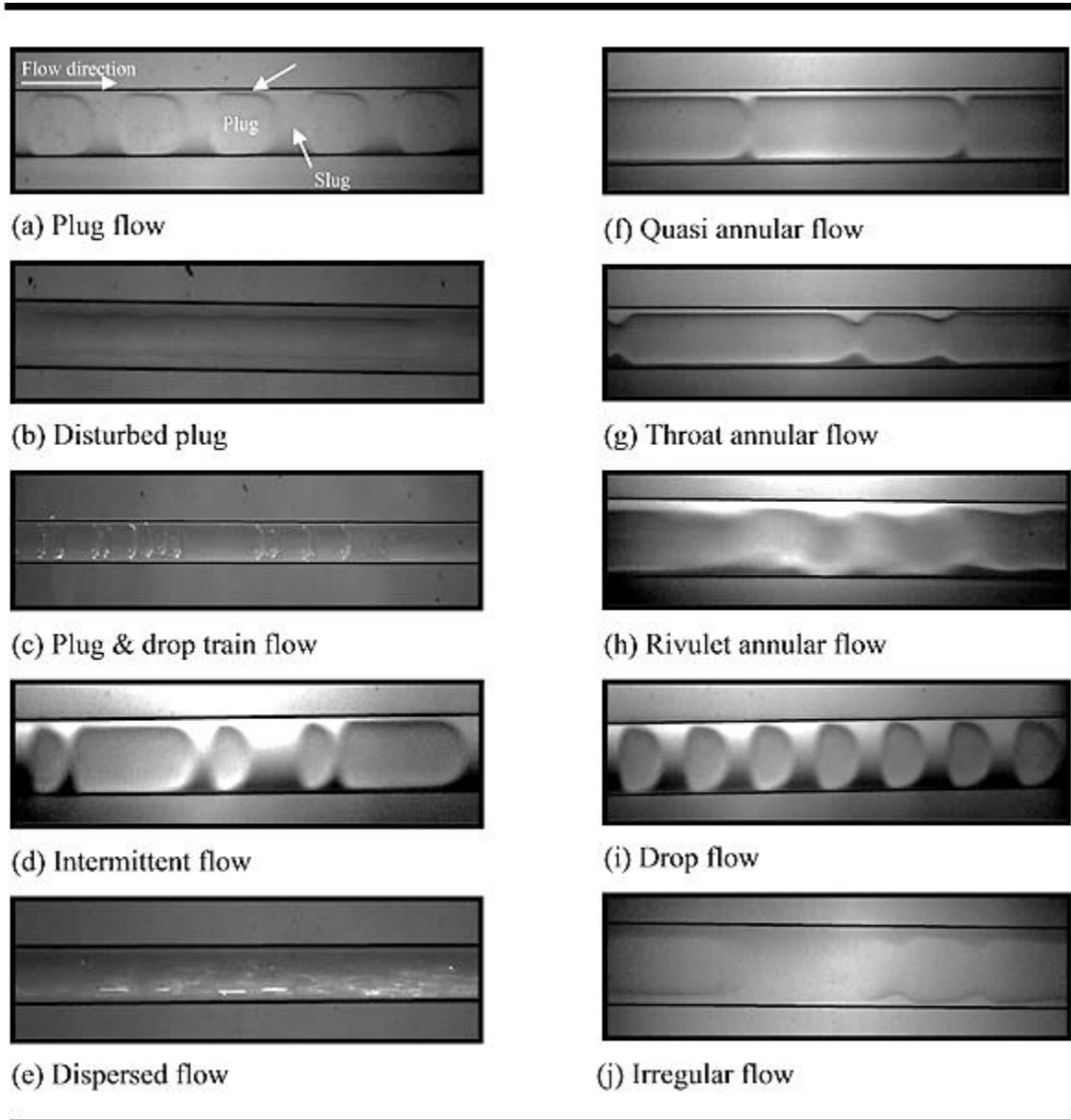


**Figure 4.2: Photographs of ionic liquid-water two-phase flow patterns in microchannels.**

#### Plug & drop train flow

The term “plug & drop train” is used to describe the pattern where ionic liquid plugs of different sizes and drops are flowing together in a row within the water phase, while there is no distinct water slug (**Figure 4.2(c)**). This pattern occurred at ionic liquid volume fractions

$\varepsilon_{IL} > 0.5$  and high total flow rates. At  $u_{mix} > 0.013 \text{ m s}^{-1}$ , the number of plugs increased with increasing ionic liquid fraction and their size was irregular, which led to the formation of this pattern. The low interfacial tension between water and ionic liquid, which favours drop break-up could explain the formation of this pattern. It is worth mentioning that, in this pattern, the ionic liquid could also come in contact with the pipe wall.

#### Intermittent flow (plugs with drops at tail)

The intermittent flow regime is characterised by ionic liquid plugs with drops of various sizes at their tails (**Figure 4.2(d)**). It is located mainly at ionic liquid volume fractions  $0.33 < \varepsilon_{IL} < 0.5$  and  $u_{mix} > 0.001 \text{ m s}^{-1}$ . This is a transitional pattern between plug and “plug & drop train” flow, or between plug (at low  $\varepsilon_{IL}$ ) and elongated plug (at high  $\varepsilon_{IL}$ ) flow. With increasing total flow rate, the drops at the tails of the plugs become larger. Moreover, at  $u_{mix} > 0.012 \text{ m s}^{-1}$  with increasing ionic liquid volume fraction, the drops at the tails of the plugs increase in size and eventually break up into smaller ones, which spread in the water slug and can even reach the front of the following plug, establishing the plug & drop train flow.

#### Dispersed flow

The dispersed pattern (ionic liquid as dispersed phase, **Figure 4.2(e)**), occurs at very high flow rates  $u_{mix} > 0.625 \text{ m s}^{-1}$  and for low ionic liquid volume fractions,  $\varepsilon_{IL} < 0.1$ . The small interfacial tension that favours drop break-up contributes to this.

When ionic liquid came in contact with the tube wall, the flow patterns became disturbed. This particularly happened at low total flow rates. In this case, the channel was cleaned and the series of experiments were repeated. A few experiments were also conducted with the ionic liquid injected first in the channel instead of water. In this case, ionic liquid became the continuous phase and water was flowing as the dispersed, while the patterns were almost the same as those formed in the Teflon microchannels (see [section 4.2.1.2](#)). For example, throat annular flow with water in the core of the channel (**Figure 4.2 (g)**) and drop flow were almost detected at the same range of mixture velocities as in the case of the Teflon channels. It is worth mentioning, that the same throat annular flow was not found when water was first injected in the glass microchannel and was the continuous phase; instead at these conditions dispersed flow was observed. This can be attributed to the low superficial water flowrates that cannot easily sustain a continuous water film along the channel. In addition when the ionic liquid is the dispersed phase, inertial forces are negligible ( $We_{IL} \ll 1$ ), and do not lead to

the formation of an annulus core. At low ionic liquid flow rates  $Q_{IL} < 1.13 \text{ cm}^3 \text{ h}^{-1}$  and for volume fractions  $\varepsilon_{IL} > 0.330$  ( $u_{mix} < 0.03 \text{ m s}^{-1}$ ), plug flow was formed but there was no continuous phase film surrounding the dispersed plugs. In this case, both phases were alternately contacting the channel wall. It is possible that at these conditions, the ionic liquid film surrounding water is very thin and can easily break up allowing the water plugs to come into contact with the channel wall.

#### 4.2.1.2 Flow patterns in Teflon microchannels

The flow pattern map obtained with the Teflon microchannels (made from FEP and from Tefzel) can be seen in **Figure 4.3**. The symbols correspond to the FEP microchannel, while the lines correspond to the Tefzel one.

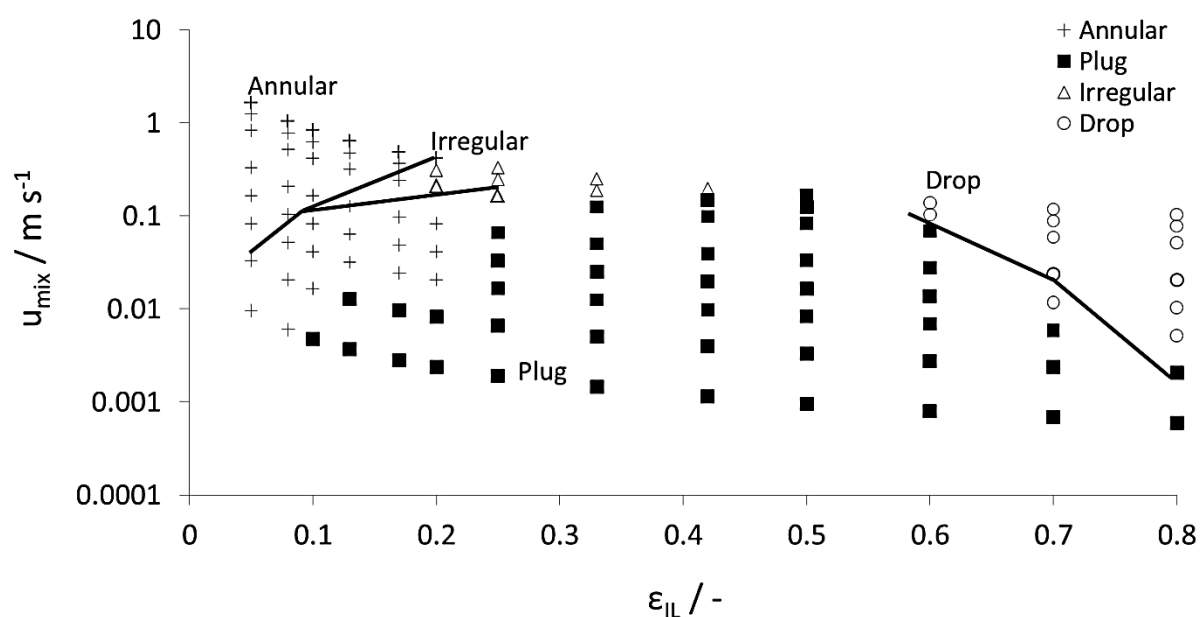


**Figure 4.3:** Ionic liquid-water flow patterns in the two Teflon microchannels, i.e. FEP and Tefzel, with a T-junction inlet. Symbols correspond to FEP channel, while lines to Tefzel.

##### Plug flow

In the two Teflon microchannels (FEP and Tefzel), as would be expected for hydrophobic channel walls, water forms convex shaped plugs and ionic liquid forms concave slugs; a film of ionic liquid surrounds the water plugs. As it can be seen from **Figure 4.3**, plug flow occupies a large area of the flow pattern map for both channels (similar to the glass microchannel). Plug flow is established for a narrower range of mixture velocities and

volume fractions for the FEP microchannel compared to the Tefzel one. At low  $\varepsilon_{IL} < 0.13$  and  $0.006 \text{ m s}^{-1} < u_{mix} < 0.055 \text{ m s}^{-1}$ , the plugs in the Tefzel microchannel had irregular sizes.

It was also found that, for a constant ionic liquid flow rate, an increase in the water flow rate, increased the size of water plugs, while that of the ionic liquid slugs was slightly decreased. At volume fraction 0.5, it was found that as the mixture velocity increased, the plugs were decreased in size but increased in number due to the rapid penetration of one phase into the other at the inlet, which breaks the water stream into a larger number of segments. In this way, a high specific interfacial area is achieved that can improve mass transfer rates.

### Annular flow

In annular flow, the lighter of the two phases (water) flows in the centre of the channel (core flow), while the heavier one (ionic liquid) is contained in a thin film wetting the channel wall. Annular flow occurs at high velocities of the water phase, where the inertia of the water is sufficiently high to break through the ionic liquid in slug flow. Depending on mixture velocity and ionic liquid volume fraction different kinds of annular flow, namely quasi, throat and rivulet, were observed (**Figure 4.2**).

In the FEP microchannel, annular flow exists at ionic liquid volume fractions from 0.05 to 0.2 and mixture velocities from 0.006 to 1.65  $\text{m s}^{-1}$ . At  $u_{mix}$  from 0.006 to 0.065  $\text{m s}^{-1}$ , the elongated plugs of water coalesce with each other and create a core (quasi annular flow) as shown in **Figure 4.2(f)**. At higher mixture velocities  $0.082 \text{ m s}^{-1} < u_{mix} < 0.330 \text{ m s}^{-1}$ , throat annular flow was observed (**Figure 4.2(g)**). In the Tefzel microchannel, quasi annular flow was not seen, and the throat annular flow was slightly shifted to lower ionic liquid volume fractions and higher mixture velocities compared to the FEP one. In both types of channels, at high  $u_{mix} > 0.330 \text{ m s}^{-1}$  and ionic liquid volume fraction  $\varepsilon_{IL} < 0.13$ , there is a large velocity difference between the two phases and the interface becomes irregular, leading to the rivulet annular flow (**Figure 4.2(h)**) with the core occasionally coming in contact with the channel wall.

### Drop flow

The term drop flow (**Figure 4.2(i)**) is used to describe a pattern where water drops, with sizes smaller than the channel diameter, are flowing in a row in the channel. This pattern is seen

mainly at relatively high mixture velocities and ionic liquid volume fractions, as it can be seen in **Figure 4.3**.

#### Irregular flow

Irregular flow (**Figure 4.2(j)**) was detected only at high mixture velocities for both microchannels and represents a transition between plug and annular flow.

#### *4.2.1.3 Comparison of flow pattern boundaries in the three test sections*

The flow pattern boundaries observed in the three different test sections used in this work are compared in **Figure 4.4**. The patterns and their boundaries are similar in the two Teflon microchannels. In the Tefzel channel, the plug flow occupies a slightly larger area of the map compared to the FEP channel, and the boundary to annular flow is shifted to higher  $Re_w$  numbers, while the boundary to drop flow is shifted to slightly higher  $Re_{IL}$  numbers. Finally, the irregular flow was observed at almost the same  $Re_{IL}$  numbers in both microchannels, but at higher  $Re_w$  in the Tefzel channel compared to the FEP one. These differences in flow pattern boundaries are attributed to the small differences in the inner diameter between the FEP (ID=220  $\mu\text{m}$ ) and Tefzel (ID=270  $\mu\text{m}$ ) channels, which is in agreement with previous findings ([Kashid et al., 2005](#)). In contrast, in the glass microchannel with water as the continuous phase, annular and drop flow were not detected. Instead of annular flow, at high Reynolds number of both phases, dispersed flow appeared, whilst instead of drop flow at high  $Re_{IL}$  plug & drop train flow occurred. The largest area of the map was occupied by some type of plug flow, divided into plug, intermittent and "elongated plug" flow (at low  $Re_{IL}$ ).

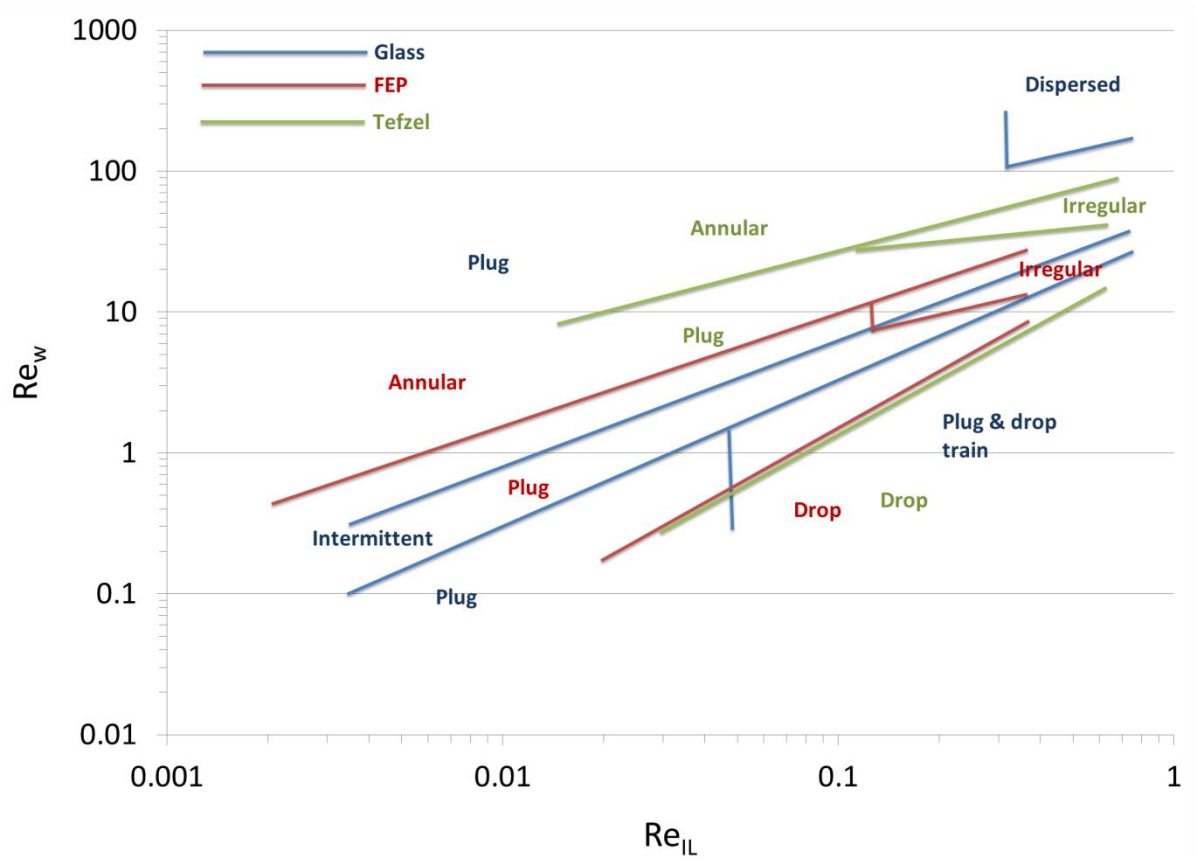


**Figure 4.4: Comparison of the flow pattern boundaries in the FEP, Tefzel, and glass microchannels with a T-junction as inlet.**

The flow pattern boundaries were compared against the criteria by Kashid and Kiwi-Minsker (Kashid and Kiwi-Minsker, 2011). It should be noted here that these criteria had been tested against results from low viscosity oils. As a result the  $Re_c/Ca_c$  numbers were higher compared to those in the present study. According to the criteria, the patterns in the glass capillary with water as the continuous phase should all be in the surface tension dominated region ( $Re_d ID/\epsilon_d < 0.1$  m). This agrees with the experimental observations since no annular flow was found. For the two Teflon microchannels (mainly for the FEP one, with  $ID=220$   $\mu$ m) plug flow was correctly predicted to fall within the surface tension dominated region ( $Re_d ID/\epsilon_d < 0.1$  m). However, annular flow was predicted to be in the transition ( $0.1$  m  $< Re_d ID/\epsilon_d < 0.35$  m) rather than the inertia region ( $Re_d ID/\epsilon_d > 0.35$  m). Similar disagreement was found between the model predictions and the experimental results of Salim et al. (Salim et al., 2008) who used a highly viscous continuous phase as in the current study resulting in low  $Re_c/Ca_c$  numbers; in their case a stratified flow inertia regime, was predicted to be within the transition region.



### 4.2.2 Effects of flow configuration on pressure drop during liquid-liquid flow

The pressure drop ( $\Delta P$ ) across a given length of microchannel (100 mm) was measured for different flow rates of both phases and various ionic liquid volume fractions,  $\epsilon_{IL}$ . The data obtained are presented against input ionic liquid volume fraction for constant ionic liquid flow rates. The pressure drop of the single-phase ionic liquid ( $\epsilon_{IL}=1$ ), having the same flow rate as the ionic liquid phase in the two-phase mixture, was also measured and presented. For the two Teflon microchannels, the relevant flow patterns established are also shown, while for the glass microchannel pressure drop was only measured during plug flow.

#### 4.2.2.1 Teflon microchannels

The pressure drop results for the two Teflon microchannels can be seen in **Figure 4.5** and **Figure 4.6** for the FEP and the Tefzel materials, respectively. Pressure drop was measured at least seven times for each set of conditions, and the mean values were calculated. The deviation from the mean value was very low (on average below  $\pm 4\%$ ) for all cases (the standard deviation lines cannot be seen in the graphs because they are smaller than the symbols), apart from high mixture velocities and low ionic liquid volume fractions where the deviation was between 5.5-12%.

In the FEP channel, pressure gradients are very similar for both the T- and Y- junction inlets used, **Figure 4.5(a)** and **Figure 4.5(b)**. As expected at a constant flow rate of ionic liquid, an increase in the water flow rate (decrease in the ionic liquid volume fraction) led to an increase in the measured pressure drop, because the mixture flow rate increased. At higher ionic liquid flow rates the increase became more prominent when annular flow established. When the pattern changes from plug to annular for the same ionic liquid flow rate, the water is restricted to a smaller part of the cross section and its velocity will be increased resulting in higher frictional pressure drop. Interestingly, at ionic liquid flow rate of  $5.65 \text{ cm}^3 \text{ h}^{-1}$  and at low ionic liquid volume fractions, this trend changes and a decrease in the two-phase pressure drop was observed. This happens during annular flow when the pattern changes from throat to rivulet annular and water, that has a lubricating effect, comes in contact with the channel wall. In the case of  $Q_{IL}=8.48 \text{ cm}^3 \text{ h}^{-1}$ , the pressure drop at low ionic liquid volume fractions was not measured because it was outside the range of the pressure meter used.

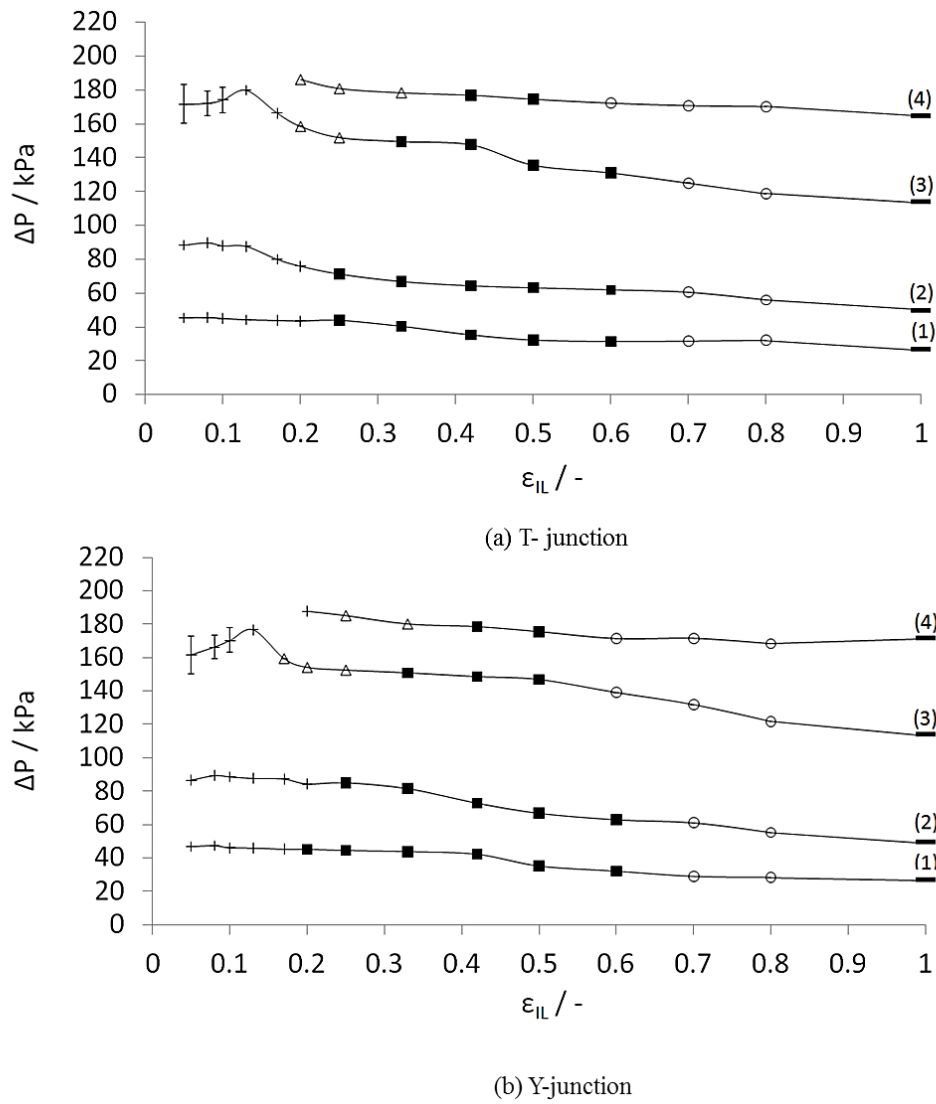


**Figure 4.5:** Two-phase pressure drop versus input ionic liquid volume fraction at different ionic liquid flow rates for the FEP microchannel and (a) T-junction, (b) Y-junction inlet.  $Q_{IL}$ : (1) =  $1.13 \text{ cm}^3 \text{ h}^{-1}$ , (2) =  $2.26 \text{ cm}^3 \text{ h}^{-1}$ , (3) =  $5.65 \text{ cm}^3 \text{ h}^{-1}$ , (4) =  $8.48 \text{ cm}^3 \text{ h}^{-1}$ . Flow pattern symbols: Annular (+), Plug (■), Drop (○), Irregular (Δ)

Similar results for both inlets were also found in the Tefzel channel and are presented in **Figure 4.6** for the T-junction. Pressure drop increases with increasing water flow rate, similar to the FEP microchannel. This increase is more profound at ionic liquid flow rates higher than  $5.65 \text{ cm}^3 \text{ h}^{-1}$ .

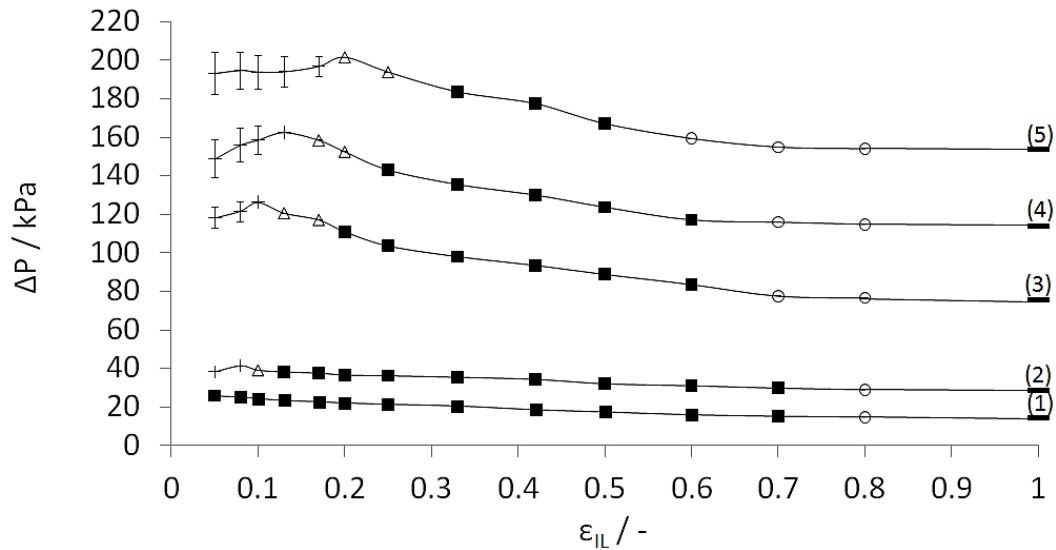


**Figure 4.6:** Two-phase pressure drop versus input ionic liquid volume fraction at different ionic liquid flow rates for the Tefzel microchannel with T-junction as inlet.  $Q_{IL}$ : (1) =  $1.13 \text{ cm}^3 \text{ h}^{-1}$ , (2) =  $2.26 \text{ cm}^3 \text{ h}^{-1}$ , (3) =  $5.65 \text{ cm}^3 \text{ h}^{-1}$ , (4) =  $8.48 \text{ cm}^3 \text{ h}^{-1}$ , (5) =  $11.3 \text{ cm}^3 \text{ h}^{-1}$ . Flow pattern symbols: Annular (+), Plug (■), Drop (○), Irregular (Δ)

#### 4.2.2.2 Glass microchannel

In the glass microchannel, the pressure drop was measured only for ionic liquid volume fractions between 0.05-0.42 where short plugs were detected. As found for the Teflon microchannels, the pressure drop is similar for both inlet configurations and increases with increasing water flow rate (**Figure 4.7** for the T-junction). However, in the glass microchannel, the pressure drop of single phase flow ionic liquid at the same flow rate as in the mixture is always higher than the pressure drop of the two-phase mixture. This is because, in the glass microchannel, the phase in contact with the channel wall is the low viscosity water. High values of pressure drop, approaching those of single-phase water, were obtained at flow rates  $Q_{IL} > 5.65 \text{ cm}^3 \text{ h}^{-1}$  and low  $\epsilon_{IL}$ , but were still less than those of single-phase ionic liquid. In the case of the glass microchannel, the deviation from the mean value was in all cases very low. These findings are very important because they demonstrate that the high viscosities of the ionic liquids are not limiting factors for their use in small channels, provided suitable flow patterns are established.

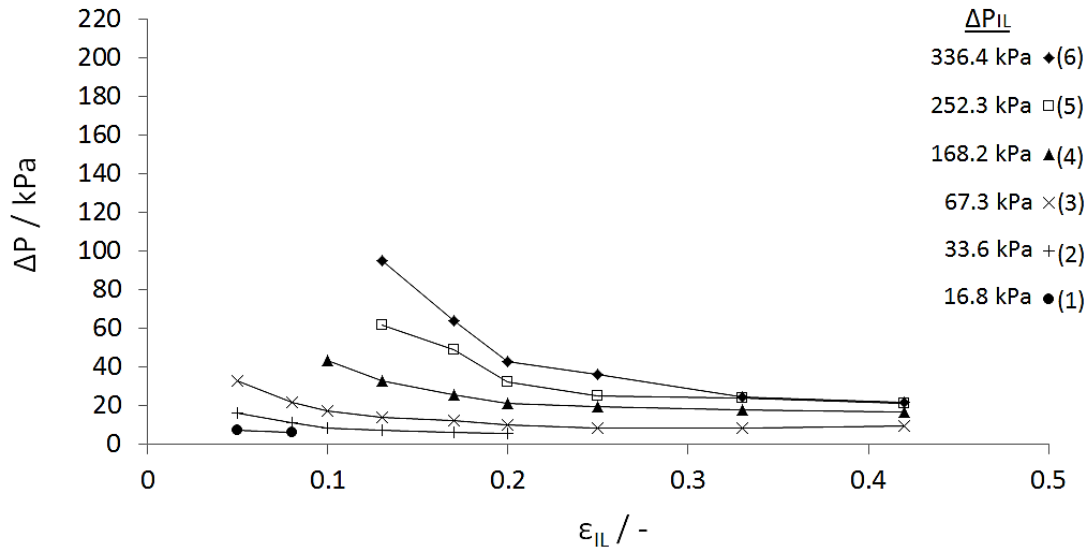


**Figure 4.7: Two-phase pressure drop versus input ionic liquid volume fraction during plug flow at different ionic liquid flow rates for the glass microchannel with a T-junction as inlet. The pressure drop values for single phase ionic liquid are given on the right.  $Q_{IL}$ : (1) =  $1.13 \text{ cm}^3 \text{ h}^{-1}$ , (2) =  $2.26 \text{ cm}^3 \text{ h}^{-1}$ , (3) =  $5.65 \text{ cm}^3 \text{ h}^{-1}$ , (4) =  $8.48 \text{ cm}^3 \text{ h}^{-1}$ , (5) =  $11.3 \text{ cm}^3 \text{ h}^{-1}$ , (6) =  $14.1 \text{ cm}^3 \text{ h}^{-1}$**

Some indicative experiments were performed in the glass microchannel when the ionic liquid was the continuous phase. In this case, pressure drop was found to be higher than that of single phase ionic liquid as is the case for the two Teflon microchannels.

#### 4.2.2.3 Comparison of the pressure drop for the 3 test sections

The pressure drops for the three different microchannels are compared in **Figure 4.8** for a constant ionic liquid flow rate of  $Q_{IL}=2.26 \text{ cm}^3 \text{ h}^{-1}$ . Because of the small differences in the diameters of the three channels, to enable the comparisons the data have been non-dimensionalised by dividing the two-phase pressure drop with that of the ionic liquid flowing alone in the channel ( $\eta$ ).

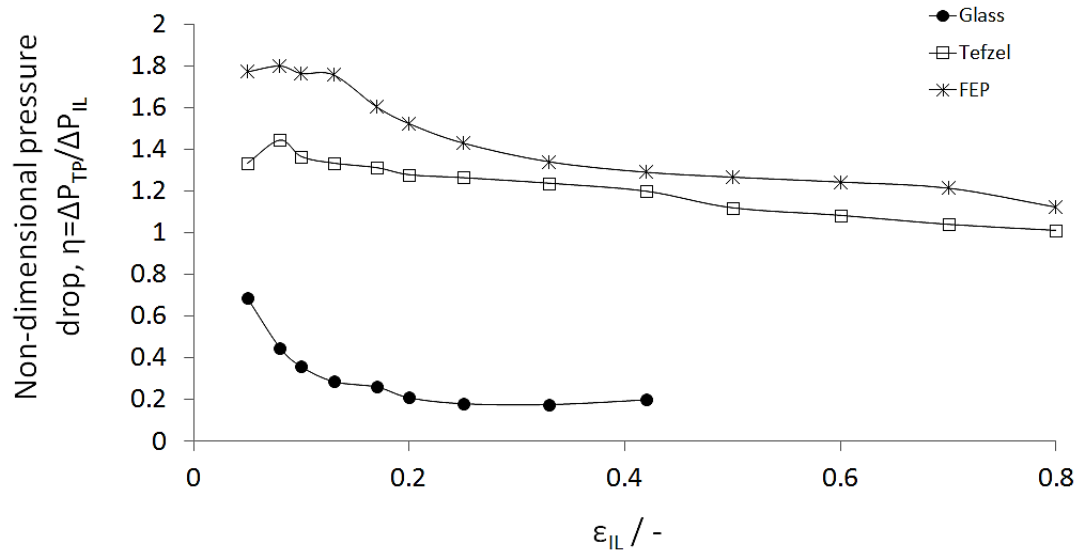


**Figure 4.8: Comparison of non-dimensional pressure drop in the FEP, Tefzel and glass microchannels with internal diameter of 220  $\mu\text{m}$ , 270  $\mu\text{m}$ , and 200  $\mu\text{m}$ , respectively, with a T-junction as inlet, at a constant ionic liquid flow rate,  $Q_{IL} = 2.26 \text{ cm}^3 \text{ h}^{-1}$ .**

As it can be seen in **Figure 4.8**, the dimensionless pressure drop ( $\eta$ ) in the two Teflon microchannels is higher than in glass. This can be explained by the fact that in the two Teflon microchannels, the continuous phase is the ionic liquid which has higher viscosity and, therefore, causes higher frictional pressure drop than water which is the continuous phase in the glass microchannel. It was also observed that, in all cases,  $\eta$  decreases as the ionic liquid volume fraction increases. This decrease is more obvious at low  $\epsilon_{IL} < 0.25$ .

In the case of the two Teflon microchannels, it is seen that the dimensionless pressure drop for the FEP channel is higher over the whole range of ionic liquid volume fractions studied. During plug flow ( $\epsilon_{IL} > 0.25$ ), this difference is attributed to the number of slugs present. Compared to the FEP channel, under the same phase flow rates longer plugs are formed in the Tefzel channel, because of larger internal diameter, and their number is reduced; this will result in a lower capillary pressure drop contribution to the overall pressure drop (Jovanović et al., 2011). At lower ionic liquid volume fractions ( $\epsilon_{IL} < 0.25$ ), the difference of the dimensionless pressure drop between the two Teflon microchannels is higher. In the FEP channel, annular flow starts just below  $\epsilon_{IL} < 0.25$ , explaining the increase in pressure drop at this volume fraction. In the Tefzel channel, the flow remains plug until  $\epsilon_{IL} = 0.1$ , where it becomes irregular (with both plug and annular flow characteristics); annular flow establishes only at  $\epsilon_{IL} < 0.08$  where the increase in pressure drop is seen.

### 4.3 Plug flow characteristics

Plug flow was further investigated in various channel sizes of different material for both liquid-liquid flow systems, i.e. ionic liquid-deionised water (**Table 4.1**), and TBP/ionic liquid (30% v/v)-nitric acid solutions (**Table 3.2**). Experiments were carried out at various mixture velocities ( $0.0028\text{--}0.067\text{ m s}^{-1}$ ) and volume fractions ( $\epsilon_{\text{IL}}=0.4\text{--}1$ ). In the Teflon channels plug flow was established in all cases with the aqueous phase flowing as non-continuous plugs within the TBP/ionic liquid phase (30%, v/v) (carrier phase), whilst in the glass microchannel experiments were carried out with the aqueous phase as the carrier fluid as well. The experimental procedure and the techniques followed for these measurements are explained in [sections 3.4 and 3.5](#). The setup used for the measurements is shown in **Figure 3.2**.

#### 4.3.1 Plug formation

The plug formation cycle is shown in **Figure 4.9** and **Figure 4.10** for the case of water and ionic liquid ( $[\text{C}_4\text{mim}][\text{NTf}_2]$ ) as carrier fluid, respectively, at mixture velocity of  $0.0037\text{ m s}^{-1}$  and equal flow rates of the two phases. The formation was observed in the 0.2 mm ID glass microchannel (**Figure 3.3A**). In these figures, average velocity fields are superimposed on corresponding mask images as described in [section 3.5.2](#). In both cases, the flow pattern formed at the T-junction consisted of a regular and highly periodic plug train. There are significant differences however, in terms of plug formation frequency, size, shape and local velocities.

When water was the carrier phase, a formation frequency of around 1 Hz is observable (**Figure 4.9**). Six cycles with a period ( $T$ ) of 1.05 s were acquired and thus six instantaneous fields were averaged in phase for each stage, which is identified here by the non-dimensional time  $\tau_f$ , defined as  $t/T$ . In this case scenario, the more viscous dispersed medium can completely fill the junction (for  $0 \leq \tau_f \leq 0.4$ ) before the carrier fluid can effectively squeeze ( $0.4 < \tau_f \leq 0.93$ ) and finally pinch off the plug (at  $\tau_f \sim 1$ ). A similar mechanism at a T-junction has been also reported for gas-liquid Taylor flow ([van Steijn et al., 2007](#)) in the squeezing regime ([Garstecki et al., 2006](#)). During the filling stage the carrier fluid progressively decelerates upstream the filling zone, while it accelerates through the contraction in between the plug and the channel wall. The potential energy accumulated upstream during the filling stage will be eventually released in the form of kinetic energy during the squeezing and

detaching stages. As the energy is dissipating, the upstream interface results in a further concave shape and a vortex appears and develops in its proximity. Resulting plugs are of average length of  $0.77 \text{ mm} \pm 1\%$  (measured at the straight channel further downstream) and with no apparent water film thickness.

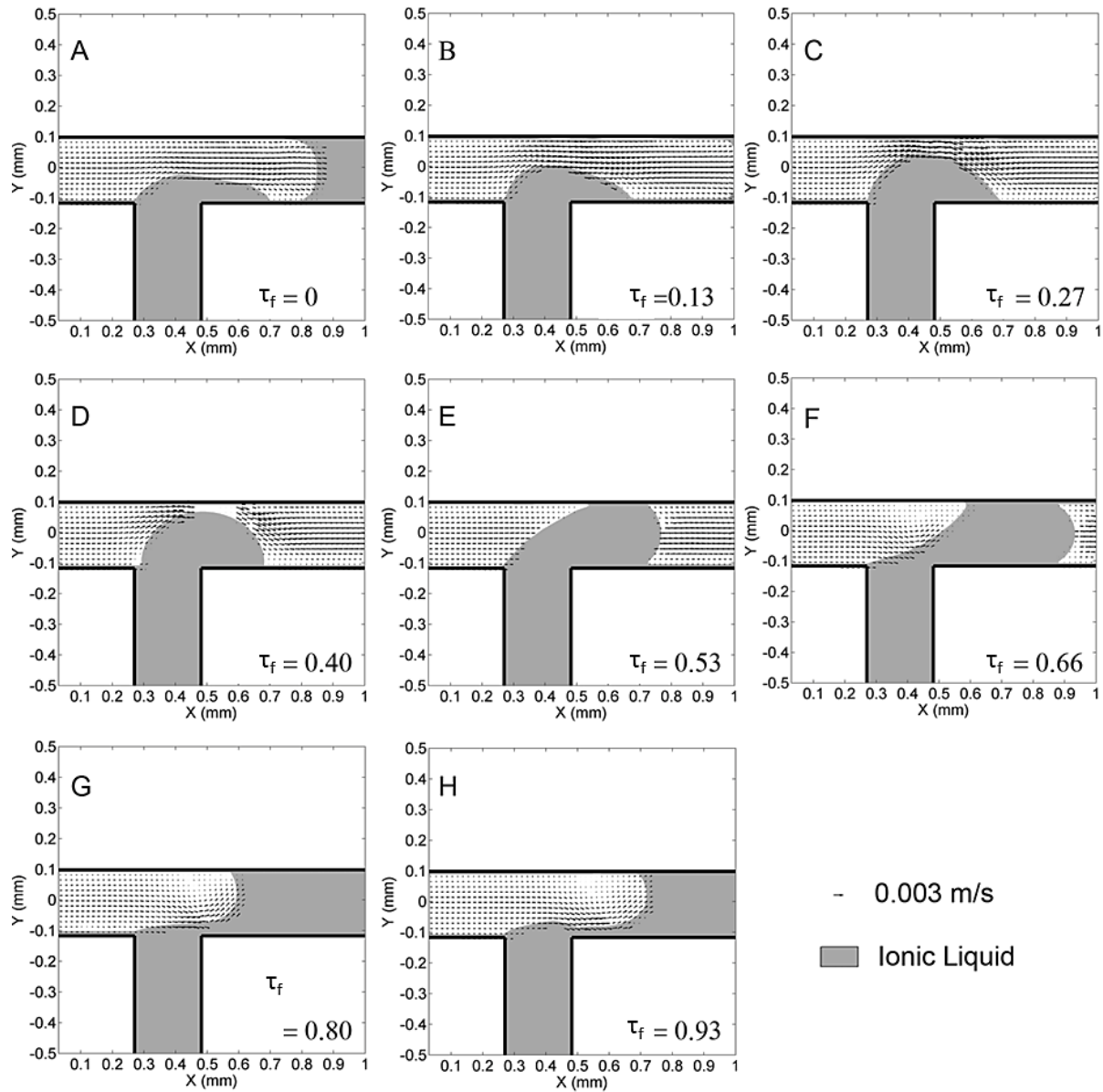


**Figure 4.9:** Phase averaged vector fields in the water for different stages of the ionic liquid plug formation cycle, when water is the carrier fluid. Six instantaneous fields per stage were averaged.

When ionic liquid acts as the carrier fluid (**Figure 4.10**), the formation cycle was almost three times faster ( $\tau_f=0.35$  and formation frequency of 2.86 Hz) than the previous case. The break up point moves downstream and the dispersed medium never blocks the junction zone,

resulting in a dripping behaviour. The resulting plugs are shorter with length ( $L_p$ ) of 0.43 mm ( $\pm 1\%$ ), and surrounded by a relatively thick film of approximately 14  $\mu\text{m}$  ( $\pm 4\%$ ). As a consequence of the higher Capillary number (order of  $10^{-2}$  for ionic liquid carrier and  $10^{-4}$  for water carrier) associated with the more viscous carrier fluid, in fact, the latter tends to dominate over the aqueous medium, leading to its break up. This is in accordance with the transition from a squeezing to dripping regime found by other investigators at  $Ca=10^{-2}$  (Thorsen et al., 2001, De Menech et al., 2008), when the break up is dominated by shear forces.

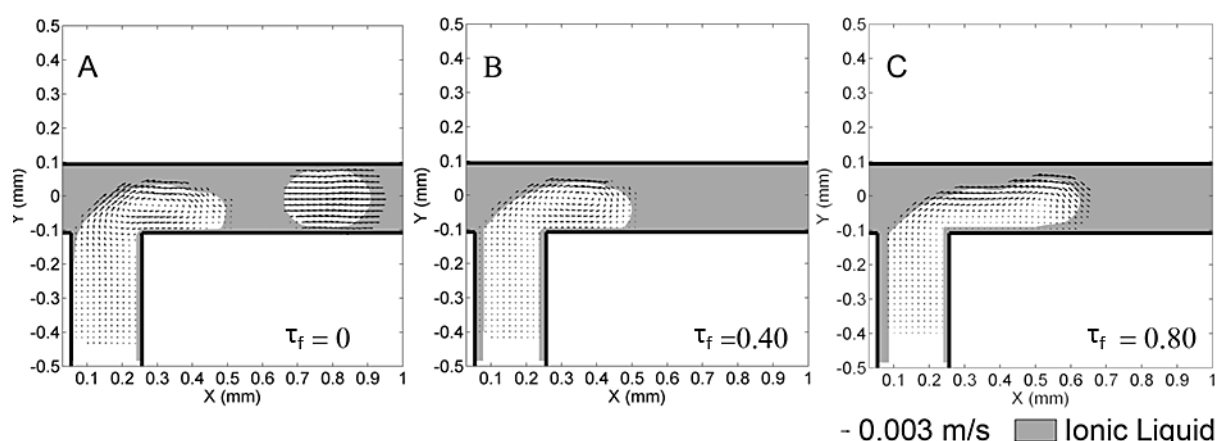


**Figure 4.10: Phase averaged vector fields in the water for different stages of the “aqueous plug” formation, when ionic liquid is the carrier fluid. Twenty instantaneous fields per stage were averaged.**

### 4.3.2 Plug size

The effects of different parameters, such as mixture velocities, channel size, flow rate ratio, and fluid properties on the plug size are shown in **Figure 4.11-Figure 4.14**. Plug flow was investigated with a high-speed camera and the plug size was evaluated from the high resolution images using an edge processing routine on the binary images (Section 3.5.2). The values were averaged over a set of 30 to 60 images. It was found that very regular plug lengths were established in the channels at a particular set of conditions, as indicated by the low values of error ( $<3\%$ ).

Two different liquid-liquid systems were tested, viz.  $[\text{C}_4\text{mim}][\text{NTf}_2]$ -water and TBP/IL (30%, v/v)-nitric acid solution (3 M). The first system has been tested in the glass channel of 0.2 mm ID, whilst the second one in the Teflon channels of 0.5 to 2 mm ID. In all cases the



aqueous phase formed the dispersed plugs. As it can be seen in **Figure 4.11** the normalised plug length  $L_p/ID$  decreases as the  $Ca$  increases in all channels at equal flow rates of the two phases. This decrease is attributed to the rapid penetration of the continuous phase (IL) into the other as the velocity increases, which segregates the stream of the dispersed phase into smaller segments. As mentioned earlier, at these experimental conditions the plug formation is expected to be affected by both squeezing and dripping mechanism since the  $Ca$  numbers are above the critical value ( $Ca=10^{-2}$ ) (De Menech et al., 2008).

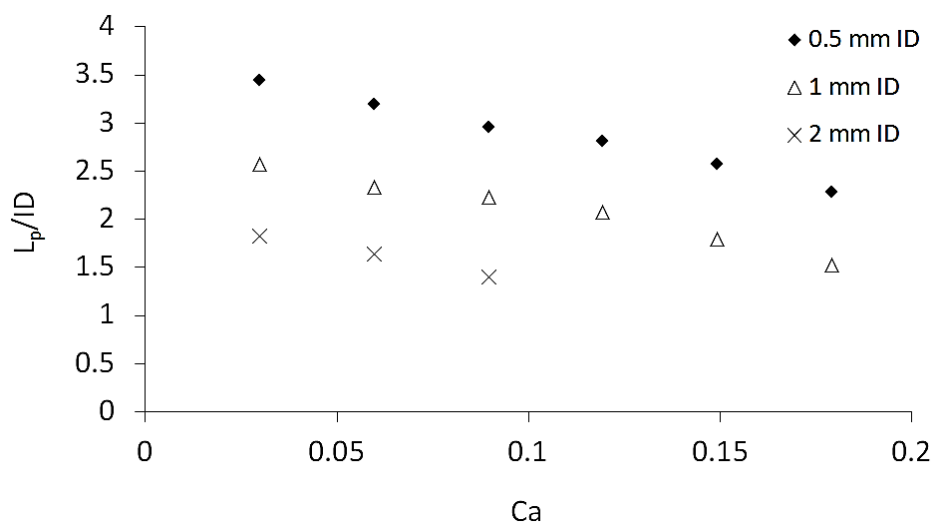


**Figure 4.11:** Normalised plug length  $L_p/ID$  as a function of the  $Ca$  at three different channel sizes (Teflon channels) for equal flow rates of the two phases (two-phase system: TBP/[C<sub>4</sub>mim][NTf<sub>2</sub>] (30%, v/v)-nitric acid solution).

The effect of the channel diameter on the plug formation and its length is also important. As it can be seen from the same figure (**Figure 4.11**) as the channel diameter decreases the plug length increases, which is in agreement with literature, where droplet diameter (normalised with the channel diameter) is described as a function of  $1/Ca$  (Thorsen et al., 2001, Cristini and Tan, 2004, Xu et al., 2008). This finding has an important impact on the design of a small-scale device, since the plug length is related to the number of plugs for a constant flow rate and thus to the interfacial area available for mass transfer.

The same decrease of plug length was observed for the other system, i.e. [C<sub>4</sub>mim][NTf<sub>2</sub>]-water as a function the  $Ca$  number at various ionic liquid volume fractions (**Figure 4.12**). As it can be seen, the plug length decreases by increasing the  $Ca$  number for all volume fractions of the carrier fluid. In addition, for a given  $Ca$  number it can be seen that shorter plugs are formed as the  $\varepsilon_{IL}$  increases for the whole range of  $Ca$  numbers.

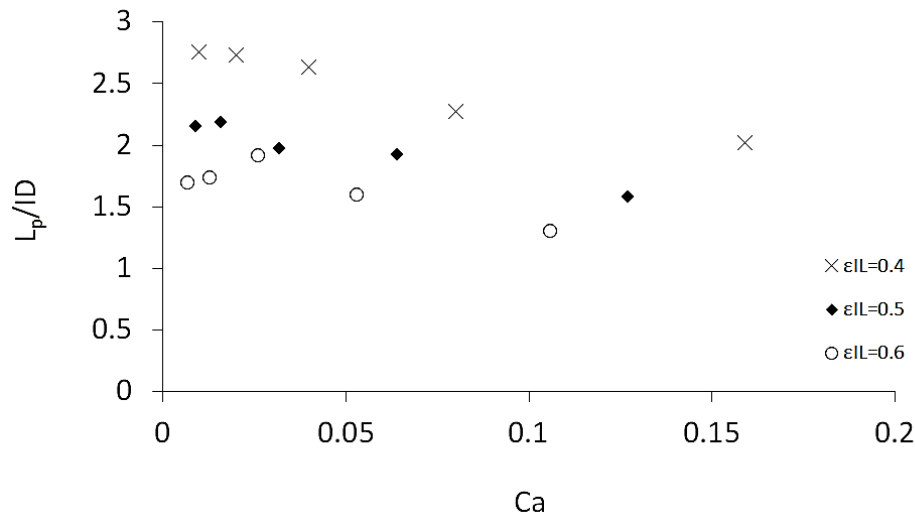


**Figure 4.12:** Normalised plug length  $L_p/ID$  as a function of the  $Ca$  for three different volume fractions of the carrier fluid (ionic liquid) in a 0.2 mm ID glass microchannel (two-phase system:  $[C_4mim][NTf_2]$ -water).

The effect of volume fraction of the dispersed phase  $\epsilon_d$  on plug length at constant mixture velocity and at constant velocity of the carrier phase is shown in **Figure 4.13**. In all channel sizes the length of the plug was found to increase as  $\epsilon_d$  increased. Moreover, shorter plugs are formed for the whole range of  $\epsilon_d$  as the velocity of the carrier fluid increases **Figure 4.13B**.

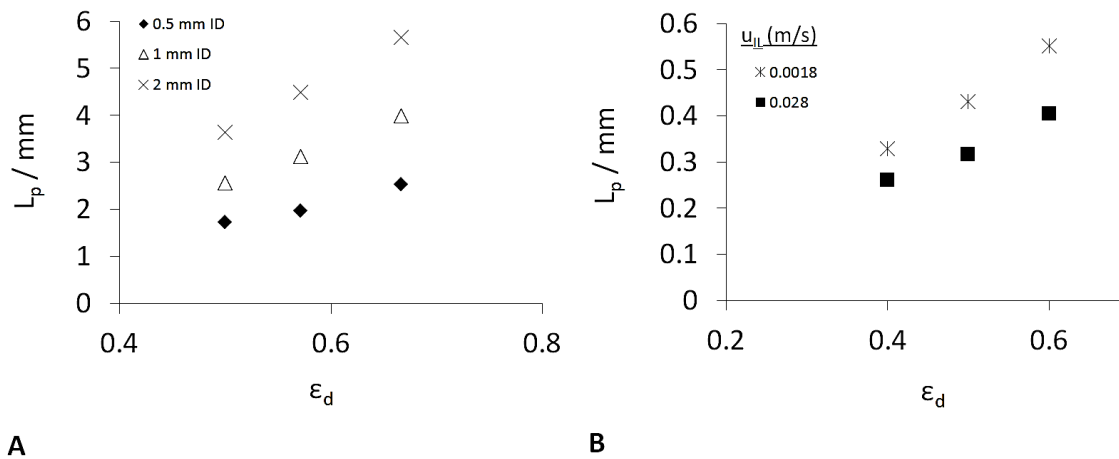


**Figure 4.13:** Plug length  $L_p$  as a function of the flow rate ratio of the dispersed phase at (A) constant mixture velocity  $u_{mix}=0.01 \text{ m s}^{-1}$ , and (B) constant velocity of the carrier phase in the 0.2 mm ID glass channel.

The shape of the plug was also found to be affected by the total mixture velocity. By increasing the total volumetric flow rate the plugs exhibited a “bullet” shape, where the rear interface of the plug became more flat, and the front sharper, as shown in **Figure 4.14**, which

agrees with literature findings (Bretherton, 1961, Kreutzer et al., 2005a, Han and Shikazono, 2009). As the Ca number increases the interfacial forces cannot sustain the hemispherical shape of the front and the rear part of the plugs.

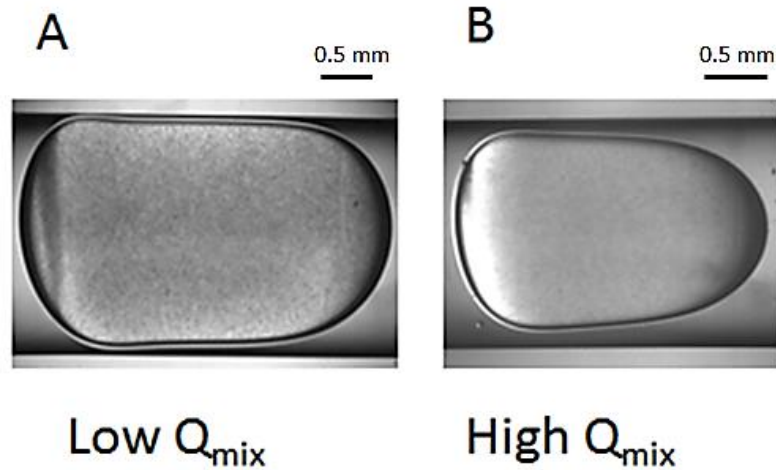


**Figure 4.14: Plug shape at (A) low and (B) high total volumetric flow rate in a 2 mm ID channel.**

#### 4.3.2.1 Comparison with literature models

The experimental plug lengths obtained in the different channel sizes (i.e. 0.2-2 mm ID), were compared with the literature models discussed in section 2.2.2. The models by Garstecki et al. (Garstecki et al., 2006) and Leclerc et al. (Leclerc et al., 2010) showed good agreement with the experimental results for low Ca numbers (i.e. squeezing regime), which demonstrates that at this regime the size of the plug is defined by the microchannel geometry and the flow rates of the two phases, whilst it is independent of the fluid properties. This is mainly valid in the case of the 0.2 mm ID glass channel when water is the carrier fluid and the Ca numbers were  $<0.01$ . The experimental plug length was found  $\sim 0.77$  mm, whilst the models for gas-liquid Taylor flows predict a plug size of 0.8 mm (Qian and Lawal, 2006). However, when the ionic liquid was the carrier fluid in the glass channel, the Ca numbers increased ( $Ca=10^{-2}$ ) and the break up mechanism changed from the squeezing to the dripping regime found by other investigators at Ca equal to  $10^{-2}$  (Thorsen et al., 2001, De Menech et al., 2008), where the break up is dominated by shear forces and the ratio between the fluid viscosities. As a result, the plug volume sharply decreases with an increase of Ca and the correlations in section 2.2.2 are no longer valid.

In the Teflon channels (0.5-2 mm ID) TBP/ionic liquid was always the continuous phase which resulted in large Ca numbers (0.03-0.1). As a consequence, none of the aforementioned models (Garstecki et al., 2006, Leclerc et al., 2010) could interpret satisfactory the experimental results. Laborie et al (Laborie et al., 1999) studied experimentally gas-liquid Taylor flow in capillaries of internal diameter varying from 1 to 4 mm, for  $55 < Re_{ub} = \rho ID u_b / \mu < 2000$ ,  $0.13 < Bo < 5$ ,  $0.0015 < Ca < 0.1$ . In their model it was found that the bubble length decreased when the capillary size increased, which is in contrast with the findings of the current work. Qian and Lawal (Qian and Lawal, 2006) performed extensive numerical simulations on the formation length of Taylor bubbles for gas-liquid systems in a 1 mm ID capillary for  $0.000278 < Ca < 0.01$  and  $15 < Re_{ub} < 1500$ . In their work they found that channel size, and gas and liquid superficial velocities affected the length of the bubble, while surface tension and liquid viscosity had negligible effect. However, their model seems to over-predict the current experimental results with a mean relative error of 41%.

A correlation (Eq. (4.2.1)) to describe the different parameters, as well as the properties of the fluids that affect the plug length has been developed, that takes into account the Ca number of the mixture in the main channel, the Re numbers of each phase in the inlet channels (based on superficial velocities), the Re number of the mixture in the main channel (based on mixture velocity), the flow rate ratio  $q = Q_{IL}/Q_{HNO_3}$ , and the diameter of the channel. In **Figure 4.15** the results tabulated are from 4 channel sizes, for mixture velocities from 0.0028 to 0.067 m s<sup>-1</sup> and flow rate ratios from 0.5 to 1.5. The viscosity ratio  $\mu_d/\mu_c$  has not been taken into account since it was  $>1/29$ , and the Ca number were less than 0.1, so it does not affect the plug size (Christopher et al., 2008, Liu and Zhang, 2009).

$$\frac{L_p}{ID} = 0.0265 Re_d q^{0.88} Ca_{mix}^{0.088} (Re_c Re_{mix})^{-1.76} \quad (4.2.1)$$

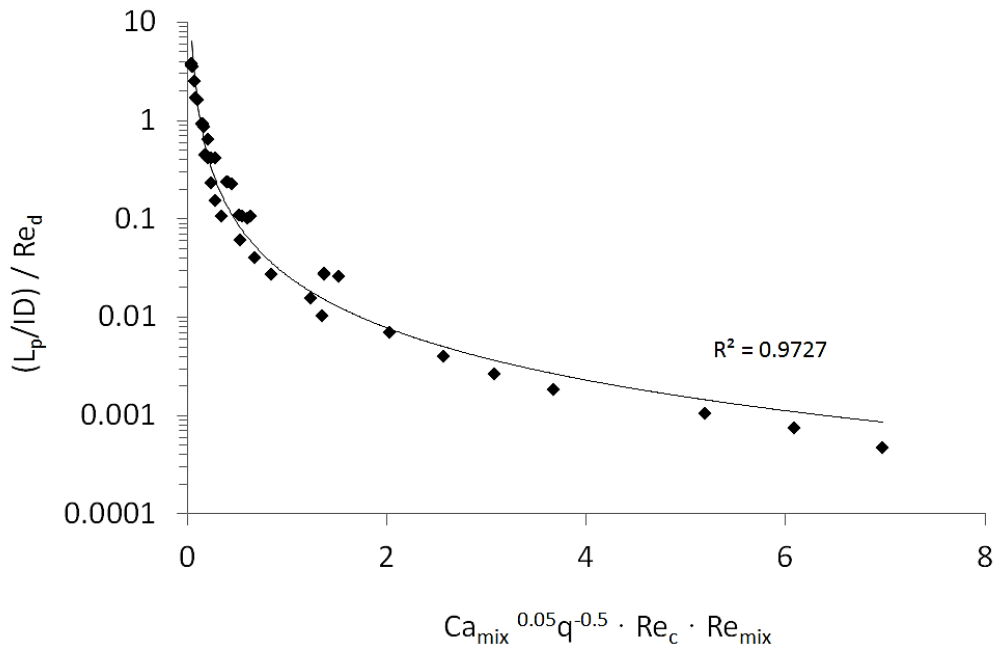


**Figure 4.15:** Relationship between the various parameters affecting the plug length.

### 4.3.3 Film thickness

A thin film was always present on the channel wall at all experimental conditions investigated, when ionic liquid was the carrier liquid. The thickness of the film was measured by analysing the images acquired using the experimental setups showed in [sections 3.5.1.1 and 3.5.1.2](#). The plug interfaces were easily detected by applying the post-processing routine discussed ([section 3.5.3](#)). The Bo numbers for each channel were calculated and it was found that the gravitational force can be considered negligible for channel sizes from 0.2 to 1 mm ID ( $Bo=0.0165-0.272$ ), which means that the flow can be axisymmetric, which was also verified by the experiments in the next chapter ([chapter 5](#)). However, in the 2 mm ID channel the Bo number was higher than 1, which means that the interface could not be considered symmetrical. The film thickness is found to be mainly a function of the mixture velocity (i.e. capillary number, Ca) and tends to increase as the velocity increases. In **Figure 4.16** the non-dimensional film thickness ( $\delta/ID$ ) is plotted as a function of Ca. Experimental results are compared with the models of Bretherton ([Bretherton, 1961](#)), Eq. (4.2.2) Taylor ([Taylor, 1961](#)), Eq. (4.2.3), Irandoust and Andersson ([Irlandoust and Andersson, 1989](#)), Eq. (4.2.4), and Aussillous and Quere ([Aussillous and Quéré, 2000](#)), Eq. (4.2.5).

$$\frac{\delta}{ID} = 0.5\{1.34Ca^{\frac{2}{3}}\} \quad (4.2.2)$$

$$\frac{\delta}{ID} = 0.5\{0.5Ca^{0.5}\} \quad (4.2.3)$$

$$\frac{\delta}{ID} = 0.5\{0.36[1 - \exp(-3.08 Ca^{0.54})]\} \quad (4.2.4)$$

$$\frac{\delta}{ID} = 0.5\left\{\frac{1.34Ca^{2/3}}{1+2.5(1.34Ca^{\frac{2}{3}})}\right\} \quad (4.2.5)$$

The film thickness obtained in the glass microchannels of 0.2 mm ID seems to be under-predicted by all the models, although the Ca numbers range for this work ( $0.007 < Ca < 0.159$ ) falls within the Ca numbers range that the models are valid as shown in **Table 2.2**. The large film thickness values in the case of the small channel may be due to the high Ca numbers achieved at relatively low mixture velocities because of the high viscosity of the ionic liquid.

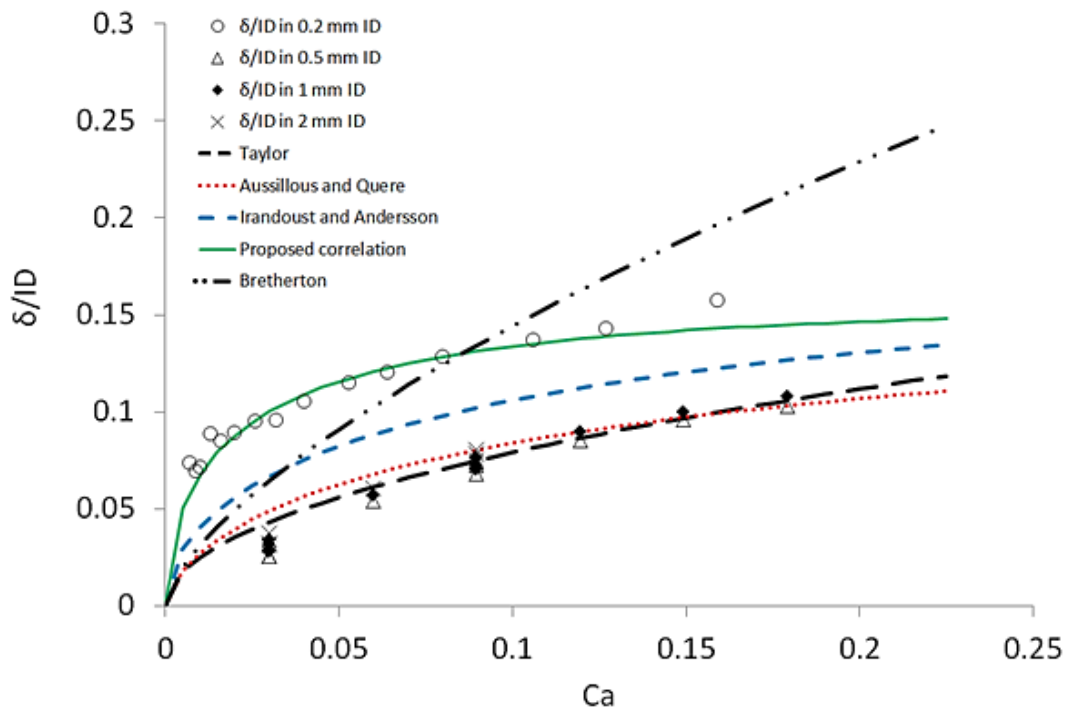


**Figure 4.16: Non-dimensional film thickness ( $\delta/ID$ ) as a function of Ca number and comparison with literature correlations.**

Commonly in the literature high Ca numbers are obtained by increasing mixture velocity rather than fluid viscosity. The model by Irandoust and Andersson (Irاندoust and Andersson, 1989), Eq. (4.2.4), is the closest to the results obtained in the 0.2 mm ID glass microchannel. A best fit curve (green line) was also found, Eq. (4.2.6), which resembles their model.

$$\frac{\delta}{ID} = 0.15[1 - \exp(-6.90Ca^{0.54})] \quad (4.2.6)$$

The film thickness obtained in the Teflon capillaries seems to agree well with the model proposed by Taylor (Taylor, 1961). A small deviation from the model was found at low Ca numbers where the film thickness is expected to be small. It can also be seen (Figure 4.16) that for  $Ca > 0.1$  the results agreed with the model proposed by Aussillous and Quere (Aussillous and Quere, 2002) as well, while for  $Ca < 0.1$  the results were over-predicted. Bretherton (Bretherton, 1961) model did not seem to agree with experimental results for any of the channels tested, since the Ca number of the current work exceed the range where this model is applicable ( $Ca < 0.003$ ). It is worth noticing here that there are no experimental correlations for film thickness in literature for the fluidic system employed in this study, even though there are reports of experimental film thickness in liquid-liquid systems (Ghaini et al., 2010, Mac Giolla Eain et al., 2013). As shown, most correlations available are for gas-liquid systems.

#### 4.3.4 Plug velocity

Plug velocity is an important parameter that affects the performance of the mass transfer unit, as it gives an indication of the residence time (time that the plug remains in the channel). In Figure 4.17 the plug velocity, calculated from the plug displacement between successive images, is plotted against the mixture velocity  $u_{mix}$ . In Taylor flow the film between the plug and the channel wall is expected to increase the plug velocity compared to the continuous fluid velocity. As the velocity increases, the Ca number also increases and the film becomes thicker; this results in an increasing plug speed. As it can be seen in all channels the velocity of the plug ( $u_p$ ) is higher than the mixture velocity. In addition, as the mixture velocity increases the difference between plug velocity and mixture velocity also increases. For constant  $u_{mix}$  the plug is flowing faster as the diameter of the channel increases. A relationship was derived between  $u_p$  and  $u_{mix}$  (Eq. (4.2.7)) from the experimental data, which can predict the plug velocity in each channel within 2% error.

$$u_p = [3.55 \ln(ID) + 32.3]u_{mix}^2 + 1.017u_{mix} \quad (4.2.7)$$

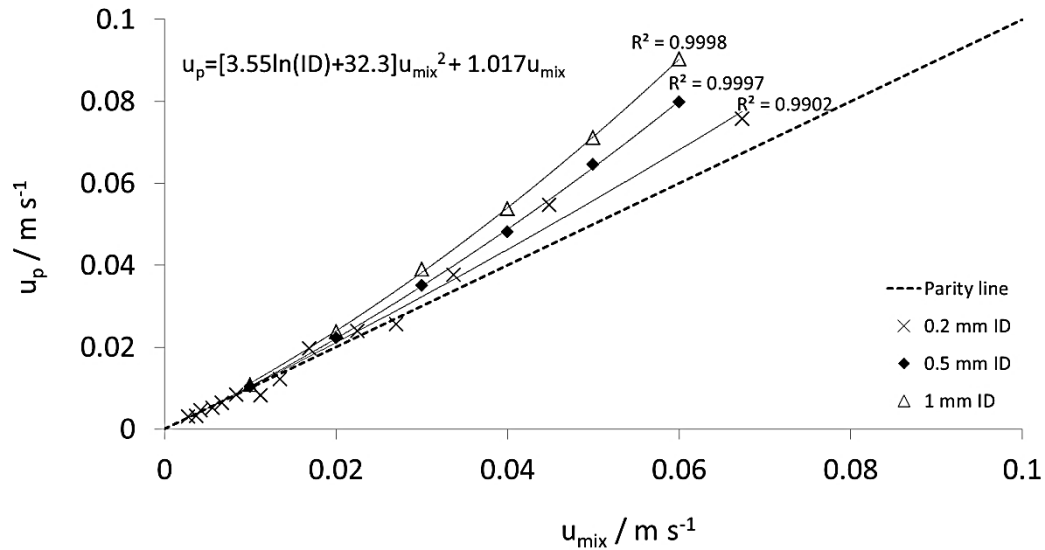


**Figure 4.17:** Plug velocity  $u_p$  as a function of the mixture velocity  $u_{mix}$ .

The plug velocity was found to be independent of the flow rate ratio as it can be seen in **Figure 4.18** for a constant mixture velocity  $u_{mix}$  of 0.01 m s<sup>-1</sup>. This means that the residence time will be the same, even though the length of the plug changes. In addition, it can be seen that the plug velocity is almost the same for channels with 0.5 and 1 mm ID, while  $u_p$  increases in the case of the 2 mm ID channel. This difference is attributed to the fact that the dimensionless film thickness at a mixture velocity of 0.01 m s<sup>-1</sup> was almost identical in 0.5 and 1 mm ID channels ( $\delta/ID=0.033$ ), whilst in the case of the 2 mm ID channels it was ~10% higher, i.e.  $\delta/ID=0.038$ . This contributed to a decrease in the cross sectional area of the channel which leads to an increase in the plug velocity.

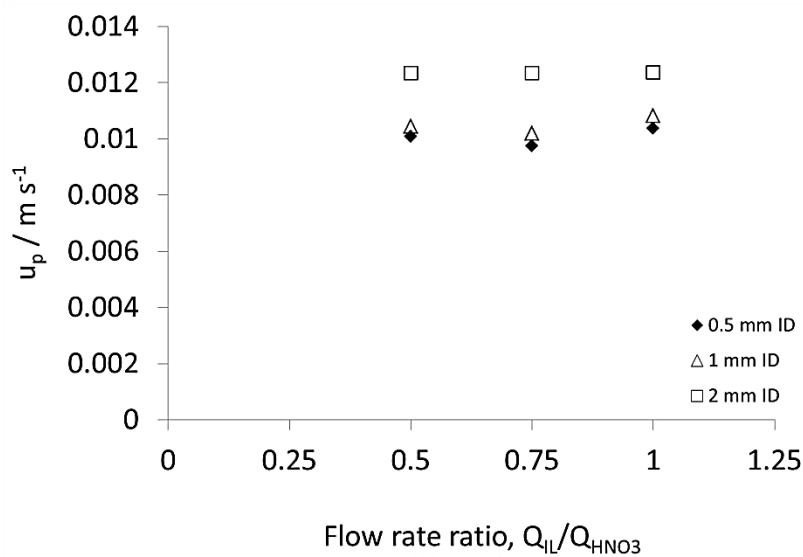


**Figure 4.18:** Plug velocity  $u_p$  as a function of the flow rate ratio  $Q_{IL}/Q_{HNO_3}$  at constant mixture velocity of 0.01 m s<sup>-1</sup>.



The experimental results were compared (**Figure 4.19**) with the empirical models proposed for the bubble velocity during gas-liquid Taylor flow and the analytical approach of Bretherton (Bretherton, 1961) (**Table 2.3**), as well as with the analytical solution derived for a large droplet volume (Lac and Sherwood, 2009, Jovanović et al., 2011, Gupta et al., 2013) as described in section 2.2.4. The analytical approach of Bretherton (Bretherton, 1961) showed relatively good agreement with the results only at low Ca numbers regardless of the channel size. However, as the Ca number increases the deviation from the experimental results exceeded 50%. The correlation derived by Liu et al. (Liu et al., 2005) by correlating experimental data in both circular and square capillaries showed good agreement with all the experimental data from the four different channel sizes used here. The highest mean relative error was observed in the smallest channel, whilst for the three large channels, i.e. 0.5, 1, and 2 mm ID, the mean relative error was 11%. In addition, the results were compared with the analytical approach showed in section 2.2.4 and the largest deviation was observed for the 2 mm ID channel, whilst for channels of 0.2 and 0.5 mm ID the mean relative error was 16%. For the comparison with the experimental results Eq. (2.2.13) was used, since the viscosity ratio ( $\mu_d/\mu_c$ ) in the current work was very low ( $\lambda=0.03$ ), and there is no significant effect on the droplet velocity (Christopher et al., 2008).

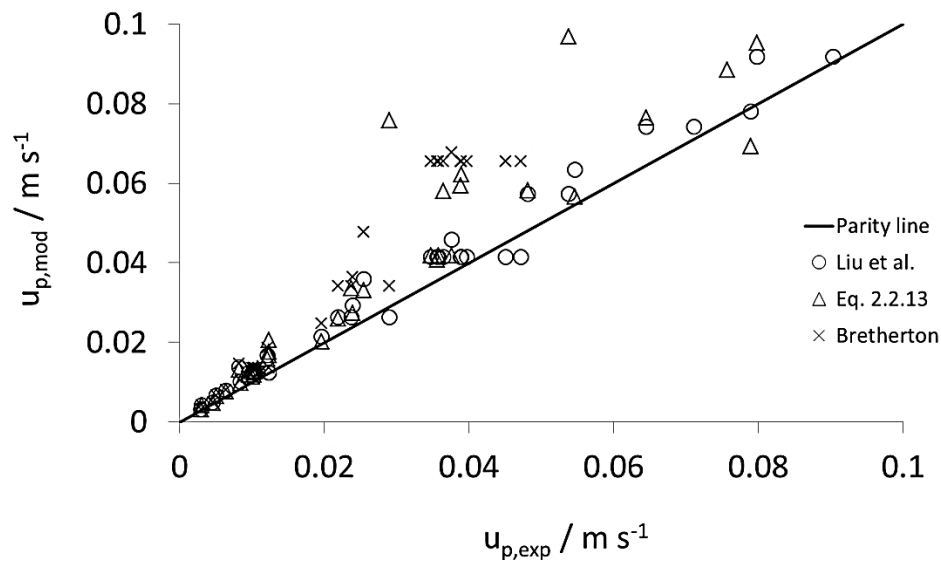


**Figure 4.19:** Comparison of experimental plug velocity with literature models.

### 4.3.5 Pressure drop

Pressure drop was measured in 4 different channel sizes from 0.22 to 2 mm ID made of Teflon over a length of 10 cm, for different flow rates and flow rate ratios. As mentioned earlier, in the Teflon channels ionic liquid was always the continuous phase. The results shown in **Figure 4.20** indicate that pressure drop increases by increasing mixture velocity (at flow rate ratio equal to 1) and decreases by increasing channel size. Pressure drop was always higher than that of the single phase ionic liquid having the same flow rate as in the two-phase mixture.

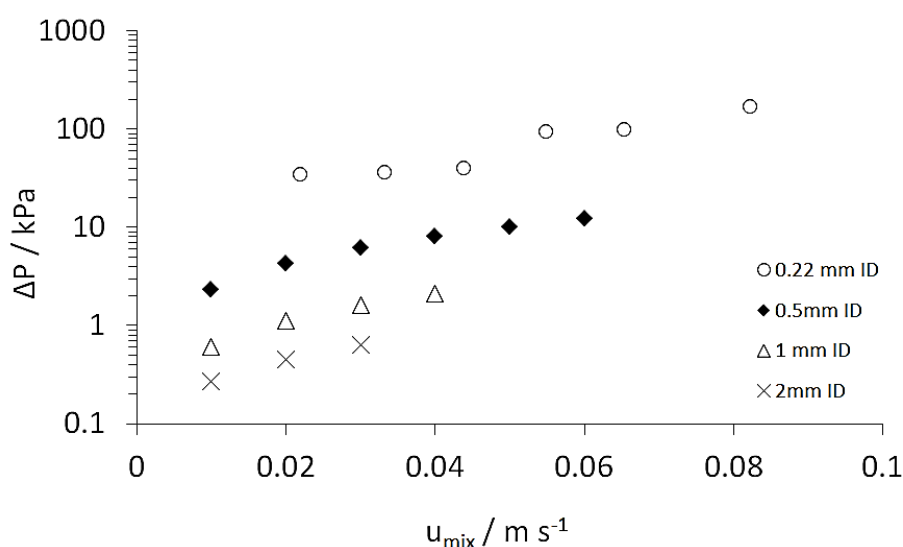


**Figure 4.20:** Experimental pressure drop during liquid-liquid plug flow as a function of the mixture velocity in 4 different channels at flow rate ratio equal to 1.

Three terms are considered to contribute to the frictional pressure drop during plug flow 1) frictional pressure drop of the continuous phase slug, 2) frictional pressure drop of the dispersed phase plug, and 3) interfacial pressure drop at the front and rear caps of the plug (Kreutzer et al., 2005a, Kashid and Agar, 2007, Jovanović et al., 2011). The pressure drop measurements during plug flow are compared with the existing models of Kashid and Agar (Kashid and Agar, 2007) and Jovanovic et al. (Jovanović et al., 2011), discussed in section 2.2.6. In both works, plug flow is considered as a series of unit cells, consisting of a plug and a slug.

As explained, Kashid and Agar (Kashid and Agar, 2007) did not consider the film that surrounds the plugs and suggest that pressure drop is equal to the frictional pressure drop of the dispersed and of the continuous phases, and of the interfacial pressure drop (Eq. (2.2.24),

Eq. (2.2.25), and Eq. (2.2.27)). The frictional pressure drop is calculated from the Hagen-Poiseuille equation, while the interfacial pressure drop from the Young-Laplace equation. The predictions from this model are compared against the experimental data from the current work for channels from 0.22 to 2 mm ID in **Figure 4.21**. The interfacial pressure drop was calculated using the measured static liquid-liquid-solid contact angles. Good agreement was found at low mixture velocities for all channel sizes, where the ionic liquid film is thin and expected to be almost stagnant, and thus the contribution of the dispersed aqueous phase seems to be predicted correctly. At higher velocities and higher Ca numbers, however, the ionic liquid film thickness increases and would have some velocity, causing additional frictional pressure drop. Since the model assumes that the less viscous water comes in contact with the wall periodically, it underestimates the frictional pressure drop of the continuous phase, which should depend on the combination of ionic liquid-wall stresses and interfacial shear stresses. In addition, as We number increases the interfacial forces become weak and the plugs cannot maintain their shape; the front part elongates whilst the back end flattens. This leads to deviations from the pressure drop calculated for a static contact angle. The mean relative error for all the channel sizes was 15%, whilst the maximum error found in cases of high mixture velocities was about 29%.

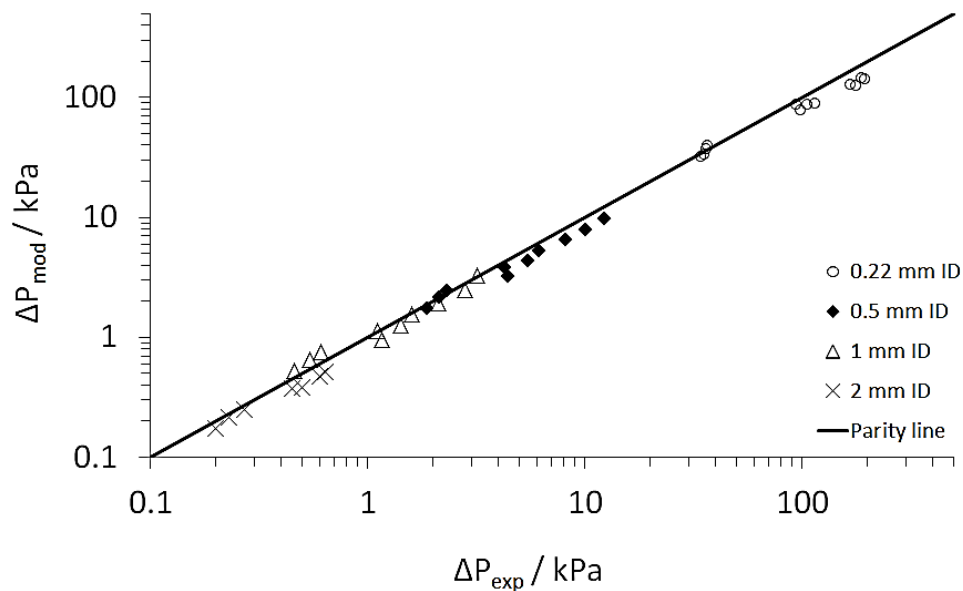


**Figure 4.21:** Comparison of the pressure drop calculated by Kashid and Agar ([Kashid and Agar, 2007](#)) model to the experimental results of this work for 4 different channel sizes, mixture velocities from 0.01 to 0.16 ms<sup>-1</sup>, and flow rate ratios (q) from 0.5 to 1.

The results were also compared with the model of Jovanovic et al. (Jovanović et al., 2011), which included the film around the plugs. They found that the influence of the film velocity on the plug pressure drop is negligible (lower than 1.4%) and suggested Eq. (2.2.31) for stagnant film as discussed in section 2.2.6. The comparisons between experimental pressure drop data during plug flow and the stagnant film model showed good agreement only at low flow rates. Bretherton's equation for film thickness (corrected by the factor proposed by Bico and Quere (Bico and Quere, 2000)) that was used in the Jovanovic et al. (Jovanović et al., 2011) model is not valid for high capillary numbers and film thickness larger than 1% of the channel radius as is found in the current study. Clearly film thickness has an important effect on pressure drop. Previously, it was reported (section 4.3.2) that current correlations are not able to predict the film thicknesses in ionic liquid-aqueous flows in micro-channels (0.2 mm ID) and a new correlation was suggested, given by Eq. (4.2.5). As it can be seen in **Figure 4.22**, the pressure drop predicted using the film thickness calculated by Eq. (4.2.5) agree very well with the experimental data (mean relative error ~8%) for the channel with internal diameter of 0.22 mm. However, the model was unable to predict the pressure drop for the other 3 channel sizes, i.e. 0.5, 1 and 2 mm with mean relative error less than 32% as shown in **Figure 4.22** even if the experimental film thickness was taken into account. The model seems to over-predict the experimental results for the bigger channels and this is attributed to the fact that the interfacial pressure drop calculated by Eq. (2.2.30) assumes ideally semi-spherical caps, which is not the case at all experimental conditions. By substituting the constant C in Eq. (2.2.31) to C=1.7, the correlation was able to predict pressure drop during plug flow in the channels with 0.5, 1, and 2 mm ID with mean relative error of 14% (red highlighted symbols).

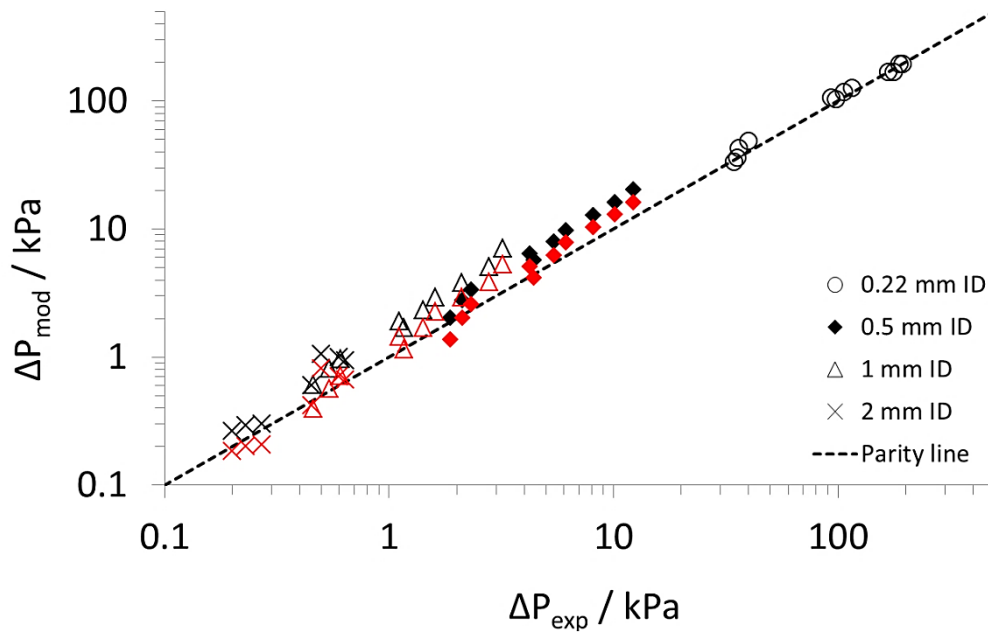


Figure 4.22: Comparison of the pressure drop calculated via the stagnant film model (Jovanovic et al., 2011) to the experimental results of this work for 4 different channel sizes, mixture velocities from 0.01 to 0.16 ms<sup>-1</sup>, and flow rate ratios (q) from 0.5 to 1. Red highlighted symbols correspond to C=1.7 in Eq (2.2.31).

## 4.4 Conclusions

Two liquid-liquid flow systems, i.e. ionic liquid-deionised water, and TBP/ionic liquid (30% v/v)-nitric acid solutions have been studied in channels made either of glass or Teflon. Channel sizes varied in internal diameter from 0.2 to 2 mm. Flow patterns were obtained for two inlet configurations (T- and Y- junction), for total flow rates of 0.065-214.9 cm<sup>3</sup> h<sup>-1</sup> and ionic liquid volume fractions from 0.05 to 0.8. The continuous phase in the glass capillary depended on the fluid that initially filled the channel. When water was introduced first, it became the continuous phase with the ionic liquid forming plugs or a mixture of plugs and drops within it. In the Teflon microchannels, the order that fluids were introduced did not affect the results and the ionic liquid was always the continuous phase. The main patterns observed were annular, plug, and drop flow. Pressure drop in the Teflon microchannels at a constant ionic liquid flow rate, was found to increase as the ionic liquid volume fraction decreased, and was always higher than in the single phase ionic liquid value at the same flow rate as in the two-phase mixture. However, in the glass microchannel during plug flow,

pressure drop for a constant ionic liquid flow rate was always lower than the single phase ionic liquid value.

Further investigations on the hydrodynamic characteristics during plug flow were performed for the different channel sizes. The plug formation was studied at the T-junction when either the less or the more viscous fluid acted as the carrier continuous phase. When ionic liquid was the continuous phase (higher Ca number), the plug formation frequency was three times faster than in the case of water as the continuous phase, and was dominated by the dripping plug formation mechanism. In all other measurements, ionic liquid was the continuous phase. Plug length was measured for all channel sizes. It was found that as the mixture velocity increased at equal flow rates of the two phases, the length of the plug decreases due to the rapid penetration of the one phase into the other. Plug length was compared with literature models but little agreement was found for low Ca numbers. A correlation was developed based on dimensionless groups, which predicted reasonably well the plug lengths obtained in channel sizes from 0.2 to 2 mm ID. A thin film was found to be present at all experimental conditions. Film thickness was measured in the different channel sizes and results were compared with literature correlations. The existence of the film was expected to increase the velocity of the plug. The experimental data on velocity agreed with the correlation of Liu et al. (Liu et al., 2005) within 11% mean relative error. A modified plug flow pressure drop model showed relatively good agreement with the experimental data.

# Chapter 5.

## Circulation patterns and mixing characteristics of liquid-liquid flows in small channels

### 5.1 Introduction

In this chapter, circulation patterns and mixing characteristics within aqueous plugs were investigated by means of  $\mu$ -PIV (micro Particle Image Velocimetry). Experiments were carried out in two different systems, viz. a glass microchannel with circular cross section of 0.2 mm ID using an ionic liquid (i.e.  $[\text{C}_4\text{mim}][\text{NTf}_2]$ ) or water as carrier fluid (**Table 4.1**), and Teflon channels of different sizes, i.e. 0.5, 1, and 2 mm ID using different TBP/IL mixtures (30%, v/v) (**Table 3.2**) and nitric acid solution (3 M), relevant to spent nuclear fuel reprocessing. The results were used to explain the mass transfer performance of the extractors. The mixing efficiency was quantified by calculating the non-dimensional circulation time in the aqueous plugs. The effects of different parameters on the location of the stagnation points, the size of the vortex cores, and the velocity profiles within the plugs were also discussed.

### 5.2 Velocity fields and velocity profiles in plugs

During plug flow in small channels as the liquid plug flows downstream at constant velocity, the fluid inside the plug circulates, forming vortices with patterns symmetrical about the channel centreline. To calculate the circulation time, the exact value of the velocity of the plug within the microchannel needs to be known. As shown in [section 4.3.3](#) at all experimental conditions tested there is a thin film that separates the plug from the wall, and so the velocity of the plug will be higher than that of the mixture. **Figure 5.1** shows a sample of the total velocity field, within an aqueous plug at mixture velocity of  $0.0028 \text{ m s}^{-1}$ , and

$\varepsilon_{IL}=0.6$  in a 0.2 mm ID channel, ensemble averaged over more than 60 cross correlated image pairs (reference frame is stationary and attached to the image).

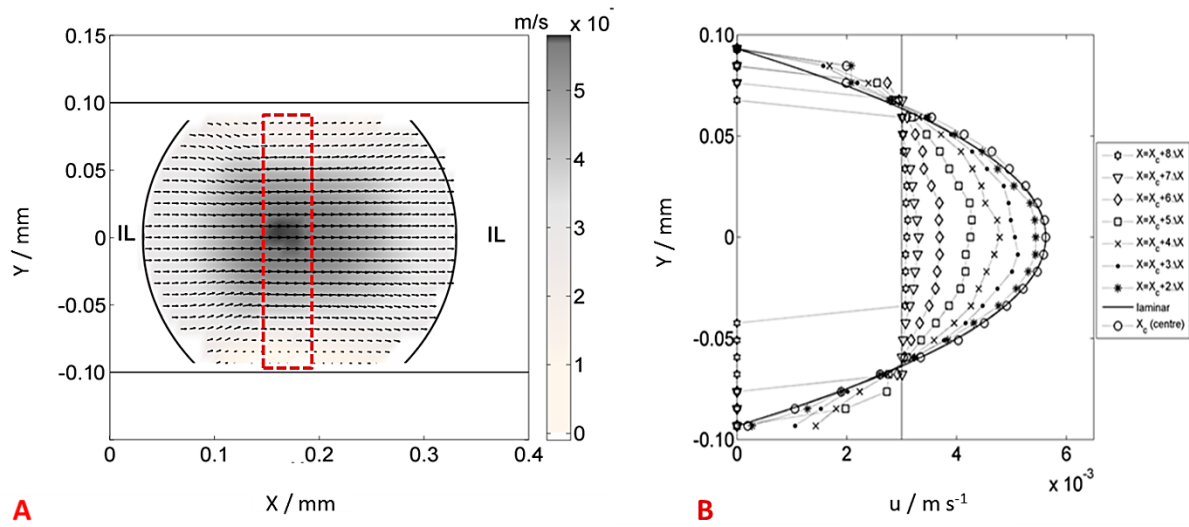


**Figure 5.1: (A) Ensemble average velocity field within an aqueous plug at  $u_{mix}=0.0028 \text{ m s}^{-1}$  and  $\varepsilon_{IL}=0.6$  in a 0.2 mm ID channel. The magnitude of the velocity is superimposed in grey scale. (B) Vertical profiles of the horizontal component ( $u_x$ ) of the total velocity across half of the aqueous plug.  $x_c$  is the axial location of the plug centre, while the spacing between profiles,  $\Delta x$ , is approximately equal to  $24 \text{ }\mu\text{m}$ .  $[\text{C}_4\text{mim}][\text{NTf}_2]$  as carrier fluid.**

It can clearly be seen that the horizontal component of the velocity is dominant as the main flow direction is along the x-axis. The magnitude of the velocity is maximum at the core of the plug while it is decreasing towards the channel wall and the liquid-liquid interface. Since the plug is moving at constant velocity  $u_p$ , the internal recirculation is not apparent if a stationary reference frame is employed as in **Figure 5.1A**. By subtracting  $u_p$  from the total velocity field (i.e. reference frame attached to the moving plug), the internal re-circulation is revealed. Therefore, the plug velocity  $u_p$  needs to be found experimentally from the images acquired with the high-speed camera.

The sample profiles of the horizontal component of the velocity are shown in **Figure 5.1B**. It was found that for all channel sizes the velocity decreases and the profiles become more uniform as the interface is approached, and that the profiles are symmetrical about the channel centre line (x-axis). In **Figure 5.1B** it can be seen that the average velocity of the two phase flow is the same as the velocity where all the profiles intersect (equal to  $0.0028 \text{ m s}^{-1}$ ).



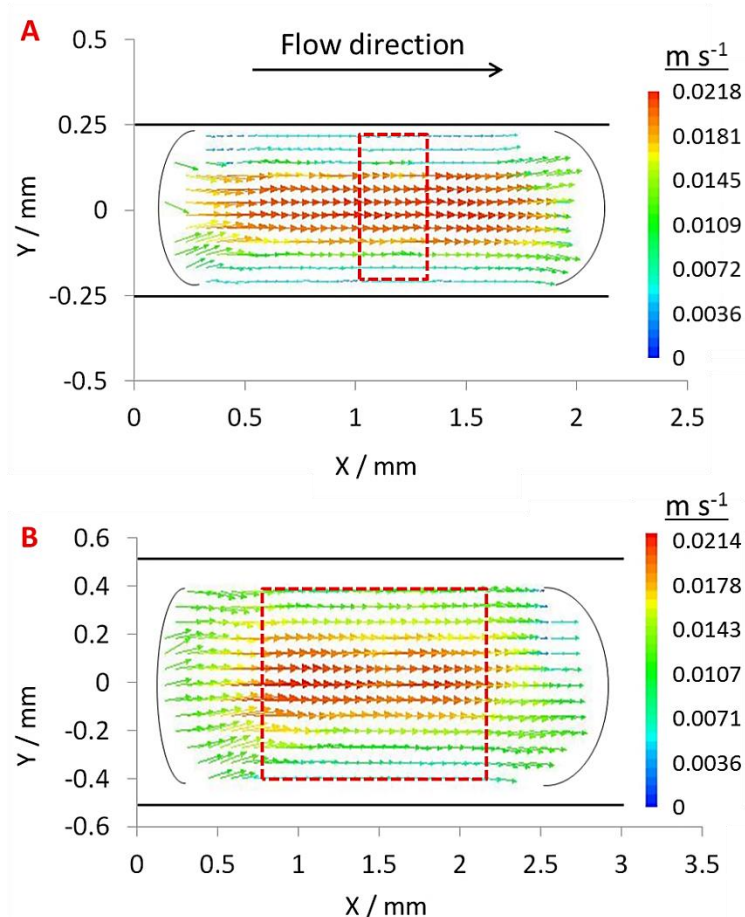


**Figure 5.2:** Ensemble average velocity field in grey scale within an aqueous plug at mixture velocity of  $0.01 \text{ m s}^{-1}$  (flow rate ratio equal to 1) in a channel of (A) 0.5 mm ID, and (B) 1 mm ID. Thirty instantaneous fields were averaged. TBP/[C<sub>4</sub>mim][NTf<sub>2</sub>] (30%, v/v) as carrier fluid.

For  $L_p/ID > 1$  a laminar profile is fully established at the centre of the plug. However, the area where a fully developed laminar profile is developed is different for each channel. As it can be seen in **Figure 5.1**, for the 0.2 mm ID channel the laminar profile was close to the centreline (as indicated with the highlighted rectangle, **Figure 5.1A**), while this area increased (**Figure 5.2**) as the channel size increased for the same experimental conditions. The velocity fields at channel sizes of 0.5 and 1 mm ID for mixture velocity of  $0.01 \text{ m s}^{-1}$  are shown in **Figure 5.2**. Similarly to the case of the 0.2 mm ID channel, the velocity magnitude reaches a maximum at the channel core, whilst it decreases towards the liquid-liquid interface. It is expected that as the channel size increases the velocity gradient between the channel axis and the wall is less steep since the thicker film that is created leads to less shear between the aqueous plug and the wall. Therefore, the velocity gradients are expected to be higher in the case of the smaller channels where the film thickness is less. Moreover, the bulk

convective flow can be clearly seen in both cases. A fully developed laminar profile can be considered away from the front and the rear end of the plug. As can be observed in **Figure 5.2** a laminar profile can be considered in the middle of the plug for an area that occupies  $\sim 45\%$  of the length of the plug in the case of the 0.5 mm ID and  $\sim 54\%$  in the case of the 1 mm ID. In the case of the microchannel (0.2 mm ID) laminar flow has been developed for almost  $\sim 32\%$  of the plug for the same experimental conditions ( $u_{\text{mix}} = 0.01 \text{ m s}^{-1}$ ). In **Figure 5.3** the velocity profiles for the area indicated in **Figure 5.2** are presented. The velocity profiles seem to agree well with the laminar profile within 6% mean relative error for both 0.5 and 1 mm ID channel. Comparing **Figure 5.1** and **Figure 5.3** it can be observed that symmetry of the velocity profiles is independent on the channel size.

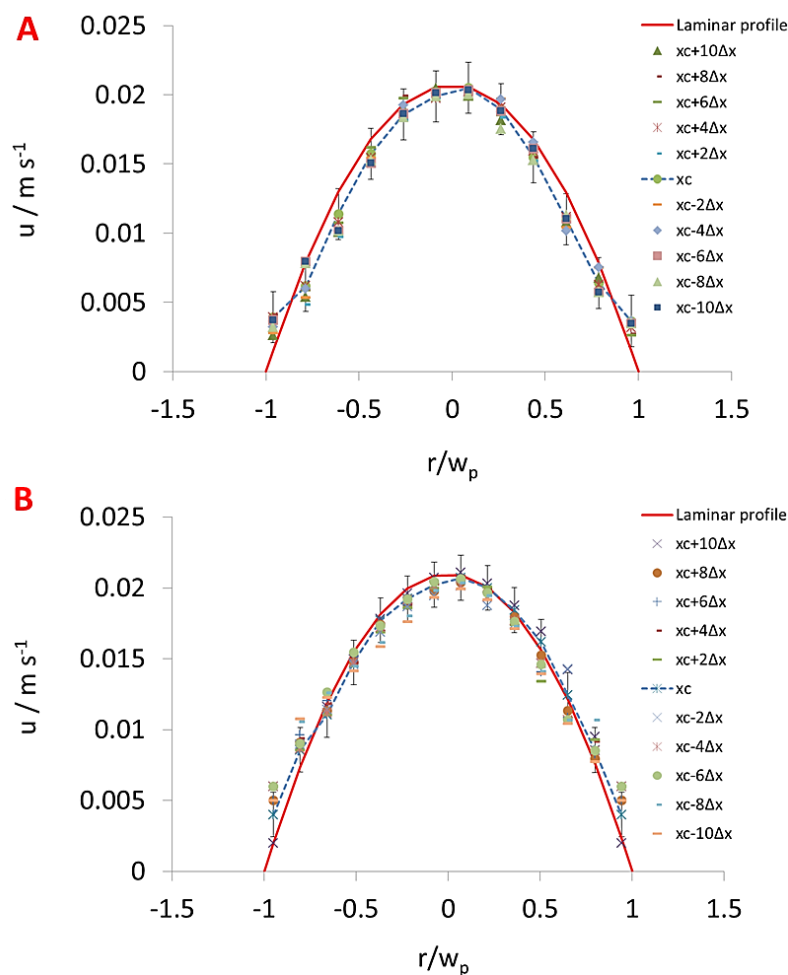


**Figure 5.3:** Vertical profiles of the horizontal component of the total velocity across the aqueous plug at mixture velocity of  $0.01 \text{ m s}^{-1}$  (flow rate ratio equal to 1).  $x_c$  is the axial location of the plug centre, while the spacing between profiles,  $\Delta x$ , is approximately equal to 0.041 mm and 0.068 mm in the case of the 0.5 mm ID and 1 mm ID, respectively. TBP/[C<sub>4</sub>mim][NTf<sub>2</sub>] (30%, v/v) as carrier fluid.

Average velocity profiles of the horizontal velocity component,  $u_x$ , normalised with the maximum velocity of the plug are shown in **Figure 5.4**. The velocity profiles of a plug of length 2.6 mm at two different mixture velocities show that in both cases strong velocity gradients have been developed. In addition, the velocity profiles are symmetrical about the channels axis regardless of the mixture velocity.

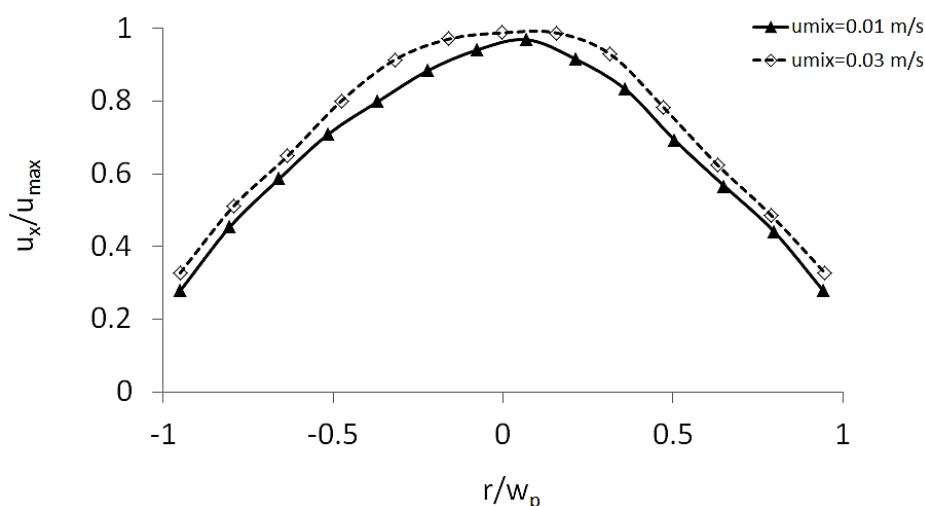


**Figure 5.4:** Averaged velocity profiles of the horizontal velocity component  $u_x$  (normalised with the maximum velocity of the plug) for a plug of length 2.6 mm in a channels of 1 mm ID. TBP/[C<sub>4</sub>mim][NTf<sub>2</sub>] (30%, v/v) as carrier fluid.

### 5.3 Circulation patterns

The circulation patterns inside the plugs were obtained by subtracting the plug velocity  $u_p$  from the total average velocity vector field measured using PIV. Depending on the mixture velocity,  $u_{\text{mix}}$ , flow rate ratio, and channel size, circulation patterns have different characteristics. In **Figure 5.5**, circulation patterns in a 0.2 mm ID channel are shown for the upper half channel. For relatively low mixture velocities (0.0028-0.0042 m s<sup>-1</sup>) the circulation pattern consists of two distinct vortices, counter rotating and symmetrical about the channel axis. Two stagnation points at the vortex cores are clearly visible, which move towards the rear of the plug when the plug length decreases (i.e. the ionic liquid volume fraction increases). As the  $\varepsilon_{\text{IL}}$  decreases, larger aqueous plugs are formed that exhibit a more symmetrical circulation pattern with respect to the plug centreline (x-axis). For intermediate mixture velocities (0.0056-0.0169 m s<sup>-1</sup>), two extra vortices appear at the front of the plugs, which for small plugs, occupy a significant area. As a result of the higher speed of the carrier

fluid the rear interface is more flat compared to the lower velocity, while the front interface is sharper, exhibiting a “bullet” shape. The fluid can thus recirculate also within the sharp nose. The stagnation points move towards the rear of the plug as the plug size increases similar to what was seen at lower mixture velocities. For relatively high mixture velocities ( $0.0225$ - $0.0674 \text{ m s}^{-1}$ ), the plugs again exhibit the two counter rotating vortices and a smoother plug shape (i.e. interface shapes at the rear and front interfaces are close). However, as a result of a thicker film at the channel walls the plug seems “squeezed” against the channel axis and the stagnation points slightly move towards the channel centreline.

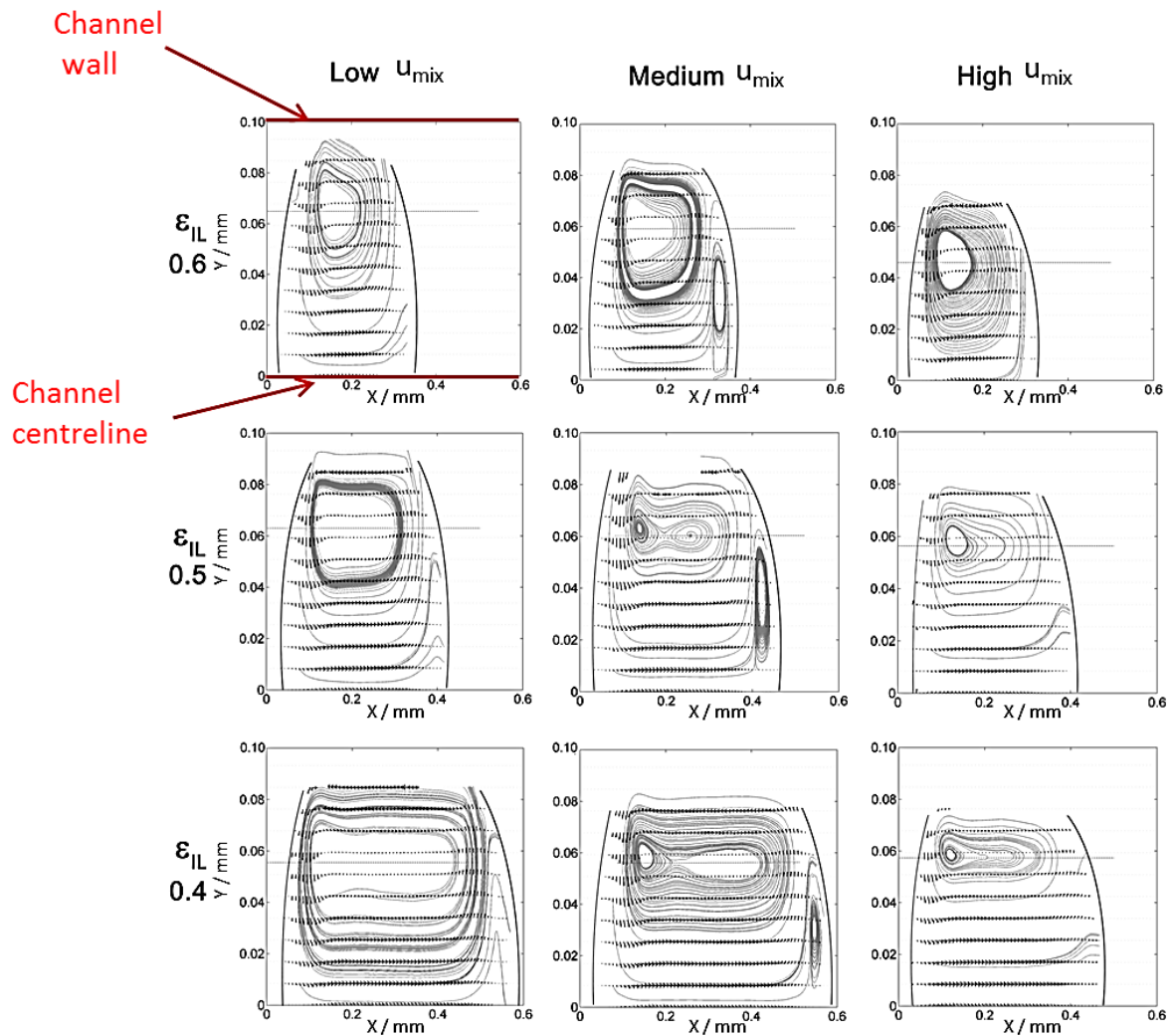


**Figure 5.5:** Representative circulation patterns in the top half of water plugs found for the three regimes depending on mixture velocity, as a function of input ionic liquid volume fraction. Sixty instantaneous fields were averaged  $[\text{C}_4\text{mim}][\text{NTf}_2]$  as carrier fluid.

By increasing the channel size circulation patterns do not change significantly. Typical counter-rotating vortices also appear at the top and bottom of the channel in the cases of 0.5 and 1 mm ID. In **Figure 5.6** circulation patterns in two different channel sizes at the same mixture velocity of  $0.06 \text{ m s}^{-1}$  (flow rate ratio equal to 1) are observed. In the 0.5 mm channel the vortices are not symmetrical around the channel centreline, with the stagnation point in the top half close to the back cap and that in the bottom part closer to the front cap. However, as the channel size further increases to 1 mm ID the vortex cores move towards the centre, and the two vortices (upper and lower half) lie almost on a vertical line.

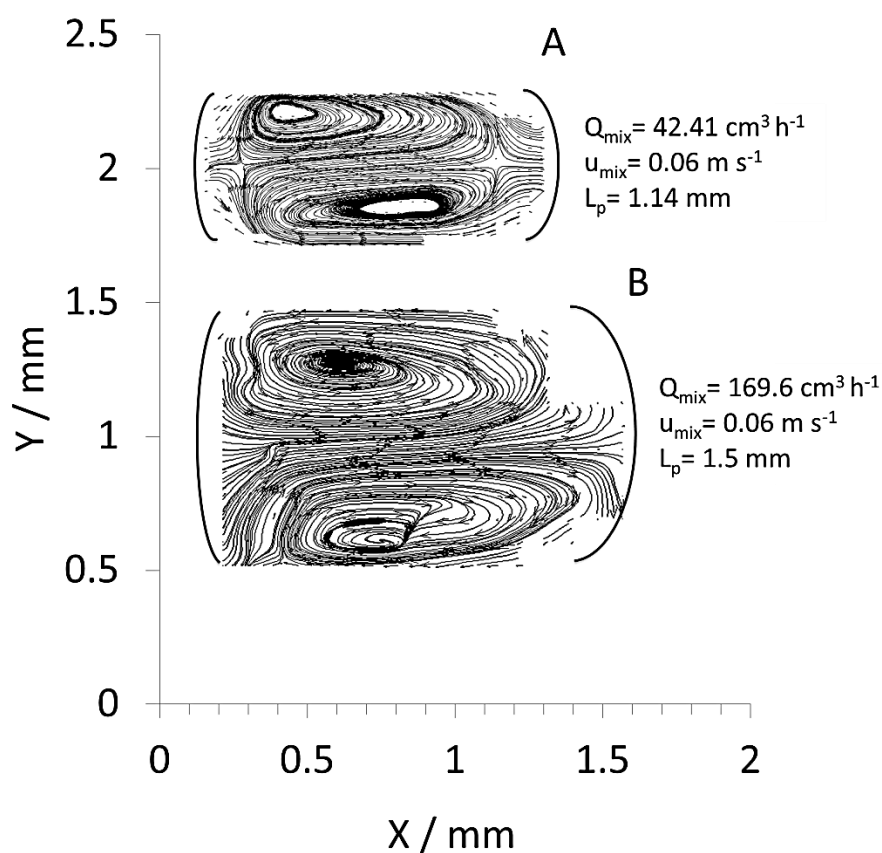


**Figure 5.6:** Ensemble averaged circulation patterns within aqueous plugs at the same mixture velocity ( $u_{\text{mix}}=0.06 \text{ m s}^{-1}$ ) and flow rate ratio equal to 1 in a channel of A) 0.5 mm ID, and B) 1 mm ID. Thirty instantaneous fields were averaged. TBP/[C<sub>4</sub>mim][NTf<sub>2</sub>] (30%, v/v) as carrier fluid.

The effect of mixture velocity on the formation of circulation patterns in bigger channels can be seen in **Figure 5.7** for the case of the 1 mm ID channel. Symmetry to the channel axis is improving as the mixture velocity increases. The two distinct vortex cores that appear, move to the centre of the plug (along x-axis) as the mixture velocity increases.

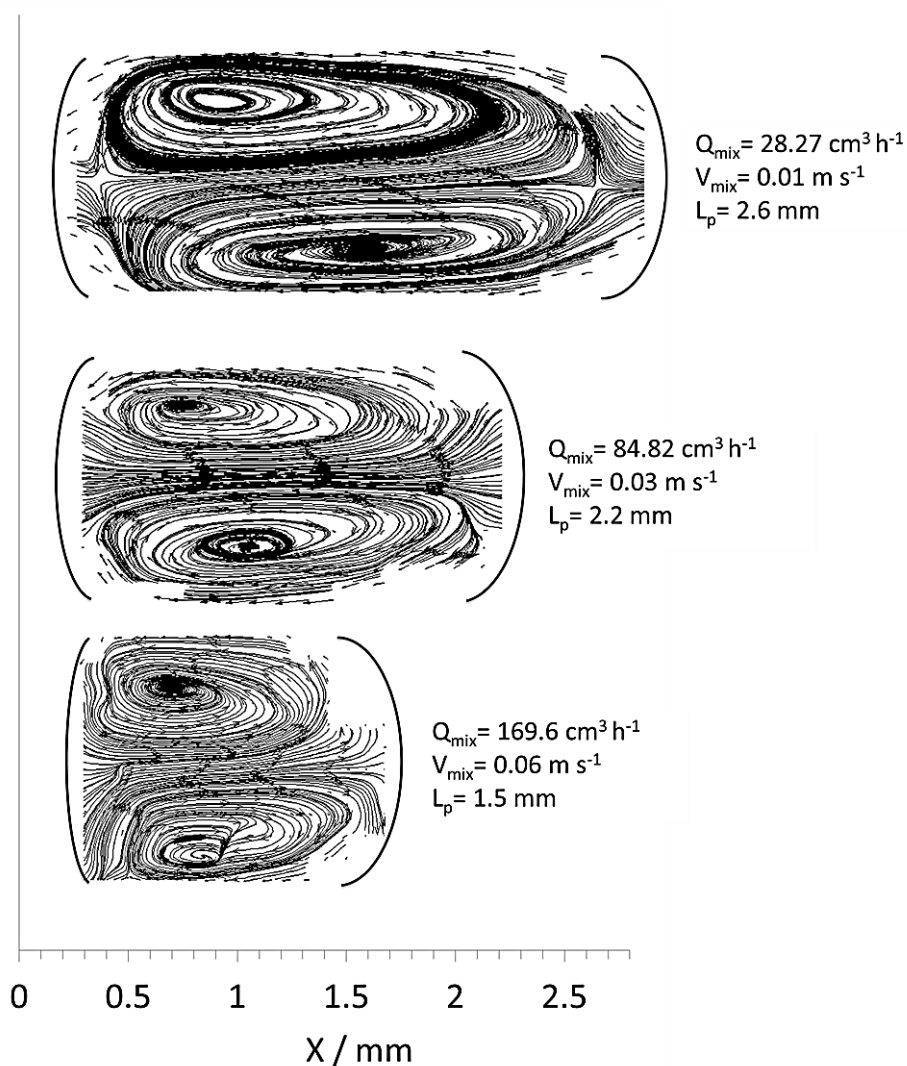


**Figure 5.7:** Ensemble averaged circulation patterns in aqueous plugs for different mixture velocities (flow rate ratio equal to 1) in the 1 mm ID channel. Thirty instantaneous fields were averaged. TBP/[C<sub>4</sub>mim][NTf<sub>2</sub>] (30%, v/v) as carrier fluid.

In **Figure 5.8** a comparison of the circulation patterns within the aqueous phase when water and ionic liquid are the carrier phases, respectively, in the 0.2 mm ID channel at mixture velocity of  $0.0037 \text{ m s}^{-1}$  (flow rate ratio equal to 1) is shown for both cases. Two counter rotating vortices are observable, where the stagnation points at the vortex cores are pushed towards the rear interface for the shorter plug case (ionic liquid as carrier phase).



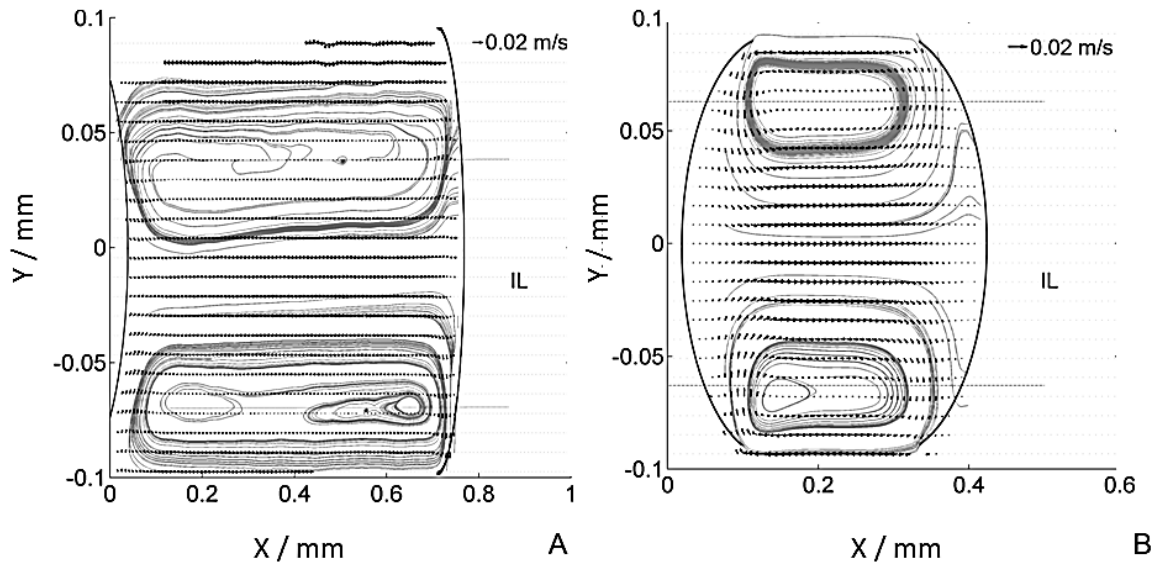


**Figure 5.8:** Ensemble averaged circulation patterns within the water phase at mixture velocity of  $0.0037 \text{ m s}^{-1}$  and flow rate ratio equal to 1, when (A) water is the carrier phase, and (B) ionic liquid is the carrier phase. Sixty instantaneous fields were averaged.  $[\text{C}_4\text{mim}][\text{NTf}_2]$  as carrier fluid.

#### 5.4 Circulation time, $\tau$

As shown in the previous section, during plug flow in small channels, counter rotating vortices form in the phases with closed streamlines and a pattern symmetrical about the channel axis (**Figure 5.9**). The rate of mixing inside the plug is quantified through the dimensionless circulation time,  $\tau$ , which relates the time for circulation,  $t_{\text{circ}} = \frac{V_{\text{circ}}}{Q_{\text{circ}}}$  (the average time to displace material from one side of the plug to the other) to the time that a plug needs to travel a distance equal to its own length,  $t_{\text{travel}} = \frac{L_p}{u_p}$ .

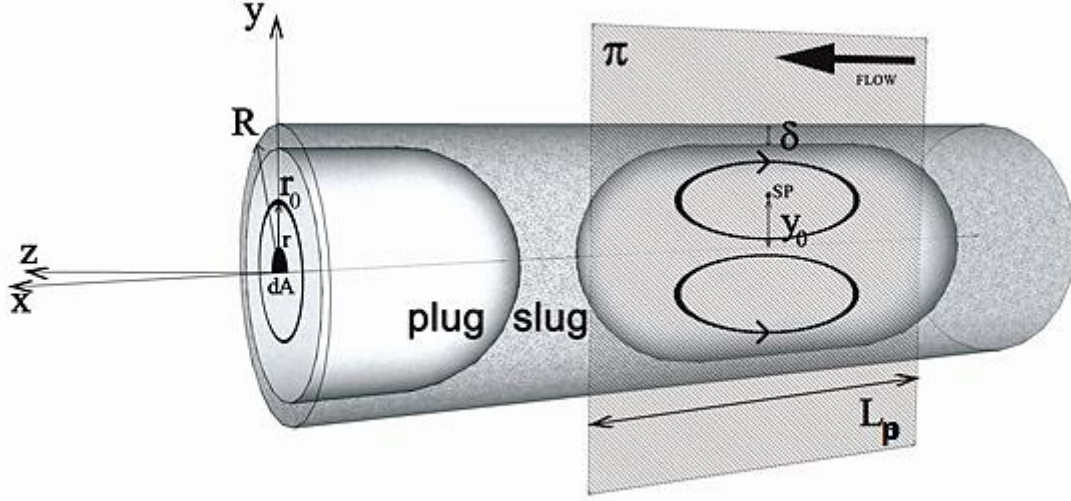


**Figure 5.9:** Schematic of the flow pattern inside the micro-channel of radius  $R$  in 3-D (Eq. (5.4.1)) and 2-D (Eq. (5.4.2)) reference frames. The internal recirculation parameters are sketched inside a single water plug, projected onto the mid-xy plane ( $\pi$ ), where quantities in Eq. (5.4.2) are defined.

Assuming a fully developed laminar profile within the plug and the 3-D flow model in **Figure 5.9**, the non-dimensional circulation time in cylindrical coordinates ( $r, x$ ), is (Thulasidas et al., 1997):

$$\tau_{3-D} = \frac{V_{\text{circ}}}{Q_{\text{circ}}} \frac{u_p}{L_p} = \frac{\pi L_p r_0^2 / 2}{\iint_{A_0} u(x, y, z) dA} \frac{u_p}{L_p} = \frac{u_p r_0^2}{2 \int_0^{r_0} u(r, x) dr} \cong \frac{u_p r_0^2}{2 \Delta r \sum_{i=1}^{i=N} u_i r_i |_x} \quad (5.4.1)$$

where  $V_{\text{circ}}$  is the fluid volume,  $Q_{\text{circ}}$  the flow rate, and  $r_0$  is the location of the stagnation surface.

When a planar domain at the centre of the channel is considered (i.e.,  $\pi$  plane in **Figure 5.9**) and given the axisymmetric assumption, Eq. (5.4.1) is still valid with  $r$  simply substituted by  $y$ . Alternatively a 2-D definition of the non-dimensional circulation time can be obtained by rewriting Eq. (5.4.1), valid in the observation  $xy$  plane  $\pi$  (**Figure 5.9**):

$$\tau = \frac{L_p y_0}{\int_0^{y_0} u(x, y) dy} \frac{u_p}{L_p} \cong \frac{u_p y_0}{\Delta y \sum_{i=1}^{i=N} u_i |_x} \quad (5.4.2)$$



where  $y_0$  is the location of the stagnation point projected on to the observation mid-plane  $\pi$  (**Figure 5.9**). Eqs. (5.4.1) and (5.4.2) demonstrate how the measurement of local velocities and the knowledge of the structure of the internal recirculation (i.e. location of stagnation points) are essential for quantifying mixing inside the plug. Optical techniques such as  $\mu$ -PIV are thus ideal to reconstruct the recirculation with high degree of detail.

A sample of the non-dimensional circulation time profile across the length of an aqueous plug in the 0.2 mm ID channel is shown in **Figure 5.10C**, which was calculated using Eq. (5.4.2) with the 2-D PIV circulation velocity data. If Eq. (5.4.1) is used instead, the circulation time is averaged over the cross sectional area (3-D model) which will only lead to higher values of the circulation time compared to Eq. (5.4.2), i.e.  $\tau_{3-D}=1.6\tau$ , without changing any trends or their significance (**APPENDIX A**). This result is consistent with the fact that the velocity averaged along the  $y$  direction within the  $xy$  mid-plane is expected to be higher than the average velocity within the whole channel depth, thus giving rise to smaller circulation time.

For all the experiments, the circulation time reaches a minimum value at the axial location of the vortex cores, where the average velocity is maximum as the comparison between the circulation velocity field (**Figure 5.10A**) and the velocity magnitude map (**Figure 5.10B**) demonstrates. Towards the front and rear caps of the plug, the circulation time tends to infinity, as it cannot be defined where the laminar profile is not developed. It is worth noticing here that previous studies on Taylor flow ([Thulasidas et al., 1997](#)) used Eq. (5.4.1) to calculate the non-dimensional circulation time, which always gives slightly larger values. In addition, previous investigators did not consider the variation of the circulation time along the length of the plug and computed it at the centre of the plug only. This implied the assumption of symmetry about both the plug axes and a laminar profile at the centre of the plug. In the liquid-liquid systems under investigation though, an asymmetry about the plug centreline ( $x$ -axis) is generally observed, which is affected by the length of the plug, the film thickness, and the mixture velocity (**Figure 5.5-Figure 5.8**).

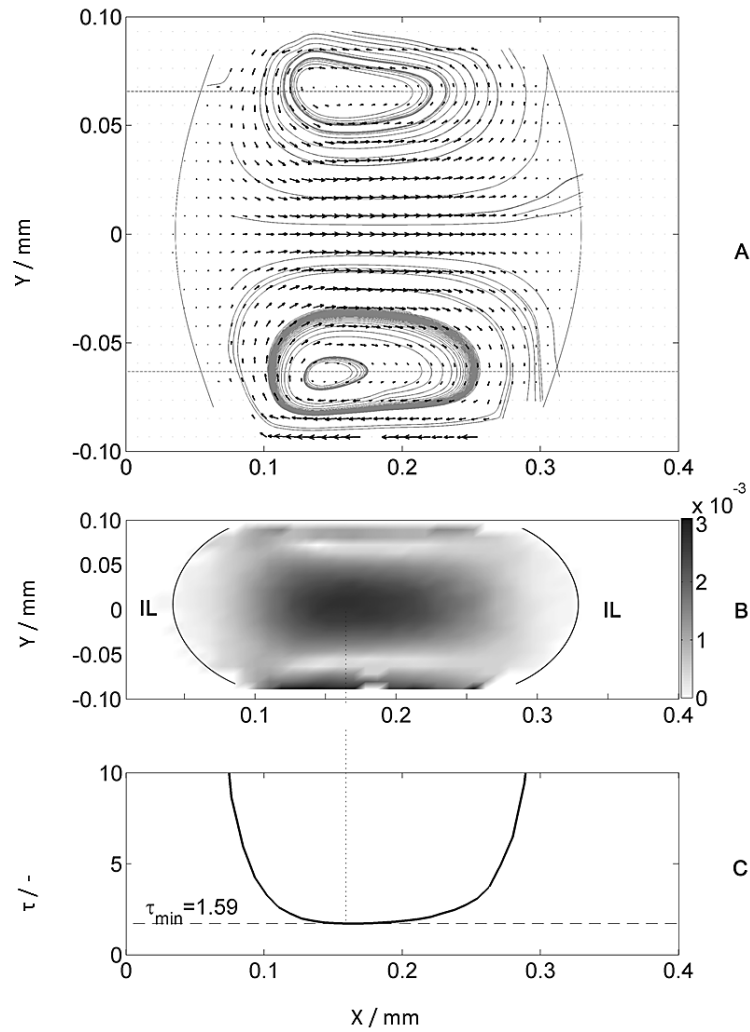


**Figure 5.10:** (A) Circulation pattern, (B) magnitude velocity in gray scale, and (C) non-dimensional circulation time ( $\tau$ ) profile (C) in a 0.2 mm ID channel for  $u_{\text{mix}}=0.0028 \text{ m s}^{-1}$ , calculated using Eq. (5.4.2). The minimum of  $\tau$  is at the axial location of the vortex cores (i.e. maximum of circulation velocity at the channel centreline).  $[\text{C}_4\text{mim}][\text{NTf}_2]$  as carrier fluid.

Circulation time along the plug can be seen in **Figure 5.11** for plugs of different lengths (different  $\epsilon_{\text{IL}}$ ) in the case of the 0.2 mm ID channel. The circulation time, and the mixing rate, is fairly constant across the length of large plugs where circulation patterns are symmetric. On the contrary, for shorter plugs, since the vortex cores are pushed towards the rear interface (**Figure 5.10**), the circulation patterns are not symmetric and the minimum of the circulation time is shifted along the x-axis towards the vortex cores.

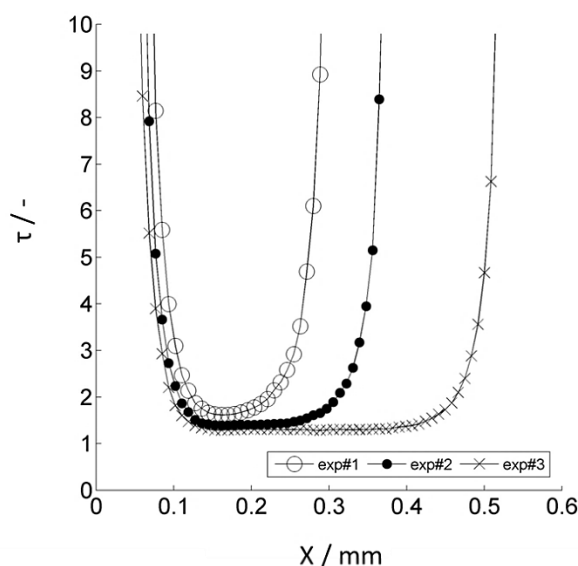


**Figure 5.11: Non-dimensional circulation time profiles across the water plug for different input ionic liquid volume fraction at low mixture velocities. Exp#1:  $u_{\text{mix}}=0.0028 \text{ m s}^{-1}$ ,  $\varepsilon_{\text{IL}}=0.6$ ,  $L_p=0.34 \text{ mm}$ ; Exp#2:  $u_{\text{mix}}=0.0037 \text{ m s}^{-1}$ ,  $\varepsilon_{\text{IL}}=0.5$ ,  $L_p=0.43 \text{ mm}$ ; Exp#3:  $u_{\text{mix}}=0.0042 \text{ m s}^{-1}$ ,  $\varepsilon_{\text{IL}}=0.4$ ,  $L_p=0.55 \text{ mm}$ .  $[\text{C}_4\text{mim}][\text{NTf}_2]$  as carrier fluid.**

The effect of the plug length at constant mixture velocity of  $0.01 \text{ m s}^{-1}$  in the  $1 \text{ mm}$  ID channel on the non-dimensional circulation time can be observed in **Figure 5.12**. The non-dimensional circulation time was calculated for the region included in the dashed line, where a fully developed laminar profile was established. It can be seen that  $\tau$  decreases as the length of the plug increases.

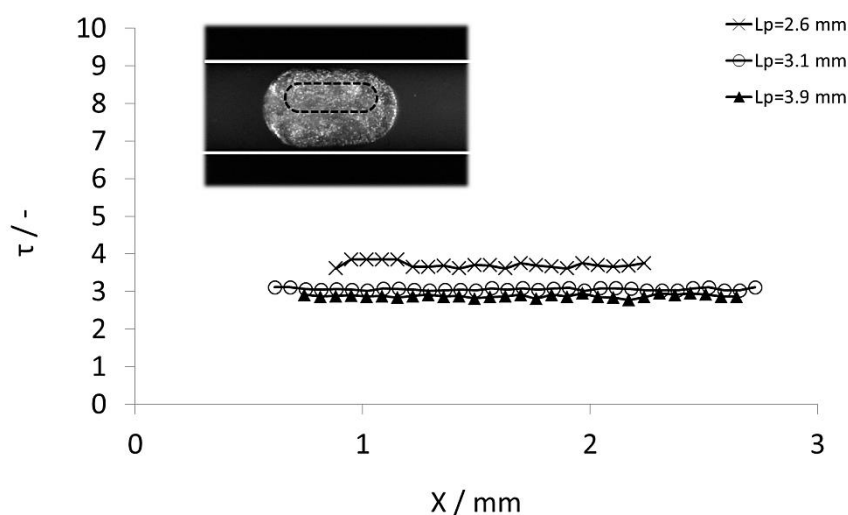


**Figure 5.12: Non-dimensional circulation time profile across the upper half of aqueous plug of different lengths at constant mixture velocity ( $u_{\text{mix}}=0.01 \text{ m s}^{-1}$ ) in the  $1 \text{ mm}$  ID channel. TBP/ $[\text{C}_4\text{mim}][\text{NTf}_2]$  (30%, v/v) as carrier fluid.**

The locations of the stagnation points along the y-direction are influenced by the length of the plug (as shown in [section 5.4.1](#)), which thus play an important role in the mixing rate.

The effect of the mixture velocity is shown in **Figure 5.13** for plugs of the same length ( $L_p=2.6$  mm) in the 1 mm ID channel. The time is lower in the case of the higher mixture velocity, which indicates more intense mixing, while it is fairly constant across the length of the plug which means that the circulation patterns are symmetric about the plug centreline (y-axis).

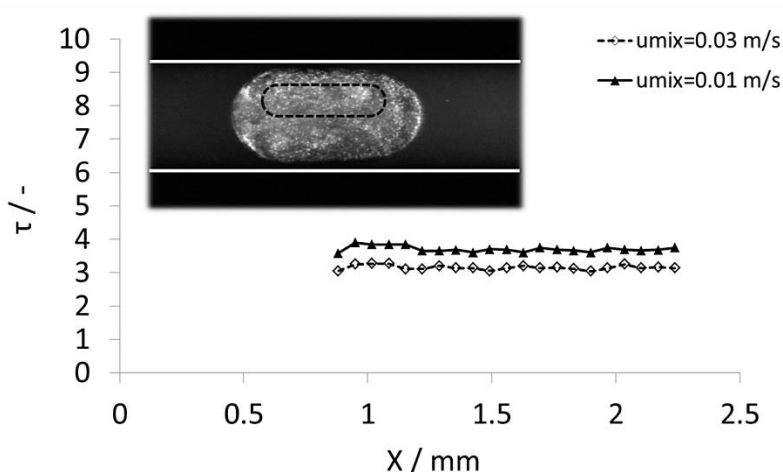


**Figure 5.13:** Non-dimensional circulation time profile across the upper half of the aqueous plug for constant plug length ( $L_p=2.6$  mm) at different mixture velocities ( $u_{\text{mix}}$ ) in the 1 mm ID channel. TBP/[C<sub>4</sub>mim][NTf<sub>2</sub>] (30%, v/v) as carrier fluid.

The channel size also affects the circulation patterns and as it can be seen in **Figure 5.14** for the same mixture velocity ( $u_{\text{mix}}=0.01$  m s<sup>-1</sup>) the non-dimensional circulation time decreases as the channel size decreases corresponding to higher mixing rates. In the case of the 0.2 mm ID channel the minimum value of  $\tau$  falls within the range of 1.00-1.75, while an order of magnitude increase of the channel internal diameter (i.e. 2 mm ID) leads to a non-dimensional circulation time of 4-4.75.

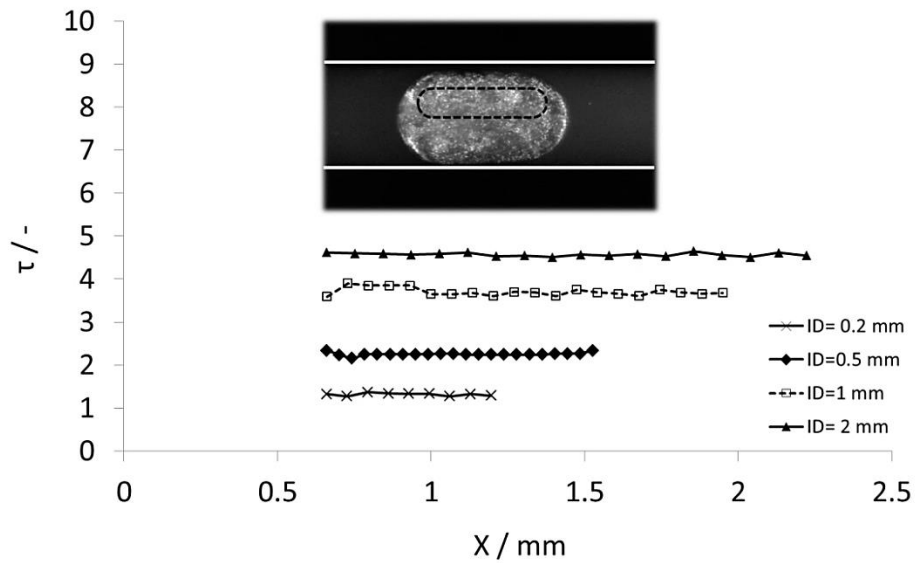


**Figure 5.14:** Non-dimensional circulation time profile along the upper half of the aqueous plug for 4 channel sizes at the same mixture velocity  $u_{\text{mix}}=0.01 \text{ m s}^{-1}$  and equal flow rates of the two phases. TBP/[C<sub>4</sub>mim][NTf<sub>2</sub>] (30%, v/v) as carrier fluid.

The effect of using different TBP/ionic liquid mixtures (30%, v/v) as carrier phase in a 0.5 mm ID channel at constant mixture velocity of  $0.02 \text{ m s}^{-1}$  is shown in **Figure 5.15**. As it can be seen the non-dimensional circulation time is slightly dependent on the type of the ionic liquid that is used as carrier phase, and mostly depends on the length of the plug and decreases at the length of the plug increases.

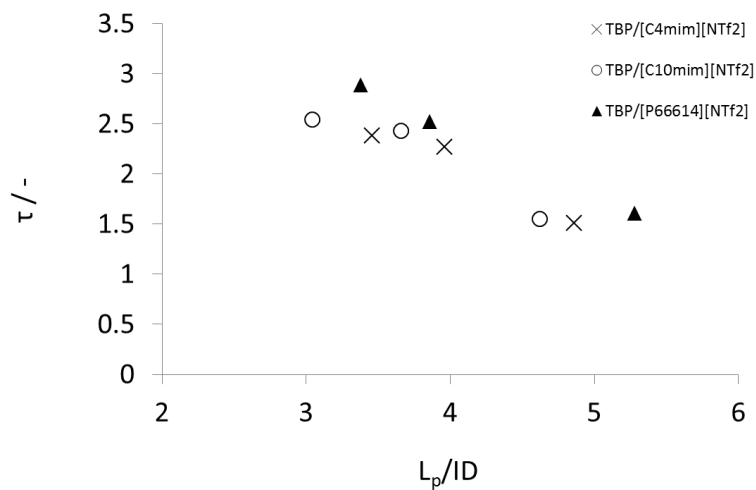


**Figure 5.15:** Non-dimensional circulation time as a function of the non-dimensional plug length for the three TBP/ionic liquid mixtures (30%, v/v) at mixture velocity of  $0.02 \text{ m s}^{-1}$ .

The variation of the maximum of the circulation velocity with the Ca number is depicted in **Figure 5.16** for the 0.2 mm ID channel. For all  $\varepsilon_{\text{IL}}$ , as the Ca number increases (i.e.  $u_{\text{mix}}$

increases) the circulation velocity increases almost linearly. The film thickness also increases consistently as was shown in **Figure 4.16**, resulting in a smaller  $y_0$ , the vertical location of the stagnation point. To demonstrate the effect of mixture velocity, the  $\tau_{\min}$  is plotted against Ca number in **Figure 5.17**. In contrast to circulation velocity there does not seem to be a clear correlation of  $\tau_{\min}$  with Ca number (i.e.  $u_{\text{mix}}$ ). This suggests that the circulation time, and thus the mixing rate, is a more complex function of other hydrodynamic parameters including not only circulation velocity, but also location of the stagnation points, and the film thickness, which in turn influences the vertical location of the stagnation points.

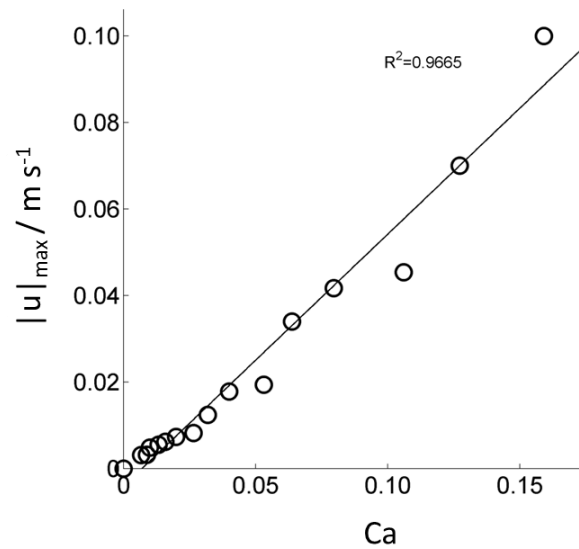


**Figure 5.16: Maximum circulation velocity at the centre of the plug as a function of the Ca number.**

This lack of a clear correlation in **Figure 5.17** is particularly true for shorter plugs and intermediate velocities, where the circulation patterns show anomalies (see **Figure 5.5**). On the other hand, for relatively long plugs ( $\epsilon_{\text{IL}}=0.4$ ) the decreasing trend of the minimum of circulation time with Ca (**Figure 5.17**) is well consistent with the increasing trend of the maximum circulation velocity (**Figure 5.16**), providing optimal conditions for the mixing rate.

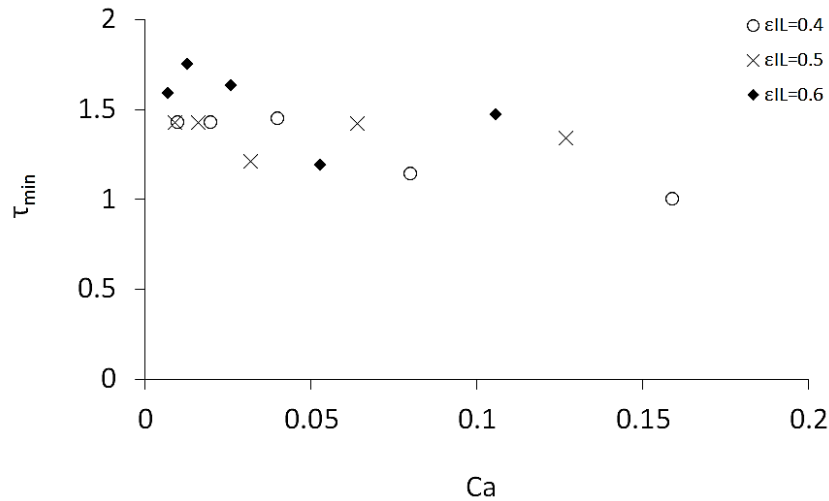


**Figure 5.17:** Minimum of non-dimensional circulation time as a function of Ca number and for varying input ionic liquid volume fraction.

#### 5.4.1 Stagnation points and vortex length

As already discussed, another important parameter which affects the internal circulation in the plug and the circulation time is the position of the stagnation points of the vortices. These positions were determined by plotting the average horizontal velocity components ( $u_x$ ) relative to the plug velocity as a function of the plug width; the position of the stagnation point in the upper and bottom half of the plug is determined from the point where the lines intersect the horizontal axis (**Figure 5.18**). In **Figure 5.18** the effect of the plug length (by changing the ionic liquid volume fraction) on the location of the stagnation points at constant mixture velocity ( $u_{mix}=0.01 \text{ m s}^{-1}$ ) is shown for the 1 mm ID channel. It can be seen that as the length of the plug increases the stagnation points approach the centreline of the channel. However, it is seen that by increasing the plug length more than 3.1 mm the location of the stagnation points do not shift further. In all cases the positions of the stagnation points for the upper and lower half of the plug appear fairly symmetric.

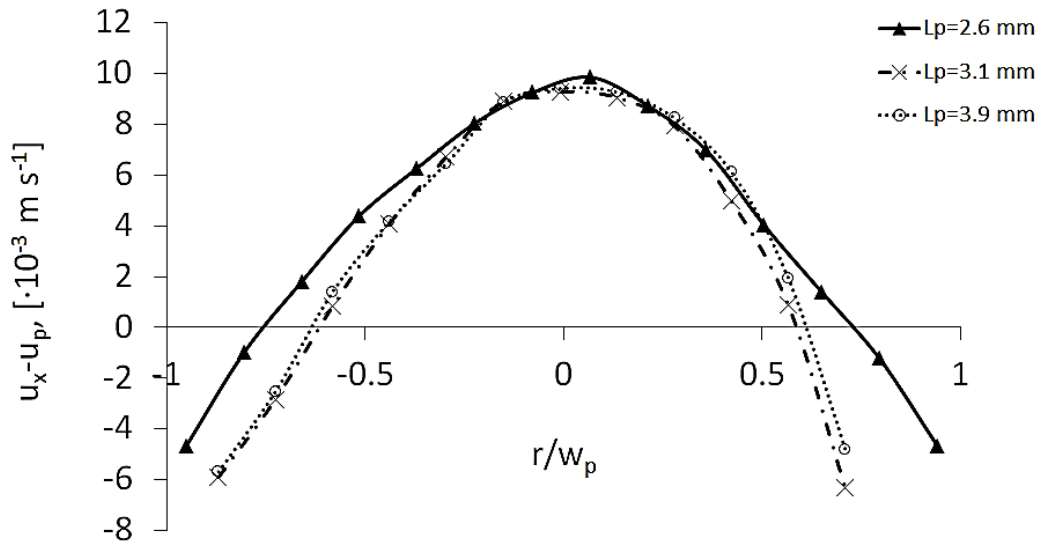


**Figure 5.18:** Horizontal velocity component,  $u_x$ , relative to the plug velocity,  $u_p$ , as a function of the dimensionless radius of the plug for different plug lengths at mixture velocity of  $0.01 \text{ m s}^{-1}$  ( $Q_{\text{mix}}=28.3 \text{ cm}^3 \text{ h}^{-1}$ ) for the estimation of the location of the stagnation point.

For constant plug length ( $L_p=2.6 \text{ mm}$ ) the position of the stagnation points seems to be only slightly affected by mixture velocity ( $u_{\text{mix}}$ ) (**Figure 5.19**). The location of the stagnation points found experimentally were compared with the Eq. (2.2.20) (Thulasidas et al., 1997). In the case of constant mixture velocity (**Figure 5.18**) the location of the stagnation point was predicted with an average error of 9% for the three plug lengths. The lowest error was observed in the case of the shortest plug length of 2.6 mm (error of 1.7%). However, for constant plug length ( $L_p=2.6 \text{ mm}$ ) it was found that Eq (2.2.20) was unable to predict the location of the stagnation as the mixture velocity was increased. Deviations from the experimental results can be attributed to the fact that the equation does not take into account plug length or film thickness. The non-dimensional maximum vortex length ( $l^*$ ) (which is the ratio of the length of the longest vortex in the upper half over the length of the plug) was found to be higher at high velocity, indicating a higher mixing efficiency, because more of the plug material is recirculated, which is in agreement with the results from the non-dimensional circulation time in **Figure 5.13**.



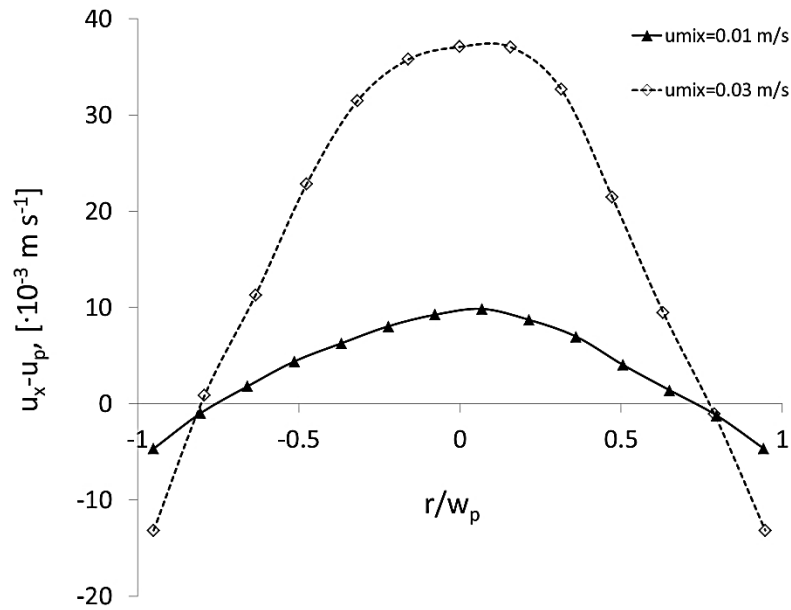


**Figure 5.19:** Horizontal velocity component  $u_x$  relative to the plug velocity as a function of the dimensionless radius of the plug ( $L_p = 2.6 \text{ mm}$ ).

## 5.5 Conclusions

Particle Image Velocimetry (PIV) was used to obtain velocity profiles in plugs with high accuracy and spatial resolution and in a non-intrusive manner. The mixing rate was locally quantified by means of the non-dimensional circulation time, which was calculated across the plug length. Consistently with the circulation patterns, the non-dimensional circulation time was found to have a profile along the direction of the flow that mirrors the shape of the plug, with a minimum at the axial location of the vortex cores, while it tended to infinity towards the front and the rear ends of the plug. Circulation time was found to be affected by different parameters, such as channel size, plug length, location of the stagnation points, and mixture velocity. It was found to increase as the channel size increased which suggests less efficient mixing. For increasing mixture velocities (i.e. increasing  $Ca$ ) and sufficiently long plugs ( $\varepsilon_{IL} = 0.4$ ) a general decrease (i.e. higher mixing rate) of the minimum circulation time was found, although the behaviour was rather complex. On the other hand, the circulation velocity linearly increased as the  $Ca$  number (mixture velocity) increased. The location of the stagnation points was also found to affect the circulation time. The location of the stagnation points was moving near the channel centreline as the length of the plug increased at constant mixture velocity. However, for constant plug length the location of the stagnation points was independent of mixture velocity. The mixing characteristics of the plugs within the different

channels will be used to explain the mass transfer performance of the extractor in the following chapter.

## Chapter 6.

# Liquid-liquid mass transfer using ionic liquids

### 6.1 Introduction

In this chapter the mass transfer during liquid-liquid plug flow in small channels is presented. The extraction of dioxouranium(VI) ions from nitric acid solutions into TBP/IL mixtures (**Table 3.2**), relevant to spent nuclear fuel reprocessing was investigated. A schematic of the experimental set-up used for the extraction of dioxouranium(VI) ions from nitric acid solutions by TBP dissolved in ionic liquids is depicted in **Figure 3.2** ([section 3.4](#)).

The effects of initial nitric acid concentration, residence time, flow rate ratio, mixture velocity, and ionic liquid type are discussed. In addition, the effects of scaling up on the mass transfer performance of the extractor are examined. The overall mass transfer coefficients ( $k_L a$ ) obtained for the three different channel sizes varied between 0.049 and 0.312 s<sup>-1</sup>. Finally, the possibility of industrial application of the intensified extraction units is discussed.

### 6.2 Extraction of dioxouranium(VI) at equilibrium

All equilibrium extractions were carried out at room temperature with 1:1 ionic liquid to aqueous phase ratio. The ionic liquid in its pure state absorbs a small amount of water depending on the initial nitric acid concentration that can vary from 17000 to 25000 ppm for 0.01 to 3 M nitric acid concentration, respectively. In the experiments a solution of 30% (v/v) TBP in ionic liquids was prepared and equilibrated with the nitric acid solution at the required concentration by mechanical shaking at various time lengths. Saturation was confirmed by measuring the viscosity for both pure and saturated ionic liquid with a digital Rheometer DV-III Ultra (Brookfield). It was found that the ionic liquid was saturated after about 45 min shaking. Then, the two phases were separated and the pre-equilibrated IL phase was brought

into contact with a fresh aqueous phase with the same nitric acid concentration, which also contained 0.05 M dioxouranium(VI) added in the form of dioxouranium(VI) nitrate hexahydrate. The concentration of nitric acid varied from 0.01 M to 3 M, while the initial concentration of dioxouranium(VI) in the aqueous phase was kept constant at 0.05M ( $\pm 4\%$ ). Mechanical shaking was applied for 3 hours before the two phases were separated. The dioxouranium(VI) concentration was measured in the aqueous and ionic liquid phase before and after the equilibration and was determined by UV-Vis spectroscopy (USB2000+, from Ocean Optics). Experiments were performed several times and a standard deviation of approximately 15% was calculated. The maximum error was found for low distribution coefficient  $K_U$  values, where the concentrations measured were very low.  $K_U$  is calculated from Eq. (6.2.1).

$$K_U = \frac{C_{aq,init} - C_{aq,eq}}{C_{aq,eq}} \quad (6.2.1)$$

The distribution coefficients,  $K_U$  are shown in **Figure 6.1** as a function of initial nitric acid concentration for TBP/[C<sub>4</sub>mim][NTf<sub>2</sub>] (30% v/v). As it can be seen the distribution coefficient is high at low nitric acids concentrations (0.01 M), decreases to its lowest level at [HNO<sub>3</sub>]<sub>aq,init</sub>=1 M, followed by an increase up to concentration of 3 M. Similar trends were found by other investigators as well (Giridhar et al., 2008, Billard et al., 2011b) for [C<sub>4</sub>mim][NTf<sub>2</sub>], even though some experimental details, i.e. dioxouranium(VI) concentration, temperature, and experimental procedure for phase preparation were not the same from one work to the other. The dioxouranium(VI) concentration used in this work is 0.05 M, while Giridhar et al. (Giridhar et al., 2008) and Billard et al. (Billard et al., 2011b) used concentration of  $4.2 \times 10^{-4}$  M and  $10^{-3}$  M (or  $10^{-2}$  M) respectively. Giridhar et al (Giridhar et al., 2008) found distribution coefficient values  $K_U$  of 15.3 and 0.7 at initial nitric acid concentrations 0.01 M and 1 M, respectively. At high initial nitric acid concentrations ([HNO<sub>3</sub>]<sub>aq,init</sub>), the extraction of uranium(VI) by the TBP/IL has been attributed to an ion exchange mechanism in which UO<sub>2</sub>(NO<sub>3</sub>)<sub>3</sub><sup>-</sup> anions are exchanged with the anion of the ionic liquid i.e. NTf<sub>2</sub><sup>-</sup>. By contrast, at low [HNO<sub>3</sub>]<sub>aq,init</sub> values, the extraction mechanism strongly depends on the cationic part of the ionic liquid (Dietz and Stepinski, 2008).

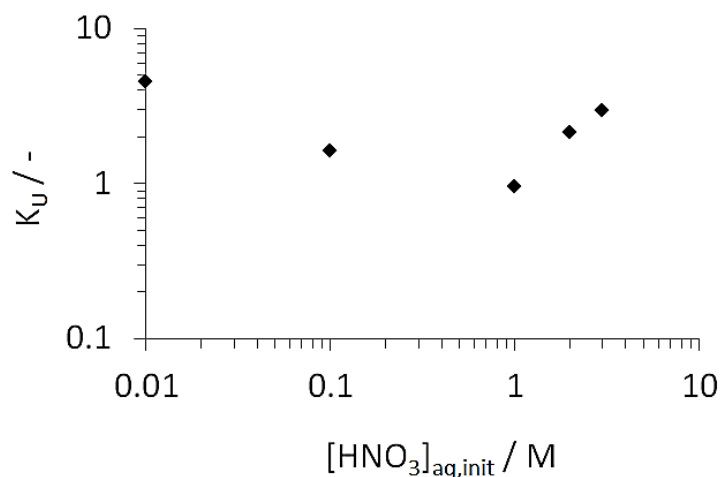


**Figure 6.1: Dioxouranium(VI) distribution coefficient  $K_U$  between a nitric acid aqueous solution and TBP/[C<sub>4</sub>mim][NTf<sub>2</sub>] (30% v/v) as a function of initial nitric acid concentration**

The UV-Vis aqueous phase absorption spectra of dioxouranium(VI) solution before and after the extraction are depicted in **Figure 6.2**. The initial dioxouranium(VI) solutions show characteristic absorption bands similar to those described in the literature for dioxouranium(VI) ions in aqueous solutions (Wang et al., 2009). As it can be seen, the shifts in the absorption peaks with nitric acid concentration are negligible, i.e. the peak at 414 nm with 0.01 M nitric acid has shifted to 415 nm and to 416 nm as the nitric acid concentration is increased to 1 M and 3 M, respectively. This slight shift is probably due to the formation of dioxouranium(VI) nitrate complexes in the acid solution (Wang et al., 2009).

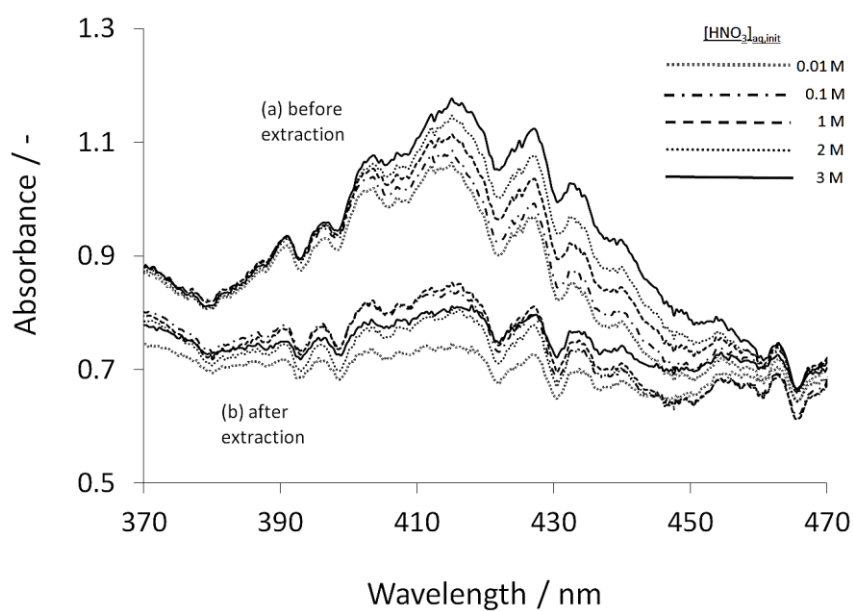


**Figure 6.2: UV-Vis aqueous phase spectra of dioxouranium(VI) (a) before and (b) after the extraction with different nitric acid concentrations.**

A comparison of the dioxouranium(VI) extraction coefficients ( $K_U$ ) as a function of initial nitric acid concentration for the different TBP/ionic liquid (30% v/v) systems, i.e. TBP/[C<sub>4</sub>mim][NTf<sub>2</sub>], TBP/[C<sub>10</sub>mim][NTf<sub>2</sub>], TBP/[P<sub>66614</sub>][NTf<sub>2</sub>] is shown in **Figure 6.3**.

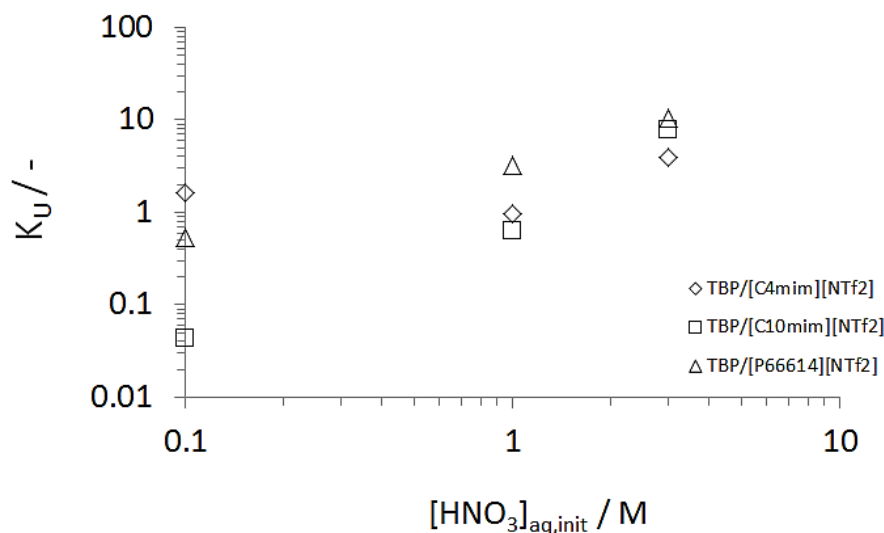


**Figure 6.3:** Dioxouranium(VI) distribution coefficients ( $K_U$ ) between a nitric acid solution and different TBP/IL (30% v/v) systems as a function of initial nitric acid concentration,  $[HNO_3]_{aq,init}$ .

It can be observed that the distribution coefficients for the different ionic liquid systems differ at low acidities, while they converge as the  $[HNO_3]_{aq,init}$  increases. This suggests that at low acidities the extraction is cation-dependent, while at high acidities the cationic part of the ionic liquid does not play an important role on the extraction of uranium(VI).

Comparing the two imidazolium-based ionic liquids, i.e. [C<sub>4</sub>mim][NTf<sub>2</sub>] and [C<sub>10</sub>mim][NTf<sub>2</sub>], it can be seen that they follow different curves. In particular, the [C<sub>4</sub>mim][NTf<sub>2</sub>] distribution coefficient is high at low nitric acid concentration of 0.1 M, decreases to its lowest level at  $[HNO_3]_{aq,init}=1$  M and then increases up to concentration of 3 M. In the case of [C<sub>10</sub>mim][NTf<sub>2</sub>],  $K_U$  increases with increasing initial nitric acid concentration for the whole range of concentrations investigated. Higher distribution coefficients are obtained in the case of the TBP/[C<sub>10</sub>mim][NTf<sub>2</sub>] system for initial nitric acid concentration above 1 M. It is worth noting here that the error of the measurements (15%) does not affect the trend of the distribution coefficients ( $K_U$ ). Dioxouranium(VI) extraction at low acidities is dependent on the alkyl chain length of the ionic liquid. As the alkyl chain is increased from butyl to decyl, the  $[HNO_3]_{aq,init}$  value at which the mechanism changes from cation-dependent to cation-independent decreases. By changing from [C<sub>4</sub>mim]<sup>+</sup> to [C<sub>10</sub>mim]<sup>+</sup>, there is a decrease in the

ionic liquid cation solubility in the aqueous phase, so that the cation exchange mechanism is dominant for a narrower range of acidities. This phenomenon was also observed by Dietz and Stepinski (Dietz and Stepinski, 2008) who investigated the extraction of dioxouranium(VI) into TBP dissolved in various  $[C_n\text{mim}][\text{NTf}_2]$  solvents ( $n=5, 8$ , and  $10$ ). As also reported by Billard et al. (Billard et al., 2011a), the value of  $[\text{HNO}_3]_{\text{aq,init}}$  at which the mechanism changes, varies from  $0.02\text{ M}$  for  $[\text{C}_{10}\text{mim}][\text{NTf}_2]$  to  $1.5\text{ M}$  for  $[\text{C}_4\text{mim}][\text{NTf}_2]$ . However, we were not able to observe this change in the case of  $[\text{C}_{10}\text{mim}][\text{NTf}_2]$ , since the starting initial nitric acid concentration for these experiments is  $0.1\text{ M}$ . With respect to **Figure 6.3**, it can be concluded that  $[\text{C}_{10}\text{mim}][\text{NTf}_2]$  would be suitable for both extraction and stripping processes. This is because the distribution coefficient varies from very low to high values (usually above unity) as a function of initial nitric acid concentration. Large distribution coefficients favour extraction while low ones favour stripping.

### 6.3 Continuous extraction of dioxouranium(VI) in small channels

The extraction experiments were carried out in circular channels with different internal diameters, i.e.  $0.5$ ,  $1$ , and  $2\text{ mm}$ , whilst the lengths varied from  $10$  to  $31.5\text{ cm}$ . Experiments were performed for total volumetric flow rates ( $Q_{\text{mix}}$ ) varying from  $7$  to  $340\text{ cm}^3\text{ h}^{-1}$ , and flow rate ratios ( $Q_{\text{IL}}/Q_{\text{HNO}_3}$ ) varying from  $0.25$  to  $1$ . At all experimental conditions plug flow was established with the aqueous phase ( $\text{HNO}_3$ ) flowing as non-continuous (dispersed) plugs within the TBP/IL phase (continuous) which was in contact with the channel wall. Extraction experiments were repeated several times with an overall mean relative error of the measurements of % of extracted material (Eq. (6.2.2)) of  $6.4\%$ . The extraction efficiency ( $\%E_{\text{eff}}$ ) of the system, which is the ratio of the amount of the species transferred to the maximum amount transferable, is calculated from Eq. (6.2.3) and the overall mean relative error of the measurements was less than  $7\%$ . In addition, the overall volumetric mass transfer coefficient ( $k_L\alpha$ ) was determined from Eq. (6.2.4) with an overall mean relative error of  $8.2\%$ .

$$\%E = \frac{[c]_{\text{aq,init}} - [c]_{\text{aq,fin}}}{[c]_{\text{aq,init}}} \quad (6.2.2)$$

$$\%E_{\text{eff}} = \frac{[c]_{\text{aq,fin}} - [c]_{\text{aq,init}}}{[c]_{\text{aq,eq}} - [c]_{\text{aq,init}}} \quad (6.2.3)$$

$$k_L \alpha = \frac{1}{\tau_{re}} \ln \left( \frac{[c]_{aq,eq} - [c]_{aq,init}}{[c]_{aq,eq} - [c]_{aq,fin}} \right) \quad (6.2.4)$$

### 6.3.1 Effect of initial nitric acid concentration on dioxouranium(VI) extraction in small channels

The dioxouranium(VI) extraction (%E) from the nitric acid solutions into TBP/IL (30% v/v) in the 0.5 mm ID microchannel is plotted in **Figure 6.4**. The total volumetric flow rate was  $Q_{mix}=14.6 \text{ cm}^3 \text{ h}^{-1}$  and the ratio of IL to aqueous phase was 1. The length of the microchannel was 10 cm. As it can be seen, with increasing nitric acid concentration the extraction of dioxouranium(VI) decreases until 1 M and then increases again. The highest conversion (~64%) is achieved at the lowest nitric acid concentration, i.e.  $[\text{HNO}_3]_{aq,init}=0.01 \text{ M}$ .

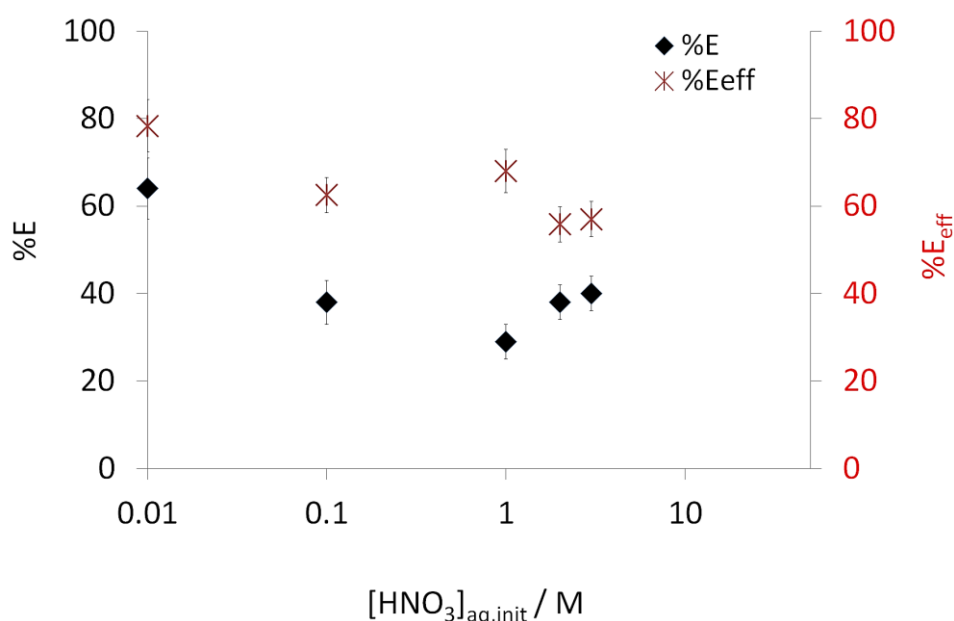


**Figure 6.4:** Dioxouranium(VI) extraction (%E) and extraction efficiency (%E<sub>eff</sub>) as a function of initial nitric acid concentration into TBP/[C<sub>4</sub>mim][NTf<sub>2</sub>] (30% v/v) in a 10 cm capillary.

The extraction efficiency (%E<sub>eff</sub>), however, does not follow the same trend. Within the 10 cm of the reactor (4.8 s residence time) the amount extracted reaches 78% of the equilibrium value for nitric acid concentration of 0.01 M and is followed by a reduction for 0.1 M, while it is slightly increased for 1 M to 61%. The initial decrease from 0.01 to 0.1 M is expected since the driving force (concentration difference from equilibrium, **Figure 6.1**) is reduced. However, the increase from 0.1 to 1 M is not justified from the equilibrium trend (**Figure 6.1**), which shows a decrease in driving force with an increase in nitric acid concentration. At



nitric acid concentrations over 1 M the extraction efficiency decreases; the decrease from 1 to 2 M is not consistent with the equilibrium data. This difference in the trend between the extraction percentage and the extraction efficiency as a function of the initial nitric acid concentration, at concentration close to 1 M can be attributed to the change of the extraction mechanism. It has been proposed that the mechanism of uranium(VI) extraction changes with nitric acid concentration from cation exchange at low concentrations to anion exchange at high ones (Billard et al., 2011b). Because of the change of mechanism different dioxouranium(VI) complexes form that may have different mass transfer rates and can therefore affect the extraction efficiency.

A comparison between the three TBP/ionic liquid (30%, v/v) systems at different nitric acid concentrations is illustrated in **Figure 6.5**. As it can be seen, the %E of dioxouranium(VI) follows the same trend as the distribution coefficients (**Figure 6.3**) for each TBP/ionic liquid system. However, different trends are found though for the extraction efficiency (%E<sub>eff</sub>).

In the cases of [C<sub>10</sub>mim][NTf<sub>2</sub>] and [P<sub>66614</sub>][NTf<sub>2</sub>], the extraction efficiency increases with initial nitric acid concentration, following a similar trend to that observed for the %E and the distribution coefficient. The increase in %E<sub>eff</sub> is however higher for the phosphonium-based ionic liquid compared to the imidazolium-based one as opposed to %E. In contrast, for [C<sub>4</sub>mim][NTf<sub>2</sub>] the extraction efficiency remains almost constant for the whole range of [HNO<sub>3</sub>]<sub>aq,init</sub>. For all TBP/ionic liquid systems the highest efficiency is achieved at the highest initial nitric acid concentration, where the extraction mechanism is considered to be cation-independent.

The high extraction efficiencies for [C<sub>4</sub>mim][NTf<sub>2</sub>] compared to the other two ionic liquids suggest that mass transfer occurs faster in [C<sub>4</sub>mim][NTf<sub>2</sub>]. This could be due to the lower viscosity of [C<sub>4</sub>mim][NTf<sub>2</sub>] compared to the other ionic liquids which would favour mass transfer by diffusion. Aqueous plug and ionic liquid slug lengths were measured for all cases. The lengths of the plugs varied only slightly between 1.54 and 1.74 mm, while those of the slugs between 1.19 and 1.33 mm and do not have a significant effect on mass transfer. Furthermore, the studies (section 5.4) of circulation time within the nitric acid plugs show that  $\tau$  is generally lower in [C<sub>4</sub>mim][NTf<sub>2</sub>] compared to [C<sub>10</sub>mim][NTf<sub>2</sub>] and [P<sub>66614</sub>][NTf<sub>2</sub>], suggesting that circulation and mixing are slightly faster for [C<sub>4</sub>mim][NTf<sub>2</sub>] which will also improve mass transfer rates (see **Figure 5.15**).

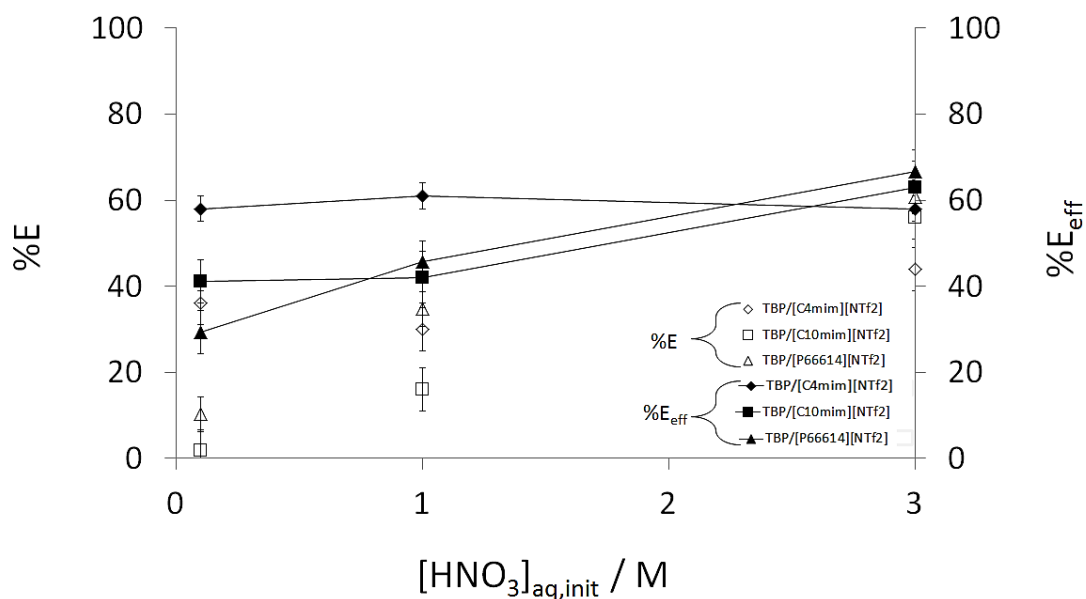


**Figure 6.5: Dioxouranium(VI) extraction (%E) and extraction efficiency (%E<sub>eff</sub>) as a function of initial nitric acid concentration into different TBP/IL (30% v/v) systems in a 10 cm capillary. The lines are used just to aid interpretation.**

### 6.3.2 Effects of residence time on dioxouranium(VI) extraction in small channels

To study the effects of residence time on dioxouranium(VI) extraction, experiments were conducted for different channel lengths, ranging from 10 to 31.5 cm at the same total volumetric flow rate,  $Q_{\text{mix}}=14.6 \text{ cm}^3 \text{ h}^{-1}$ , and ionic liquid to aqueous phase flow rate ratio of 1 for initial nitric acid concentration varying from 0.01 to 3 M. Changes in the mixture velocity would alter the hydrodynamic characteristics of the two phase flow, such as plug length and circulation patterns (as shown in [chapter 5](#)), which also affect mass transfer.

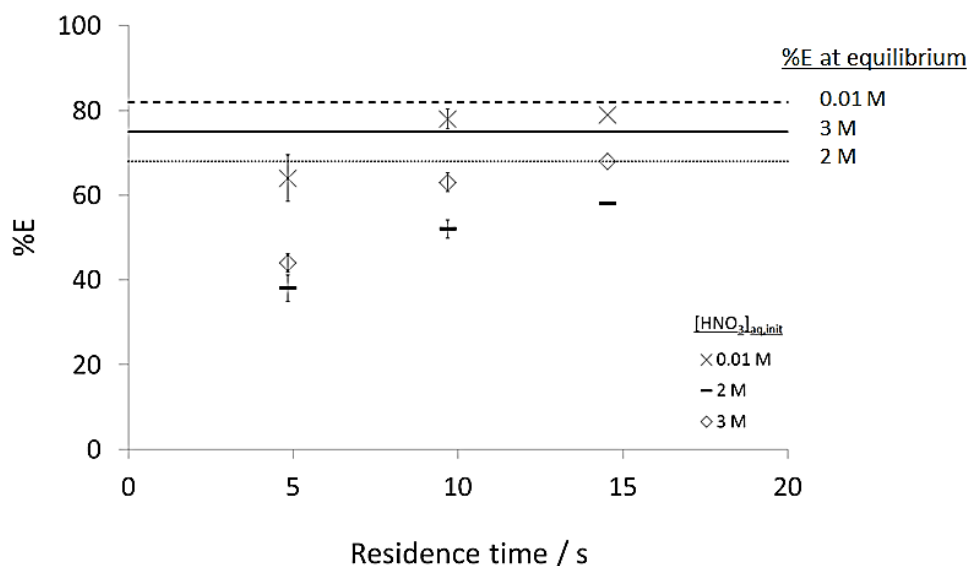


**Figure 6.6:** Dioxouranium(VI) extraction (%E) as a function of residence time from different nitric acid solutions into TBP/[C<sub>4</sub>mim][NTf<sub>2</sub>] (30%, v/v). Lines correspond to dioxouranium(VI) %extraction at equilibrium at 3 different initial nitric acid concentrations.

As it can be seen in **Figure 6.6**, the extraction of dioxouranium(VI) increases by increasing the residence time. At initial nitric acid concentration of 0.01 M, the extraction of dioxouranium(VI) reaches 95% of the equilibrium value in 9.7 s, while in the cases of  $[\text{HNO}_3]_{\text{aq,init}}=2$  M and  $[\text{HNO}_3]_{\text{aq,init}}=3$  M within 14.5 s it reaches 85% and 91% of the equilibrium value, respectively. This is in agreement with the results shown in **Figure 6.4** for the 10 cm channel where concentrations closer to equilibrium were achieved for the  $[\text{HNO}_3]_{\text{aq,init}}=0.01$  M compared to 2 M and 3 M (lower %E<sub>eff</sub>).

In **Figure 6.7** the UV-Vis spectra of the dioxouranium(VI) species extracted by the TBP/[C<sub>4</sub>mim][NTf<sub>2</sub>] (30%, v/v) are shown at different residence times and at equilibrium (3 h). As the residence time is increased, the absorption spectra approach the equilibrium limit. There is a slight shift of the most intense peaks compared to the absorption spectra of the dioxouranium(VI) species in the nitric acid solutions (see **Figure 6.2**). A shift to longer wavelengths in the absorption peaks of dioxouranium(VI) ions in ionic liquids with TBP and CMPO was also reported by Visser and Rogers ([Visser and Rogers, 2003](#)) and was attributed to the chemical environment in the ionic liquid which favours the formation of a dioxouranium(VI) nitric acid complex and thus causes red-shift.

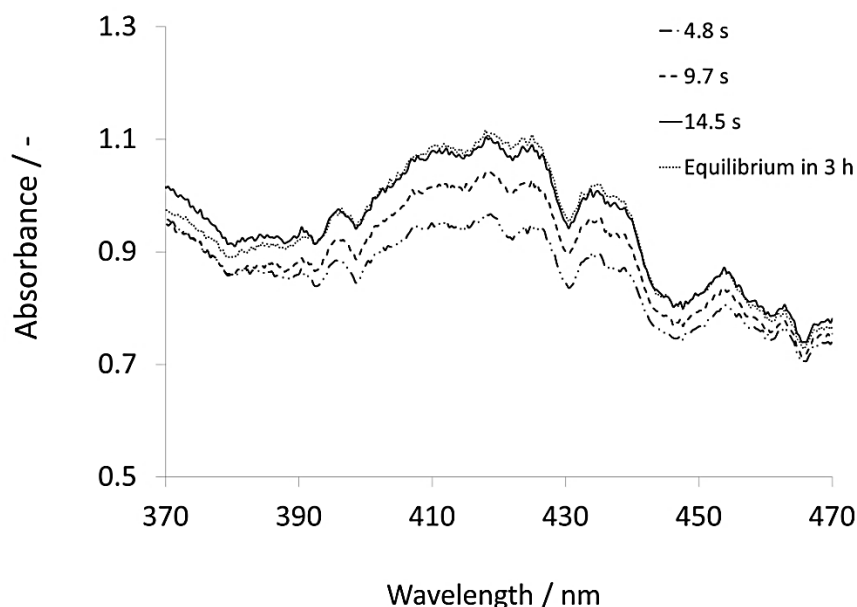


**Figure 6.7:** Absorption spectra of dioxouranium(VI) in TBP/[C<sub>4</sub>mim][NTf<sub>2</sub>] (30% v/v) extracted from a 3 M nitric acid solution at different residence times in a 0.5 mm ID channel and at equilibrium after 3 h of mechanical shaking.

In **Figure 6.8** the effect of residence time for 3 different types of TBP/ionic liquid mixtures (30%, v/v) at constant nitric acid concentration of 3 M, at flow rate ratio equal to 1 is shown. It is observed that by increasing the residence time, the dioxouranium(VI) extraction also increases. As mentioned earlier, within 14.5 s, the extraction of dioxouranium(VI) reaches 91% of the equilibrium value for [C<sub>4</sub>mim][NTf<sub>2</sub>], while in the cases of [C<sub>10</sub>mim][NTf<sub>2</sub>] and [P<sub>66614</sub>][NTf<sub>2</sub>] it reaches 84% and 88% of the equilibrium value, respectively. Within 9.7 s, it can be seen that for each case the dioxouranium(VI) extraction reaches almost 80% of the equilibrium value. The largest increase in %E was found for the less viscous TBP/ionic liquid system.

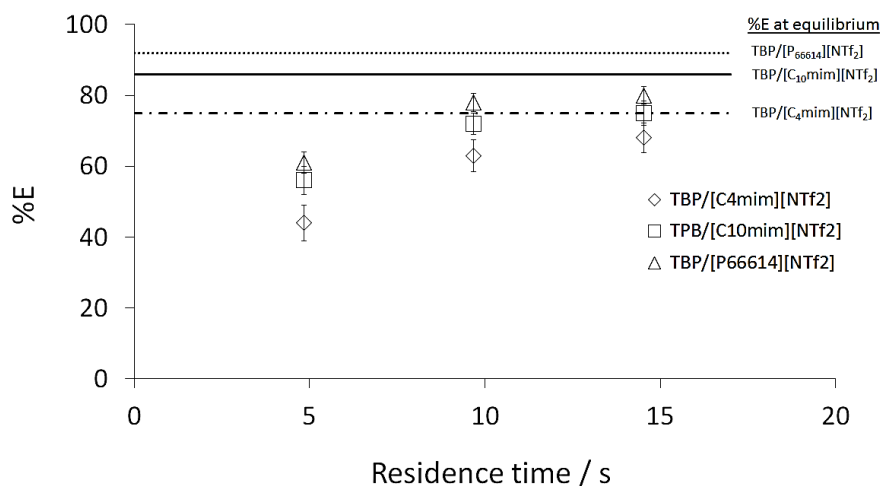


**Figure 6.8: Dioxouranium(VI) extraction (%E) as a function of residence time from nitric acid solutions of 3 M into different TBP/IL (30%, v/v) systems. Lines correspond to dioxouranium(VI) %extraction at equilibrium into the three different ionic liquids.**

### 6.3.3 Effects of flow rate ratio on dioxouranium(VI) extraction

The effect of the phase flow rate ratio on the dioxouranium(VI) extraction in the 0.5 mm ID channel is shown in **Figure 6.9**. For these experiments the total volumetric flow rate ( $Q_{\text{mix}}$ ) was kept constant at  $14.6 \text{ cm}^3 \text{ h}^{-1}$ , while the ratio of TBP/IL mixture to the aqueous phase was varied from 0.25 to 1. According to the stoichiometry of the reaction even in the case of 0.25 phase ratio, TBP is still in excess for the extraction of dioxouranium(VI) from the nitric acid solution. The length of the microchannel was 10 cm. The corresponding flow patterns were recorded and two indicative pictures (for extraction with 3 M nitric acid concentration) for the lowest and highest ratio i.e. 0.25 and 1 are shown in **Figure 6.9**, for initial nitric acid concentrations 1 M and 3 M. The length of the plugs varied from 1.61 mm to 3.65 mm as the phase ratio decreased from 1 to 0.25. It is evident that by decreasing the ratio from 1 to 0.25 the dioxouranium(VI) %E also decreases for both cases which is attributed to the decrease in interfacial area available for mass transfer. Considering two hemispherical caps in the front and back end of the plug the interfacial area depending on the Ca number can be calculated from (Di Miceli Raimondi et al., 2008):

$$\alpha_p = \frac{\pi w_p(L_p - w_p) + \pi w_p^2}{L_{UC} w_{ch}^2} \quad \text{for } Ca > 0.04 \quad (6.2.5)$$

$$\alpha_p = \frac{4w_p(L_p - w_p) + \pi w_p^2}{L_{UC} w_{ch}^2} \quad \text{for } Ca < 0.04 \quad (6.2.6)$$

For initial nitric acid concentration of 3 M the decrease of %E with flow rate ratio is more obvious than for 1 M maybe as a result of the change of the extraction mechanism; the mass transfer at 3 M is more dependent on the mixing of the transferred species within a phase and the kinetics of the complex formation than on interfacial area.

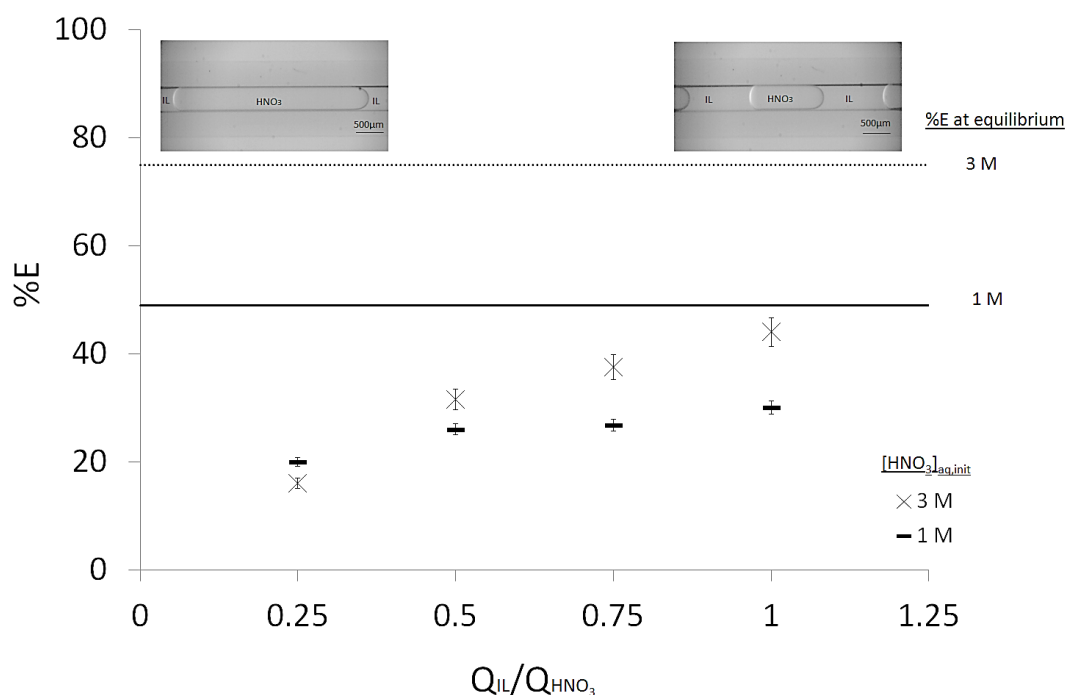


**Figure 6.9: Dioxouranium(VI) extraction (%E) as a function of phase flow rate ratio from nitric acid solutions into TBP/[C<sub>4</sub>mim][NTf<sub>2</sub>] (30%, v/v). Horizontal lines corresponds to dioxouranium(VI) extraction at equilibrium.**

### 6.3.4 Effects of channel size on the mass transfer performance

The extraction of dioxouranium(VI) ions from nitric acid solutions (3 M) by TBP/[C<sub>4</sub>mim][NTf<sub>2</sub>] (30%, v/v) in channels with different diameters (0.5–2 mm), was measured for different residence times, flow rate ratios, and mixture velocities, with a mean relative error of 4.3%. To study the effects of residence time (i.e.  $\tau = V_{ch}/Q_{mix}$ ) on mass transfer at the different channel sizes, the channel length was varied from 10.5 to 31.5 cm. In **Figure 6.10** the extraction efficiency (%E<sub>eff</sub>) of dioxouranium(VI) is plotted against the residence time at a constant mixture velocity of 0.03 m s<sup>-1</sup> for equal flow rates of the two

phases. As the residence time increases, the  $\%E_{\text{eff}}$  also increases at all channel sizes. An extraction efficiency of  $>90\%$  is achieved in the case of the 0.5 mm ID channel in less than 11 s, whilst in the 1 mm ID and the 2 mm ID channels for the same time interval the  $\%E_{\text{eff}}$  was  $<70\%$  and  $<40\%$ , respectively. It is worth noticing that a significant percentage of mass transfer occurs within the first 10 cm of the channel which includes the plug formation region as well. Significant mass transfer at the inlet region has also been observed by Tan et al. (Tan et al., 2012) for gas-liquid systems. Depending on the channel size the increase in the extraction efficiency follows a different trend. In the 0.5 mm ID channel an increase of  $\sim 70\%$  on the  $\%E_{\text{eff}}$  is observed in a period of 7 s (from 4 to 11 s), whilst in the 1 mm and 2 mm ID channels for the same time interval the increase on the  $\%E_{\text{eff}}$  is  $\sim 62\%$  and  $\sim 33\%$ , respectively. The short diffusional distances in the small channels improve mass transfer. Moreover, as the channel size decreases, the mixing becomes more intense within the aqueous plugs, since for the same conditions the plug size is shorter (see **Figure 4.11**) and the circulation faster (see **Figure 5.14**). The intense mixing enhances the mass transfer due to convection, and renews the interface between the two phases, thus increasing the concentration gradients which improve the diffusive penetration of the transferred species. In addition, a decrease in plug size with decreasing channel size at the same mixture velocity results in more plugs and increase the interfacial area available for mass transfer.

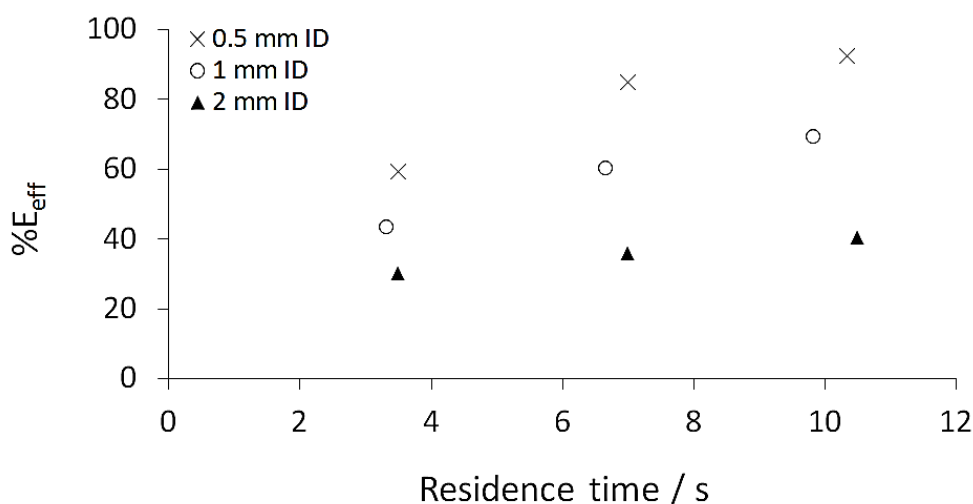


**Figure 6.10:** Extraction efficiency ( $\%E_{\text{eff}}$ ) of dioxouranium(VI) into TBP/[C<sub>4</sub>mim][NTf<sub>2</sub>] (30%, v/v) as a function of the residence time at constant mixture velocity ( $u_{\text{mix}} = 0.03 \text{ m s}^{-1}$ ) in the 3 different channels.

The effect of mixture velocity on extraction efficiency can be seen in **Figure 6.11** for the three different channel sizes. The length of the channels was in all cases equal to  $L_{\text{ch}} = 10.5$

cm. The results illustrate that for a given channel size, as the mixture velocity increases, the extraction efficiency decreases, and that for the same mixture velocity the extraction efficiency is always higher as the channel size decreases.

An increase in mixture velocity decreases the residence time available for mass transfer. At the same time, as the mixture velocity increases, the recirculation time within the plugs decreases and consequently the mixing becomes more intense (see **Figure 5.17**). In addition, the specific interfacial area available for mass transfer also increases with mixture velocity, since the length of the plug decreases (see **Figure 4.11**). For example, in the case of 0.5 mm ID channel there is an increase of ~45% on the interfacial area available for mass transfer from mixture velocity of 0.01 to 0.06 m s<sup>-1</sup>, whilst the extraction efficiency falls about 55%. The same effect is observed for the two bigger channel sizes as well. However, as the mixture velocity increases, the decrease in residence time seems to overcome any increases in mass transfer from improved mixing within the plugs and increased interfacial area and the extraction efficiency reduces.

The decrease of the extraction efficiency with increasing mixture velocity follows a non-linear trend. The extraction efficiency at high mixture velocities, i.e. 0.05 m s<sup>-1</sup> and 0.06 m s<sup>-1</sup> does not change significantly in the case of the 0.5 and the 1 mm ID channel. Interestingly, even though the residence time is quite short at these mixture velocities (~2 s for 0.05 m s<sup>-1</sup> and ~1.7 s in the case of 0.06 m s<sup>-1</sup>) the extraction efficiency still reaches 40 % and 30% for the 0.5 mm ID channel and the 1 mm ID channel, respectively.

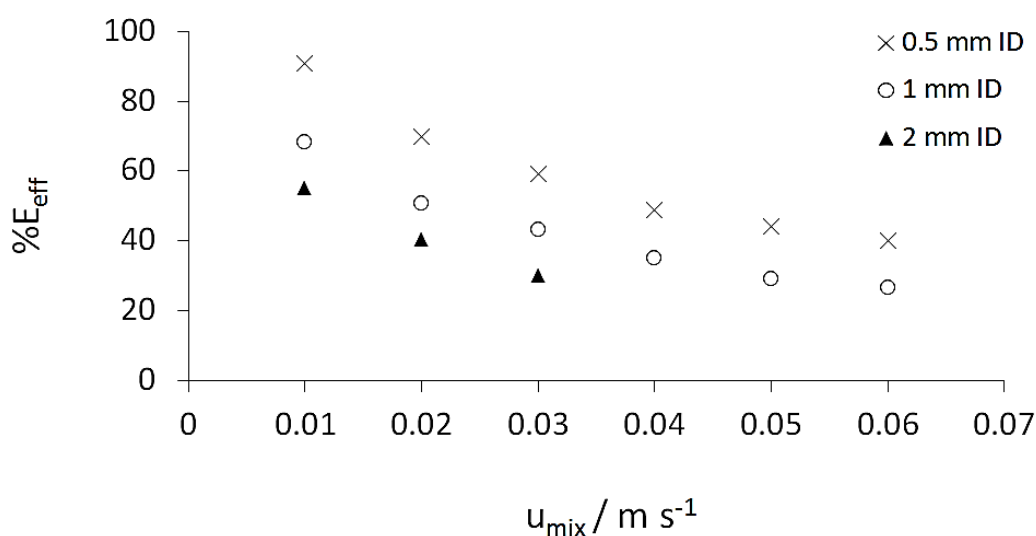


**Figure 6.11:** Extraction efficiency (%E<sub>eff</sub>) of dioxouranium(VI) into TBP/[C<sub>4</sub>mim][NTf<sub>2</sub>] (30%, v/v) as a function of the mixture velocity ( $L_{\text{ch}}$ =10.5 cm). (mean relative error 4.3%)



## 6.4 Volumetric mass transfer coefficients

### 6.4.1 Effect of initial nitric acid concentration on $k_L\alpha$

The volumetric mass transfer coefficients ( $k_L\alpha$ ) were determined from Eq (6.2.4) during plug flow at different initial nitric acid concentrations and residence times at flow rate ratio from 0.25 to 1 for the three different types of TBP/IL mixtures (30%, v/v). In **Figure 6.12** the mass transfer coefficients in the 0.5 mm ID channel are shown as a function of initial nitric acid concentration for experiments performed in the shortest (10 cm long) channel. The total volumetric flow rate was  $Q_{\text{mix}}=14.6 \text{ cm}^3 \text{ h}^{-1}$ , and the flow rate ratio was equal to 1. The mass transfer coefficients increase with increasing nitric acid concentration for  $[\text{C}_{10}\text{mim}][\text{NTf}_2]$  and  $[\text{P}_{66614}][\text{NTf}_2]$ , while they remain almost constant for  $[\text{C}_4\text{mim}][\text{NTf}_2]$ . At the highest nitric acid concentration, where the largest  $k_L\alpha$  are achieved, the transfer mechanism is cation-independent.

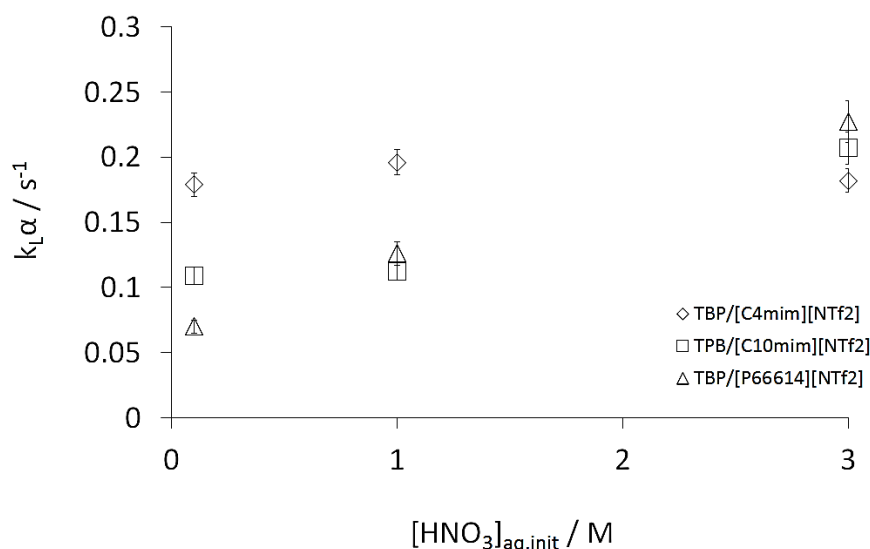


**Figure 6.12:** Total volumetric mass transfer coefficient ( $k_L\alpha$ ) as a function of  $[\text{HNO}_3]_{\text{aq,init}}$  in the 0.5 mm ID channel ( $L_{\text{ch}}=10 \text{ cm}$ ). Symbols correspond to the three different ionic liquids.

In **Table 6.1** the overall volumetric mass transfer coefficients as a function of IL to aqueous phase ratio at initial nitric acid concentrations of 1 M and 3 M in a 10 cm microchannel for the case of  $\text{TBP}/[\text{C}_4\text{mim}][\text{NTf}_2]$  (30%, v/v) are shown. As the ratio decreases from 1 to 0.25  $k_L\alpha$  also decreases. As was discussed in [section 6.3.3](#) a decrease in the phase ratio decreases the interfacial area available for mass transfer (**Figure 6.9**) which leads to a decrease of the mass transfer.

**Table 6.1: Volumetric mass transfer coefficient ( $k_L\alpha$ ) as a function of IL (TBP/[C<sub>4</sub>mim][NTf<sub>2</sub>] (30%, v/v)) to aqueous phase ratio at initial nitric acid concentration of 1 M and 3 M in a 0.5 mm ID channel ( $L_{ch}$ =10 cm).**

IL to aqueous flow rate ratio	$k_L\alpha$ at $[\text{HNO}_3]_{\text{aq,init}} / \text{s}^{-1}$	
	1 M	3 M
1	0.196	0.182
0.75	0.163	0.143
0.5	0.156	0.112
0.25	0.108	0.049

#### 6.4.2 Effect of residence time on $k_L\alpha$

The overall mass transfer coefficients ( $k_L\alpha$ ) were also determined for the three different types of TBP/IL mixtures (30%, v/v) as a function of residence time at constant nitric acid concentration (3 M) and are shown in **Figure 6.13**. As it can be seen, the mass transfer coefficients in general were quite similar in the first 10 s. The extraction efficiency ( $E_{\text{eff}}$ ) in this time period was below 70%. The decrease of the volumetric mass transfer coefficient as a function of the residence time can be explained by the decrease in the driving force (i.e. difference in concentration from the equilibrium concentration which decreases as the residence time increases).

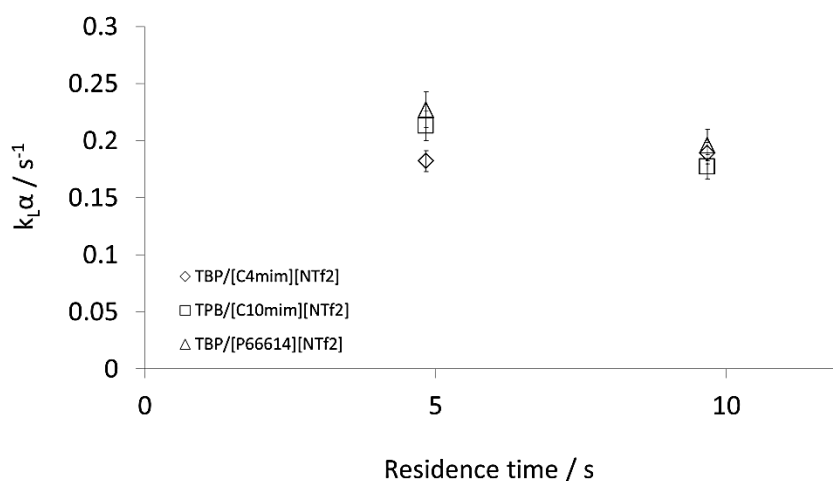


**Figure 6.13: Total volumetric mass transfer coefficient ( $k_L\alpha$ ) as a function of residence time at  $[\text{HNO}_3]_{\text{aq,init}}$ =3 M. Symbols correspond to the three different ionic liquids.**

In all the above cases the mass transfer coefficients varied between  $0.049 \text{ s}^{-1}$  and  $0.23 \text{ s}^{-1}$ . These are comparable to the values found in other plug flow microchannel mass transfer units (Dessimoz et al., 2008, Ghaini et al., 2010, N. Kashid et al., 2011), whilst they are higher than those found in conventional contactors (see Table 2.4) (Fernandes and Sharma, 1967, Verma and Sharma, 1975).

### 6.4.3 Effect of channel size

The volumetric mass transfer coefficients were calculated for different channel sizes and as it can be seen in Figure 6.14, for a constant channel length of 10.5 cm an increase in the mixture velocity leads to an increase of the  $k_L\alpha$  in all channel sizes. As discussed above, an increase in mixture velocity intensifies the mixing within the plugs and increases the interfacial area available for mass transfer. In addition, the mass transfer coefficients reduce as they channel size increases. This is attributed to more intense mixing and an increase in interfacial area as the channel size decreases. For example, for  $u_{\text{mix}}=0.01 \text{ m s}^{-1}$ , the specific interfacial area decreases by about 66% by increasing the channel size from 0.5 to 1 mm ID and 60% by increasing from 1 to 2 mm ID. At the same conditions, as it can be seen from Figure 6.14 the  $k_L\alpha$  decreases by about 50% from 0.5 to 1 mm ID, and about 33% from 1 to 2 mm ID.

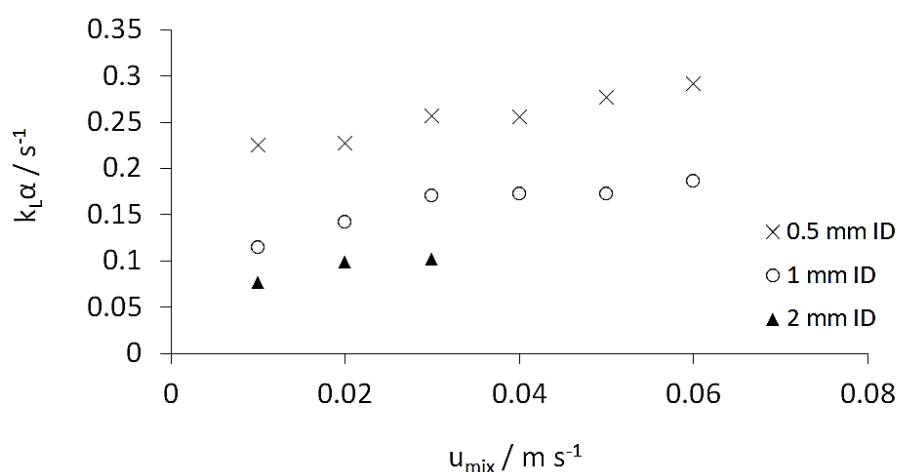


**Figure 6.14:** Mass transfer coefficient as a function of the mixture velocity for the 3 different channels and channel length  $L_{\text{ch}}=10.5 \text{ cm}$ . TBP/[C<sub>4</sub>mim][NTf<sub>2</sub>] (30%, v/v) used for the extractions.

However, when the mass transfer coefficients achieved at a constant residence time, different trends are observed for the different channel sizes as it can be seen in **Figure 6.15**. With increasing mixture velocity in the 0.5 mm ID channel the  $k_L\alpha$  increases, in the 1 mm ID channel it remains almost constant, while in the 2 mm ID channel it reduces. These differences are attributed to the different circulation pattern and mixing intensity ([section 5.4](#), **Figure 5.14**), as well as the film thickness and the plug length in the different channels.

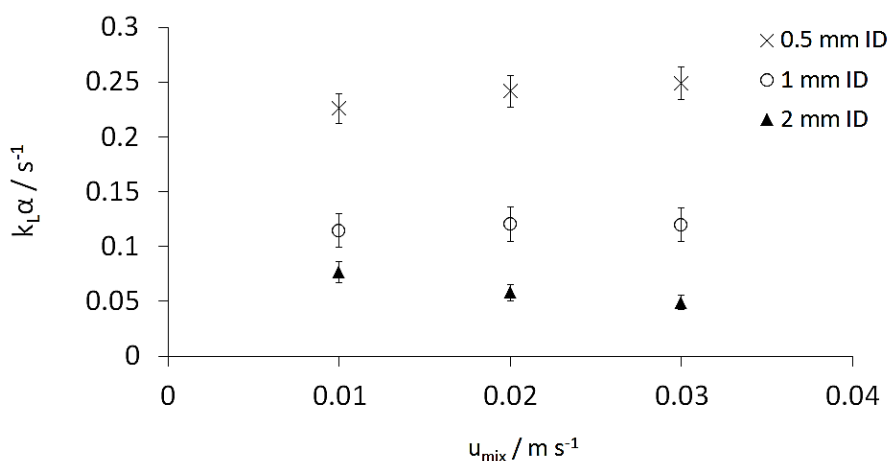


**Figure 6.15:** Mass transfer coefficient as a function of the mixture velocity for the 3 different channels at the same residence time ( $\sim 10$  s). TBP/[C<sub>4</sub>mim][NTf<sub>2</sub>] (30%, v/v) used for the extractions.

The evolution of  $k_L\alpha$  along the channel at a constant mixture velocity ( $u_{\text{mix}} = 0.03 \text{ m s}^{-1}$ ) also seems to depend on channel size (**Figure 6.16**). For these measurements the results from the different length channels (10, 20 and 30 cm) were used. For the 0.5 mm ID channel the mass transfer coefficient increases along the length of the channel until it reaches a maximum value and then decreases. The mass transfer coefficient reaches a value of  $0.24 \text{ s}^{-1}$  in the first 10 cm channel length, while it subsequently increases by 12.5% to  $0.27 \text{ s}^{-1}$ , followed by a decrease of 8 % to  $0.25 \text{ s}^{-1}$ , in the next 20 cm and 30 cm respectively. This indicates that most of the mass transfer is achieved between the mixing point of the two fluids and the first 10 cm of the separator. In contrast, in the 1 mm and the 2 mm ID channels the mass transfer coefficient decreases continuously along the separator after the first 10 cm.

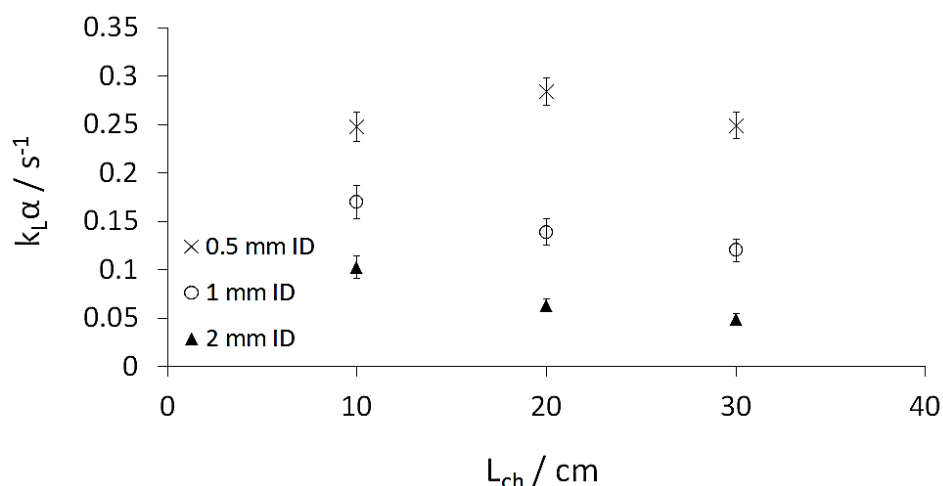


**Figure 6.16:** Mass transfer coefficient as a function of the channel length for the 3 different channels at constant mixture velocity  $u_{\text{mix}} = 0.03 \text{ m s}^{-1}$ . TBP/[C<sub>4</sub>mim][NTf<sub>2</sub>] (30%, v/v) used for the extraction.

In all cases and for similar conditions, a significant decrease of 50% in the mass transfer coefficients takes place when the channel size increases from 0.5 mm to 1 mm while after that by increasing the size further to 2 mm ID the decrease on the mass transfer coefficient is less, i.e. from 0.5 to 2 mm ID the decrease on  $k_L \alpha$  is 72%.

## 6.5 Scaling aspects of a liquid-liquid small scale extractor

The industrial application of intensified extraction units requires a good understanding of the hydrodynamics of the two-phase flow in the small channels of the units, the pressure drop, and the mass transfer rates together with accurate predictive models. To increase throughput in small scale devices, scale out (instead of scale up) is often used; this can however, require a prohibitively large number of channels. An alternative approach would be to increase the channel sizes enough, while still preserving the benefits of small scale operation, such as laminar flows and well defined, regular patterns. For successful application in nuclear reprocessing there should be sufficient interfacial area between the two phases to promote the desired transfer of the extractable components in all channels. In addition, the design of the extractor should be mechanically reliable and easy to maintain, reasonably compact, and have the flexibility to operate over a wide range of phase flow rates. Another important parameter that needs to be taken into account is the pressure drop.

The investigations of the hydrodynamics of plug flow in small channels revealed that the increase in channel size does not affect the flow patterns, and regular and well defined plug flow was observed for channel sizes from 0.5 to 2 mm ID. Correlations, based on experimental data derived from various channel sizes, have been developed and can predict reasonably well plug length, film thickness, and pressure drop. In addition, measurements of the mixing efficiency in these systems (quantified by the non-dimensional circulation time) revealed a decrease of 85% in non-dimensional circulation time as the internal diameter of the channel decreases from 2 to 0.5 mm ID (**Figure 5.14**). All these parameters are strongly related to the performance of a plug flow extractor. It was also found that the pressure drop decreases almost one order of magnitude by increasing the channel size from 0.5 to 2 mm ID at the same mixture velocity and channel length. Mass transfer coefficients were measured for the different channel sizes and the values varied between 0.05 to 0.3 s<sup>-1</sup>. It was found that by increasing the channel size from 0.5 mm to 2 mm ID an average decrease of 72% on  $k_L\alpha$  occurred. However,  $k_L\alpha$  even in the case of the 2 mm ID channel (0.07-0.11 s<sup>-1</sup>), are still higher than those of an agitated contactor or a packed bed column, while the interfacial area (830-1129 m<sup>2</sup> m<sup>-3</sup>) in the 2 mm ID channel is one order of magnitude higher (**Table 2.4**).

In a reprocessing plant, the irradiated spent fuel is dissolved in nitric acid solution (3 M) to give a solution with concentration of uranium(VI) approximately of 1 M (uranium(VI) is almost 95% of the spent fuel). The extraction percentage (%E) of dioxouranium(VI) at equilibrium, in the current ionic liquid-based system TBP/[C<sub>4</sub>mim][NTf<sub>2</sub>] (30%, v/v) is 78%. To achieve >99% extraction required industrially in a nuclear recycling plant, multi-stage extraction arranged in a counter-current way should be adopted. For >99% dioxouranium(VI) extraction, 4 stages are required. At the end of each stage the two phases are separated online and the HNO<sub>3</sub>/UO<sub>2</sub><sup>2+</sup> solution is fed to the next stage with fresh solvent as shown in **Figure 6.17**.

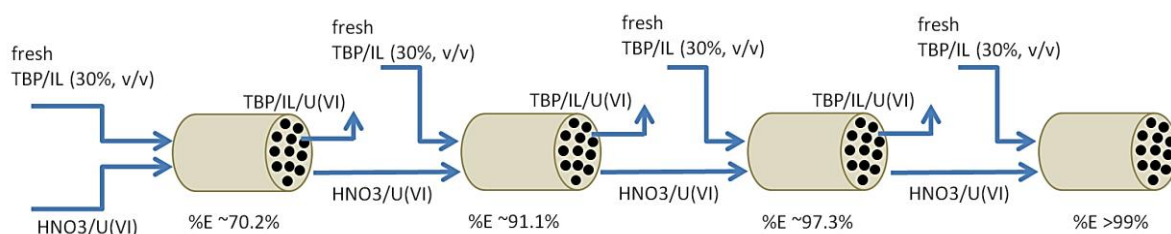


**Figure 6.17: Schematic of a 4 stage extraction.**

A number of parameters would need to be considered to optimise this configuration. These include among others, the channel size, pressure drop, and the %E<sub>eff</sub> achieved in each stage. The number of stages will also affect solvent degradation. As a base case per channel it is assumed that the two phase streams flow at a mixture velocity of 0.03 m s<sup>-1</sup>, >90% extraction efficiency is achieved per stage, and online separation is efficient. Considering the 3 channel sizes tested in this work for extractions the requirements for scale up are given in **Table 6.2**.

**Table 6.2: Conditions of solvent extraction capillaries for >90% extraction efficiency per stage.**

Attributes	0.5 mm ID	1 mm ID	2 mm ID
Flow rates per channel (cm <sup>3</sup> h <sup>-1</sup> )	11	43	170
Pressure drop per channel (kPa)	18.6 (L <sub>ch</sub> =30 cm)	11.6 (L <sub>ch</sub> =72 cm)	18.5 (L <sub>ch</sub> =285 cm)
Residence time (s)	10	24	95
Total liquid volume per channel (m <sup>3</sup> )	8.9·10 <sup>-6</sup>	5.6·10 <sup>-7</sup>	5.8·10 <sup>-8</sup>
Tonnes of spent fuel per year for 6 channels assembly	0.025	0.5	2.6

It can be seen that both 0.5 and 2 mm ID channels have almost the same pressure drop (i.e. 18.6 kPa), whilst the pressure drop in the 1 mm ID channel is 11.6 kPa. The residence time required for >90% extraction efficiency per stage increases as the channel size increases. It was found that >90% efficiency is possible in only 10 s in the case of 0.5 mm ID channel, and increases to 24 and 95 s as the channel size increases to 1 and 2 mm ID, respectively. It has been reported in the literature (Kashid et al., 2010) that numbering up can be efficiently achieved for up to six channels of 1 mm ID. The fluids were distributed using the same pump and introduced to the channels via a flow distributor. Kashid et al. (Kashid et al., 2010) found that the flow distribution between the six capillaries was almost identical and plug flow was established in all six channels as in the case of a single channel at the same conditions. This way hydrodynamic features and mass transfer performance of a single channel can be preserved with a 6-fold increased throughput. The continuous separation of organic and an

aqueous phase for total flow rates up to  $40 \text{ cm}^3 \text{ min}^{-1}$  using a hydrophobic membrane has been reported in the literature (Cervera-Padrell et al., 2012); however, no reported studies exist on phase separation during plug flow in high throughput systems. Gravity settlers or plate pack coalescers are commonly used to separate immiscible liquid phases when dealing with large production volumes. In this work it was found that liquid-liquid separation during plug flow was good using an in-house flow splitter for flow rates up to  $8 \text{ cm}^3 \text{ min}^{-1}$ . Online separation would eventually reduce the time and the costs, and will facilitate the online stripping of the ionic liquid phase to recycle the uranium(VI). In **Table 6.2** the amount of tonnes of spent fuel that can be reprocessed for an assembly of six channels is also shown. With the 2 mm ID channel an assembly of 6 channels would reprocess about 2.6 tonnes of spent fuel per year. The amount is reduced to 0.5 and 0.025 tonnes per year for assemblies of 1 and 0.5 mm ID channels, respectively.

These findings are compared with extraction units already in operation in spent nuclear reprocessing plants. A summary of three solvent extraction contactors that are currently employed in recycling plants with throughput of 5 tonnes per year (e.g. THORP, Sellafield, UK; UP3, Cap La Hague, France; and the Rokkasho Reprocessing Plant, RRP, Rokkasho Mura, Japan) as found in literature (Nash and Lumetta, 2011) is shown in **Table 6.3**.

**Table 6.3: Chemical engineering attributes of solvent extraction contactors typical for a nuclear recycling plant throughput of 5 tonnes/year (Nash and Lumetta, 2011)**

Attributes	Mixer settler	Pulsed column	Centrifugal contactor
<b>Dimension</b>	12m x 3m x 2m	12m high by 0.3m diameter	Contactor bank comprising 12 units each 20 cm diameter and 40 cm high
<b>Residence time</b>	18 hours	15 minutes	2 minutes
<b>Total liquid volume</b>	$60 \text{ m}^3$	$0.8 \text{ m}^3$	$0.1 \text{ m}^3$

It can be seen that relative to capacity the size of the manifold capillaries is still much smaller than that of conventional contactors. In addition, the residence time within each extractor is lower in the case of the capillary than the other conventional contactors, which will prevent solvent degradation.



AREVA La Hague plant in France has two production lines with a production level equivalent to 450 tWh of electricity per year, which produce 1700 tonnes of spent fuel per year. In 2011, the plant processed 1045 tonnes of spent fuel. Same amounts of spent fuel (1734 tonnes of spent fuel per year) are reprocessed in Sellafield in the Thermal Oxide Reprocessing Plant (Hanson, 2014; personal contact).

To reprocess these amounts of spent nuclear fuel (i.e. 1045 tonnes per year) approximately 400 assemblies of six channels of 2 mm ID would be required. The maximum space that this system would occupy should not exceed  $0.05 \text{ m}^3$ , which is one order of magnitude lower than the centrifugal contactor and the pulsed column in **Table 6.3**. The number increases sharply to 2090 and 41800 assemblies in the case of 1 and 0.5 mm ID respectively. However, the number of assemblies can be reduced by increasing the channel size or the flow rates.

## 6.6 Conclusions

The mass transfer characteristics during liquid-liquid plug flow in small channels with internal diameter ranging from 0.5 to 2 mm was discussed. The extraction of dioxouranium(VI) ions from nitric acid solutions into TBP/IL mixtures (30%, v/v), relevant to spent nuclear fuel reprocessing was investigated and the effects of channel size, ionic liquid type, initial nitric acid concentration, mixture velocity, flow rate ratio, and residence time were studied. The results were compared to those obtained from equilibrium experiments. The variation of extraction of dioxouranium(VI) with the initial nitric acid concentration was similar to the trend of the equilibrium values. However, the extraction efficiency followed a slightly different trend, which may be due to the change of extraction mechanism from cation transfer to anion transfer as the nitric acid concentration increases. Studies on the extraction performance of different types of TBP/ionic liquid systems (30%, v/v) showed that  $[\text{C}_{10}\text{mim}][\text{NTf}_2]$  can be considered as a promising candidate for extraction and back-extraction (stripping), as the dioxouranium(VI) %extraction (%E) varied from very low to high values as a function of the initial nitric acid concentration. It was also found that at low initial nitric acid concentrations where the extraction mechanism was cation-dependent, the highest extraction of dioxouranium(VI) was achieved for  $[\text{C}_4\text{mim}][\text{NTf}_2]$ , while at high initial nitric acid concentrations, where the cation does not play an important role, the highest dioxouranium(VI) extraction was achieved when  $[\text{P}_{66614}][\text{NTf}_2]$  was used.

Furthermore, experiments with  $[\text{C}_4\text{mim}][\text{NTf}_2]$  showed that higher extraction efficiencies are achieved at shorter residence times and smaller channel sizes. It was also found that  $\%E_{\text{eff}}$  increases at all channel sizes as the residence time increases. An extraction efficiency of  $>90\%$  is achieved in the case of the 0.5 mm ID channel in less than 11 s, whilst it was decreasing as the channel size increases to 1 and 2 mm ID. The overall mass transfer coefficients, however, follow different trends, depending on the channel size. In addition, a decrease of the volumetric mass transfer coefficient as a function of the residence time was observed which can be explained by the decrease in the driving force. In all channels it was found that significant extraction takes place as soon as the phases join at the inlet of the channel. For all conditions studied the mass transfer coefficients varied between 0.049 and  $0.312 \text{ s}^{-1}$ , which is in agreement with literature values for other small scale liquid-liquid contactors. It was found that an assembly of 6 capillaries of 2 mm ID can reprocess 2.6 tonnes of spent nuclear fuel per year, and achieve  $>90\%$  extraction efficiency in less than 95 s. In addition, efficient separation of the two liquids during plug flow achieved with the in-house flow splitter for flow rates up to  $8 \text{ cm}^3 \text{ min}^{-1}$ . Finally, experimental results showed that comparable amounts of spent nuclear fuel to the extraction units that are currently used in spent nuclear reprocessing plants can be processed for extraction of dioxouranium(VI) larger than 99% extraction of dioxouranium in 4 stages (cycles) with approximately 400 assemblies.

## Chapter 7.

# Modelling of a micro-extractor

### 7.1 Introduction

In liquid-liquid systems several parameters that affect the performance of the extractor (with or without chemical reaction) such as channel size, flow patterns, fluid properties, mixing zone, and flow orientation have been investigated ([Burns and Ramshaw, 2001](#), [Zhao et al., 2007](#), [Kashid et al., 2007b](#), [Dessimoz et al., 2008](#), [Su et al., 2010](#), [Ghaini et al., 2010](#), [Tsaoulidis et al., 2013a](#), [Tsaoulidis et al., 2013b](#), [Sarrazin et al., 2008](#)). A number of investigations have focused on the development of numerical and empirical models to describe the mass transfer for fixed interface location ([Kashid et al., 2007a](#), [Raimondi and Prat, 2011](#), [Skelland and Wellek, 1964](#)). Harries et al. ([Harries et al., 2003](#)) developed a numerical model for liquid-liquid plug flow to investigate the hydrodynamics within both continuous and dispersed phase segments and the mass transfer of dissolved chemical species in both phases and across the interface. In their model segmented flow was represented by two adjacent rectangular units with moving wall, whilst good agreement was found with experimental results. A similar model has been developed by Kashid et al. ([Kashid et al., 2007a](#)), to investigate the flow patterns and the mass transfer with or without reaction between two consecutive segments with fixed location. The effect of viscosity on the flow patterns within the two phases was studied, and it was found that flow patterns are independent of the viscosity. Raimondi et al. ([Di Miceli Raimondi et al., 2008](#)) carried out numerical simulations of the mass transfer during liquid-liquid plug flow in square microchannels, where it was assumed that mass transfer did not deform the interface, enabling the hydrodynamics to be decoupled from the mass transfer.

To evaluate the performance of a two-phase separator (gas-liquid or liquid-liquid) the mass transfer coefficient or the extraction efficiency need to be known. A number of models have been developed for gas-liquid systems, which estimate the mass transfer coefficient in the continuous liquid phase. In these models the individual contributions of the caps of the plugs and of the fully developed film separating the plugs from the channel wall are estimated. A

study for mass transfer during Taylor flow based on CFD (computational fluid dynamics) results was carried out by van Baten and Krishna (Van Baten and Krishna, 2004), who confirmed that both the caps and the film contribute to mass transfer. For short contact ( $Fo < 0.1$ ) of the two phases (as explained in section 2.2.7) the mass transfer coefficient is calculated by

$$k_L \alpha = k_{L,cap} \alpha_{cap} + k_{L,film} \alpha_{film} = 2 \frac{\sqrt{2}}{\pi} \sqrt{\left(\frac{D_c u_p}{ID}\right)} \frac{4}{L_{UC}} + \frac{2}{\sqrt{\pi}} \sqrt{\frac{D_c u_p}{L_{film}}} \frac{4 L_{film}}{ID L_{UC}} \quad (7.1.1)$$

Based on the  $k_{L,film}$  suggested by van Baten and Krishna (Van Baten and Krishna, 2004), Vandu et al. (Vandu et al., 2005) developed a correlation (Eq. (7.1.2)), with a fitted parameter  $C$  based on their experimental data of air absorption in water.

$$k_L \alpha = C \sqrt{\frac{D_c u_g}{L_{UC}}} \frac{1}{ID} \quad (7.1.2)$$

An empirical correlation for liquid-liquid plug flow was developed by Kahsid et al. (Kashid et al., 2010) based on dimensional analysis in PTFE capillaries.

$$k_L \alpha \frac{L}{u_{mix}} = a Ca^b Re^c \left(\frac{ID}{L}\right)^d \quad (7.1.3)$$

In this chapter experimental mass transfer coefficients are compared against these three predictive models. In addition, a numerical finite element model is developed which solves for the hydrodynamics and mass transfer in both phases and the predictions on amount of extraction are compared against the experimental findings. This model allows parameters, such as film thickness, plug length, length of unit cell, and flow rates to be investigated.

## 7.2 Model formulation

The numerical model was developed to simulate the mass transfer of  $\{UO_2\}^{2+}$  ions in the ionic liquid-aqueous system during plug flow. For the simulations a unit cell (one dispersed phase plug and one continuous phase slug) in 2-D axisymmetric cylindrical coordinates is used. The two-phase flow and the concentration profiles are considered symmetric over the channel axis, and only half of the unit cell is simulated. The whole computational domain is depicted in **Figure 7.1**. The geometric characteristics, such as length of the plug and the slug and film thickness were chosen based on experimental findings.

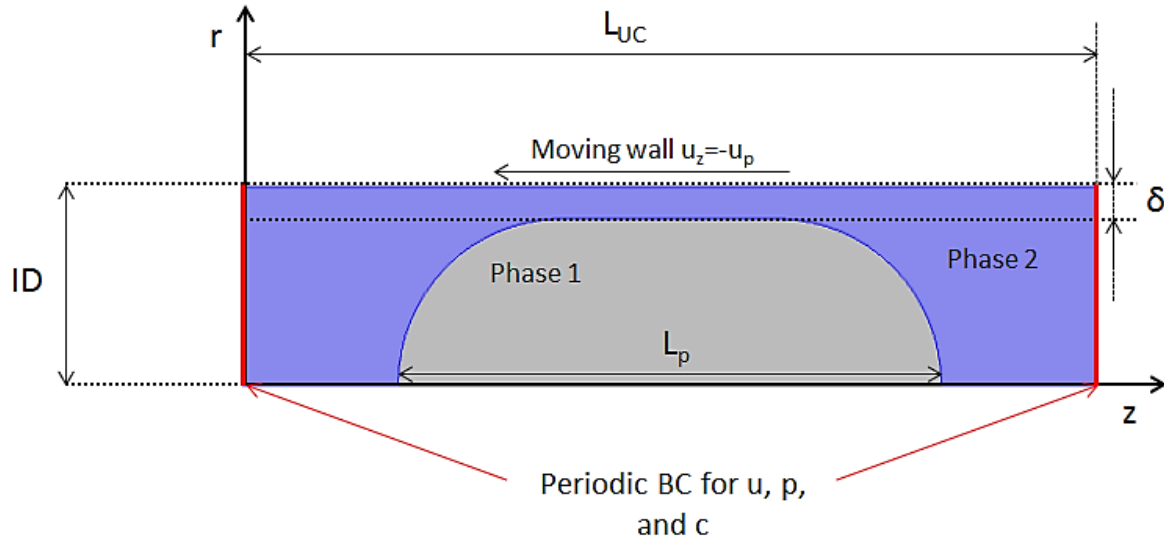


**Figure 7.1: Geometry and boundaries of the unit cell computational domain.**

In the model it was assumed that surface tension gradients and gravity are negligible. Both liquids were Newtonian, viscous and the flow was incompressible. It was also assumed that mass transfer does not affect the interface shape and volume of the unit cell. The computational procedure followed two steps. First, the hydrodynamics of the system were determined by solving the velocity field ( $\mathbf{u}$ ) and the pressure for the two liquid phases using the Navier-Stokes and the continuity equations (Eqs. (7.2.1) and (7.2.2)). Subsequently, the convection-diffusion equation for both phases (Eq. (7.2.3)) was solved.

$$\rho(\mathbf{u} \cdot \nabla)\mathbf{u} = \nabla \cdot [-P\mathbf{I} + \mu(\nabla\mathbf{u} + (\nabla\mathbf{u})^T)] + \mathbf{F} \quad (7.2.1)$$

$$\rho \nabla \cdot \mathbf{u} = 0 \quad (7.2.2)$$

$$\frac{\partial c_i}{\partial t} + \nabla \cdot (D_i \nabla c_i + \mathbf{u} c_i) = 0 \quad (7.2.3)$$

The position and the shape of the plug in the computational domain remained fixed, while the wall of the channel was moving with a constant velocity equal to the plug velocity,  $u_p$ , but with direction opposite to the flow. The plug has higher velocity than the mixture because of the thin film on the wall; for the simulations the experimental plug velocity is used. The following boundary conditions were used for the fluid flow equations:

- 1) axial and radial velocity of the channel wall equal to  $u_z = -u_p$  and  $u_r = 0$  respectively;
- 2) no-slip boundary condition at the channel wall;

3) equal stresses at the interface between the two phases. This approach is correct when the plug geometry accurately represents the equilibrium state of the plug where forces are balanced.

For the mass transfer equation a boundary condition was applied to satisfy the flux continuity at the interface, while zero flux was set at the channel wall. Periodic boundary conditions are used at the front and the back of the computational domain for the velocity, the pressure, and the concentration (see **Figure 7.1**).

All simulations were performed with a commercial finite element software (Comsol Multiphysics 4.4.). The hydrodynamic equations for both liquid domains were solved in a steady-state mode to establish the velocity and pressure profiles, while the mass transfer equations, one for each phase, were solved in a transient manner to represent mass transfer during the movement of the plug along the channel. A free triangular mesh was used in the simulations in the whole computational domain, which was additionally refined along the interface and the channel wall, where the characteristic length scales are very short and the concentration gradients are steep. Sensitivity analysis was carried out to establish the grid size needed for grid independent mass transfer. It was found that the minimum and the maximum element size along the interface should be  $0.4\ \mu\text{m}$  and  $3\ \mu\text{m}$ , respectively, for the 1 and 2 mm ID channels and  $0.1\ \mu\text{m}$  and  $1.6\ \mu\text{m}$ , respectively, for the 0.5 mm ID channel. In the subdomains (phase 1 and 2) the grid size should be less than  $32\ \mu\text{m}$ . It was also found that a time step equal to 0.05 s was satisfactory since there were small discrepancies in concentration with shorter time steps. Finally, in order to avoid very large instantaneous flux across the interface, a step function was added to the model.

## 7.3 Results and discussion

### 7.3.1 Comparison with literature models

The mass transfer coefficients obtained experimentally were compared with literature models (section 7.1) and the results are shown in **Figure 7.2**. In general, the experimental results seem to agree well with the model proposed by Kashid et al. (Kashid et al., 2010) for liquid-liquid plug flow in micro-capillaries. The fitting parameters in Eq. (7.1.3) have been adjusted to the current experimental results (i.e.,  $a=0.44$ ,  $b=-0.1$ ,  $c=-0.65$ ,  $d=-0.1$ ) and the mass

transfer coefficients are predicted within a range of errors from 0.6 to 13.2%. The highest errors were observed at high mixture velocities regardless of the channel size. The modified correlation seems to predict better the mass transfer coefficients in the 1 mm ID channel with a mean relative error of 3.5%.

The models of van Baten and Krishna (Van Baten and Krishna, 2004) and Vandu et al. (Vandu et al., 2005), for gas-liquid bubble flows, showed little or no agreement with the experimental results. Van Baten and Krishna (Van Baten and Krishna, 2004) developed their model (Eq. (7.1.1)) over a wide range of parametric values ( $ID=1.5\text{--}3\text{ mm}$ ,  $L_{UC}=0.015\text{--}0.05\text{ m}$ ). Their model underestimated the current mass transfer coefficients for all the channels. It is worth noting that in this work the length of the unit cells ( $L_{UC}$ ) and the velocity of the dispersed phase ( $u_p$ ) were one order of magnitude lower than those used by Van Baten and Krishna (Van Baten and Krishna, 2004). In the model by Vandu et al. (Vandu et al., 2005) (Eq. (7.1.2)), which was evaluated for channel sizes from 1 to 3 mm ID and unit cell lengths from 5 to 60 mm, the only contribution on the mass transfer coefficient is by the film. The  $k_L\alpha$  obtained for 0.5 mm ID and 1 mm ID channel seem to fall within the predictions of their model (for  $C=8.5$ ), whilst mass transfer is underestimated in all cases for the 2 mm ID channel with a relative error from 40 to 60%. The discrepancies between the experimental results and the gas-liquid models may be attributed to the more complex hydrodynamics in the liquid-liquid systems. In addition, there is less resistance to mass transfer by diffusion within a gas plug compared to a liquid one.

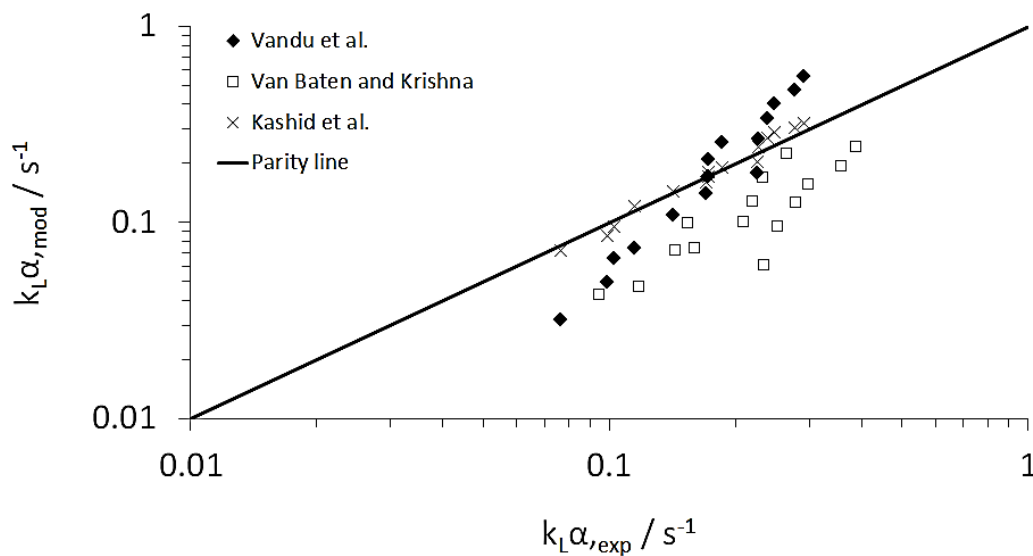


**Figure 7.2:** Comparison of experimental  $k_L\alpha$  with those predicted by correlations for the 3 different channels.

### 7.3.2 Comparison with numerical model

The numerical model developed in [section 7.2](#) was applied to the current system. The geometric characteristics of the flow needed for the simulations, i.e. film thickness ( $\delta$ ), length of unit cell ( $L_{UC}$ ), and plug length ( $L_p$ ) and the plug velocity ( $u_p$ ), discussed in detail in [chapter 4](#), are tabulated in **Table 7.1**. The residence time, ( $t=u_p/L_{ch}$ ) selected for the simulations represents the time that the aqueous plug flows in the extraction channel ( $L_{ch}=31.5$  cm). The properties of the fluids used for the simulations are shown in **Table 7.2**. The diffusivity coefficient of  $\{UO_2\}^{2+}$  in the TBP/IL (30%, v/v) mixture and in the aqueous nitric acid solution has been selected based on literature information.

**Table 7.1: Parametric values used in the numerical simulations.**

Case	ID [mm]	$\varepsilon_d$	$L_{UC}$ [mm]	$L_p$ [mm]	$\delta$ [ $\mu m$ ]	$u_p$ [ $m\ s^{-1}$ ]
1	0.5	0.5	2.18	1.48	36.1	0.035
2	2	0.5	4.4	2.8	160.7	0.045
3	1	0.5	3.4	2.2	76.3	0.039
4	1	0.57	3.7	2.6	70.2	0.037
5	1	0.67	4.3	3.43	72.3	0.039

**Table 7.2: Properties of the fluids used for the simulations**

Properties	TBP/IL (30%, v/v)	HNO <sub>3</sub> (3 M)
Viscosity ( $kg\ m^{-1}\ s^{-1}$ )	0.029	0.001
Density ( $kg\ m^{-3}$ )	1260	1070
Diffusivity ( $m^2\ s^{-1}$ )	$7 \cdot 10^{-11}$ ( <a href="#">Liu et al., 2011</a> , <a href="#">Giridhar et al., 2007</a> )	$7 \cdot 10^{-10}$ ( <a href="#">Liu et al., 2011</a> )

In **Figure 7.3A** the recirculation in the plug and the slug for Case 3 as calculated from the model is shown. As shown in [chapter 5](#) internal circulation is created in both continuous and dispersed phases. According to Gupta et al. ([Gupta et al., 2013](#)), who run CFD simulations in liquid-liquid plug flows, three circulation zones have been observed in the upper half of a liquid plug; a large one in the middle of the plug and two small ones close to the front and



rear cap of the plug. Experiments were carried out in a similar channel (ID=1.06 mm), but the mixture velocities were one order of magnitude higher than those in the present study. In the current simulations a recirculation zone has been observed in the middle of the upper half of the plug which occupies the whole area excluding the caps, whilst there are no apparent recirculation zones close to the caps. However, the circulation obtained from the model resembles the experimental results as shown in **Figure 7.3**.

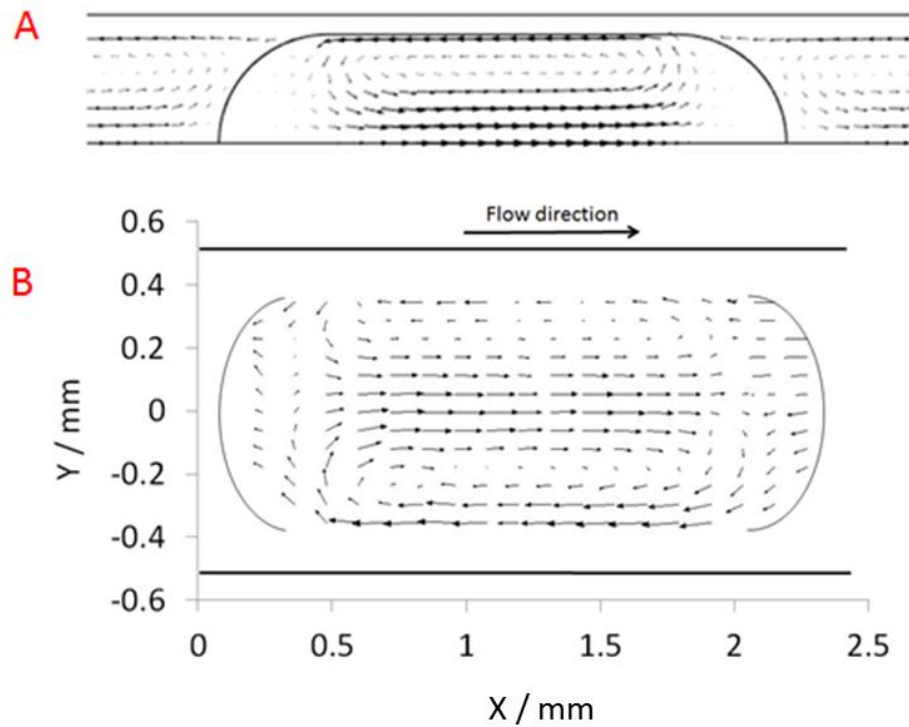


**Figure 7.3:** Circulation patterns (A) obtained by model in both plug and slug, and (B) obtained experimentally in the plug for Case 3.

In **Figure 7.4** the total velocity field for Case 3 as predicted by the numerical model and by the experimental results (Insight 4G, Tecplot) is shown. Similar to experimental results it can be seen that the magnitude of the velocity is maximum at the core of the plug while it is decreasing towards the channel walls and the liquid/liquid interfaces, i.e. front and rear cap of the plug.

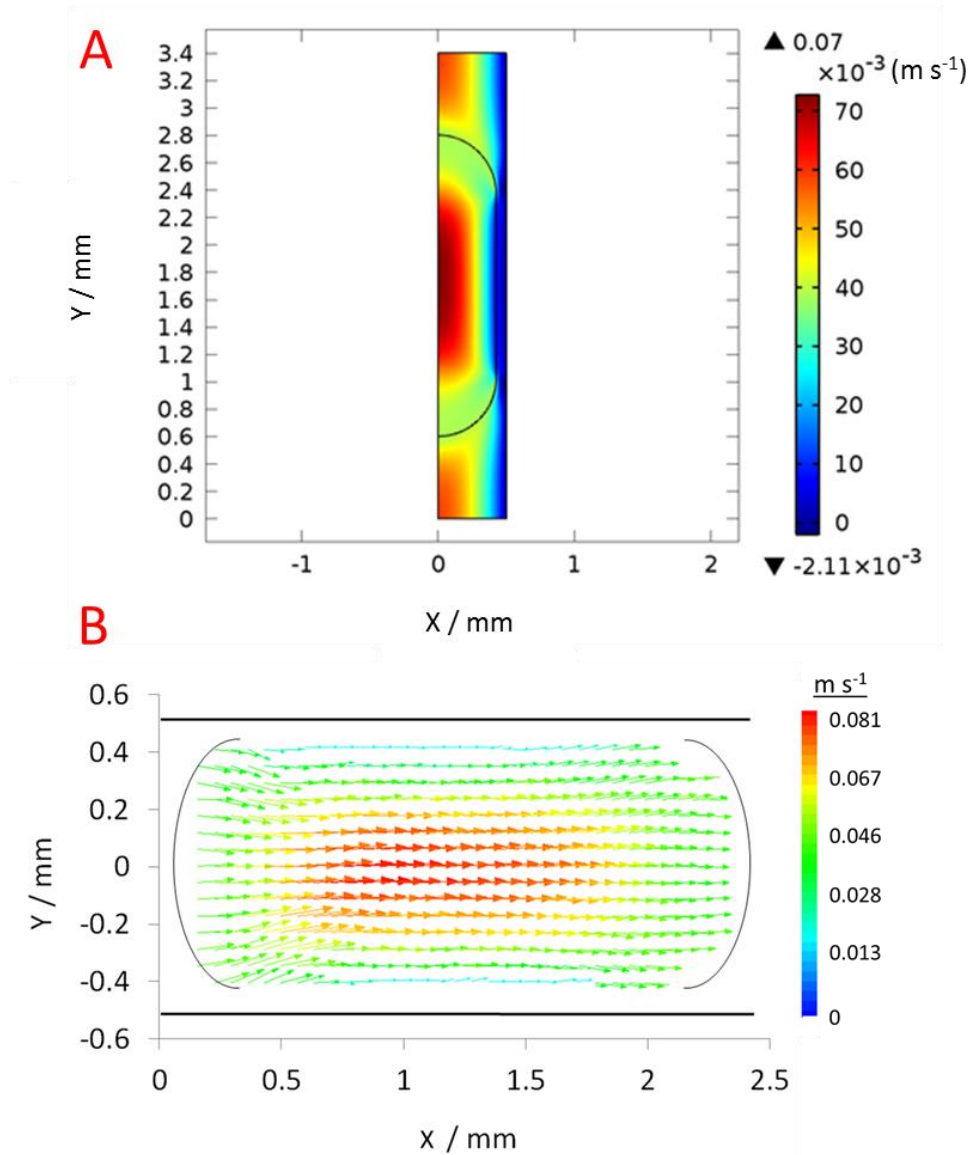


**Figure 7.4: Total velocity field in the computational domain for Case 3 predicted by (A) the numerical model, and (B) the experimental PIV results (Insight 4G, Tecplot).**

The evolution of the concentration profile at different residence times from  $t=0$  until the plug exits the channel ( $L_{\text{ch}}=31.5 \text{ cm}$ ) is shown in **Figure 7.5** for Case 3. It can be seen that most of the concentration profile has already been developed within the first second while after that and until the end of the channel changes are not so pronounced.

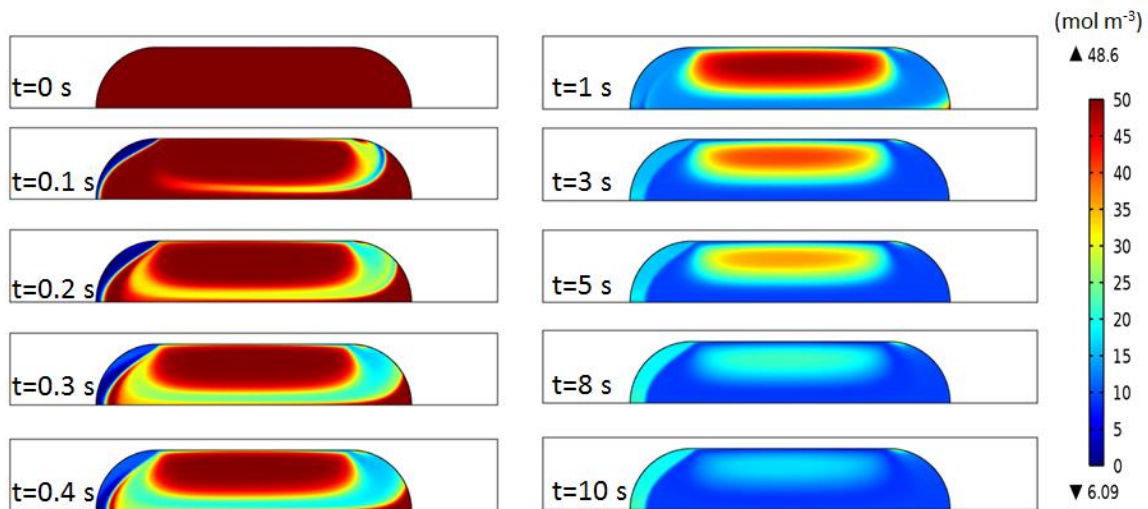


**Figure 7.5:** Evolution of the concentration profile within the aqueous plug for Case 3 at different residence times as taken from numerical solution.

The effect of the channel size on extraction efficiency is shown in **Figure 7.6** as a function of residence time ( $t=u_p/L_{ch}$ ). Higher extraction efficiency can be achieved at a certain residence time for decreased channel size. The experimental results agree with the model within an error of 1.4 to 12.3%. However, in almost all cases the model underpredicts the experimental data. As was discussed in [section 6.3.4](#), significant mass transfer seems to take place at the beginning of the channel close to the inlet where the plug flow is not well formed yet. This is not accounted for in the model which considers fully developed plug flow and would explain the underprediction.

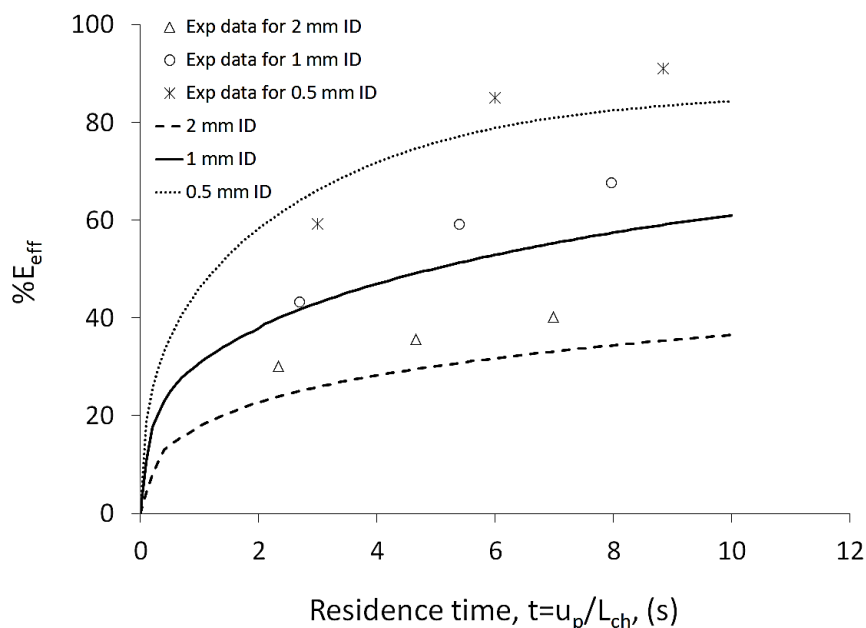


**Figure 7.6:** Extraction efficiency (%E<sub>eff</sub>) of dioxouranium(VI), predicted by the numerical model, as a function of the residence time in 3 different channel sizes at constant mixture velocity of 0.03 m s<sup>-1</sup>.

Increased interfacial area can be achieved by changing the flow rate ratio between the two liquid phases. The effect of flow rate ratio ( $q = Q_{IL}/Q_{HNO_3}$ ) on the extraction efficiency is shown in **Figure 7.7** as a function of the residence time. For these results the total flow rate of the mixture ( $Q_{mix}$ ) was kept constant at 84.82 cm<sup>3</sup> h<sup>-1</sup> (mixture velocity,  $u_{mix}$  of 0.03 m s<sup>-1</sup>), whilst the flow rate of the dispersed aqueous phase ( $Q_{HNO_3}$ ) varied from 42.41 to 56.55 cm<sup>3</sup> h<sup>-1</sup> and that of the continuous ionic liquid phase ( $Q_{IL}$ ) from 28.27 to 42.41 cm<sup>3</sup> h<sup>-1</sup>, which results in flow rate ratios ( $q$ ) increasing from 0.5 to 1. The change in flow rate ratio does not limit the extraction of dioxouranium(VI) from the nitric acid solution because, according to the reaction stoichiometry, TPB is in excess in the IL phase at all cases. As the flow rate ratio increases from 0.5 to 1, the plug length also increases while the interfacial area decreases by ~23%. This results to a smaller number of unit cells in the extractor ( $L_{ch}=10.5$  cm) and to a lower extraction efficiency as shown in **Figure 7.7**. However, the amount of solvent used is reduced by 33.4%. Reduction in solvent use can be important for solvents such as ionic liquids which have high productions costs. The experimental extraction efficiencies seem to agree well with those predicted by the simulations (mean relative error 4.6%).

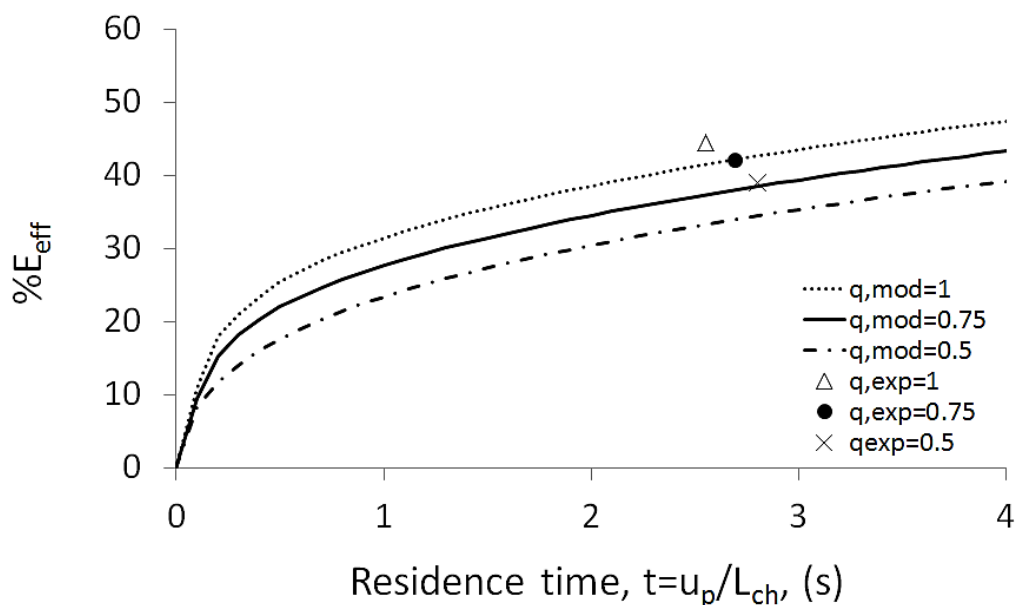


**Figure 7.7:** Comparison of predicted extraction efficiencies of dioxouranium(VI) against the experimental ones as a function of the residence time at three different flow rate ratios ( $q=Q_{II}/Q_{HNO_3}$ ) for constant  $Q_{mix}=84.82 \text{ cm}^3 \text{ h}^{-1}$  in the 1 mm ID channel.

## 7.4 Conclusions

The experimentally obtained mass transfer coefficients were compared with existing models for liquid-liquid and gas-liquid flows from the literature. The results showed good agreement with the empirical correlation proposed for a liquid-liquid system. A numerical finite element model for the hydrodynamics and mass transfer during dioxouranium(VI) extraction in small channels in plug flow was also developed, and the results are compared with the experimental findings. The model reproduced well the circulation patterns within the plugs. It was also able to predict the experimental extraction efficiencies reasonably well with an average relative error of 11.3%.

## Chapter 8.

# Conclusions & future developments

The worldwide energy demand is growing rapidly, whilst the use of fossil fuels becomes an unattractive solution because of reduced availability and impact on climate change. Nuclear energy is currently considered as a serious low carbon alternative which can provide sufficient amounts of energy using only a small amount of fission material. Moreover, the pressing demands of sustainable, efficient and safer processes make operations in intensified small scale devices an appealing option.

The main contribution of the thesis was to provide insight into the fundamentals and to develop small-scale processes for ionic liquid-based extractions that can intensify the liquid-liquid separations of the spent nuclear fuel reprocessing cycle. The industrial application of small scale processes requires the hydrodynamics and mass transfer behaviour to be well characterised and well predicted. In addition, the thesis proposes modelling methodologies to evaluate the applicability of the small-scale extractors in reprocessing large volumes of nuclear waste in industrial scale.

### 8.1 Overview of thesis

The study of the ionic liquid-based extraction processes in small channels has been performed stage by stage as follows. The first objective of this research was to investigate the hydrodynamics in small scale systems during liquid-liquid (ionic liquid/aqueous solutions) flows. The identification of the flow pattern formations within the channels is crucial since they are strongly related to the performance of the micro-extractor, as they influence the pressure drop, and the mass transfer. A universal flow pattern map does not exist and the exact position of the transition boundaries between the flow regimes are inherently related to the liquid-liquid system studied. Experiments were carried out in capillaries made of different materials (Teflon and glass) with sizes between 200 and 270  $\mu\text{m}$ . Flow patterns were obtained for two inlet configurations (T- and Y- junction), and for various total flow rates and flow

rate ratios. Results showed that the mixing zone was not affecting the flow configurations for a wide range of mixture velocities and volume fractions. The most significant impact on the formation of the flow patterns originated from the fluid properties, channel material, flow rate ratio, and first injected liquid. It was found that the continuous phase in the glass capillary depended on the fluid that initially filled the channel. When the aqueous phase was introduced first, it became the continuous phase with the ionic liquid forming plugs or a mixture of plugs and drops within it. In the Teflon microchannels, the order that fluids were introduced did not affect the results and the ionic liquid was always the continuous phase. The main patterns observed were plug flow, annular flow, and drop flow. Pressure drop in the Teflon microchannels at a constant ionic liquid flow rate, was found to increase as the ionic liquid volume fraction decreased, and was always higher than the single phase ionic liquid value at the same flow rate as in the two-phase mixture. However, in the glass microchannel during plug flow, when water was the continuous phase pressure drop for a constant ionic liquid flow rate was always lower than the single phase ionic liquid value. After identifying the flow patterns formed for a wide range of operating conditions, the study focused on the investigation of plug flow.

Plug flow was thoroughly investigated in various channel sizes of different material mainly for TBP/ionic liquid (30%, v/v) mixtures-nitric acid solutions, which is a system relevant to spent nuclear reprocessing. Investigations on the plug formation at the T-inlet showed that when ionic liquid was the carrier fluid (high Ca number), the plug formation frequency was three times faster than when the aqueous phase was the carrier fluid. The length of the plug decreased with increasing mixture velocity, due to the rapid penetration of the one phase into the other. The length of the plug plays an important role on the mass transfer performance of the system since it affects the internal circulations within the plugs, as well as the interfacial area available for mass transfer. Correlations on the literature were compared with experimental results but they showed little or no agreement since the two-phase system in the current work when ionic liquid is the carrier phase has high Ca numbers beyond the range of most models. A predictive model on plug length has been developed, which correlated reasonably well the data from channel sizes varying from 0.2 to 2 mm for  $0.007 < Ca < 0.18$ .

During plug flow a thin film was found to be present, which separated the dispersed plug from the wall. Film thickness is an important parameter to identify since it affects the velocity of the plug, the internal circulation within the plug, and the pressure drop. Film thickness was

measured for the different channels and results were compared with literature correlations. It was found that there is no model able to predict film thickness for the whole range of internal diameters tested. In the case of the smallest channel (0.2 mm ID) the models underpredicted the experimental data. This is attributed to the high viscosity of the ionic liquid used which enhances the formation of thicker film even at low velocities. The existence of the film is expected to increase the velocity of the plug as was also found (**Figure 4.17**). For all channel sizes plugs were flowing at higher velocity than the mixture velocity. The knowledge of the velocity of the plug gives an accurate estimation of the residence time that the two phases are in contact in the channel. The experimental data on plug velocity agreed with the correlation of Liu et al. (Liu et al., 2005) within 11% mean relative error. Pressure drop was also investigated during plug flow and it was found that by increasing the channel size from 0.5 to 2 mm ID there is a decrease in pressure drop of one order of magnitude. A modified plug flow pressure drop model showed relatively good agreement with the experimental data.

After characterising the important properties of the plug flow (i.e. plug size, plug velocity, film thickness, and pressure drop), the work focused on the circulation patterns and mixing characteristics within aqueous plugs, investigated by means of  $\mu$ -PIV (micro Particle Image Velocimetry). The mixing within the plug was quantified with the non-dimensional circulation time and the results were correlated with the mass transfer performance. It was found that different parameters such as plug length, mixture velocity, location of the stagnation points, film thickness, and channel size were strongly related to each other, and influence the mixing within the plug and the mass transfer. However, the most decisive parameter was the channel size. Non-dimensional circulation time increased (i.e. less efficient mixing) by about 85% when channel size increased from 0.5 to 2 mm ID, which affects the mass transfer performance of the system.

The last stage of the experimental part of this research involved extractions of dioxouranium(VI) ions from nitric acid solutions into TBP/IL mixtures (30%, v/v), relevant to spent nuclear fuel reprocessing. The effects of channel size, ionic liquid type, initial nitric acid concentration, mixture velocity, flow rate ratio, and residence time on the extraction performance of the contactor were studied. The extraction experiments were carried out in Teflon capillaries with internal diameter ranging from 0.5 to 2 mm. The results were also compared to those obtained from equilibrium experiments.



Studies of dioxouranium(VI) extraction from nitric acid concentrations to TBP/ionic liquid (30%, v/v) solutions suggest different mechanisms of the extraction, i.e. cation exchange, anion exchange and solvation, depending on the nitric acid concentration and the type of ionic liquid. The variation of extraction of dioxouranium(VI) with the initial nitric acid concentration was similar to the trend of the equilibrium values. However, the extraction efficiency followed a slightly different trend, which may be due to the change of extraction mechanism from cation transfer to solvation and anion transfer as the nitric acid concentration increases. The investigation of different types of TBP/ionic liquid systems (30%, v/v) showed that  $[C_{10}mim][NTf_2]$  can be considered as a promising candidate for extraction and back-extraction (stripping), as the dioxouranium(VI) %extraction (%E) varied from very low to high values as a function of the initial nitric acid concentration. It was also found that at low initial nitric acid concentrations where the extraction mechanism was cation-dependent, the highest extraction of dioxouranium(VI) was achieved for  $[C_4mim][NTf_2]$ , while at high initial nitric acid concentrations, where the cation does not play an important role, the highest dioxouranium(VI) extraction was achieved when  $[P_{66614}][NTf_2]$  was used. Studies on the extraction efficiency showed that for the same residence time higher extraction efficiencies are achieved as the channel size decreases. In all channels it was found that significant extraction takes place as soon as the phases join at the inlet of the channel. The overall mass transfer coefficients, however, follow different trends, depending on the channel size. For all conditions studied the mass transfer coefficients varied between  $0.049$  and  $0.312\text{ s}^{-1}$ , which is in agreement with literature values for other small scale liquid-liquid contactors. A significant decrease of 50% of the mass transfer coefficients takes place when the channel size increases from 0.5 mm to 1 mm while after that by increasing further the channel size to 2 mm ID the decrease on the mass transfer coefficient is less pronounced, i.e. from 0.5 to 2 mm ID the decrease on  $k_{L\alpha}$  is 72%. Extraction efficiency was also measured as a function of flow rate ratio ( $q=Q_{IL}/Q_{HNO_3}$ ). It was found that as the flow rate ratio decreases from 1 to 0.5, the plug length increases while the interfacial area decreases by ~23%. This results to a smaller number of unit cells in the extractor and to a lower extraction efficiency (**Figure 7.7**). However, the amount of solvent used is reduced by 33.4%. Reduction in solvent use can be important for solvents such as ionic liquids which have high productions costs. Moreover, experimental results have been compared with extraction units already in operation in spent nuclear reprocessing plants. It was found that 400 assemblies (1 assembly consists of 6 capillaries of 2 mm ID) can reprocess comparable amounts of spent fuel and

achieve >99% extraction of dioxouranium(VI) in 4 stages (cycles) with extraction efficiency per stage >90% in less than 95 s. In addition, it was found that efficient liquid-liquid separation during plug flow was achievable with the in-house flow splitter for flow rates up to  $8 \text{ cm}^3 \text{ min}^{-1}$ .

Finally, experimental mass transfer coefficients were compared against predictive models derived from the literature and good agreement was found with a model for liquid-liquid contactors and experimentally adjusted coefficients. In addition, a numerical finite element model for the hydrodynamics and mass transfer was developed, and the results were compared well with the experimental findings. The model allows rapid analysis of different operating conditions, such as film thickness between the plug and the channel wall, plug length, length of unit cell, and flow rates.

## **8.2 Future developments**

To design and fully characterize integrated ionic liquid-based separators for spent nuclear reprocessing, thorough investigations in many areas are still required.

Liquid-liquid flows in small channels are quite challenging due to the wide variation of physical properties of the two phases. It was found that hydrodynamics in small scale channels are strongly related to the performance of the reactor. The first step would be to develop accurate predictive tools for the hydrodynamics within the small scale devices. The generation of a unified theory for the prediction of flow patterns, which should be independent of the fluid and the microchannel characteristics and correlate the flow regimes using the relative forces responsible as well as the surface properties, should be investigated with more parametric studies. The absence of this kind of theory lies on the fact that most investigations have been carried out under similar conditions (i.e. fluids and channel material). Furthermore, regarding the hydrodynamics of plug flow investigations should focus on the development of models that will predict plug size in larger channels and higher Ca numbers. Another important issue that has received relatively little attention is the prediction of the film thickness during plug flow. Most of the studies have been focused in gas-liquid flows, which employed liquids of relatively low viscosity. However, as shown in this research the effect of viscosity especially as the channel size decreases becomes more apparent and existing models fail to predict film thickness accurately. Regarding the high

pressure drop that is developed within a two phase system, surface treatment should be employed to force the less viscous fluid to be in contact with the wall and thus minimize pressure drop. As shown in this research, ionic liquids even if they have comparable wettabilities with aqueous solutions on some surfaces, they tend to become the continuous phase which affects the resulting pressure drop.

More investigations are also needed on the mixing characteristics within the plugs for the quantification of circulation time. In addition, employing other techniques (two-colour PIV) on the identification of the circulation within the two phases simultaneously would be useful for fully characterizing a system with its mass transfer performance.

The mechanism of extraction and the complexes that are formed depend on the ionic liquid concerned and are quite different than the mechanisms involved with conventional solvents. Knowledge of the mechanisms involved and the species formed would be necessary for comprehensive characterisation and modelling of two-phase extractors. Task specific ionic liquids (TSILs) could also play an important role in extractions, wherein the functional groups in both cations and anions would enhance the extraction efficiency and selectivity. Since most studies deal with single component extraction it would be extremely useful to investigate the performance of ionic liquids in the selective separation of a certain component from mixtures that simulate the actual nuclear waste. Finally, the possibility to recycle the actinides that are immobilized in the ionic liquids should be the next research area of the near future.

To increase throughput of small channel extractors, scale out strategies (internal scale-up, external scale-up, bifurcation, etc.) need to be further investigated to establish well-predicted design equations. Several companies (Corning S.A.S, Avon, France; Ehrfeld Mikrotechnik BTS GmbH, Wendelsheim, Germany; Runcorn, UK) have developed high-throughput reactors based on microchannel structures. However, studies on high throughput systems during plug flow and their interpretation with phase separators are missing.

Finally, while most of the studies on either hydrodynamics or mass transfer characteristics during liquid-liquid plug flow are based on empirical approaches, they are limited to specific systems. For this reason it is important to develop numerical approaches, which will provide information on flow and fluid properties that may be difficult or costly to obtain by

measurements. Preliminary studies on the design process via numerical tools could help to achieve better or more consistent performance.

## References

- ABADIE, T., AUBIN, J., LEGENDRE, D. & XUERE, C. 2012. Hydrodynamics of gas–liquid Taylor flow in rectangular microchannels. *Microfluidics and nanofluidics*, 12, 355–369.
- AHMED, B., BARROW, D. & WIRTH, T. 2006. Enhancement of reaction rates by segmented fluid flow in capillary scale reactors. *Advanced Synthesis & Catalysis*, 348, 1043–1048.
- ALLEN, D., BASTON, G., BRADLEY, A. E., GORMAN, T., HAILE, A., HAMBLETT, I., HATTER, J. E., HEALEY, M. J., HODGSON, B. & LEWIN, R. 2002. An investigation of the radiochemical stability of ionic liquids. *Green Chemistry*, 4, 152–158.
- ANGELESCU, D., MERCIER, B., SIESS, D. & SCHROEDER, R. 2010. Microfluidic capillary separation and real-time spectroscopic analysis of specific components from multiphase mixtures. *Analytical chemistry*, 82, 2412–2420.
- ANGELI, P. & GAVRIILIDIS, A. 2008. Hydrodynamics of Taylor flow in small channels: a review. *Proceedings of the Institution of Mechanical Engineers Part C-Journal of Mechanical Engineering Science*, 222, 737–751.
- ANGELI, P. & HEWITT, G. 1999. Pressure gradient in horizontal liquid–liquid flows. *International journal of multiphase flow*, 24, 1183–1203.
- ANGELI, P. & HEWITT, G. 2000. Flow structure in horizontal oil–water flow. *International journal of multiphase flow*, 26, 1117–1140.
- AOTA, A., NONAKA, M., HIBARA, A. & KITAMORI, T. 2007. Countercurrent laminar microflow for highly efficient solvent extraction. *Angewandte Chemie*, 119, 896–898.
- ASSMANN, N. & VON ROHR, P. R. 2011. Extraction in microreactors: intensification by adding an inert gas phase. *Chemical Engineering and Processing: Process Intensification*, 50, 822–827.
- AUSSILLOUS, P. & QUERE, D. 2002. Bubbles creeping in a viscous liquid along a slightly inclined plane. *Europhysics Letters*, 59, 370–376.
- AUSSILLOUS, P. & QUÉRE, D. 2000. Quick deposition of a fluid on the wall of a tube. *Physics of Fluids (1994-present)*, 12, 2367–2371.
- BANNWART, A. C. 2001. Modeling aspects of oil–water core–annular flows. *Journal of petroleum science and engineering*, 32, 127–143.
- BECHT, S., FRANKE, R., GEIBELMANN, A. & HAHN, H. 2009. An industrial view of process intensification. *Chemical Engineering and Processing: Process Intensification*, 48, 329–332.
- BELL, T. J. & IKEDA, Y. 2011. The application of novel hydrophobic ionic liquids to the extraction of uranium (vi) from nitric acid medium and a determination of the uranyl complexes formed. *Dalton Transactions*, 40, 10125–10130.
- BERČIČ, G. & PINTAR, A. 1997. The role of gas bubbles and liquid slug lengths on mass transport in the Taylor flow through capillaries. *Chemical Engineering Science*, 52, 3709–3719.
- BERETTA, A., FERRARI, P., GALBIATI, L. & ANDREINI, P. 1997. Horizontal oil–water flow in small diameter tubes. Flow patterns. *International communications in heat and mass transfer*, 24, 223–229.
- BICO, J. & QUERE, D. 2000. Liquid trains in a tube. *EPL (Europhysics Letters)*, 51, 546.

- BILLARD, I., OUADI, A. & GAILLARD, C. 2011a. Liquid–liquid extraction of actinides, lanthanides, and fission products by use of ionic liquids: from discovery to understanding. *Analytical and bioanalytical chemistry*, 400, 1555-1566.
- BILLARD, I., OUADI, A., JOBIN, E., CHAMPION, J., GAILLARD, C. & GEORG, S. 2011b. Understanding the Extraction Mechanism in Ionic Liquids: UO<sub>2</sub> 2+/HNO<sub>3</sub>/TBP/C4-mimTf<sub>2</sub>N as a Case Study. *Solvent Extraction and Ion Exchange*, 29, 577-601.
- BINNEMANS, K. 2007. Lanthanides and actinides in ionic liquids. *Chemical reviews*, 107, 2592-2614.
- BONHOTE, P., DIAS, A.-P., PAPAGEORGIOU, N., KALYANASUNDARAM, K. & GRÄTZEL, M. 1996. Hydrophobic, highly conductive ambient-temperature molten salts. *Inorganic chemistry*, 35, 1168-1178.
- BRAUNER, N. 1991. Two-phase liquid-liquid annular flow. *International journal of multiphase flow*, 17, 59-76.
- BRETHERTON, F. P. 1961. The Motion of Long Bubbles in Tubes. *Journal of Fluid Mechanics*, 10, 166-188.
- BUDWIG, R. 1994. Refractive index matching methods for liquid flow investigations. *Experiments in fluids*, 17, 350-355.
- BURNS, J. R. & RAMSHAW, C. 2001. The intensification of rapid reactions in multiphase systems using slug flow in capillaries. *Lab on a Chip*, 1, 10-15.
- CASTELL, O. K., ALLENDER, C. J. & BARROW, D. A. 2009. Liquid–liquid phase separation: characterisation of a novel device capable of separating particle carrying multiphase flows. *Lab on a Chip*, 9, 388-396.
- CERVERA-PADRELL, A. E., MORTHENSEN, S. T., LEWANDOWSKI, D. J., SKOVBY, T., KIIL, S. & GERNAEY, K. V. 2012. Continuous Hydrolysis and Liquid–Liquid Phase Separation of an Active Pharmaceutical Ingredient Intermediate Using a Miniscale Hydrophobic Membrane Separator. *Organic Process Research & Development*, 16, 888-900.
- CHAKRABARTI, D., DAS, G. & RAY, S. 2005. Pressure Drop in Liquid-liquid Two Phase Horizontal Flow: Experiment and Prediction. *Chemical engineering & technology*, 28, 1003-1009.
- CHARPENTIER, J.-C. 1981. Mass-transfer rates in gas-liquid absorbers and reactors. *Advances in chemical engineering*, 11, 1-133.
- CHEN, I. Y., YANG, K.-S. & WANG, C.-C. 2002. An empirical correlation for two-phase frictional performance in small diameter tubes. *International journal of heat and mass transfer*, 45, 3667-3671.
- CHIAPPE, C. & PIERACCINI, D. 2005. Ionic liquids: solvent properties and organic reactivity. *Journal of physical organic chemistry*, 18, 275-297.
- CHRISTOPHER, G. F., NOHARUDDIN, N. N., TAYLOR, J. A. & ANNA, S. L. 2008. Experimental observations of the squeezing-to-dripping transition in T-shaped microfluidic junctions. *Phys Rev E Stat Nonlin Soft Matter Phys*, 78, 036317.
- COCALIA, V. A., JENSEN, M. P., HOLBREY, J. D., SPEAR, S. K., STEPINSKI, D. C. & ROGERS, R. D. 2005. Identical extraction behavior and coordination of trivalent or hexavalent f-element cations using ionic liquid and molecular solvents. *Dalton Transactions*, 1966-1971.
- CRISTINI, V. & TAN, Y. C. 2004. Theory and numerical simulation of droplet dynamics in complex flows--a review. *Lab Chip*, 4, 257-64.
- CROSS, W. & RAMSHAW, C. 1986. Process intensification: laminar flow heat transfer. *Chemical engineering research & design*, 64, 293-301.

- DE MENECH, M., GARSTECKI, P., JOUSSE, F. & STONE, H. 2008. Transition from squeezing to dripping in a microfluidic T-shaped junction. *Journal of Fluid Mechanics*, 595, 141-161.
- DEETLEFS, M., SEDDON, K. R. & SHARA, M. 2006. Predicting physical properties of ionic liquids. *Physical Chemistry Chemical Physics*, 8, 642-649.
- DEHKORDI, A. M. 2001. Novel type of impinging streams contactor for liquid-liquid extraction. *Industrial & engineering chemistry research*, 40, 681-688.
- DEHKORDI, A. M. 2002. Liquid-liquid extraction with chemical reaction in a novel impinging-jets reactor. *AIChE journal*, 48, 2230-2239.
- DESSIMOZ, A.-L., CAVIN, L., RENKEN, A. & KIWI-MINSKER, L. 2008. Liquid-liquid two-phase flow patterns and mass transfer characteristics in rectangular glass microreactors. *Chemical Engineering Science*, 63, 4035-4044.
- DI MICELI RAIMONDI, N., PRAT, L., GOURDON, C. & COGNET, P. 2008. Direct numerical simulations of mass transfer in square microchannels for liquid-liquid slug flow. *Chemical Engineering Science*, 63, 5522-5530.
- DIETZ, M. L. & DZIELAWA, J. A. 2001. Ion-exchange as a mode of cation transfer into room-temperature ionic liquids containing crown ethers: implications for the 'greenness' of ionic liquids as diluents in liquid-liquid extraction. *Chemical Communications*, 2124-2125.
- DIETZ, M. L. & STEPINSKI, D. C. 2008. Anion concentration-dependent partitioning mechanism in the extraction of uranium into room-temperature ionic liquids. *Talanta*, 75, 598-603.
- DORE, V., TSAOULIDIS, D. & ANGELI, P. 2012. Mixing patterns in water plugs during water/ionic liquid segmented flow in microchannels. *Chemical Engineering Science*, 80, 334-341.
- DUMMANN, G., QUITTMANN, U., GRÖSCHEL, L., AGAR, D. W., WÖRZ, O. & MORGENSCHWEIS, K. 2003. The capillary-microreactor: a new reactor concept for the intensification of heat and mass transfer in liquid-liquid reactions. *Catalysis Today*, 79, 433-439.
- DZYUBA, S. V. & BARTSCH, R. A. 2002. Influence of structural variations in 1-alkyl (aralkyl)-3-methylimidazolium hexafluorophosphates and bis (trifluoromethylsulfonyl) imides on physical properties of the ionic liquids. *ChemPhysChem*, 3, 161-166.
- EDVINSSON, R. K. & IRANDOUST, S. 1996. Finite-element analysis of Taylor flow. *AIChE journal*, 42, 1815-1823.
- FAIRBROTHER, F. & STUBBS, A. E. 1935. 119. Studies in electro-endosmosis. Part VI. The "bubble-tube" method of measurement. *Journal of the Chemical Society (Resumed)*, 527-529.
- FANG, W.-F., TING, S.-C., HSU, C.-W., CHEN, Y.-T. & YANG, J.-T. 2012. Locally enhanced concentration and detection of oligonucleotides in a plug-based microfluidic device. *Lab on a Chip*, 12, 923-931.
- FERNANDES, J. & SHARMA, M. 1967. Effective interfacial area in agitated liquid-liquid contactors. *Chemical Engineering Science*, 22, 1267-1282.
- FOROUGH, H. & KAWAJI, M. 2011. Viscous oil-water flows in a microchannel initially saturated with oil: Flow patterns and pressure drop characteristics. *International Journal of Multiphase Flow*, 37, 1147-1155.
- GAAKEER, W., DE CROON, M., VAN DER SCHAAF, J. & SCHOUTEN, J. 2012. Liquid-liquid slug flow separation in a slit shaped micro device. *Chemical Engineering Journal*, 207, 440-444.



- GARSTECKI, P., FUERSTMAN, M. J., STONE, H. A. & WHITESIDES, G. M. 2006. Formation of droplets and bubbles in a microfluidic T-junction-scaling and mechanism of break-up. *Lab Chip*, 6, 437-46.
- GARSTECKI, P., STONE, H. A. & WHITESIDES, G. M. 2005. Mechanism for flow-rate controlled breakup in confined geometries: a route to monodisperse emulsions. *Phys Rev Lett*, 94, 164501.
- GAVRIILIDIS, A., ANGELI, P., CAO, E., YEONG, K. & WAN, Y. 2002. Technology and applications of microengineered reactors. *Chemical Engineering Research and Design*, 80, 3-30.
- GHAINI, A., KASHID, M. & AGAR, D. 2010. Effective interfacial area for mass transfer in the liquid-liquid slug flow capillary microreactors. *Chemical Engineering and Processing: Process Intensification*, 49, 358-366.
- GHAINI, A., MESCHER, A. & AGAR, D. W. 2011. Hydrodynamic studies of liquid-liquid slug flows in circular microchannels. *Chemical Engineering Science*, 66, 1168-1178.
- GIRIDHAR, P., VENKATESAN, K., SRINIVASAN, T. & RAO, P. 2007. Electrochemical behavior of uranium (VI) in 1-butyl-3-methylimidazolium chloride and thermal characterization of uranium oxide deposit. *Electrochimica Acta*, 52, 3006-3012.
- GIRIDHAR, P., VENKATESAN, K., SRINIVASAN, T. & RAO, P. V. 2004. Effect of alkyl group in 1-alkyl-3-methylimidazolium hexafluorophosphate ionic liquids on the extraction of uranium by tri-n-butylphosphate diluted with ionic liquids. *J Nucl Radiochem Sci*, 5, 21-26.
- GIRIDHAR, P., VENKATESAN, K., SUBRAMANIAM, S., SRINIVASAN, T. & VASUDEVA RAO, P. 2008. Extraction of uranium (VI) by 1.1 M tri-n-butylphosphate/ionic liquid and the feasibility of recovery by direct electrodeposition from organic phase. *Journal of Alloys and Compounds*, 448, 104-108.
- GÜNTHER, A. & JENSEN, K. F. 2006. Multiphase microfluidics: from flow characteristics to chemical and materials synthesis. *Lab on a Chip*, 6, 1487-1503.
- GÜNTHER, A., KHAN, S. A., THALMANN, M., TRACHSEL, F. & JENSEN, K. F. 2004. Transport and reaction in microscale segmented gas-liquid flow. *Lab on a Chip*, 4, 278-286.
- GUPTA, A. & KUMAR, R. 2010. Effect of geometry on droplet formation in the squeezing regime in a microfluidic T-junction. *Microfluidics and Nanofluidics*, 8, 799-812.
- GUPTA, A., MURSHED, S. S. & KUMAR, R. 2009. Droplet formation and stability of flows in a microfluidic T-junction. *Applied physics letters*, 94, 164107.
- GUPTA, R., LEUNG, S. S., MANICA, R., FLETCHER, D. F. & HAYNES, B. S. 2013. Hydrodynamics of liquid-liquid Taylor flow in microchannels. *Chemical Engineering Science*, 92, 180-189.
- HAN, Y. & SHIKAZONO, N. 2009. Measurement of the liquid film thickness in micro tube slug flow. *International Journal of Heat and Fluid Flow*, 30, 842-853.
- HARRIES, N., BURNS, J. R., BARROW, D. A. & RAMSHAW, C. 2003. A numerical model for segmented flow in a microreactor. *International Journal of Heat and Mass Transfer*, 46, 3313-3322.
- HEIL, M. 2001. Finite Reynolds number effects in the Bretherton problem. *Physics of Fluids (1994-present)*, 13, 2517-2521.
- HESEL, V., ANGELI, P., GAVRIILIDIS, A. & LÖWE, H. 2005. Gas-liquid and gas-liquid-solid microstructured reactors: contacting principles and applications. *Industrial & engineering chemistry research*, 44, 9750-9769.
- HOANG, D., PORTELA, L., KLEIJN, C., KREUTZER, M. & VAN STEIJN, V. 2013. Dynamics of droplet breakup in a T-junction. *Journal of Fluid Mechanics*, 717, R4.



- HOLBREY, J. D. & SEDDON, K. R. 1999. The phase behaviour of 1-alkyl-3-methylimidazolium tetrafluoroborates; ionic liquids and ionic liquid crystals. *Journal of the Chemical Society, Dalton Transactions*, 2133-2140.
- IRANDOUST, S. & ANDERSSON, B. 1989. Liquid film in Taylor flow through a capillary. *Industrial & engineering chemistry research*, 28, 1684-1688.
- JENSEN, M. P., NEUEFEIND, J., BEITZ, J. V., SKANTHAKUMAR, S. & SODERHOLM, L. 2003. Mechanisms of metal ion transfer into room-temperature ionic liquids: the role of anion exchange. *Journal of the American Chemical Society*, 125, 15466-15473.
- JOANICOT, M. & AJDARI, A. 2005. Droplet control for microfluidics. *Science*, 309, 887-888.
- JOVANOVIĆ, J., ZHOU, W., REBROV, E. V., NIJHUIS, T., HESSEL, V. & SCHOUTEN, J. C. 2011. Liquid-liquid slug flow: hydrodynamics and pressure drop. *Chemical Engineering Science*, 66, 42-54.
- KAGIMOTO, J., TAGUCHI, S., FUKUMOTO, K. & OHNO, H. 2010. Hydrophobic and low-density amino acid ionic liquids. *Journal of Molecular Liquids*, 153, 133-138.
- KASHID, M., GUPTA, A., RENKEN, A. & KIWI-MINSKER, L. 2010. Numbering-up and mass transfer studies of liquid-liquid two-phase microstructured reactors. *Chemical Engineering Journal*, 158, 233-240.
- KASHID, M. & KIWI-MINSKER, L. 2011. Quantitative prediction of flow patterns in liquid-liquid flow in micro-capillaries. *Chemical Engineering and Processing: Process Intensification*, 50, 972-978.
- KASHID, M. N. & AGAR, D. W. 2007. Hydrodynamics of liquid-liquid slug flow capillary microreactor: flow regimes, slug size and pressure drop. *Chemical Engineering Journal*, 131, 1-13.
- KASHID, M. N., AGAR, D. W. & TUREK, S. 2007a. CFD modelling of mass transfer with and without chemical reaction in the liquid-liquid slug flow microreactor. *Chemical Engineering Science*, 62, 5102-5109.
- KASHID, M. N., GERLACH, I., GOETZ, S., FRANZKE, J., ACKER, J., PLATTE, F., AGAR, D. & TUREK, S. 2005. Internal circulation within the liquid slugs of a liquid-liquid slug-flow capillary microreactor. *Industrial & engineering chemistry research*, 44, 5003-5010.
- KASHID, M. N., HARSHE, Y. M. & AGAR, D. W. 2007b. Liquid-liquid slug flow in a capillary: An alternative to suspended drop or film contactors. *Industrial & Engineering Chemistry Research*, 46, 8420-8430.
- KASHID, M. N., RENKEN, A. & KIWI-MINSKER, L. 2011. Gas-liquid and liquid-liquid mass transfer in microstructured reactors. *Chemical Engineering Science*, 66, 3876-3897.
- KAWAHARA, A., CHUNG, P.-Y. & KAWAJI, M. 2002. Investigation of two-phase flow pattern, void fraction and pressure drop in a microchannel. *International Journal of Multiphase Flow*, 28, 1411-1435.
- KIES, F. K., BENADDA, B. & OTTERBEIN, M. 2004. Experimental study on mass transfer of a co-current gas-liquid contactor performing under high gas velocities. *Chemical Engineering and Processing: Process Intensification*, 43, 1389-1395.
- KILARU, P., BAKER, G. A. & SCOVAZZO, P. 2007. Density and surface tension measurements of imidazolium-, quaternary phosphonium-, and ammonium-based room-temperature ionic liquids: data and correlations. *Journal of Chemical & Engineering Data*, 52, 2306-2314.
- KING, C., WALSH, E. & GRIMES, R. 2007. PIV measurements of flow within plugs in a microchannel. *Microfluidics and Nanofluidics*, 3, 463-472.

- KINOSHITA, H., KANEDA, S., FUJII, T. & OSHIMA, M. 2007. Three-dimensional measurement and visualization of internal flow of a moving droplet using confocal micro-PIV. *Lab on a Chip*, 7, 338-346.
- KRALJ, J. G., SAHOO, H. R. & JENSEN, K. F. 2007. Integrated continuous microfluidic liquid-liquid extraction. *Lab on a Chip*, 7, 256-263.
- KREUTZER, M. T., KAPTEIJN, F., MOULIJN, J. A. & HEISZWOLF, J. J. 2005a. Multiphase monolith reactors: Chemical reaction engineering of segmented flow in microchannels. *Chemical Engineering Science*, 60, 5895-5916.
- KREUTZER, M. T., KAPTEIJN, F., MOULIJN, J. A., KLEIJN, C. R. & HEISZWOLF, J. J. 2005b. Inertial and interfacial effects on pressure drop of Taylor flow in capillaries. *Aiche Journal*, 51, 2428-2440.
- KUHN, S., HARTMAN, R. L., SULTANA, M., NAGY, K. D., MARRE, S. & JENSEN, K. F. 2011. Teflon-Coated Silicon Microreactors: Impact on Segmented Liquid- Liquid Multiphase Flows. *Langmuir*, 27, 6519-6527.
- LABORIE, S., CABASSUD, C., DURAND-BOURLIER, L. & LAINE, J. 1999. Characterisation of gas-liquid two-phase flow inside capillaries. *Chemical Engineering Science*, 54, 5723-5735.
- LAC, E. & SHERWOOD, J. 2009. Motion of a drop along the centreline of a capillary in a pressure-driven flow. *Journal of Fluid Mechanics*, 640, 27-54.
- LECLERC, A., PHILIPPE, R., HOUZELOT, V., SCHWEICH, D. & DE BELLEFON, C. 2010. Gas-liquid Taylor flow in square micro-channels: new inlet geometries and interfacial area tuning. *Chemical Engineering Journal*, 165, 290-300.
- LIN, R. & TAVLARIDES, L. L. 2009. Flow patterns of *n*-hexadecane-CO<sub>2</sub> liquid-liquid two-phase flow in vertical pipes under high pressure. *International Journal of Multiphase Flow*, 35, 566-579.
- LINDKEN, R., ROSSI, M., GROBE, S. & WESTERWEEL, J. 2009. Micro-particle image velocimetry ( $\mu$ PIV): Recent developments, applications, and guidelines. *Lab on a Chip*, 9, 2551-2567.
- LIU, C., SHANG, J. & ZACHARA, J. M. 2011. Multispecies diffusion models: A study of uranyl species diffusion. *Water Resources Research*, 47.
- LIU, H., VANDU, C. O. & KRISHNA, R. 2005. Hydrodynamics of Taylor flow in vertical capillaries: flow regimes, bubble rise velocity, liquid slug length, and pressure drop. *Industrial & engineering chemistry research*, 44, 4884-4897.
- LIU, H. & ZHANG, Y. 2009. Droplet formation in a T-shaped microfluidic junction. *Journal of applied physics*, 106, 034906.
- LUM, J.-L., AL-WAHAIBI, T. & ANGELI, P. 2006. Upward and downward inclination oil-water flows. *International journal of multiphase flow*, 32, 413-435.
- MAC GIOLLA EAIN, M., EGAN, V. & PUNCH, J. 2013. Film thickness measurements in liquid-liquid slug flow regimes. *International Journal of Heat and Fluid Flow*, 44, 515-523.
- MALSCH, D., KIELPINSKI, M., MERTHAN, R., ALBERT, J., MAYER, G., KÖHLER, J., SÜBE, H., STAHL, M. & HENKEL, T. 2008.  $\mu$ PIV-analysis of Taylor flow in micro channels. *Chemical Engineering Journal*, 135, S166-S172.
- MARCHESSAULT, R. & MASON, S. 1960. Flow of entrapped bubbles through a capillary. *Industrial & Engineering Chemistry*, 52, 79-84.
- MEINHART, C. D., WERELEY, S. T. & SANTIAGO, J. G. 1999. PIV measurements of a microchannel flow. *Experiments in Fluids*, 27, 414-419.
- MURALI, M., BONVILLE, N. & CHOPPIN, G. 2010. Uranyl ion extraction into room temperature ionic liquids: species determination by ESI and MALDI-MS. *Solvent Extraction and Ion Exchange*, 28, 495-509.

- N. KASHID, M., RENKEN, A. & KIWI-MINSKER, L. 2011. Influence of flow regime on mass transfer in different types of microchannels. *Industrial & Engineering Chemistry Research*, 50, 6906-6914.
- NAKASIMA, K., KUBOTA, F., MARUYAMA, T. & GOTO, M. 2003. Ionic liquids as a novel solvents for lanthanides extraction. *Anal Science*, 19, 1097-1098.
- NASH, K. L. & LUMETTA, G. J. 2011. *Advanced separation techniques for nuclear fuel reprocessing and radioactive waste treatment*, Elsevier.
- NOCKEMANN, P., SERVAES, K., VAN DEUN, R., VAN HECKE, K., VAN MEERVELT, L., BINNEMANS, K. & GÖRLLER-WALRAND, C. 2007. Speciation of uranyl complexes in ionic liquids by optical spectroscopy. *Inorganic chemistry*, 46, 11335-11344.
- OLSEN, M. & ADRIAN, R. 2000. Out-of-focus effects on particle image visibility and correlation in microscopic particle image velocimetry. *Experiments in Fluids*, 29, S166-S174.
- OUADI, A., KLIMCHUK, O., GAILLARD, C. & BILLARD, I. 2007. Solvent extraction of U (VI) by task specific ionic liquids bearing phosphoryl groups. *Green Chem.*, 9, 1160-1162.
- PLECHKOVA, N. V. & SEDDON, K. R. 2008. Applications of ionic liquids in the chemical industry. *Chem Soc Rev*, 37, 123-50.
- PORCELLI, J. V. 2003. Process intensification-Has its time finally come? *Chemical engineering progress*, 99, 50-55.
- QIAN, D. & LAWAL, A. 2006. Numerical study on gas and liquid slugs for Taylor flow in a T-junction microchannel. *Chemical Engineering Science*, 61, 7609-7625.
- RAIMONDI, N. D. M. & PRAT, L. 2011. Numerical study of the coupling between reaction and mass transfer for liquid-liquid slug flow in square microchannels. *AIChE Journal*, 57, 1719-1732.
- RAMSHAW, C. 1983. Hige distillation-an example of process intensification. *Chem. Engr.*, 389, 13-14.
- RODRIGUEZ, O. & OLIEMANS, R. 2006. Experimental study on oil–water flow in horizontal and slightly inclined pipes. *International Journal of Multiphase Flow*, 32, 323-343.
- ROGERS, R. D. & SEDDON, K. R. Ionic liquids(industrial applications for green chemistry). A. C. S. symposium series, 2002. American Chemical Society.
- ROMERO, A., SANTOS, A., TOJO, J. & RODRIGUEZ, A. 2008. Toxicity and biodegradability of imidazolium ionic liquids. *Journal of Hazardous Materials*, 151, 268-273.
- ROVINSKY, J., BRAUNER, N. & MOALEM MARON, D. 1997. Analytical solution for laminar two-phase flow in a fully eccentric core-annular configuration. *International journal of multiphase flow*, 23, 523-543.
- SALIM, A., FOURAR, M., PIRONON, J. & SAUSSE, J. 2008. Oil–water two-phase flow in microchannels: Flow patterns and pressure drop measurements. *The Canadian Journal of Chemical Engineering*, 86, 978-988.
- SANTIAGO, J. G., WERELEY, S. T., MEINHART, C. D., BEEBE, D. J. & ADRIAN, R. J. 1998. A particle image velocimetry system for microfluidics. *Experiments in Fluids*, 25, 316-319.
- SARRAZIN, F., BONOMETTI, T., PRAT, L., GOURDON, C. & MAGNAUDET, J. 2008. Hydrodynamic structures of droplets engineered in rectangular micro-channels. *Microfluidics and Nanofluidics*, 5, 131-137.

- SARRAZIN, F., LOUBIERE, K., PRAT, L., GOURDON, C., BONOMETTI, T. & MAGNAUDET, J. 2006. Experimental and numerical study of droplets hydrodynamics in microchannels. *AIChE Journal*, 52, 4061-4070.
- SCHEIFF, F., HOLBACH, A. & AGAR, D. W. 2013. Slug Flow of Ionic Liquids in Capillary Microcontactors: Fluid Dynamic Intensification for Solvent Extraction. *Chemical Engineering & Technology*, 36, 975-984.
- SCHEIFF, F., MENDORF, M., AGAR, D., REIS, N. & MACKLEY, M. 2011. The separation of immiscible liquid slugs within plastic microchannels using a metallic hydrophilic sidestream. *Lab on a Chip*, 11, 1022-1029.
- SCHWARTZ, L., PRINCEN, H. & KISS, A. 1986. On the motion of bubbles in capillary tubes. *Journal of Fluid Mechanics*, 172, 259-275.
- SEDDON, K. R., STARK, A. & TORRES, M.-J. 2000. Influence of chloride, water, and organic solvents on the physical properties of ionic liquids. *Pure and Applied Chemistry*, 72, 2275-2287.
- SKELLAND, A. H. P. & WELLEK, R. M. 1964. Resistance to Mass Transfer inside Droplets. *Aiche Journal*, 10, 491-496.
- SMIGLAK, M., REICHERT, W. M., HOLBREY, J. D., WILKES, J. S., SUN, L., THRASHER, J. S., KIRICHENKO, K., SINGH, S., KATRITZKY, A. R. & ROGERS, R. D. 2006. Combustible ionic liquids by design: is laboratory safety another ionic liquid myth? *Chemical Communications*, 2554-2556.
- SONG, H., TICE, J. D. & ISMAGILOV, R. F. 2003. A microfluidic system for controlling reaction networks in time. *Angewandte Chemie*, 115, 792-796.
- SRINIVASAN, V., PAMULA, V. K. & FAIR, R. B. 2004. Droplet-based microfluidic lab-on-a-chip for glucose detection. *Analytica Chimica Acta*, 507, 145-150.
- STANKIEWICZ, A. I. & MOULIJN, J. A. 2000. Process intensification: transforming chemical engineering. *Chemical Engineering Progress*, 96, 22-34.
- SU, Y., ZHAO, Y., CHEN, G. & YUAN, Q. 2010. Liquid-liquid two-phase flow and mass transfer characteristics in packed microchannels. *Chemical Engineering Science*, 65, 3947-3956.
- TAHA, T. & CUI, Z. 2004. Hydrodynamics of slug flow inside capillaries. *Chemical Engineering Science*, 59, 1181-1190.
- TALIMI, V., MUZYCHKA, Y. & KOCABIYIK, S. 2012. A review on numerical studies of slug flow hydrodynamics and heat transfer in microtubes and microchannels. *International Journal of Multiphase Flow*, 39, 88-104.
- TAN, J., LU, Y., XU, J. & LUO, G. 2012. Mass transfer characteristic in the formation stage of gas-liquid segmented flow in microchannel. *Chemical Engineering Journal*, 185, 314-320.
- TAYLOR, G. I. 1961. Deposition of a Viscous Fluid on the Wall of a Tube. *Journal of Fluid Mechanics*, 10, 161-165.
- THORSEN, T., ROBERTS, R. W., ARNOLD, F. H. & QUAKE, S. R. 2001. Dynamic pattern formation in a vesicle-generating microfluidic device. *Phys Rev Lett*, 86, 4163-6.
- THULASIDAS, T. C., ABRAHAM, M. A. & CERRO, R. L. 1997. Flow patterns in liquid slugs during bubble-train flow inside capillaries. *Chemical Engineering Science*, 52, 2947-2962.
- TICE, J. D., LYON, A. D. & ISMAGILOV, R. F. 2004. Effects of viscosity on droplet formation and mixing in microfluidic channels. *Analytica Chimica Acta*, 507, 73-77.
- TICE, J. D., SONG, H., LYON, A. D. & ISMAGILOV, R. F. 2003. Formation of droplets and mixing in multiphase microfluidics at low values of the Reynolds and the capillary numbers. *Langmuir*, 19, 9127-9133.



- TOH, S., MCFARLANE, J., TSOURIS, C., DEPAOLI, D., LUO, H. & DAI, S. 2006. Room-temperature ionic liquids in liquid–liquid extraction: effects of solubility in aqueous solutions on surface properties. *Solvent extraction and ion exchange*, 24, 33-56.
- TRIPLETT, K., GHIAASIAAN, S., ABDEL-KHALIK, S., LEMOUEL, A. & MCCORD, B. 1999. Gas–liquid two-phase flow in microchannels: part II: void fraction and pressure drop. *International Journal of Multiphase Flow*, 25, 395-410.
- TSAOULIDIS, D., DORE, V., ANGELI, P., PLECHKOVA, N. V. & SEDDON, K. R. 2013a. Dioxouranium(VI) extraction in microchannels using ionic liquids. *Chemical Engineering Journal*, 227, 151-157.
- TSAOULIDIS, D., DORE, V., ANGELI, P., PLECHKOVA, N. V. & SEDDON, K. R. 2013b. Extraction of dioxouranium(VI) in small channels using ionic liquids. *Chemical Engineering Research & Design*, 91, 681-687.
- UFER, A., MENDORF, M., GHAINI, A. & AGAR, D. W. 2011. Liquid-Liquid Slug Flow Capillary Microreactor. *Chemical Engineering & Technology*, 34, 353-360.
- VAN BATEN, J. & KRISHNA, R. 2004. CFD simulations of mass transfer from Taylor bubbles rising in circular capillaries. *Chemical Engineering Science*, 59, 2535-2545.
- VAN DER GRAAF, S., NISISAKO, T., SCHROEN, C., VAN DER SMAN, R. & BOOM, R. 2006. Lattice Boltzmann simulations of droplet formation in a T-shaped microchannel. *Langmuir*, 22, 4144-4152.
- VAN GERVEN, T. & STANKIEWICZ, A. 2009. Structure, energy, synergy, time • The fundamentals of process intensification. *Industrial & engineering chemistry research*, 48, 2465-2474.
- VAN STEIJN, V., KLEIJN, C. R. & KREUTZER, M. T. 2010. Predictive model for the size of bubbles and droplets created in microfluidic T-junctions. *Lab on a Chip*, 10, 2513-2518.
- VAN STEIJN, V., KREUTZER, M. T. & KLEIJN, C. R. 2007.  $\mu$ -PIV study of the formation of segmented flow in microfluidic T-junctions. *Chemical Engineering Science*, 62, 7505-7514.
- VANDU, C. O., LIU, H. & KRISHNA, R. 2005. Mass transfer from Taylor bubbles rising in single capillaries. *Chemical Engineering Science*, 60, 6430-6437.
- VASUDEVA RAO, P., VENKATESAN, K. & SRINIVASAN, T. 2008. Studies on applications of room temperature ionic liquids. *Progress in Nuclear Energy*, 50, 449-455.
- VERMA, R. & SHARMA, M. 1975. Mass transfer in packed liquid–liquid extraction columns. *Chemical Engineering Science*, 30, 279-292.
- VISSER, A. E. & ROGERS, R. D. 2003. Room-temperature ionic liquids: new solvents for  $i>f</i>$ -element separations and associated solution chemistry. *Journal of Solid State Chemistry*, 171, 109-113.
- WAELECHLI, S. & RUDOLF VON ROHR, P. 2006. Two-phase flow characteristics in gas–liquid microreactors. *International journal of multiphase flow*, 32, 791-806.
- WANG, C., NGUYEN, N.-T. & WONG, T. N. 2007. Optical measurement of flow field and concentration field inside a moving nanoliter droplet. *Sensors and Actuators A: Physical*, 133, 317-322.
- WANG, J. S., SHEAFF, C. N., YOON, B., ADDLEMAN, R. S. & WAI, C. M. 2009. Extraction of uranium from aqueous solutions by using ionic liquid and supercritical carbon dioxide in conjunction. *Chemistry-A European Journal*, 15, 4458-4463.
- WARNIER, M., REBROV, E., DE CROON, M., HESSEL, V. & SCHOUTEN, J. 2008. Gas hold-up and liquid film thickness in Taylor flow in rectangular microchannels. *Chemical Engineering Journal*, 135, S153-S158.
- WASSERSCHIED, P. & WELTON, T. 2008. *Ionic liquids in synthesis*, Wiley Online Library.

- WEGMANN, A. & RUDOLF VON ROHR, P. 2006. Two phase liquid–liquid flows in pipes of small diameters. *International journal of multiphase flow*, 32, 1017-1028.
- WEI, G.-T., YANG, Z. & CHEN, C.-J. 2003. Room temperature ionic liquid as a novel medium for liquid/liquid extraction of metal ions. *Analytica Chimica Acta*, 488, 183-192.
- WESTERWEEL, J. & SCARANO, F. 2005. Universal outlier detection for PIV data. *Experiments in Fluids*, 39, 1096-1100.
- XU, B., CAI, W., LIU, X. & ZHANG, X. 2013. Mass transfer behavior of liquid–liquid slug flow in circular cross-section microchannel. *Chemical Engineering Research and Design*, 91, 1203-1211.
- XU, J., LUO, G., LI, S. & CHEN, G. 2006. Shear force induced monodisperse droplet formation in a microfluidic device by controlling wetting properties. *Lab on a Chip*, 6, 131-136.
- XU, J. H., LI, S. W., TAN, J. & LUO, G. S. 2008. Correlations of droplet formation in T-junction microfluidic devices: from squeezing to dripping. *Microfluidics and Nanofluidics*, 5, 711-717.
- ZHAO, Y., CHEN, G. & YUAN, Q. 2006. Liquid-liquid two-phase flow patterns in a rectangular microchannel. *AIChE journal*, 52, 4052-4060.
- ZHAO, Y., CHEN, G. & YUAN, Q. 2007. Liquid–liquid two-phase mass transfer in the T-junction microchannels. *AIChE journal*, 53, 3042-3053.
- ZHENG, B., TICE, J. D., ROACH, L. S. & ISMAGILOV, R. F. 2004. A Droplet-Based, Composite PDMS/Glass Capillary Microfluidic System for Evaluating Protein Crystallization Conditions by Microbatch and Vapor-Diffusion Methods with On-Chip X-Ray Diffraction. *Angewandte chemie international edition*, 43, 2508-2511.

## Appendix A: Calculation of the circulation time

The two-dimensional simplification of Eq. (5.4.1) into Eq. (5.4.2) is valid for a plane (xy). Since the PIV measurements were also obtained on a plane, Eq. (5.4.2) gives the circulation times on this plane. If 2D data were used in Eq. (5.4.1), this would assume a certain velocity profile along the channel depth (axisymmetric flow). This may not be wrong but it does involve an assumption, as 3D experimental data were not obtained. The use of Eq. (5.4.1) will only lead to higher values of the circulation time compared to Eq. (5.4.2), i.e.  $\tau_{3-D}=1.6\tau$ , without changing any trends or their significance. This is because Eq. (5.4.1) represents an average along the  $z$  direction; while Eq. (5.4.2) represents the mid-plane only where velocities are expected to be higher (i.e. circulation time is expected to be lower). This slight difference can be seen in **Figure A 1** below where the non-dimensional circulation times found from both equations are compared.

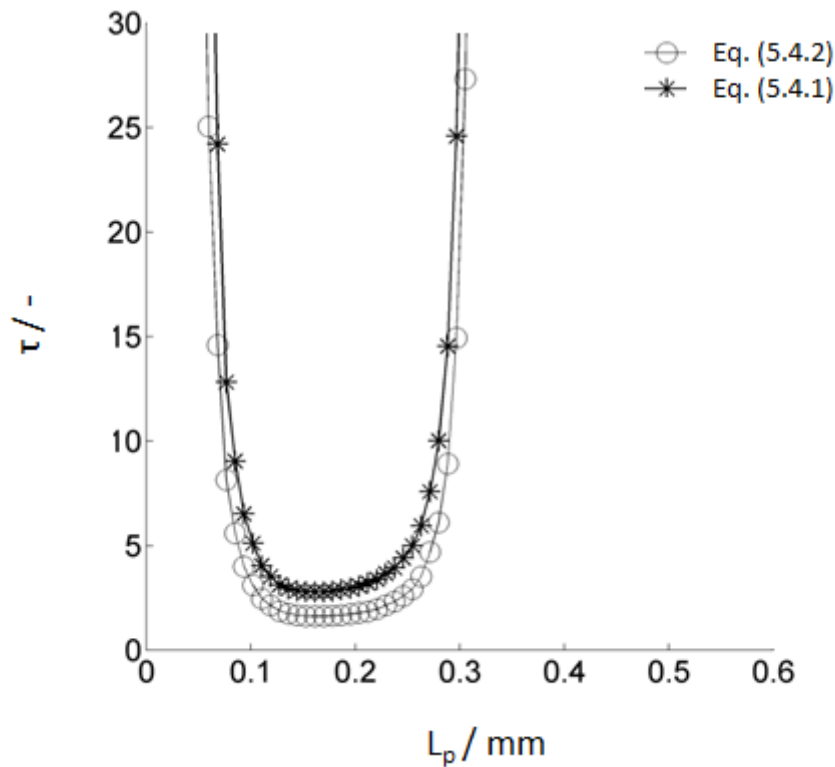


**Figure A 1:** Comparison between non dimensional circulation time profiles found using Eq. (5.4.1) and Eq. (5.4.2) for the same experimental conditions.

## Appendix B: Circulation patterns at the bend of the channel

Circulation patterns were also obtained at the bend of the channel for different orientations of the plug centre, using both liquids (i.e. ionic liquid and water) as carrier fluid. It was found that the vortex internal symmetry is broken at the channel bend regardless which liquid is the carrier fluid, as shown in **Figure B 1**, where the stretching and the folding of the fluid are clearly observable and a single main vortex is revealed toward the inner meander of the channel. This effect, combined with the reorientation of the fluid given by a sequence of bends, triggers a more effective mixing across the transversal direction ( $y$ ).

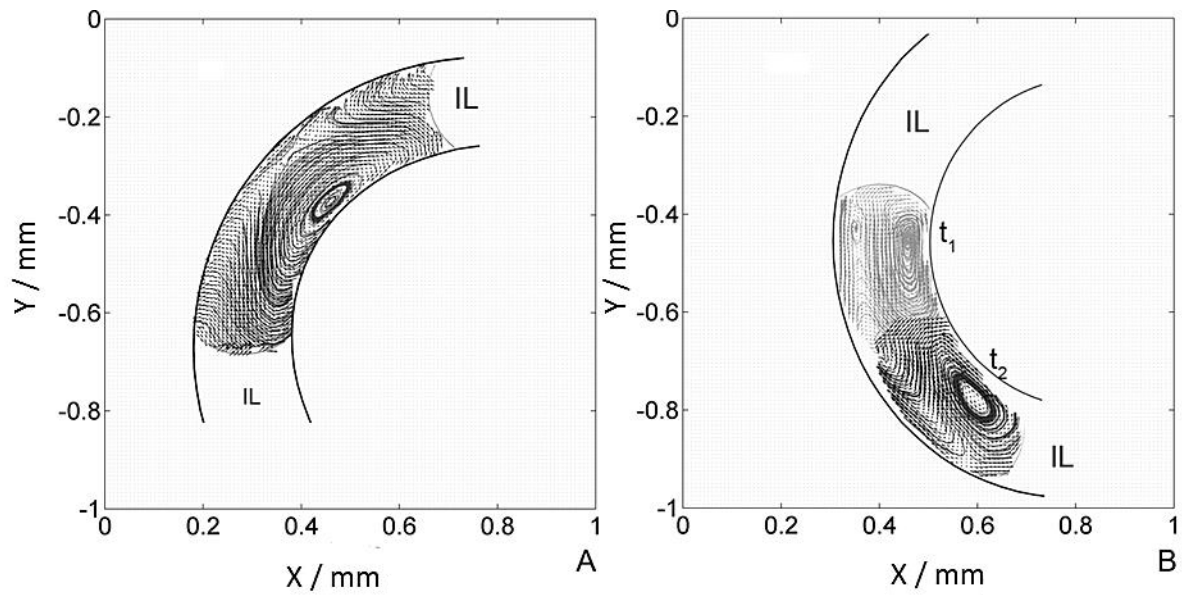


**Figure B 1:** Ensemble averaged circulation pattern within a single water plug at a bend for different orientations of the plug centre (i.e. 0,  $t_1$ , and 45 degree,  $t_2$ ), when water (A) and ionic liquid (B) was the carrier. Sixty instantaneous fields were averaged



## Appendix C: MATLAB code for image processing

The high resolution images acquired with the high speed camera were used for the measurements of the hydrodynamics and mixing characteristics as discussed in [section 3.5.1.2](#). A script that allocates the plugs in an initial position and renames the files so they can be used in Insight 4G is presented.

```
%%Move plug to initial position
clear all
close all
clc

%path of data file
path='E:\hydrop\2mm\ratio1\0.01m_s\pl\New folder (2)\';
mkdir(path,'newimage2')
path2=strcat(path,'newimage2\');

imgs=dir(strcat(path,'*.tif')); % Change to jpg when the format is
different

%initialization/allocation
if(mod(length(imgs),2)~=0),
    error('not enough number of pics to put them in pairs!');
end
col=length(imgs)/2;
imgLA=cell(1,col);
imgLB=cell(1,col);
i=0; %counter
j=0;

for k=1:numel(imgs)

    if(mod(k, 2) == 1),
        i=i+1;
        imgLA{i} = imread(strcat(path,imgs(k).name));
        if(k==1),
            [a, b]=size(imgLA{k}); %check the size of the image for
allocation , assume each image is the same size!
        end
    else
        j=j+1;
        imgLB{j} = imread(strcat(path,imgs(k).name));
    end

end

n=input('give the pixels shift: \n');

imgLA_new=cell(1,col);
imgLA_new(:) = {zeros(a, b)};
%imgLA_new=uint8(imgLA_new);
imgLB_new=cell(1,col);
imgLB_new(:) = {zeros(a, b)};
%imgLB_new=uint8(imgLB_new);
```

```
for l=1:col,

    for m=1:b-((col-1)*2*n),
        imgLA_new{l}(:,m)=imgLA{l}(:,m+(l-1)*2*n);
        imgLB_new{l}(:,m)=imgLB{l}(:,m+(l-1)*2*n);
    end

end

for h=1:col,

    imgLA_new{h}=uint8(imgLA_new{h});
    imgLB_new{h}=uint8(imgLB_new{h});

end

%%save
new_name={imgs(1).name(1:end-7)}; %cut last 5 or 7

for h=1:col,

    imwrite(imgLA_new{h},strcat(path2,new_name,sprintf('%03d',h),'.LA.tif'),'tif');

    imwrite(imgLB_new{h},strcat(path2,new_name,sprintf('%03d',h),'.LB.tif'),'tif');

end
```

## Appendix D: Sensitivity analysis of diffusion coefficient

The diffusion coefficients of dioxouranium(VI) ions in the ionic liquid phase was obtained based on literature correlations, since no exact information exists. Diffusion coefficients of dioxouranium in ionic liquids in literature (Giridhar et al., 2007, Liu et al., 2011) varied from  $10^{-12}$  to  $10^{-10} \text{ m}^2 \text{ s}^{-1}$ . However, it can be seen that the diffusion coefficient has negligible effect on the mass transfer within that range.

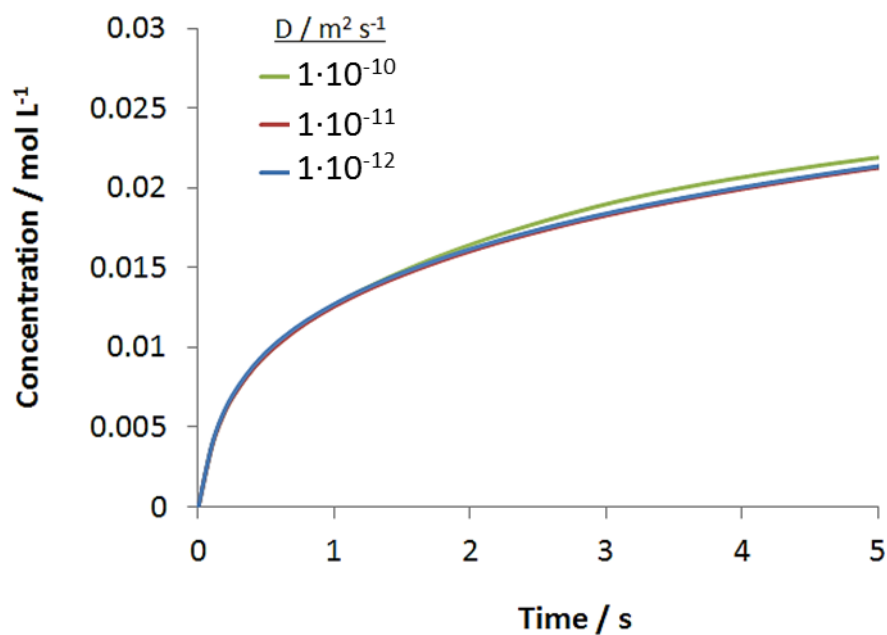


**Figure D 1: Concentration of dioxouranium(VI) in the ionic liquid phase as a function of time for different diffusion coefficients.**

## Appendix E: Numerical model report

A short report for the numerical model developed in chapter 7 is provided. The simulation environment is Comsol Multiphysics 4.4.

### 1. Global Definitions

#### 1.1. Parameters

Name	Expression	Description
K	3.16	Partition coefficient
M	10e1[m/s]	Stiff-spring velocity
u_TP	0.036-0.039[m/s]	Experimental plug velocity
c0	0.05[mol/L]	Initial concentration in the droplet
t_step	5[ms]	Step time

### 2. Model

#### 2.1. Definitions

Name	Expression	Description
c_all	c1	Concentration in droplet
c_all	c2	Concentration in IL phase
N_partition	$M \cdot (c2 - K \cdot c1) \cdot \text{step1}(t/t\_step)$	Flux across boundary
n_droplet	int_droplet(c1)	Moles of solute (droplet)
n_flow	int_flow(c2)	Moles of solute (flow)
n_tot	n_droplet + n_flow	Moles of solute (total)

#### Integration

Coupling type	Integration
Operator name	int_flow

#### Source selection

Geometric entity level	Domain
Selection	Domain 1

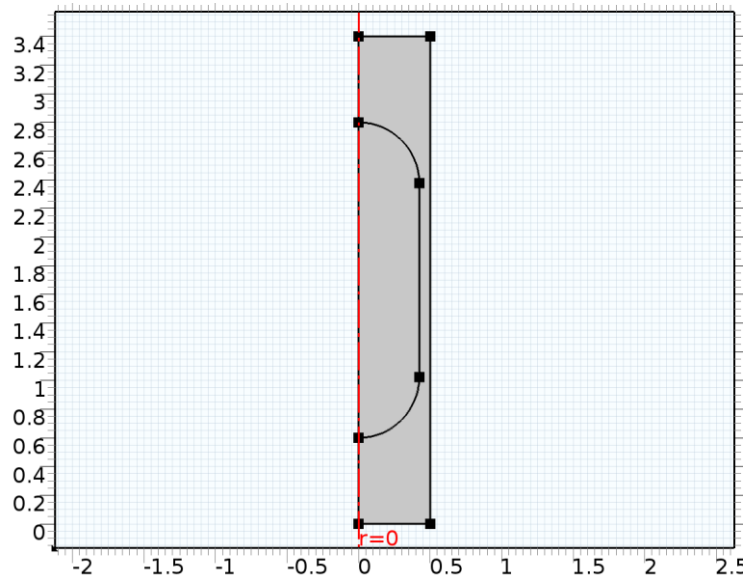
#### Boundary System 1

Coordinate system type	Boundary system
Identifier	sys1

## Settings

Name	Value
Coordinate names	{t1, to, n}
Create first tangent direction from	Global Cartesian

## 2.2. Geometry



## Units

Length unit	mm
Angular unit	deg

## Geometry statistics

Property	Value
Space dimension	2
Number of domains	2
Number of boundaries	9
Number of vertices	8

## 2.3. Laminar flow

## Selection

Geometric entity level	Domain
Selection	Domains 1–2

## Equations

$$\rho(\mathbf{u} \cdot \nabla)\mathbf{u} =$$

$$\nabla \cdot \left[ -p\mathbf{I} + \mu(\nabla \mathbf{u} + (\nabla \mathbf{u})^T) \right] + \mathbf{F}$$

$$\rho \nabla \cdot \mathbf{u} = 0$$

## Settings

Description	Value
Discretization of fluids	P1 + P1
Value type when using splitting of complex variables	{Real, Real, Real, Real, Real, Real, Real, Real, Real}
Neglect inertial term (Stokes flow)	Off
Swirl flow	Off

## Variables

Name	Expression	Unit	Description	Selection
spf.rho	model.input.rho	kg/m <sup>3</sup>	Density	Domain 1
spf.mu	model.input.mu	Pa*s	Dynamic viscosity	Domain 1
spf.divu	ur+if(abs(r)<0.0010*h,ur,u/r)+wz	1/s	Divergence of velocity field	Domain 1
spf.sr	sqrt(0.5*(4*ur^2+2*(uz+wr)^2+4*if(abs(r)<0.0010*h,ur,u/r)^2+4*wz^2)+eps)	1/s	Shear rate	Domain 1
spf.Fr	0	N/m <sup>3</sup>	Volume force, r component	Domain 1
spf.Fphi	0	N/m <sup>3</sup>	Volume force, phi component	Domain 1
spf.Fz	0	N/m <sup>3</sup>	Volume force, z component	Domain 1
spf.U	sqrt(u^2+w^2)	m/s	Velocity magnitude	Domain 1
spf.vorticityr	0	1/s	Vorticity field, r component	Domain 1
spf.vorticityphi	-wr+uz	1/s	Vorticity field, phi component	Domain 1
spf.vorticityz	0	1/s	Vorticity field, z component	Domain 1
spf.vort_magn	sqrt(spfvorticityr^2+spfvorticityphi^2+spfvorticityz^2)	1/s	Vorticity magnitude	Domain 1
spf.cellRe	0.25*spf.rho*sqrt(emetri c(u,w)/emetric2)/spf.mu	1	Cell Reynolds number	Domain 1

Name	Expression	Unit	Description	Selection
spf.nu	spf.mu/spf.rho	m <sup>2</sup> /s	Kinematic viscosity	Domain 1
spf.betaT	0	1/Pa	Isothermal compressibility coefficient	Domain 1
spf.T_stressr	2*spf.mu*ur*spf.nrmesh+spf.mu*(uz+wr)*spf.nzmesh-p*spf.nrmesh	N/m <sup>2</sup>	Total stress, r component	Boundaries 2, 5–9
spf.T_stressphi	spf.nphimesh*(2*spf.mu*if(abs(r)<0.0010*h,ur,u/r)-p)	N/m <sup>2</sup>	Total stress, phi component	Boundaries 2, 5–9
spf.T_stressz	spf.mu*(wr+uz)*spf.nrmesh+2*spf.mu*wz*spf.nzmesh-p*spf.nzmesh	N/m <sup>2</sup>	Total stress, z component	Boundaries 2, 5–9
spf.K_stressr	spf.mu*(2*ur*spf.nrmesh+(uz+wr)*spf.nzmesh)	N/m <sup>2</sup>	Viscous stress, r component	Boundaries 2, 5–9
spf.K_stressphi	2*spf.mu*if(abs(r)<0.0010*h,ur,u/r)*spf.nphimesh	N/m <sup>2</sup>	Viscous stress, phi component	Boundaries 2, 5–9
spf.K_stressz	spf.mu*((wr+uz)*spf.nrmesh+2*wz*spf.nzmesh)	N/m <sup>2</sup>	Viscous stress, z component	Boundaries 2, 5–9
spf.upwind_helprr	u	m/s		Domain 1
spf.upwind_helpphi	0	m/s		Domain 1
spf.upwind_helpz	w	m/s		Domain 1
spf.K_stress_tensorr	2*spf.mu*ur	N/m <sup>2</sup>	Viscous stress tensor, rr component	Domain 1
spf.K_stress_tensorphi	0	N/m <sup>2</sup>	Viscous stress tensor, phir component	Domain 1
spf.K_stress_tensorzr	spf.mu*(wr+uz)	N/m <sup>2</sup>	Viscous stress tensor, zr component	Domain 1
spf.K_stress_tensorrphi	0	N/m <sup>2</sup>	Viscous stress tensor, rphi component	Domain 1
spf.K_stress_tensorphi	2*spf.mu*if(abs(r)<0.0010*h,ur,u/r)	N/m <sup>2</sup>	Viscous stress tensor, phiphi component	Domain 1
spf.K_stress_tensorzphi	0	N/m <sup>2</sup>	Viscous stress tensor, zphi component	Domain 1
spf.K_stress_tensorrz	spf.mu*(uz+wr)	N/m <sup>2</sup>	Viscous stress tensor, rz component	Domain 1
spf.K_stress_tensorphi	0	N/m <sup>2</sup>	Viscous stress tensor,	Domain 1

Name	Expression	Unit	Description	Selection
z			phiz component	
spf.K_stress_tensorzz	$2 * \text{spf.mu} * \text{wz}$	N/m <sup>2</sup>	Viscous stress tensor, zz component	Domain 1
spf.K_stress_tensor_testrr	$2 * \text{spf.mu} * \text{test(ur)}$	N/m <sup>2</sup>	Viscous stress tensor test, rr component	Domain 1
spf.K_stress_tensor_testphir	0	N/m <sup>2</sup>	Viscous stress tensor test, phir component	Domain 1
spf.K_stress_tensor_testzr	$\text{spf.mu} * (\text{test(wr)} + \text{test(uz)})$	N/m <sup>2</sup>	Viscous stress tensor test, zr component	Domain 1
spf.K_stress_tensor_testrphi	0	N/m <sup>2</sup>	Viscous stress tensor test, rphi component	Domain 1
spf.K_stress_tensor_testphiphi	$2 * \text{spf.mu} * \text{if}(\text{abs(r)} < 0.0010 * \text{h}, \text{test(ur)}, \text{test(u)/r})$	N/m <sup>2</sup>	Viscous stress tensor test, phiphi component	Domain 1
spf.K_stress_tensor_testzphi	0	N/m <sup>2</sup>	Viscous stress tensor test, zphi component	Domain 1
spf.K_stress_tensor_testrz	$\text{spf.mu} * (\text{test(uz)} + \text{test(wr)})$	N/m <sup>2</sup>	Viscous stress tensor test, rz component	Domain 1
spf.K_stress_tensor_testphiz	0	N/m <sup>2</sup>	Viscous stress tensor test, phiz component	Domain 1
spf.K_stress_tensor_testzz	$2 * \text{spf.mu} * \text{test(wz)}$	N/m <sup>2</sup>	Viscous stress tensor test, zz component	Domain 1
spf.res_u	$\text{pr} + \text{spf.rho} * \text{u} * \text{ur} + \text{spf.rho} * \text{w} * \text{uz} - (\text{d}(2 * \text{ur}, \text{r}) + \text{if}(\text{abs(r)} < 0.0010 * \text{h}, \text{d}(2 * \text{ur}, \text{r}), 2 * \text{ur}/\text{r}) + \text{d}(\text{uz} + \text{wr}, \text{z}) - 2 * \text{if}(\text{abs(r)} < 0.0010 * \text{h}, \text{ur}, \text{u}/\text{r})/\text{r}) * \text{spf.mu} - \text{spf.Fr}$	N/m <sup>3</sup>	Equation residual	Domain 1
spf.res_v	$-\text{spf.Fphi}$	N/m <sup>3</sup>	Equation residual	Domain 1
spf.res_w	$\text{spf.rho} * \text{u} * \text{wr} + \text{pz} + \text{spf.rho} * \text{w} * \text{wz} - (\text{d}(\text{wr} + \text{uz}, \text{r}) + \text{if}(\text{abs(r)} < 0.0010 * \text{h}, \text{d}(\text{wr} + \text{uz}, \text{r}), (\text{wr} + \text{uz})/\text{r}) + \text{d}(2 * \text{wz}, \text{z})) * \text{spf.mu} - \text{spf.Fz}$	N/m <sup>3</sup>	Equation residual	Domain 1
spf.res_p	$\text{spf.rho} * \text{spf.divu}$	kg/(m <sup>3</sup> *s)	Pressure equation residual	Domain 1



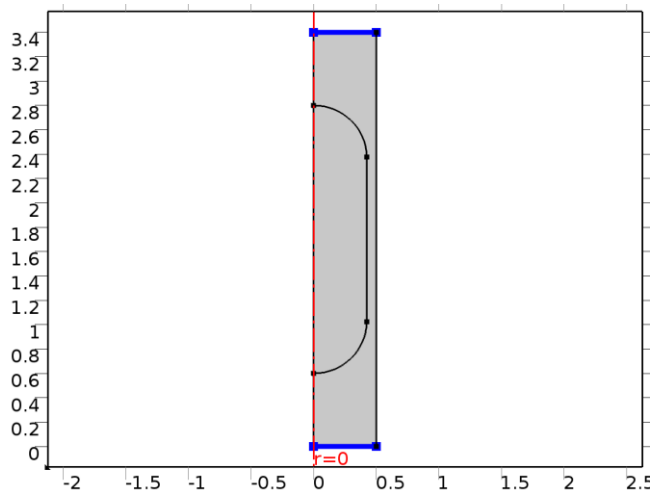
## Shape functions

Name	Shape function	Unit	Description	Shape frame	Selection
u	Lagrange (Linear)	m/s	Velocity field, r component	Material	Domain 1
w	Lagrange (Linear)	m/s	Velocity field, z component	Material	Domain 1
p	Lagrange (Linear)	Pa	Pressure	Material	Domain 1

## Weak expressions

Weak expression				Integration frame	Selection
2*((p-spf.K_stress_tensorrr)*test(ur)- spf.K_stress_tensorrz*test(uz)+(p- spf.K_stress_tensorphiphi)*if(abs(r)<0.0010*h,test(ur),test(u)/r)- spf.K_stress_tensorrzr*test(wr)+(p- spf.K_stress_tensorzz)*test(wz))*pi*r				Material	Domain 1
2*(spf.Fr*test(u)+spf.Fz*test(w)-spf.rho*(ur*u+uz*w)*test(u)- spf.rho*(wr*u+wz*w)*test(w))*pi*r				Material	Domain 1
-2*spf.rho*spf.divu*test(p)*pi*r				Material	Domain 1
2*spf.crosswindns*pi*r				Material	Domain 1
2*spf.streamlinens*pi*r				Material	Domain 1
spf.uwallz	-u_TP	m/s	Velocity of moving wall, z component	Boundary 7	

## Periodic Flow Condition 1



## Selection

Geometric entity level	Boundary
Selection	Boundaries 2, 5

## Equations

$$\underline{u}_{source} = \underline{u}_{dest}, \quad p_{source} = p_{dest}$$

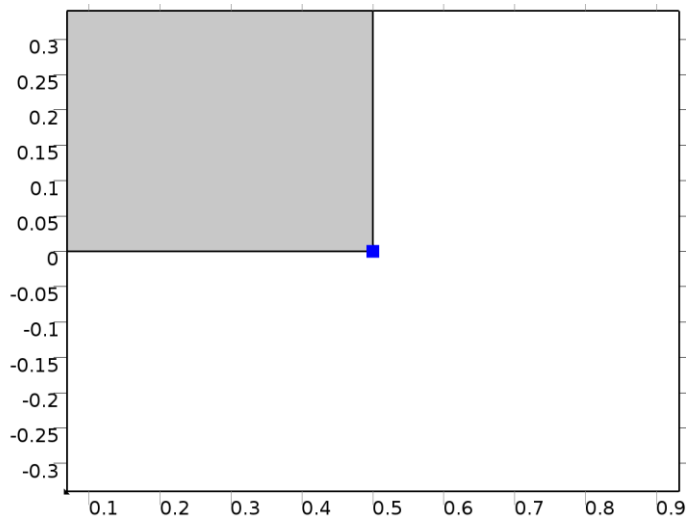
## Settings

Description	Value
Pressure difference	0
Apply reaction terms on	All physics (symmetric)
Use weak constraints	Off

## Destination Selection 1

Geometric entity level	Boundary
Selection	Boundary 2

## Pressure Point Constraint 1



## Selection

Geometric entity level	Point
Selection	Point 7

## Settings

Description	Value
Pressure	1
Apply reaction terms on	All physics (symmetric)
Use weak constraints	Off

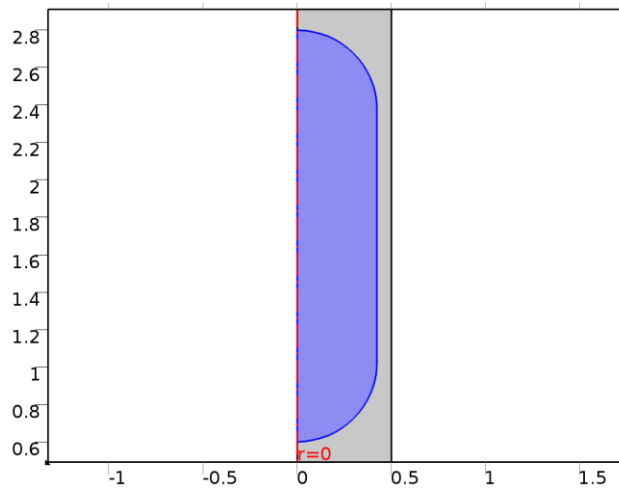
## Variables

Name	Expression	Unit	Description	Selection
spf.p0	1	Pa	Pressure	Point 7

## Shape functions

Constraint	Constraint force	Shape function	Selection
-p+spf.p0	test(-p+spf.p0)	Lagrange (Linear)	Point 7

## 2.4. Transport of diluted species



### Selection

Geometric entity level	Domain
Selection	Domain 2

### Equations

$$\frac{\partial c_i}{\partial t} + \nabla \cdot (-D_i \nabla c_i + \mathbf{u} c_i) = R_i$$

$$\mathbf{N}_i = -D_i \nabla c_i + \mathbf{u} c_i$$

### Settings

Description	Value
Concentration	Linear
Compute boundary fluxes	On
Apply smoothing to boundary fluxes	On
Value type when using splitting of complex variables	Real
Migration in electric field	0
Convection	1
Convective term	Conservative form
Equation residual	Approximate residual
Enable space-dependent physics interfaces	0
Synchronize with COMSOL Multiphysics	

### Convection-diffusion

### Selection

Geometric entity level	Domain
Selection	Domain 2

## Equations

$$\nabla \cdot (-D_i \nabla c_i + \mathbf{u} c_i) = R_i$$

$$\mathbf{N}_i = -D_i \nabla c_i + \mathbf{u} c_i$$

## Settings

Description	Value
Velocity field	Velocity field (spf)
Electric potential	User defined
Electric potential	0
Diffusion coefficient	User defined
Diffusion coefficient	{{ 7e-10[m^2/s], 0, 0}, {0, 7e-10[m^2/s], 0}, {0, 0, 7e-10[m^2/s]}}
Bulk material	None

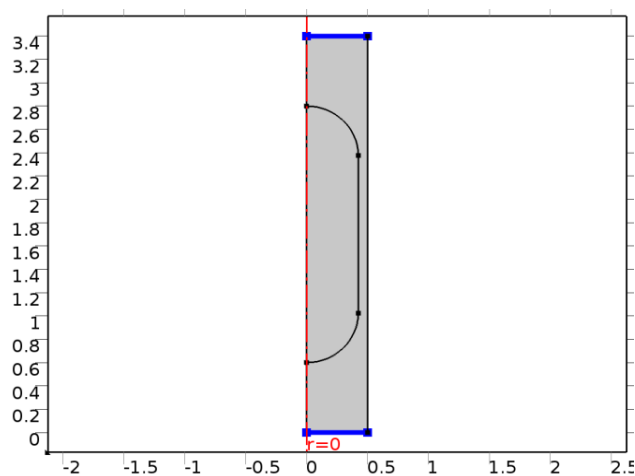
## Shape functions

Name	Shape function	Unit	Description	Shape frame	Selection
c1	Lagrange (Linear)	mol/m^3	Concentration	Material	Domain 2

## Weak expressions

Weak expression	Integration frame	Selection
2*(-d(c1,t)*test(c1)- (chds.Drr_c1*c1r+chds.Drz_c1*c1z)*test(c1r)- (chds.Dzr_c1*c1r+chds.Dzz_c1*c1z)*test(c1z))*pi*r	Material	Domain 2
2*c1*(chds.u*test(c1r)+chds.w*test(c1z))*pi*r	Material	Domain 2
2*chds.cbf_c1*test(c1)*pi*r	Material	Boundaries 3, 6, 8–9
2*chds.streamline*pi*r	Material	Domain 2
2*chds.crosswind*pi*r	Material	Domain 2

## Periodic Condition



## Equations

$$C_{i,src} = C_{i,dst}$$

$$-\mathbf{n}_{src} \cdot \mathbf{N}_{i,src} = \mathbf{n}_{dst} \cdot \mathbf{N}_{i,dst}$$

## 2.5. Meshes

## Mesh statistics

Property	Value
Minimum element quality	0.3305
Average element quality	0.9577
Triangular elements	48900
Quadrilateral elements	702
Edge elements	1418
Vertex elements	8

## Free Triangular (settings)

Name	Value
Maximum element size (μm)	1.6-3
Minimum element size (μm)	0.1-0.4
Curvature factor	0.25
Curvature factor	Off
Resolution of narrow regions	Off
Maximum element growth rate	1.25
Maximum element growth rate	Off
Predefined size	Finer
Custom element size	Custom